



# BROADBAND VARIABILITY OF THE BLACK HOLE CANDIDATE CYGNUS X-1

BREITBANDVARIABILITÄT DES  
SCHWARZLOCHKANDIDATEN CYGNUS X-1

Diplomarbeit  
im Studiengang Diplom-Physik vorgelegt von

Victoria Grinberg<sup>1</sup>  
aus Chisinau

Betreuernder Gutachter: Prof. Dr. Harald Lesch  
Zweiter Gutachter: Prof. Dr. Werner Becker

Bamberg, den 10. Juni 2010

---

<sup>1</sup>e-mail: victoria.grinberg@sternwarte.uni-erlangen.de



# Contents

<b>1</b>	<b>Introduction</b>	<b>5</b>
1.1	Astrophysics at High Energies . . . . .	5
1.2	Thesis Outline . . . . .	5
<b>2</b>	<b>Microquasars</b>	<b>7</b>
2.1	Formation . . . . .	7
2.2	Inflow: Accretion . . . . .	9
2.3	Outflow: Jets . . . . .	13
2.4	The States of Microquasars – the q-Track . . . . .	14
2.5	Cygnus X-1 . . . . .	20
<b>3</b>	<b>Radiative Processes</b>	<b>26</b>
3.1	Black Body Radiation . . . . .	26
3.2	Comptonization . . . . .	26
3.3	Synchrotron Radiation . . . . .	28
3.4	Relativistic Iron Line . . . . .	30
<b>4</b>	<b>Instrumentation and Data Reduction</b>	<b>33</b>
4.1	X-ray Detectors . . . . .	33
4.1.1	Proportional Counters . . . . .	33
4.1.2	Coded Mask Instruments . . . . .	34
4.2	<i>RXTE</i> . . . . .	36
4.2.1	The Satellite . . . . .	36
4.2.2	ASM . . . . .	36
4.2.3	PCA . . . . .	37
4.2.4	HEXTE . . . . .	40
4.2.5	Data Reduction . . . . .	41
4.3	<i>INTEGRAL</i> . . . . .	41
4.3.1	The Satellite . . . . .	41
4.3.2	The IBIS Instrument . . . . .	42
4.3.3	Observing Strategy . . . . .	44
4.3.4	Data Structure . . . . .	45
4.3.5	Data Reduction Pipeline . . . . .	46
4.4	<i>Ryle/AMI</i> . . . . .	48
<b>5</b>	<b>Analysis Methods</b>	<b>49</b>
5.1	Spectral Analysis . . . . .	49
5.1.1	From Source Flux to Detector Counts . . . . .	49
5.1.2	Spectral Fitting and ISIS . . . . .	50
5.2	Timing Analysis . . . . .	51
5.2.1	The Discrete Fourier Transform . . . . .	52
5.2.2	Power Spectral Density (PSD) . . . . .	52
5.2.3	Cross Power Density (CPD) . . . . .	54
5.2.4	Coherence Function . . . . .	54
5.2.5	Phase- and Time Lag-Spectrum . . . . .	55
5.3	Fit Functions . . . . .	56

<b>6 X-ray Spectral and Timing Analysis: <i>RXTE</i></b>	<b>60</b>
6.1 Spectral Analysis . . . . .	60
6.1.1 Overview over the Available Data . . . . .	60
6.1.2 Empirical Model: Broken Power Law . . . . .	62
6.1.3 Comptonization Model: CompTT . . . . .	63
6.1.4 Summary . . . . .	64
6.2 Timing Analysis During a Radio Flare . . . . .	65
6.2.1 PSD Evolution . . . . .	66
6.2.2 Coherence . . . . .	70
6.2.3 Time Lag Evolution . . . . .	71
6.2.4 Interpretation . . . . .	72
<b>7 X-ray Spectral and Timing Analysis: <i>INTEGRAL</i></b>	<b>75</b>
7.1 The Cyg X-1 Key Programme . . . . .	75
7.1.1 Overview of the Observations . . . . .	75
7.1.2 Observing Strategy: From Hex to Random Pointing Mode . . . . .	75
7.2 Image Reconstruction . . . . .	79
7.2.1 Comparison of Different Extraction Methods . . . . .	79
7.2.2 Mosaics . . . . .	81
7.2.3 3A 1954-319 – an Interesting Source in the Field . . . . .	82
7.3 Timing Analysis . . . . .	83
7.3.1 Comparison of <code>ii_light</code> and <code>ii_lc_extract</code> . . . . .	83
7.3.2 High Time Resolution with <code>ii_light</code> . . . . .	86
7.3.3 Alternative PIF-based Extraction Algorithm . . . . .	88
7.3.4 PSDs . . . . .	90
7.3.5 Flux Distribution . . . . .	92
7.4 Spectral Analysis . . . . .	93
7.4.1 Tungsten Instrumental Background Line . . . . .	94
7.4.2 Systematic Errors . . . . .	99
7.4.3 Spectral Modelling . . . . .	101
<b>8 Jet Fits: Joint <i>RXTE</i>, <i>INTEGRAL</i> and <i>Ryle/AMI</i> Spectral Analysis</b>	<b>105</b>
8.1 Overview over the Data . . . . .	105
8.2 Broken Power Law Fits . . . . .	107
8.3 Jet Fits . . . . .	110
8.3.1 ‘agnjet’-Model . . . . .	111
8.3.2 Fitting Method and Start Parameters . . . . .	113
8.3.3 Fit Results . . . . .	116
8.3.4 Conclusions . . . . .	122
<b>9 Summary and Outlook</b>	<b>124</b>
9.1 Summary . . . . .	124
9.2 Outlook . . . . .	125
<b>References</b>	<b>127</b>
<b>Acknowledgements</b>	<b>132</b>

# 1 Introduction

*If your telescope doesn't recoil when it detects a photon,  
it's not a proper photon.  
– Tony Bird –*

## 1.1 Astrophysics at High Energies

Although astronomy is perhaps one of the oldest sciences, high energy astronomy and astrophysics are a young branch, however of such importance, that they have their own subsection with the astrophysics' most important pre-print server astro-ph.

The perhaps first step towards observations of the sky at high energies was made by Golian et al. (1946) who used V-2 rockets and Geiger counters. While they detected the sun itself as a source of X-rays, it was for a long time afterwards believed that no radiation from extrasolar sources was strong enough to be observed. It was one and a half decades later that Giacconi et al. (1962) published their ‘Evidence for X-Rays From Sources Outside the Solar System’, where they first detected Sco X-1, again with a rocket experiment bearing three Geiger counters. More rocket borne experiments and finally a satellite mission, *Uhuru* (December 1970 – March 1973, see Forman et al., 1978, for a catalogue of sources detected), followed. The field has grown and expanded from then on – a nice, short overview is given by Charles & Fabian (2001) – and both space-borne and ground bases experiments dedicated to even higher energies than those of the X-ray (e.g, *Fermi*, *MAGIC* or *AGILE*) were built.

High energies offer an unprecedented insight into a plethora of phenomena in extreme environments: accretion onto compact objects, whether neutron stars, galactic black holes or supermassive black holes in active galactic nuclei (AGN); Gamma ray bursts, which are thought to originate in the most powerful supernova explosions in the universe; hot gas in galaxy clusters and the cooling flow problem, and many more.

## 1.2 Thesis Outline

This work concentrates on compact objects in black holes binaries, specifically on the black hole candidate Cyg X-1, as observed with the *RXTE* and *INTEGRAL* satellites and the radio telescope *Ryle/AMI*. Cyg X-1 is a microquasar, which accretes matter from its binary partner, HDE 226868, an O type supergiant.

I first introduce the general theory of microquasars and their states as well as Cyg X-1, the best suitable source for the analysis presented here, itself in chapter 2. The focus here lies especially on the so-called q-track. Radiation processes, explained in chapter 3, constitute the physical framework for the origin of the observed radiation.

A precondition for any data analysis is a thorough understanding of the instruments used. Therefore the *RXTE*, *INTEGRAL* and *Ryle/AMI* instruments as well as the basic of the data reduction for these instruments are introduced in chapter 4. The analysis methods employed for the X-ray spectral and timing variability studies are explained in chapter 5. Although the main focus of this work is the behaviour of Cyg X-1, this analysis cannot produce meaningful results without a thorough understanding of the detection process and the individual steps of the data reduction pipelines. This is especially the case for the more complex coded mask instruments like *INTEGRAL*,

but also plays a role for *RXTE*. In chapter 6 I present results of the spectral analysis of the *RXTE* ongoing bi-weekly observation campaign as well as the timing analysis results for *RXTE* observations during a radio flare. Timing and spectral analysis with a special focus on calibration issues of *INTEGRAL* data is presented in chapter 7. The last step is a joined analysis of *INTEGRAL* and *RXTE* data of Cyg X-1 in chapter 8: a complex physical model of the inflow and ejection mechanisms is used to describe the broadband spectrum in radio and in X-rays/soft gamma rays.

Finally, chapter 9 contains a short summary of the results and an outlook onto future work.

# 2 Microquasars

*Microquasars  
can also be thought of as a form of  
quasars for the impatient  
– Elena Gallo (2010) –*

In our galaxy, more than 20 compact objects in binary systems have a mass above  $\sim 3\text{--}4 M_{\odot}$  and can therefore be identified as black holes – the total population of stellar mass black holes in our galaxy may amount to as much as  $10^8$  objects (McClintock & Remillard, 2006).

Microquasars (MQs) are black holes in binary systems which mimic many phenomena seen in quasars albeit on a much smaller scale. They are the best laboratories for studying accretion: the deep potential well allows for testing of theories in an extreme environment, while the variability on short timescales – as opposed to AGN with their long variability timescales (e.g., Uttley et al., 2005) –, the luminosity and the proximity, with the two last resulting in a comparatively high flux, make observations of microquasars profitable in scientific results.

The bulk emission of microquasars falls in the range between 0.1 keV and 500 keV which is best observed with X-ray and soft gamma-ray satellites such as *RXTE* and *INTEGRAL*, which are used in this work, or *XMM-Newton*, *Chandra*, *Suzaku*, etc.

This chapter introduces microquasars in general and Cyg X-1 as an example. Formation (Sec. 2.1) as well as the inflows (accretion, Sec. 2.2) and outflows (jets, Sec. 2.3) are discussed and the general theory of the different states, i.e. distinct combinations of spectral and timing features, are discussed. (Sec. 2.4). The focus is here on the so-called q-track, which connects microquasars and other accreting objects. Finally, in Sec. 2.5 one of the most interesting examples of a MQ, Cyg X-1, is introduced.

## 2.1 Formation

### Formation of a Black Hole

For the greatest part of its life a star is stabilised by the balance between the inwards directed gravitational force and the outwards directed pressure of hot gas. The heating is provided by nuclear fusion of hydrogen to helium and later, when the hydrogen reserves are exhausted and if the star is sufficiently massive, of helium to carbon, etc., in the stellar core (Carroll & Ostlie, 2006, or any other introduction into astronomy/astrophysics). The final stage of nuclear burning is the fusion of silicon to iron. Iron has the highest binding energy per nucleon of all the elements, so that any further fusion steps would be endothermic. As there is nothing else to counterbalance the gravity, the core of the star begins to collapse and the outer shell is expelled. The whole process is known as a supernova (SN) explosion<sup>1</sup>.

While supernovae themselves are highly interesting phenomena, which are not yet fully understood in all detail, only their ultimate results are of interest here. For stars between about  $8\text{--}25 M_{\odot}$  the collapsed core has a mass above the Chandrasekhar limit of  $1.4 M_{\odot}$  and therefore cannot be supported by the degeneracy pressure of the electrons

---

<sup>1</sup>This only applies to SNs of type Ib, Ic and II. SN Ia are, most likely, the result of accretion in binary system consisting of a white dwarf and a stellar companion.

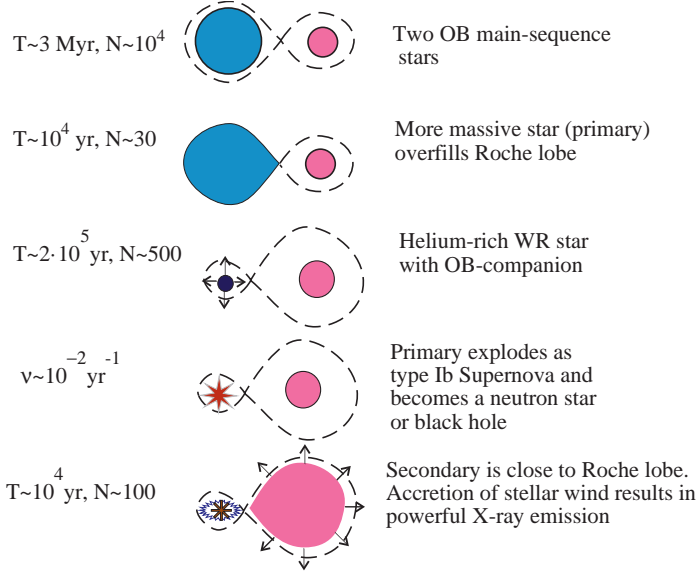


Figure 2.1: Formation scenario of a binary system with a compact object. Here,  $T$  is the time spent on average in the depicted phase.  $N$  is the number of binaries in the depicted phase in our galaxy.  $v$  is the frequency of supernova events in our galaxy. (after Postnov & Yungelson, 2006, Fig. 4)

(Chandrasekhar, 1931). It is still below the Oppenheimer-Volkoff limit (Oppenheimer & Volkoff, 1939), however, which gives the maximum mass for objects supported by neutron degeneracy pressure and, due to the lack of knowledge of the exact equation of state of the matter at such high pressures, is not as exactly known as the Chandrasekhar limit but definitely lies below  $3 M_\odot$ . Therefore, stars born with a mass of  $8-25 M_\odot$  will form neutron stars as the final stage of their evolution. No force is known that could stop the collapse of a stellar core above this mass and General Relativity predicts that a singularity surrounded by an event horizon will ultimately form: a black hole is born.

## Black Holes in Binary Systems

The starting point for the formation of microquasars are binary systems with a high mass star of  $25-60 M_\odot$  (e.g., Postnov & Yungelson, 2006).<sup>2</sup> A scheme for the formation of a compact object in such a system is presented in Fig. 2.1 for the case of two OB main sequence stars of different masses.

The two stars start their evolution largely unperturbed by their binary partner within their respective Roche lobes (volumes in which objects are bound to the star, see 2.2). The star with the higher initial mass will evolve quicker and have a stronger stellar wind, which strips the star of the outer shells (the most extreme cases with the strongest stellar winds in excess of  $10^{-5} M_\odot \text{ yr}^{-1}$  with speeds up to  $3000 \text{ km s}^{-1}$  are Wolf-Rayet (WR) stars, Carroll & Ostlie, 2006), with the originally more massive companion consisting finally almost only of the naked stellar interior. As it is the core that ultimately dictates the fate of a star, it will still evolve quicker than the companion with the initially lower mass and explode in a supernova, leaving a compact object behind. The further features of the binary system depend on the evolution of the remaining star, which may or may not fill out its Roche lobe. Postnov & Yungelson (2006, and references therein) discuss the evolution of different initial binaries in more detail.

<sup>2</sup>Note that the exact mass threshold between the predecessor stars of neutron stars and black holes is not clear and depends on further parameters, like rotation, metallicity, magnetic fields, etc. Stellar winds of stars more massive than  $60 M_\odot$  might be strong enough to strip so much material that the star becomes only a neutron star after the final collapse (Postnov & Yungelson, 2006).

The radiation detected from BHs can be produced both in inflows, see Sect. 2.2, and in outflows, see Sect. 2.3.

## 2.2 Inflow: Accretion

### Schwarzschild and Kerr Black Holes

A black hole is fully defined by its mass, angular momentum and electromagnetic charge (Carter, 1971), a fact often referred to as the ‘No-Hair Theorem’. However, any charge would quickly be neutralised by accretion, leaving mass and angular momentum as the only defining properties for astrophysical black holes.

A non-rotating (Schwarzschild) black hole with a mass  $M$  has an event horizon of

$$R_S = 2R_g = \frac{2GM}{c^2} \quad (2.1)$$

with  $R_S$  being referred to as the Schwarzschild radius and  $R_g$  as the gravitational radius. From the effective potential, which takes into account the angular momentum of the particle (see, e.g., Shapiro & Teukolsky, 1983, p.339ff), it can be shown that stable orbits are not possible for all radii. The innermost stable circular orbit (ISCO)<sup>3</sup> for a Schwarzschild black hole lies at

$$R_{\text{ISCO,Ss}} = 3R_S \quad (2.2)$$

The efficiency  $\eta$  of the gravitational energy release which relates the Luminosity  $L$  to the mass accretion rate by  $L = \eta \cdot mc^2$  is  $\sim 0.06$  for a Schwarzschild black hole (e.g. Shakura & Sunyaev, 1973).

Rotating black holes (with the maximum rotating case most often referred to as ‘Kerr black hole’<sup>4</sup>) differ in their properties due to the frame dragging effect, i.e., the

---

<sup>3</sup>This term is mainly used in high energy astrophysics. In General Relativity, the usually employed term is ‘marginally stable orbit’.

<sup>4</sup> named after Roy Kerr, who found and published this solution (Kerr, 1963) and who can be seen on the following photo with the author of this thesis (with R. Kerr in the middle, of course!) made at the ‘Black Holes in Binary Systems: Observations versus Theory’ workshop in Ferrara, Italy (September 11–12 2009):



fact that the space-time itself is non-stationary around such a rotating object. Both the radius of the event horizon,  $R_K$ , and the innermost stable orbit decrease and for the Kerr black hole

$$R_K = R_{\text{ISCO},K} = R_g \quad (2.3)$$

At the same time,  $\eta$  can reach up to 40% (e.g. Shakura & Sunyaev, 1973).

### Accretion Efficiency and Eddington Luminosity

A simple order-of-magnitude estimate will show that accretion is a highly and, in fact, the most efficient way to extract energy. If a body of mass  $M$  and radius  $R$  accrets matter of mass  $m$  from infinity the maximum energy released by the accretion is

$$\Delta E = E_{\text{pot}}(\infty) - E_{\text{pot}}(R) = \frac{GMm}{R} \quad (2.4)$$

Black holes are, however, special as accretors in the sense that they do not have a rigid surface that would bring the infalling matter to a halt. Therefore, only a part of  $\Delta E$  is released in the form of radiation, the other remains in form of kinetic energy with the accreted material resulting in the lower accretion efficiencies as mentioned above.

The kinetic energy of a mass orbiting a black hole at a radius  $r$  is, assuming Keplerian orbits and using the virial theorem

$$E_{\text{kin}} = \frac{1}{2}mv_{\text{Kepler}}(r)^2 = \frac{1}{2}E_{\text{binding}} = \frac{1}{2}(E_{\text{pot}}(\infty) - E_{\text{pot}}(r)) \quad (2.5)$$

and therefore, ignoring relativistic effects, the energy released by a mass accreted from the infinity to the ISCO of a Schwarzschild black hole will be

$$\Delta E_{\text{BH}} = E_{\text{pot}}(\infty) - E_{\text{pot}}(3R_S) - \frac{1}{2}mv_{\text{Kepler}}(3R_S)^2 = \frac{1}{12}mc^2 \quad (2.6)$$

The efficiency of hydrogen burning is only  $\sim 0.7\%$  and thus much smaller.

Accretion, though, can be impeded by the radiation it produces through scattering and absorption as the radiation transfers momentum to the material which is being accreted (e.g., Frank et al., 2002). There exists a maximum accretion luminosity, the so-called Eddington luminosity. Continuing the order-of-magnitude estimate, it will be derived in the following for the simplest case, i.e., under the assumptions of steady spherical accretion and fully ionised hydrogen as accreted material (with the second being a good proxy for many astrophysical cases) and considering only Thomson scattering of the electrons (with the scattering cross section  $\sigma_T = 8\pi/3 e^4/(c^4 m_e^2)$ ). With the energy flux  $S = L/4\pi r^2$  and neglecting the gravitational force on the much lighter electron in the second step follows

$$F_{\text{rad}} = F_G \Leftrightarrow \frac{GM(m_p + m_e)}{r^2} = \frac{\sigma_T S}{c} \Rightarrow \frac{GMm_p}{r^2} = \frac{L\sigma_T}{4\pi cr^2} \quad (2.7)$$

for the case of critical accretion when the inward gravitational force is in exact balance with the outward radiation caused force, giving (e.g., Frank et al., 2002)

$$L_{\text{Edd}} = \frac{4\pi GMm_p c}{\sigma_T} \approx 1.3 \times 10^{38} \text{ erg s}^{-1} \frac{M}{M_\odot} \quad (2.8)$$

It should be pointed out that the accretion in astrophysical environments will usually not fulfil the assumptions made here, especially those on the steadiness and the symmetry

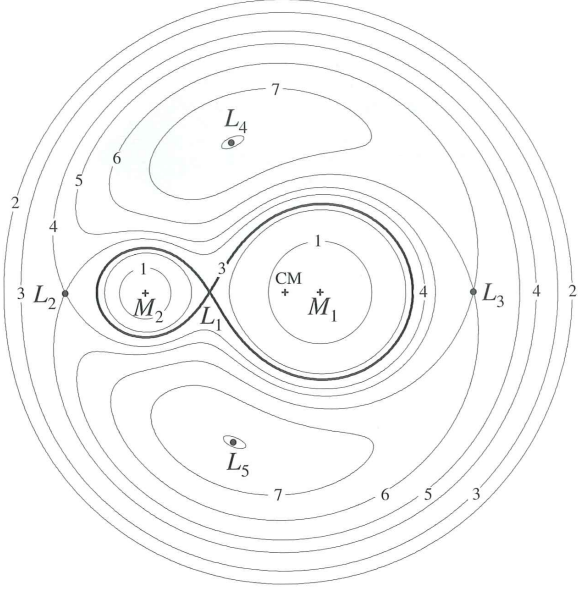


Figure 2.2: Equipotential lines in the orbital plane of a binary with  $M_1/M_2 = 0.25$ .  $\Phi_R$  increases with the increasing label number of the line. Highlighted are the five Lagrangian points  $L_1$  to  $L_5$  and the Roche lobes (thick line). (Frank et al., 2002, Fig. 4.3)

of the accretion: the accreted matter might arrive in blobs; if the accreted material possesses angular momentum, its outward transport will lead to the formation of an accretion disc; the ionised accreted material might couple to the magnetic field line of the accretor, as happens in the case of neutron stars, etc. Nevertheless, the Eddington luminosity offers a good estimate for the maximum possible accretion power.

### Roche Lobe Overflow

The two main modes of accretion for binaries are Roche lobe overflow and stellar wind accretion. Which mode acts in a system depends mainly on the mass and evolutionary stage of the companion (e.g., Shakura & Sunyaev, 1973; Pringle, 1981; Frank et al., 2002). To understand accretion, it is important to understand the potential of a binary system. The effective potential in a close rotating binary with the rotation velocity  $\omega$ , the mass  $M_\star$  and the positional vector  $\mathbf{r}_\star$  of the star and  $M_{\text{comp}}$  and  $\mathbf{r}_{\text{comp}}$  of the compact object is described by (Frank et al., 2002)

$$\Phi_R(\mathbf{r}) = -\frac{GM_\star}{|\mathbf{r} - \mathbf{r}_\star|} - \frac{GM_{\text{comp}}}{|\mathbf{r} - \mathbf{r}_{\text{comp}}|} - \frac{1}{2}(\omega \times \mathbf{r})^2 \quad (2.9)$$

Next to each body the potential is dominated by the body's own gravity and the equipotential surfaces are nearly spherical. Further away, however, they are deformed by the centrifugal and tidal forces (Fig. 2.2). The first inner surface which belongs to both bodies (indicated by the thick line in Fig. 2.2), is called Roche lobe. Within the Roche lobe, a test mass is gravitationally bound to either the primary or the compact object. Nevertheless, it is possible to pass from one lobe to the other via the inner Lagrangian point  $L_1$ , the saddle point of  $\Phi_R$ , which connects the Roche lobes.

In Low Mass X-ray Binaries (LMXBs) the primary star has evolved to the giant phase, so that it fills out its Roche lobe. Material from the star then spills out over  $L_1$  onto the compact object. As the primary's material carries notable angular momentum, an accretion disc is formed.

## Wind Accretion

O or B stars exhibit strong stellar winds. In a close binary system the gravity and the continuum radiation pressure of the companion as well as the centrifugal force due to orbital motion destroy the spherical symmetry of the wind: the wind is focused onto the compact object (Friend & Castor, 1982). Although the existence of an accretion disc is possible for systems with focused wind accretion, it will generally be smaller (Kreykenbohm, 2004, and references therein).

X-ray Binaries with O or B primaries are known as High Mass X-ray Binaries (HMXBs) and include the strong candidate black hole binaries Cyg X-1 and LMC X-3 and the neutron star binaries Vela X-1 and Cen X-3 (Friend & Castor, 1982). For these binaries, the focused wind mechanism is the dominant mode of accretion.

When the primary expands to fill the Roche lobe, the Roche lobe overflow mechanism will, however, contribute more and more. The now focused wind will look more and more like pure Roche lobe overflow. Cyg X-1 shows this mixed mode of accretion (Friend & Castor, 1982; Hanke et al., 2009).

## Accretion Disc Models

As shown above, accretion in astrophysical systems will often lead to the formation of an accretion disc, which needs to be understood in order to understand the physics of the microquasars. The outward transport of the angular momentum and the conversion of kinetic energy of the material in the differentially rotating disc into radiation proceeds via viscous torques (Frank et al., 2002). Viscosity in the cases of high Reynolds numbers is however one of the main unknowns of the astrophysics.

A basic solution, the standard geometrically thin and optically thick accretion disc model is presented by Shakura & Sunyaev (1973): The viscosity  $\nu$  is defined by the sound speed  $c_s$ , and the disc thickness  $H$  in the so-called **alpha-prescription**:

$$\nu = \alpha c_s H \quad (2.10)$$

where all the absent knowledge about viscosity is subsumed in one single parameter  $\alpha$  of which only  $\alpha < 1$  is known. The viscosity drives the accretion, as binding energy is liberated by viscous dissipation. The energy is radiated directly. 90% of the power originates within the inner  $20R_g$ : the gas temperature in the disc therefore increases with the proximity to the black hole, reaching up to  $10^7$  K (McClintock & Remillard, 2006) and most of the energy is radiated away at frequencies larger than those of the visual band (Shakura & Sunyaev, 1973).

For modelling purposes, the disc is usually approximated by a so-called multi-temperature black body (Mitsuda et al., 1984; Makishima et al., 1986) also known as the multicolour disc model with  $T(R) \propto R^{-3/4}$  (cf. McClintock & Remillard, 2006). The spectrum of black body radiation is explained in Sec. 3.1.

An overview of the different possible modifications of this simple accretion disc models is presented by Pottschmidt (2002, p. 46ff), references therein introduce the respective models in more detail. Important for this work is the idea of the so-called corona: a hot, low density plasma in addition to the actual accretion disc. A thorough discussion of coronae is presented, e.g., by Reynolds & Nowak (2003, Sec. 3.3).

The motivation for the coronae comes from the form of the spectrum of BHBs: it often has a power law component in the hard X-ray range which is exponentially cutoff

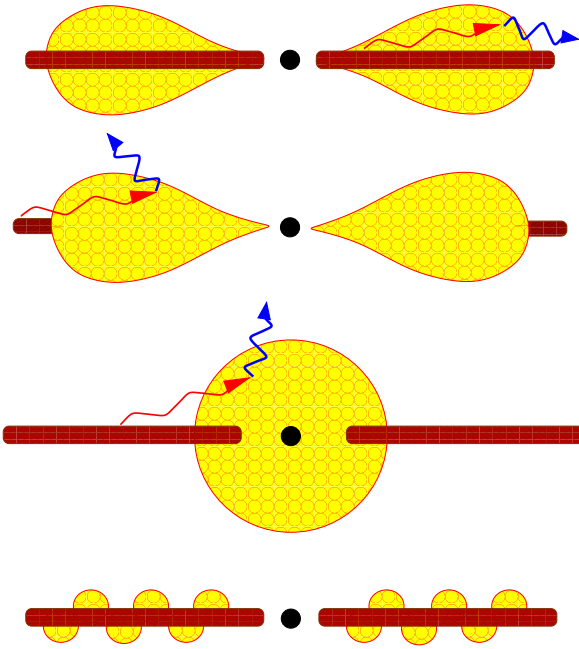


Figure 2.3: Different possibilities for corona geometries. The top figure show the ‘slab’ or ‘sandwich’ geometry, which predicts too soft spectra compared with observations. The two middle figures are referred to as ‘sphere+disc geometries’ and the last one as ‘patchy corona’. The three last variants are photon starved, i.e. the corona in this model is less effectively cooled by photons from the disc.

(Reynolds & Nowak, 2003, Fig. 6)

at energies around a few hundred keV. This component could be created by unsaturated inverse Comptonization in the corona (Reynolds & Nowak, 2003), cf. also Sec. 3.2.

The theory of accretion disc coronae is dominated by two principal uncertainties. The exact geometry of the corona is unknown – several possibilities usually considered are presented in Fig. 2.3. Also, the exact heating mechanism of the corona which would allow for the high temperatures required is yet to be found, but magnetohydrodynamical (MHD) instabilities seem a promising candidate (Reynolds & Nowak, 2003).

Coronae are also interesting in the scope of jet models, as e.g. Markoff et al. (2005) proposed that the base of the jet in a BHB might be what was interpreted as a corona up to now.

## 2.3 Outflow: Jets

Many of the black hole binaries are also sources of radio emission, which is thought to originate in jets. Jets are bipolar, collimated (with opening angles of often only a few degrees) relativistic outflows, which are a common feature of accreting systems, whether stars just being born (e.g., T Tauri stars), accreting galactic black holes or AGN. Feedback from accreting (supermassive) black holes – either in the form of wind or jets – has been a formative element for the evolution of galaxies (Cattaneo et al., 2009; Fender, 2010).

### Jet Models for Microquasars

Jets have only recently been incorporated into the general picture of BHBs, although already Shakura & Sunyaev (1973, Fig. 9) indicated an outflow launching perpendicular to the accretion disc from the vicinity of the black hole. Though observed and imaged in the radio (for an overview see Gallo, 2010, and references therein), the exact contribution of the jets to the X-ray portion of the spectrum is unclear and hotly debated. The flat radio spectrum on the other hand is clearly the results of the combination of single

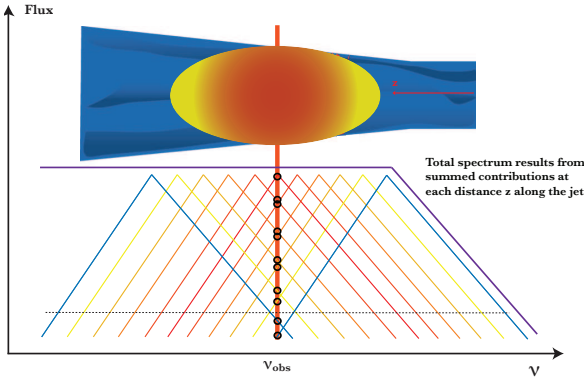


Figure 2.4: Schematic illustration of the jet spectrum: each segment of the jet contributes a single synchrotron spectrum of approximately the same shape but of different peak frequency. When combined, a flat radio spectrum appears.

(Markoff, 2010, Fig. 1)

synchrotron spectra with different peak frequencies originating at different points along the jet (see Fig. 2.4).

Part of the problem is that there is still no consistent theory on the launching mechanism and the jets' source of plasma and energy (Markoff, 2010). It seems, clear, however, that magnetic fields do play a major role – they can be generated via the magneto-rotational instability and be very strong in the innermost regions of the accretion flow (Markoff, 2010). A simulation of such a jet is presented by McKinney (2006). Blandford & Znajek (1977) described what is now known as the Blandford-Znajek mechanism for extraction of energy from rotating black holes, which leads to formation of jet-like structures. It is however doubted that the spin of many galactic black holes is high enough to allow for the Blandford-Znajek mechanism as the only launching mechanism (Gierliński & Done, 2004).

Markoff et al. (2001) introduced a model for a relativistic, adiabatically expanding jet, which explains the X-ray power law emission as optically thin synchrotron emission from a shock acceleration region in the innermost part of the jet. It is important to distinguish this model from the following iterations of this jet model as presented by Markoff et al. (2003), Markoff & Nowak (2004), and Markoff et al. (2005), as in the latter not only the synchrotron emission, but also Comptonization mechanisms contribute to the X-ray spectrum. This model has been expanded to include an irradiated accretion disc (Maitra et al., 2009). Although some assumptions of this jet model have recently come under criticism (e.g., Malzac et al., 2009), jet models are the only models to date which do account for both the X-ray and the radio spectrum of BHs and take into account the fact that jets are observed in these sources.

It is also still unclear, what the link between the proposed magnetic coronae and the jets is (Markoff, 2010) - could they be connected or even the same as proposed by Markoff et al. (2005)?

## 2.4 The States of Microquasars – the q-Track

The emission of X-ray sources – whether microquasars, AGN or neutron stars, etc. – is often strongly variable, with great differences possible both between different sources and the same source at different times. Generally, two types of MQs can be distinguished:

- *transient sources* show only outbursts of activity, which are believed to be driven by disc instabilities (Remillard & McClintock, 2006; Fender, 2010). Transients are either not detected at all in the X-ray or detected only on a very low flux level during their phases of quiescence.

- persistent sources permanently show a high level of activity. Only four known sources, V1408 Aquilae (4U 1957+11), GRS 1758–285, 1E1740.7–2942 and Cyg X-1, the source studied in this work, are persistent.<sup>5</sup>

Both kinds of sources show the same distinct radiation regimes, so-called states, which are defined by their spectral features as well as the timing properties and are therefore an empirical classification. The underlying physics is still under discussion, although there is a tentative agreement on the basic components.

One of the first transitions between states was reported by Tananbaum et al. (1972): in an observation with the *Uhuru* satellite, a significant decrease of intensity in the soft 2–6 keV energy band by a factor of 4 was accompanied by a doubling of intensity in the harder 10–20 keV energy band. Additionally, a previously not detected radio source appeared in the radio observations. Since the satellite was most sensitive in the softer energy band, this led to a definition of the *high state* with high flux in the lower energy band and the *low state* with low flux in the lower energy band.

The hard and soft state spectra can also be described by a power law of the form  $E^{-\Gamma}$ , in general a good approximation of the general spectral shape of the source, where the photon index  $\Gamma$  characterises the hardness of the source. Therefore the high state is also dubbed the *soft state* and the low state the *hard state*.

Generally, a consistent theory of states and their transitions should describe and physically motivate the changes in the properties of the source and take both the inflow and the outflow components, whether dubbed accretion disc and jet or not, into account.

## Hardness-Intensity Diagrams (HIDs) and the **q**-Track

Especially useful for characterising the spectral evolution of X-ray sources are so-called hardness-intensity diagrams (HIDs), where the total X-ray luminosity is plotted as a function of the spectral hardness. The diagram can be seen as an analogy to the Hertzsprung-Russell diagram of optical astronomy where the luminosity of the star is plotted against its colour. In practise, the hardness ratio (or X-ray colour) is often calculated by dividing the count rate in the higher energy band by the count rate in the lower band (e.g., Fender et al., 2004; Dunn et al., 2010).

The present day understanding of the states is summarised in Fig. 2.5. The blue arrows indicate the track of a canonical X-ray transient, represented by GX 339-4 (Belloni et al., 2005), as it comes from quiescence and undergoes an outburst, describing the typical **q**-shaped (or turtle head-) track in the HID - examples of the **q**-tracks of other sources can be found, e.g., in Fender et al. (2009). The states can be distinguished by a combination of spectral and timing features (Fender et al., 2004, 2009; Belloni, 2010), which shall be described in the following<sup>6</sup>:

- **Low/Hard State (LHS)**

After a phase of quiescence - which in some cases can be described as the low luminosity extension of the LHS - the source enters the LHS: the X-ray luminosity increases in this state while the hardness remains constant. The source spectrum can be roughly described by a power law with a photon index of  $\Gamma \sim 1.6\text{--}1.7$

---

<sup>5</sup>Whether GRS 1915+105 and GRO J1655–50 are persistent is still under discussion in the scientific community.

<sup>6</sup>In this description of the states the quasi periodic oscillations (QPOs) are left out: they are important in general, but of less importance for the study of Cyg X-1 presented here, as the QPOs in Cyg X-1 are, when present, rather weak (e.g. Pottschmidt et al., 2003b).

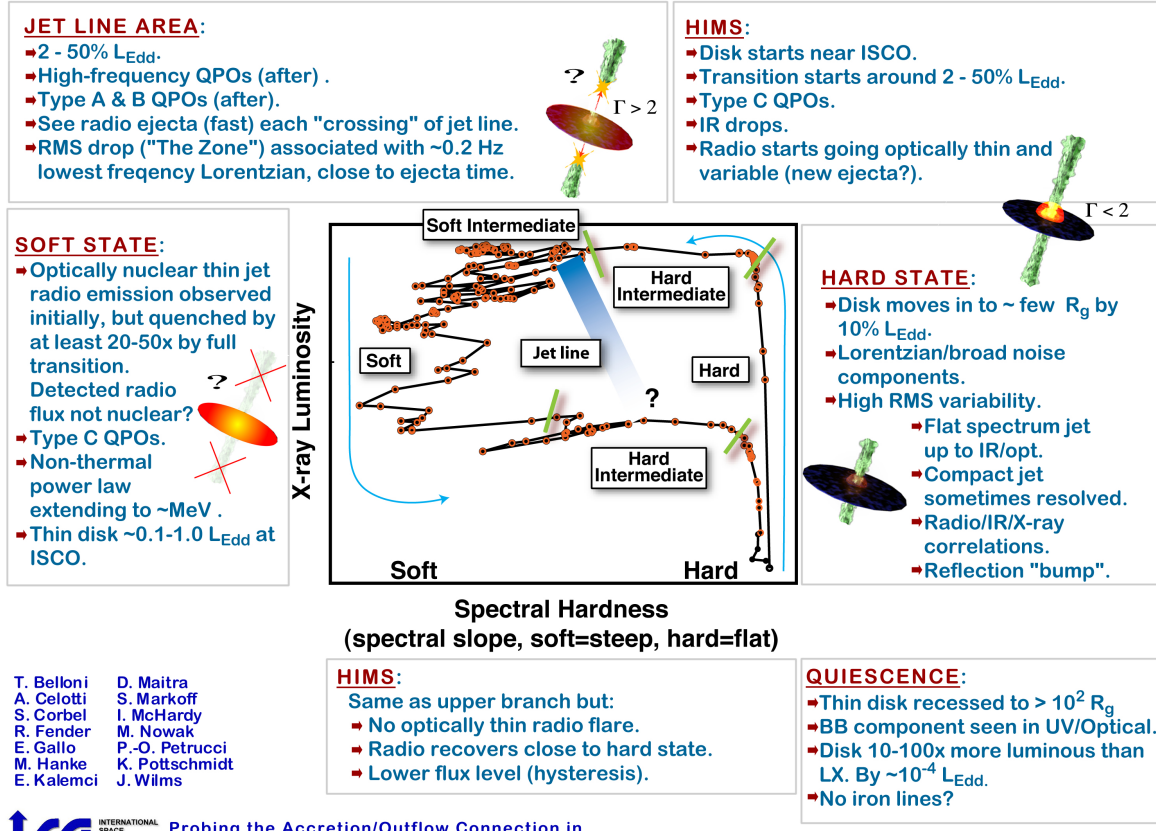


Figure 2.5: Current state of understanding of the states of BHs. See text for details.  
(Picture courtesy of International Space Science Institute (ISSI),  
<http://www.sternwarte.uni-erlangen.de/proaccretion/>)

(Belloni, 2010) with an exponential cutoff at  $\sim 150$  keV. The luminosity is generally below a few percent of  $L_{\text{Edd}}$  (Fender et al., 2004). Additionally, the spectrum often shows reflection features such as a broad Fe K $\alpha$  fluorescence line with a line profile defined by relativistic effects in the vicinity of the black hole (e.g. Reynolds & Nowak, 2003) and a reflection hump - a hardening of the spectrum above  $\sim 10$  keV. Both effects are attributed to the irradiation of a cold(er) accretion disc by hard X-rays. The accretion disc itself, which is recessed to up to a few hundred  $R_g$  during the quiescent state, moves inwards towards the ISCO, but the inner radius still remains high.

The variability is characterised by strong X-ray rms  $\geq 20$ -30% (Belloni, 2010). The power spectral density (PSD) can be modelled with a number of Lorentzian components (Nowak, 2000; Pottschmidt et al., 2003b). With increasing flux, the Lorentzian components shift to higher frequencies (Boeck et al., 2008; Belloni, 2010) and an additional weak power law component might be necessary to describe the lower variability frequencies (Pottschmidt et al., 2003b). The mean coherence function – as calculated between a softer and a harder X-ray energy band and averaged over a Fourier frequency range between about 1 and 10 Hz – is approximately unity, i.e., the coherence is almost ideal in the hard state, and the mean time lag – calculated in the same manner as the mean coherence – has a stable low value of a few ms, with the variability in the softer energy band leading the variability in the harder band (Pottschmidt et al., 2003b; Kalemci

et al., 2003).

Additionally, during the LHS radio emission is present and correlated with the X-ray emission (Gallo et al., 2003). The radio spectrum is flat or slightly inverted and can be interpreted as arising from synchrotron emission from a jet (e.g., Fender et al., 2009). As described by Markoff et al. (2005), the (Comptonized) synchrotron radiation and the photons from the jet can essentially contribute to the observed X-ray flux. In some sources, compact jets in the LHS have been directly resolved in radio observations (see Stirling et al., 2001; Dhawan et al., 2000, for Cyg X-1 and GRS 1915+105 respectively).

- *Hard Intermediate State (HIMS)*

Those sources which leave the LHS during their outbursts<sup>7</sup> enter the HIMS and go on along the q-track to the horizontal branch (approximately constant luminosity, decreasing hardness). The softening of the spectrum is a mutual effect of the increase of the slope of the power law up to  $\Gamma \sim 2.4\text{--}2.5$  and the disc component moving to higher energies and thus into the energy band accessible with *RXTE* (Belloni, 2010).

While the total fractional rms decreases, the PSD still consists of the same components as during the LHS, but the frequencies of the Lorentzians now change – they increase with decreasing hardness (Belloni, 2010). The coherence decreases and the value of the time lags grows. This part of the q-track is transversed by the source quickly.

- *Soft Intermediate State (SIMS)*

In X-rays, the transition to the SIMS is evident *almost only* in the timing properties: the noise level can now be as low as few percent, while the change in the hardness consists only of a small softening compared to the HIMS.

However, the transition between the HIMS and the SIMS, which is associated (but not necessarily coincident, see Fender et al. (2009)) with the so-called jet line is of crucial importance. The transition will often also coincide with radio ejection events – the optically thin, discrete ejecta have been imaged (e.g. Gallo et al., 2004; Fender et al., 2006, for GX 339–4 and Cyg X-1, respectively).

- *High/Soft State (HSS)*

The spectrum of the HSS is dominated by thermal emission of an accretion disc and the soft X-ray luminosity is typically higher than in the LHS. The thin accretion disc itself extends down to the ISCO. A non-thermal power law component extending into the MeV range is detected in some sources (McConnell et al., 2000, 2002).

While the variability is significantly lower than before - as low as a few percent - it can be dominated by the power law component. The coherence and the lags in a stable soft state show the same behaviour as in a stable hard state (Pottschmidt et al., 2003b, 2000).

Radio emission is strongly suppressed; where it is detected, it can be interpreted as arising in shocks as the previously produced jet moves away from its point of origin in the binary system (Fender et al., 2004, 2009).

---

<sup>7</sup>Not all transient sources will do so; some will never reach the HISIM and return directly to quiescence from the LHS.

## Other State Definitions

Other definitions for the states are still used in the literature and should therefore be mentioned here together with their relationship to the canonical states of the  $q$ -track to allow for a better understanding, especially when referencing results relating to these states:

- The so-called very high (VHS) or intermediate states (IS) (e.g., Fender et al., 2004; Belloni et al., 1996) encompass both the HIMS and the SIMS, which can be identified with the different ‘flavours’ of the VHS, i.e., different timing and spectral properties which are distinct from those of LHS and HSS. The definitions for LHS and HSS are largely the same as described above.
- Remillard & McClintock (2006) and McClintock & Remillard (2006) re-define the states as Hard, Thermal and Steep Power law (SPL) state roughly corresponding to the LHS, HSS and VHS as well as a quiescent state. They base their definition of states on clear cuts in different parameters: disc-flux-fraction, rms fraction and the power law index  $\Gamma$ . Especially, they do not use luminosity to distinguish between the states, an important assumption as numerous sources exist whose luminosity behaves differently from the canonical picture.

Remillard & McClintock (2006) acknowledge, however, that not all observations fall under a clearly defined state in this classification - they refer to such observations as intermediate state, specifying which states are ‘mixed’ to achieve them. Belloni (2010) therefore points out that this classification is not an exhaustive one, but merely offers a general guidance.

## State Transitions and the Jet Line

A physically especially interesting part of the  $q$ -track is the so-called jet-line and the area surrounding it. This area of the track is associated with X-ray flaring, radio ejection events and, as mentioned above when defining the transition between HIMS and SIMS, a sharp change in timing properties. It is, however, *not clear* whether all these features originate in the same physical process and are simultaneous.

Fender et al. (2009) point out that in their comprehensive study the variability decreases and the radio flares were consistent within a few days, but they cannot establish a direct relation between the two. Given the sparse coverage, it is impossible to decide whether both are features of some not yet determined physical process or whether they are casually connected. fFr Cyg X-1, Wilms et al. (2007) reported a quasi-simultaneous X-ray and radio flare close to a state transition from the soft to the hard state with the radio lagging the X-rays by  $\sim 7$  minutes.

Detecting the location of the jet line is highly complicated. Since only the transition from the hard to the soft state is associated with radio ejection events, data for the exact point of the re-activation of the jet are sparse. The existing observations of GX339-4 however point towards a non-trivial shape of the jet line - therefore, a direct correspondence between hardness and states, which would correspond to a vertical line in the HID, does not exist (Fender et al., 2009).

## Persistent Sources and the **q**-Track

Most of the BXRBs are transient sources showing random outbursts. Fender et al. (2004) and Fender et al. (2009), are able to deduce the whole shape of the **q**-track with the help of these sources. They are, however, not well suited for long term studies and in detail studies of the horizontal parts of the track, which are transversed quickly. Persistent sources, which also move along the **q**-track, but often only cover a part of it, are better suited for studying the horizontal branch if often found in this part of the track.

One interesting difference between the transient and the persistent sources is the lack of hysteresis: a transient source will transverse the horizontal branch at a higher luminosity when moving from the LHS to the HSS (i.e., earlier in the outburst) than when moving from the HSS to the LHS (i.e., later in the outburst). A persistent source will usually move in both directions at the same luminosity (Belloni, 2010).

Regarding the highly discussed jet line Fender et al. (2009) point out that the persistent source Cyg X-1 is one of the best candidates for further investigation: state transitions and so-called failed state transitions occur often and in both directions at almost the same luminosity. The source will therefore cross the jet-line often and in both direction allowing detailed studies of the transition as presented by Böck, VG, et al. (in prep.). Besides, this source is bright and well-observable for most of the X-ray satellites currently in orbit.

## The Unified Picture: Microquasars, AGN, Neutron Stars and Cataclysmic Variables

The **q**-track was historically first found for microquasars – meanwhile, however, there is evidence that it is universal, being able to unify different accreting systems. An overview of the microquasar-AGN connection is given by Fender (2010), who also shortly introduce the cases of neutron stars and cataclysmic variables, i.e. white dwarfs accreting matter from a companion star. The whole field cannot be introduced here, so that only two cases considered especially interesting are pointed out.

Körding et al. (2006) generalise the hardness-intensity diagrams of BHs to the so-called disc-fraction/luminosity diagrams (DFLDs), which are able to account for the different scales and therefore different energies at which the same components are visible in BHs and AGNs. They are able to show that the observed distribution of quasars and low luminosity AGN in the DFID parallels a simulated ensemble of X-ray binaries based on the known tracks of BHs. Because of the larger timescales, AGN can, of course, not be seen moving along the track. The DFID also seems to be a promising tool for the study of BHs themselves, as it tries to take into account the physics behind the observed radiation and to disentangle the disc and the non-disc/jet component while the HIDs stay purely phenomenological (Dunn et al., 2010).

DFLDs are used by Körding et al. (2008) for the characterisation outburst of the dwarf nova SS Cyg (a weakly accreting nonmagnetic white dwarf) and find that the source describes **q**-track-like shape in the diagram. They also observe the same relation of the radio luminosity to the states of the source as defined by the position on the DFID.

These findings – among others – strengthen the notion that the states are connected to inherent properties of accreting objects and their jets on all mass and time scales and that the understanding of the states and state transitions is decisive to understand

the whole phenomenon of accretion and ejection in accreting objects. A contribution to this understanding based on the example of Cyg X-1 is the aim of this work.

## 2.5 Cygnus X-1

### The Binary System

Cygnus X-1 is a persistent HMXB located near the galactic plane at  $\alpha = 19^{\text{h}}58^{\text{m}}21.7^{\text{s}}$ ,  $\delta = +35^{\circ}12'06''$  (Liu et al., 2006). The distance to the source is  $\sim 2.5 \text{ kpc}$  (e.g., Ninkov et al., 1987, who give  $2.5 \pm 0.3 \text{ kpc}$ ).

Cyg X-1 was discovered as an X-ray source during a balloon flight in 1964 (Bowyer et al., 1965). Hjellming & Wade (1971) observed the Cyg X-1 region at radio wavelengths with the NRAO three-element interferometer in 1970 and 1971: while before May 1971 no flux above 0.005 Jy was detected<sup>8</sup>, observations in May 1971 revealed a 0.015 flux units radio source whose position coincided with the position of the X-ray source as detected by *Uhuru* (Tananbaum et al., 1971) and a rocket borne experiment (Rappaport et al., 1971). Therefore an identification of the radio source with the X-ray source could be made. A first radio spectrum was subsequently reported by Hjellming et al. (1971).

An identification with the optical source HDE 226868, an O type supergiant, was first reported by Murdin & Webster (1971), who then confirmed the nature of the source as a binary system via measurements of the radial velocity, which revealed an orbital period of about 5.6 days and made first constraints on the inclination  $i$  of the source by  $0.3 \leq \sin i \leq 1.0$  (Webster & Murdin, 1972). The most exact orbital period to date was determined by Brocksopp et al. (1999b) to  $5.599829 \pm 0.000016$  days. Additionally, the long time X-ray lightcurve shows a modulation with a period of  $142 \pm 7$  days which may be due to the precession of the disc-jet system (Brocksopp et al., 1999a; Pooley et al., 1999; Ibragimov et al., 2007; Poutanen et al., 2008).

The values for mass and inclination differ in the literature and strongly depend on the method used - it is important to point out that because of the peculiarities of binary systems, including the probable mass transfer and the most likely gravitationally distorted shape of HDE 226868, standard methods for, e.g., age determination will often fail or lead to wrong results.

From the orbital elements, Hutchings (1978) estimates the mass for HDE 226868 to  $14\text{--}19 M_{\odot}$  and for the compact companion to  $5\text{--}12 M_{\odot}$  for inclinations  $60^{\circ}\text{--}30^{\circ}$ , respectively. Gies & Bolton (1986) base their estimates on optical spectroscopy of the system and obtain minimum masses of  $20 M_{\odot}$  and  $7 M_{\odot}$  and probable values of  $33 M_{\odot}$  and  $16 M_{\odot}$  for HDE 226868 and the compact companion, respectively. They also give the inclination of the system as  $i \approx 35^{\circ}$ . Abubekerov et al. (2004) estimate a consistent value of  $31^{\circ} < i < 44^{\circ}$ .

The mostly referred to result to date was reported by Herrero et al. (1995), who conduct a spectroscopic analysis using spherical non-hydrostatic models, which incorporate mass loss due to stellar winds and a non plane parallel model atmosphere. Note also that Herrero et al. (1995) state that conducting the analysis without taking these effects into account leads to results contradicting the parameters derived from the orbital data. They report a mass for HDE 226868 of  $\sim 18 M_{\odot}$  and a probable mass for the companion of  $\sim 10 M_{\odot}$ . Especially interesting is their analysis of the minimum mass

---

<sup>8</sup>Hjellming & Wade (1971) use the term ‘flux unit’ with  $1 \text{ fu} = 10^{-26} \text{ W m}^{-2} \text{ Hz}^{-1}$ , i.e.,  $1 \text{ fu} = 1 \text{ Jy}$ .

for the compact object, which they give as  $3.9 M_{\odot}$ . The minimum mass for Cyg X-1 is therefore about the Oppenheimer-Volkoff limit, making it indeed a black hole.

Lastly Ziolkowski (2005) consider the evolutionary status of HDE 226868 and derive its mass to  $40 \pm 5 M_{\odot}$  and the mass of the compact object to  $20 \pm 5 M_{\odot}$  - however, also here some caution is advised as they use a non-standard method using evolutionary tracks. They point out, that the wind mass losses are a major uncertainty factor in their calculations.

Attention should be drawn to the fact that, although only Herrero et al. (1995) specifically point this out, any of the given estimates give the mass of the compact object itself as well over the upper limit for the mass of a neutron star. Thus it is often referred to as a black hole and not a black hole candidate.

## Accretion and Jets

Accretion in the Cyg X-1 binary system is defined by the fact that HDE 226868 has a strong stellar wind with a mass loss rate of  $\dot{M} = 3.0 \times 10^{-6} M_{\odot} \text{ yr}^{-1}$  and a terminal velocity  $V_{\infty} = 2100 \text{ km s}^{-1}$  (Herrero et al., 1995, who do not give errorbars for these values). As HDE 226868 is also close to filling its Roche lobe, the wind is strongly focused towards the companion. Due to its high gravity and the non-inertial forces, the wind is highly asymmetric (Friend & Castor, 1982). The persistent nature of Cyg X-1 is due to the stellar winds as accretion is constantly powered and the accretion disc and its viscosity play a smaller role than in the purely Roche lobe overflow powered transient sources (see Hanke, 2007, for a more detailed discussion).

There is, however, definitive evidence for an accretion disc in the system: Some spectra show a soft excess that can be modelled with a multicolour black body (e.g., Wilms et al., 2006), the standard model describing an geometrically thin, optically thick accretion disc (see Sec. 2.2). Additionally, reflection components such as a Fe K $\alpha$  line at 6.4 keV and a reflection hump are present, which are also attributed to reflection from the cold material of the disc.

The average luminosity of Cyg X-1 in the X-rays is  $L_X \approx 4 \times 10^{30} \text{ W} = 1.0 \times 10^4 L_{\odot}$ , which is consistent with the value that could be obtained from accretion only. Whether accretion is the only or even the main process contributing to X-ray luminosity is unclear, however, as Markoff et al. (2005) have shown that the X-ray luminosity can be explained by radiation originating in a jet, i.e., in the outflows.

The existence of a jet in Cyg X-1 has first been verified by radio observations of Stirling et al. (2001), who have imaged a jet-like feature with an opening angle of  $2^\circ$  extending up to  $\sim 15$  mas from the core region in their milliarcsecond resolution observations with the Very Long Baseline Array. Figure 2.6 shows a high resolution image from their observation, which was conducted while the source was in a hard state. Stirling et al. (2001) derive a brightness temperature of  $10^7 \text{ K}$  at 8.4 GHz and therefore infer that the radiation is non-thermal. Together with the flat spectral index, which is attributed to synchrotron emission, and detection of polarisation, this supports the interpretation of the feature as a jet.

By observing a ring-like structure with  $\sim 5$  pc diameter (Fig. 2.7) around Cyg X-1, which appears to be inflated by the jet, Gallo et al. (2005) have estimated the power output of the Cyg X-1 jet: the particles accelerated in the jet inflate a radio lobe within the surrounding interstellar medium (ISM). As the pressure within is higher than that ISM, the lobe expands. What is perceived as the bubble is the shock compressed ISM. This explanation is supported by optical observations of line emission from the shocked

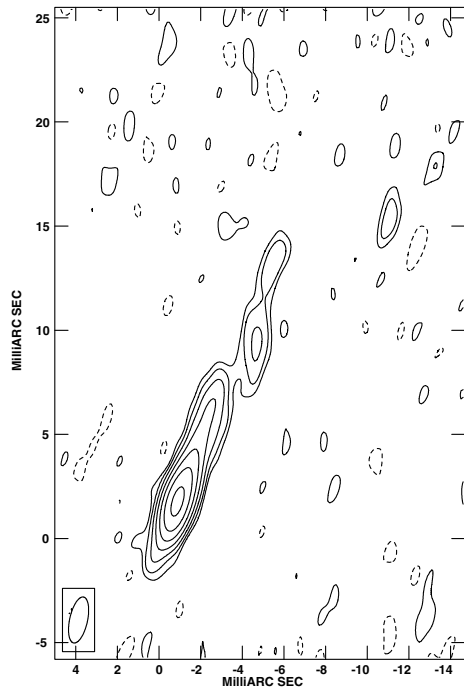


Figure 2.6: High resolution image of Cyg X-1 at 8.4 GHz, lowest contour  $0.157 \text{ mJy beam}^{-1}$ . The prolonged jet-like structure is clearly discernible.  
(Stirling et al., 2001, Fig. 3)

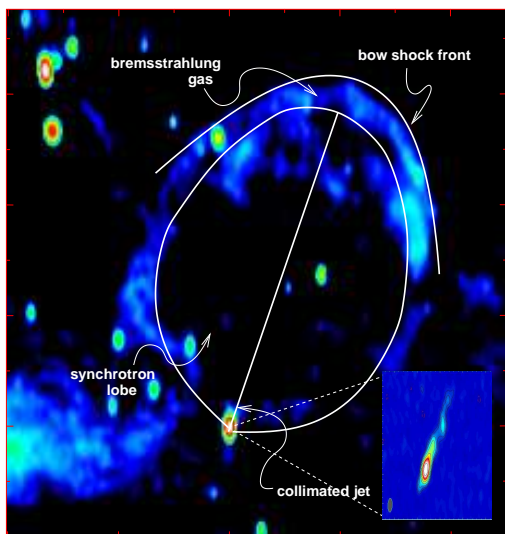
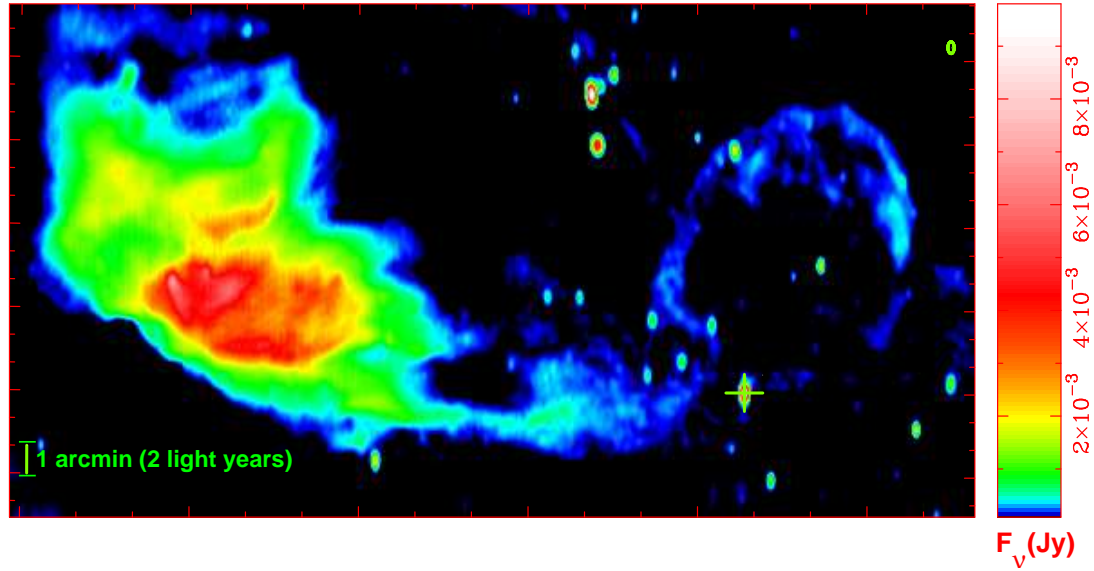


Figure 2.7: *Upper panel:* The jet inflated bubble around Cyg X-1 (marked by a green cross) as observed with the Westerbork Synthesis Radio telescope for 60 hours at 1.4 GHz. The spatial resolution is shown by the green open ellipse in the upper right corner. The extended structure on the left is the HII nebula Sh1-101.

*Left panel:* As above, with illustration of the components of the structure. The insert shows the inner radio jet of Cyg X-1.  
(Gallo et al., 2005, Fig. 1 & 2)

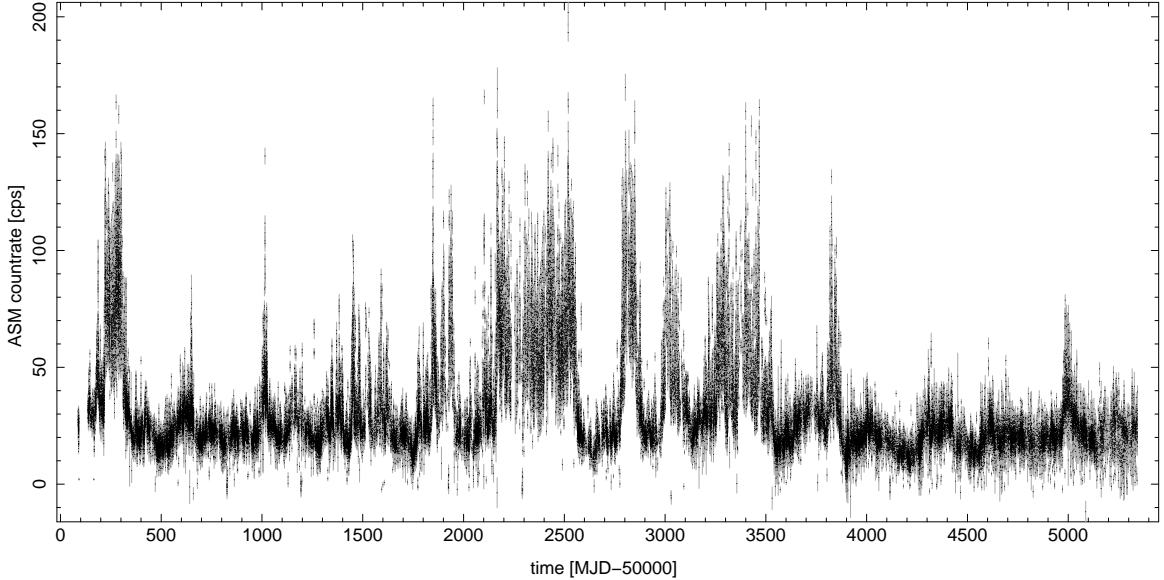


Figure 2.8: *RXTE*/ASM lightcurves of Cyg X-1 since the beginning of the *RXTE* mission in the end of 1995. Errorbars are shown in grey. The data are not binned and shown in the highest time resolution possible.

ISM gas from behind the shock and is consistent with the findings from extragalactic jets of supermassive black holes in the centres of galaxies. The inflated bubble allows one to estimate the product of the power and lifetime of the jet by assuming that the ISM acts as nature's own calorimeter: Gallo et al. (2005) estimate the total power of the jet to  $8 \cdot 10^{35} \text{ erg s}^{-1} \lesssim P_{\text{jet}} \lesssim 10^{37} \text{ erg s}^{-1}$ . The power of the jet therefore is of comparable magnitude (3–50%) with the (bolometric) X-ray luminosity in the hard state.

Both Stirling et al. (2001) and Gallo et al. (2005) concentrate on the persistent jet of the hard state. But also the transient relativistic jet has been observed: Fender et al. (2006) report such an observation with the Multi-Element Radio-Linked Interferometer Network (*MERLIN*), which was done during a phase of repeated state transitions in early 2004. Their findings support the validity of the unified state model as presented in Sec. 2.4 for Cyg X-1.

## States and State Transitions

Figure 2.8 shows the X-ray lightcurve of Cyg X-1 as observed by the ASM instrument on board the *RXTE* satellite since the launch of *RXTE* at the end of 1995. It illustrates that the source is highly variable on longer timescales and shows two distinct states of X-ray emission – the soft/high and the hard/low state, corresponding to the high and low count rates in the ASM band, respectively. Especially important are the frequent state transitions and so-called failed state transitions, that is, phases during which a softening of the spectrum and characteristic changes in the timing properties occur, which indicate a state transition, but where the soft state is never reached. These properties make Cyg X-1 the ideal candidate to study the behaviour of microquasars in the vicinity of and crossing the jet line.

Wilms et al. (2006) have pointed out that, while the source spent only  $\sim 10\%$  of the time in the soft state between 1996 and 2000, the percentage of the soft states has increased to  $\sim 30\%$  between 2000 and 2006. Since 2007 the source seems to be in a

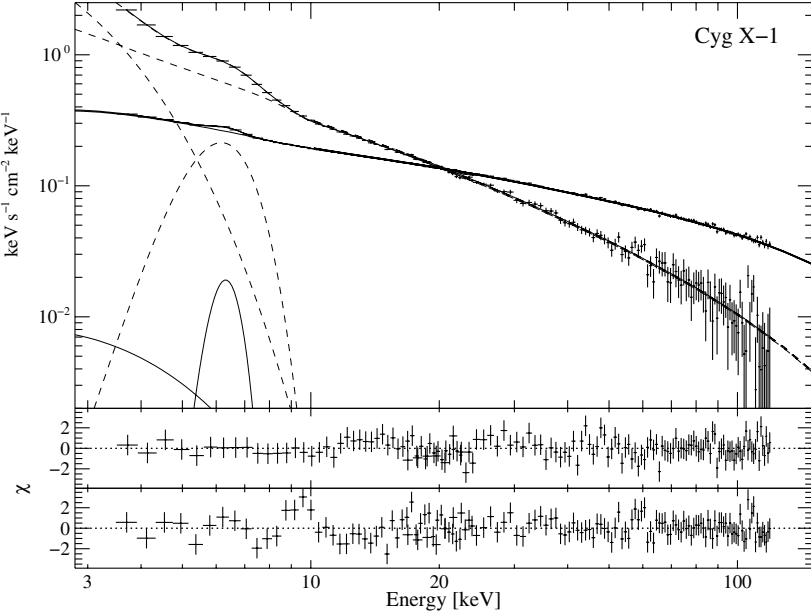


Figure 2.9: Unfolded *RXTE* spectra of Cyg X-1 in a hard (solid lines) and a soft (dashed lines) state. Shown are also residuals of the `eqpair` (Comptonization) model. Note the Fe K $\alpha$  line at  $\sim 6.4$  keV and the presence of a disc component at low energies.  
(Wilms et al., 2006, Fig. 12)

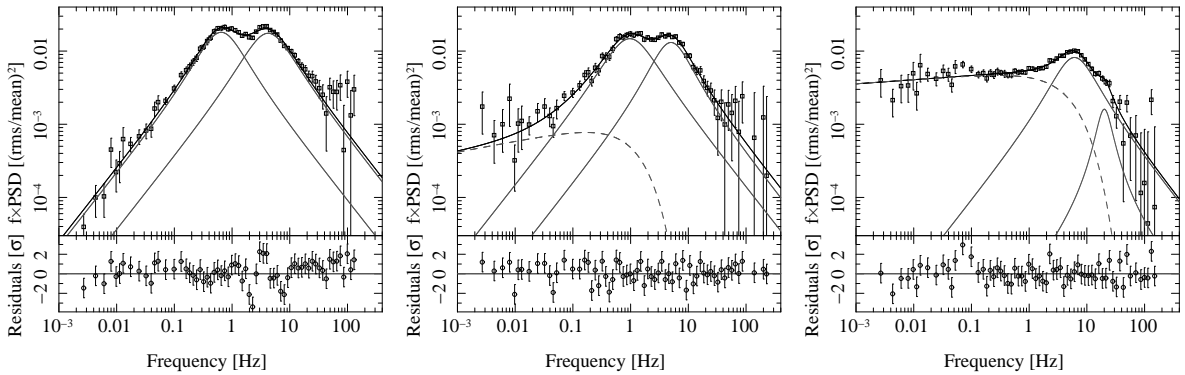


Figure 2.10: PSDs of Cyg X-1 in the hard (left), intermediate (middle) and soft (right) states. Note that while the fit shows only two Lorentzian components for the hard state, there is an indication of a third component at higher frequencies in the residuals.  
(Böck, VG, et al., in prep, Fig. 4)

persistent hard state, with a short excursion in a softer state in spring 2009.

Figure 2.9 shows typical spectra of Cyg X-1 in the hard and the soft state as observed with *RXTE*. The disc emission is dominant at lower energies for the soft state but has only a small contribution in the hard state. The spectrum of Cyg X-1 also shows the Iron K $\alpha$  line at  $\sim 6.4$  keV (Ebisawa et al., 1996). Phenomenologically, the spectrum can be described by a broken power law with a break at about 10 keV and an exponential cutoff above 150 keV, with the soft photon index  $\Gamma_1$  being higher than the hard photon index  $\Gamma_2$ . The difference,  $\Delta\Gamma = \Gamma_1 - \Gamma_2$ , grows as the spectrum softens (Wilms et al., 2006).

Interestingly, while the flux in the hard X-ray decreases during the soft states, the flux at above 1 MeV increases. Observations of Cyg X-1 in the MeV range in hard and soft states showing this behaviour have been reported by McConnell et al. (2000) and McConnell et al. (2002).

The states can also clearly be distinguished in the timing domain. Figure 2.10 shows typical PSDs of Cyg X-1 in the hard, intermediate and soft states. The naked eye alone can recognize the shapes: the PSD has a clearly double humped shape in the hard

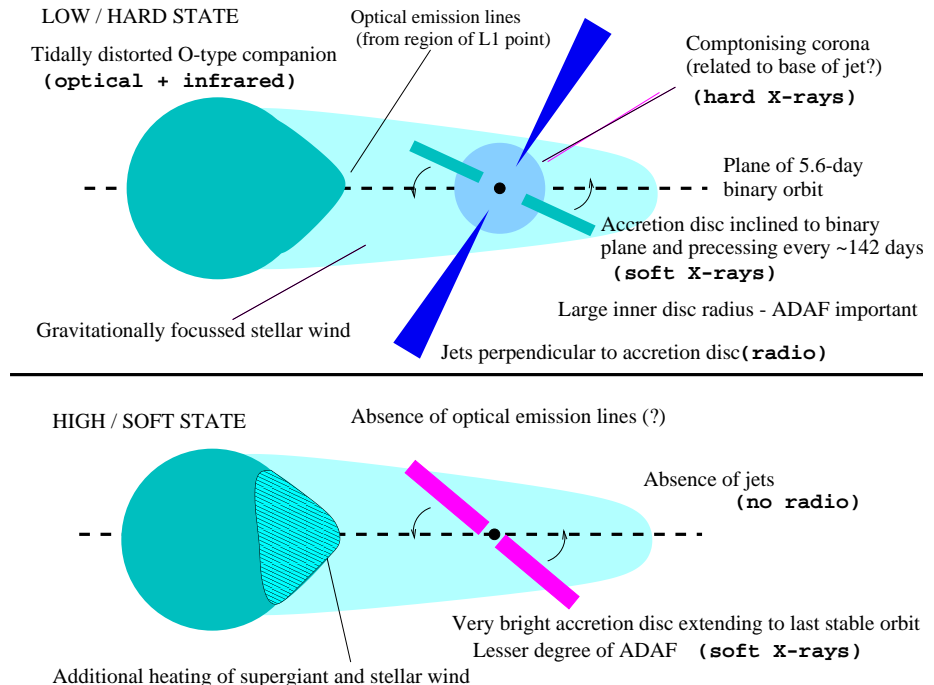


Figure 2.11: Sketch of the emission regions for the hard and soft states of Cyg X-1. ADAF stand for ‘advection dominated accretion flows’.  
 (after Brocksopp et al., 1999a, Fig. 7)

state. In the intermediate state, the humps move to higher energies while an additional, featureless component emerges at low frequencies. The soft state is dominated by this exponentially cutoff power law component, while the humps become less prominent and can fully disappear.

Radio emission from Cyg X-1 is detected in the hard state with the *Ryle/AMI* telescope. No emission is detected in the soft state. The transitions are accompanied by radio flaring activity (Gleissner et al., 2004a; Wilms et al., 2007).

Additionally to radio and X-ray measurements, individual detections of the source at even higher energies have been reported. Malzac et al. (2008) reported a 0.15–1 TeV detection with the *MAGIC* telescope during a bright hard state of the source and pointed out that the source was not detected at TeV energies during a following X-ray flare. A transient 100 Mev – 3 GeV gamma-ray emission was observed by the *AGILE* satellite on 2009 October 16 in a position consistent with that of Cyg X-1. However, *AGILE* did not detect any other high energy events from Cyg X-1 in the time period from 2007 July to 2009 mid-October (Sabatini et al., 2010). Interestingly, Cyg X-1 was also not detected with the *Fermi* gamma-ray satellite to date, even during the *AGILE* detection (J. Wilms, priv.comm.).

A fully consistent picture that would connect all the spectral and timing properties of the source at different energies is still lacking, although there is a general idea of which components are there and which part of the variability they might contribute to (cf. Fig. 2.11). There are, however, still open questions: how is the corona connected to the base of the jet? Do jets contribute to the X-ray regime and how much? What is the origin of the timing variability components? Are the jets indeed absent in the soft state? How exactly do state transitions take place? Answering this and other questions for Cyg X-1 will help to better understand accretion in other sources, both within and outside our galaxy.

# 3 Radiative Processes

Radiative processes discussed in this chapter constitute the basis of the understanding of the spectral shape of black hole binaries. A much more detailed discussion is given in the classic book by Rybicki & Lightman (1979) on which this chapter is mainly based.

The black body radiation, introduced in Sec. 3.1, is the basis for the radiation from accretion discs. Comptonization (Sec. 3.2) explains the power law spectra of BHs at high energies. Synchrotron radiation (Sec. 3.3) mainly defines the radio spectrum but can also contribute at the X-ray energies. Finally reflection features like the Iron K $\alpha$  line (Sec. 3.4) contribute to the total shape of the spectrum and allow for additional diagnostics of the source geometry.

## 3.1 Black Body Radiation

The emission of a black body with the temperature  $T$  is described by *Planck's law*

$$I(\nu, T) = \frac{2h\nu^3/c^2}{\exp(h\nu/kT) - 1} \quad (3.1)$$

(e.g., Rybicki & Lightman, 1979) with  $I(\nu, T)$  being the intensity of the emission of electromagnetic waves with the frequency  $\nu$  per solid angle, emission surface and frequency. The total luminosity of a black body corresponds to the area under the curve described by Eq. 3.1 - therefore, to obtain the total luminosity Eq. 3.1 has to be integrated.

An accretion disc will emit a black body spectrum at any point of its surface according to the local temperature at this point, which in the standard picture follows a  $T \propto R^{-3/4}$  profile. The total spectrum will consist of an overlay of different black body components. Following Mitsuda et al. (1984) this is often called a multicolour disc.

## 3.2 Comptonization

A typical spectral shape for BHs in the hard state is, as explained in Sec. 2.4, a power law in the X-ray band with an exponentially cutoff at high energies. This shape can, as will be shown in the following, be explained by Comptonization. An in-detail derivation is given, e.g., by Rybicki & Lightman (1979).

In its most simple form Compton scattering describes the scattering of a single photon with a single stationary electron. After the scattering, a photon with an initial energy  $E$  will have the energy

$$E' = \frac{E}{1 + \frac{E}{m_e c^2}(1 - \cos \theta)} \quad (3.2)$$

if its propagation direction changes by the angle  $\theta$ .

For small photon energies ( $E \ll m_e c^2$ ) and averaging over all angles  $\theta$  the relative energy change is

$$\frac{\Delta E}{E} \approx \frac{E}{m_e c^2} \quad (3.3)$$

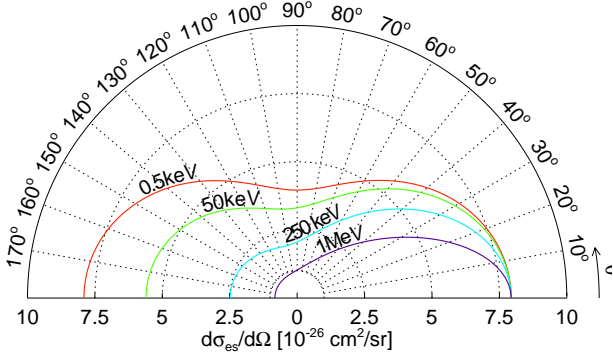


Figure 3.1: Differential Klein-Nishina cross section for different initial energies of the photon. Note the strong beaming effect with increasing energy.

(Figure created by J.Wilms)

In the limit of low energies, the cross section for the Compton scattering is the Thompson cross section  $\sigma_T$

$$\sigma_T = \frac{8\pi}{3} \left( \frac{q^2}{4\pi\epsilon_0 mc^2} \right)^2 \quad (3.4)$$

which, for an electron, has the value of  $\sigma_T \approx 6.65 \cdot 10^{-25} \text{ cm}^2$ . For higher energies, effects of quantum electrodynamics have to be taken into account. The differential cross section is then described by the Klein-Nishina formula

$$\frac{d\sigma_{kn}}{d\Omega} = \frac{3}{16\pi} \sigma_T \left( \frac{E'}{E} \right)^2 \left( \frac{E}{E'} + \frac{E'}{E} - \sin^2 \theta \right) \quad (3.5)$$

Figure 3.1 illustrates the dependency of the differential Klein-Nishina cross section on the initial energy of the photon and the viewing angle. With increasing initial energy, less and less photons are scattered to higher angles while the maximum value for the cross section, the one for  $\theta = 0$  remains constant.

The total cross section is obtained by integrating Eq. 3.5, which gives

$$\sigma_{kn} = \frac{3}{4}\pi \left[ \frac{1+x}{x^3} \left\{ \frac{2x(1+x)}{1+2x} - \ln(1+2x) \right\} + \frac{1}{2x} \ln(1+2x) - \frac{1+3x}{(1+2x)^2} \right] \quad (3.6)$$

where  $x = E/m_e c^2$ .

In an astrophysical framework the electron will be in motion, not stationary as assumed so far. In this case, Lorentz transformation between the observer's frame of rest (in which the calculations have been done so far) and the electron frame of rest have to be made and beaming effects play a major role.

When assuming a Maxwellian distribution of the electron, i.e., thermal Comptonization with a temperature  $T$ , the relative energy change is not given by Eq. 3.3, but instead by

$$\frac{\Delta E}{E} \approx \frac{4kT - E}{m_e c^2} = A \quad (3.7)$$

where  $k$  is the Boltzmann-constant and  $A$  the Compton amplification factor. Two cases are possible: either  $\Delta E > 0$  for  $E < kT$  and the photons gain energy and the electron gas cools down, or  $E > kT$  and therefore  $\Delta E < 0$ , i.e., the photons loose energy and the gas heats up.

A real electron gas has a spatially extended structure and the photons undergo multiple scatterings before leaving the electron medium. For a hot electron gas ( $E \ll kT_e$ ) the total energy change is roughly the product of the relative energy change per scattering and the number of scattering events a photons undergoes.

If the hot gas has an electron density of  $n_e$  and occupies a region of the size  $l$ , the optical depth of this gas will be  $\tau_e = n_e \sigma_T l$  and the number of scatterings according to the theory of random walk is  $\max(\tau_e, \tau_e^2)$ . The relative energy change of a photon undergoing Compton scatterings – the so-called Compton  $y$ -parameter – in this medium is then approximately

$$y = \frac{4kT_e}{m_e c^2} \max(\tau_e, \tau_e^2) \quad (3.8)$$

Note that the number of scatterings is proportional to the optical depth for optically thin media and increases quadratically with the optical depth for optically thick media.

A description of the evolution of the photon distribution as the scatterings take place is necessary to obtain the whole spectrum. It is achieved with the so-called Kompaneets equation for weak scattering with non-relativistic thermal electrons (see Padmanabhan, 2000). This equation has generally to be solved numerically.

The power law shape of the spectrum can, however, be justified as in the following simpler argumentation: after a scattering, a photon with the initial energy  $E_i$  will have the energy  $E = E_i A$ , therefore the photon energy after  $k$  scatterings is

$$E_k = E_i A^k \quad (3.9)$$

In a material with optical depth  $\tau_e$  and therefore a mean free path  $s = 1/\tau_e$ , the probability  $p_k(\tau_e)$  to undergo  $k$  scatterings is

$$p_k(\tau_e) = \tau_e \quad (3.10)$$

For  $N(E_i)$  photons with the initial energy  $E_i$  the number of photons emerging from the scattering medium with the energy  $E_k$  is then

$$N(E_k) \sim N(E_i)(1 + A)^k \sim N(E_i) \left( \frac{E_k}{E_i} \right)^{-\alpha} \quad \text{with} \quad \alpha = -\frac{\ln \tau_e}{\ln A} \quad (3.11)$$

such that the the spectrum of the emerging photons has a power law shape.

In the context of microquasars Comptonization processes are assumed to take place in the corona (see Sec. 2.2). The basic idea is, that photons – the so-called seed photons for the Comptonization – emerge from the accretion disc as essentially a (multicolour) black body spectrum and are up-scattered in the optically thin, hot plasma of the corona.

### 3.3 Synchrotron Radiation

A rigorous derivation for the synchrotron radiation is given, e.g., by Rybicki & Lightman (1979, p. 167ff) or Padmanabhan (2000, p. 304ff). In the following a qualitative discussion is given.

Synchrotron radiation is basically magnetobremsstrahlung – radiation emitted by relativistic electrons in a magnetic field (the non-relativistic case is cyclotron radiation). To derive the synchrotron radiation spectrum first a single electron is considered and than an electron distribution is taken into account.

In an uniform magnetic field  $B$  the motion of an electron with the mass  $m_e$ , charge  $e$  and total velocity  $v$  is helical: the velocity is constant in the direction of the magnetic field and circular in the plane orthogonal to it with the gyration frequency

$$\omega_B = \frac{eB}{\gamma m_e c} \quad (3.12)$$

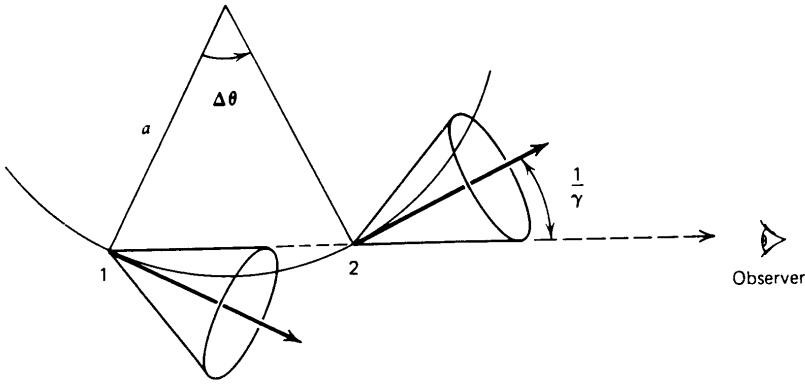


Figure 3.2: Emission cones of an electron at different point of its trajectory.  
(from: Rybicki & Lightman, 1979, Fig. 6.2)

where  $\gamma = (1 - \beta^2)^{-1/2} = (1 - v^2/c^2)^{-1/2}$  is defined as usual and  $\omega_B = \omega_L/\gamma$  with the Larmor frequency  $\omega_L$ .

Assuming a isotropic velocity distribution and averaging over all pitch angles (angles between field and velocity) yields the total emitted power:

$$P = \frac{4}{3}\sigma_T c \beta^2 \gamma^2 \frac{B^2}{8\pi} \quad (3.13)$$

Note that  $P \propto \sigma_T$  and therefore for general charged particles  $P \propto m$ , which means that the contribution of particles with higher mass than that of the electron to the synchrotron radiation can be neglected.

In the electron's frame of rest, the radiation of an individual electron will be that of a dipole. When transferred into the observer's frame of rest, however, it will be forward beamed, i.e., concentrated into a cone with the opening angle  $\Delta\theta \approx \gamma^{-1}$ . In the electron's frame of rest, this beam will pass the observer during a time (cf. Fig. 3.2)

$$\Delta t = \frac{\Delta\theta}{\omega_B} \quad (3.14)$$

To obtain the duration of the pulse  $\tau$  in the observer's frame of rest, the Doppler shift has to be taken into account. For highly relativistic electrons with  $\beta \sim 1$ ,  $\tau$  then can be approximated by:

$$\tau = (1 - \beta)\Delta t \approx \frac{1}{\gamma^2 \omega_B} \quad (3.15)$$

and the characteristic frequency of the radiation is then:

$$\omega_c = \gamma^2 \omega_B = \frac{eB}{m_e c} \left( \frac{E}{m_e c^2} \right)^2 \quad (3.16)$$

The observed time dependent  $E$ -field from one electron is therefore a series of pulses with the width  $\tau$ . These pulses can be approximated by  $\delta$  functions, so that the spectral energy distribution of a single electron (cf. Eq. 3.13) becomes

$$P_\nu(\gamma) = \frac{4}{3}\sigma_T c \beta^2 \gamma^2 \frac{B^2}{8\pi} \delta(\nu - \gamma^2 \nu_B) \quad (3.17)$$

where  $\nu = \omega/(2\pi)$ .

Contributions of individual electrons have to be accordingly weighted when an electron distribution  $n(\gamma)$  is considered:

$$P_\nu = \int_{-\infty}^{\infty} P_\nu(\gamma) n(\gamma) d\gamma \quad (3.18)$$

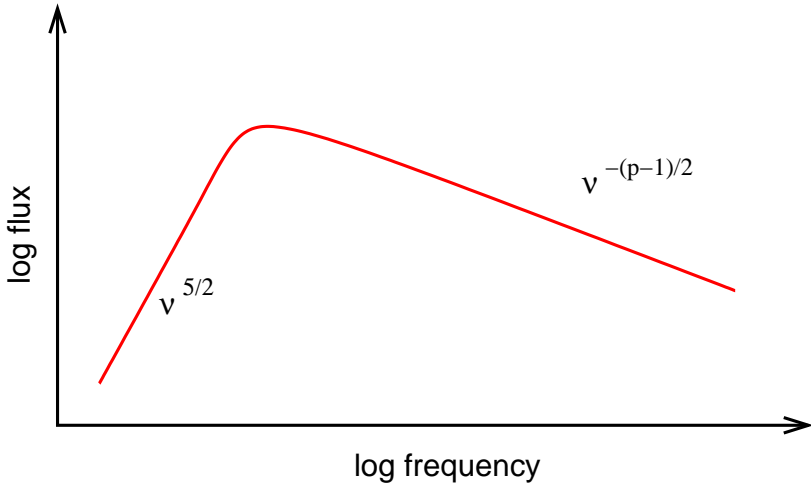


Figure 3.3:  
Synchrotron spectrum from a power law electron distribution of electrons where the synchrotron self-absorption is taken into account.  
(after: Rybicki & Lightman, 1979, Fig. 6.12)

which for the astrophysically important case of non-thermal synchrotron radiation where the electrons have a power law energy distribution  $n(\gamma)d\gamma = n_0\gamma^{-p}d\gamma$  becomes:

$$P_\nu = \frac{2}{3}\sigma_T c n_0 \frac{B^2}{8\pi} \frac{1}{\nu_B} \left(\frac{\nu}{\nu_B}\right)^{-\frac{p-1}{2}} \quad (3.19)$$

The spectrum is again a power law distribution. Thus the spectral shape of the synchrotron radiation allows to deduce the electron distribution.

Similar results are obtained analytically without approximations. Polarisation has to be taken into account for these calculations – see Rybicki & Lightman (1979) for details. An important result that cannot be obtained in the approximation presented here is that the synchrotron spectrum is polarised. A polarisation measurement can therefore be used to confirm or disprove a synchrotron origin for the radiation of a certain source and to measure the direction of the magnetic field.<sup>1</sup>

A further effect that needs to be taken into account is that not all photons, as tacitly assumed so far, escape the synchrotron emitting system. A part of them is reabsorbed. Below a cutoff frequency, the electrons are optically thick for the synchrotron radiation, above this frequency the medium is optically thin. It can be shown that for a power law distribution of electrons, the spectral distribution below the break frequency follows:

$$P_\nu \propto \nu^{5/2} \quad (3.20)$$

independent of the power law index  $p$  of the distribution. Fig. 3.3 shows a sketched synchrotron spectrum of a power law electron distribution with both optically thick and optically thin regions presented. How the flat radio typical for jets is achieved by combining single synchrotron spectra of different electron distributions within the jet is shown in Fig. 2.4.

## 3.4 Relativistic Iron Line

An important role in the shaping of the X-ray spectra of accreting systems - whether BHs or AGN - plays the irradiation of cold material in the vicinity of the accreting

---

<sup>1</sup>Note that inhomogeneities in the  $B$  field will decrease the degree of polarisation and the magnetic field in astrophysical sources is most likely not absolutely homogeneous.

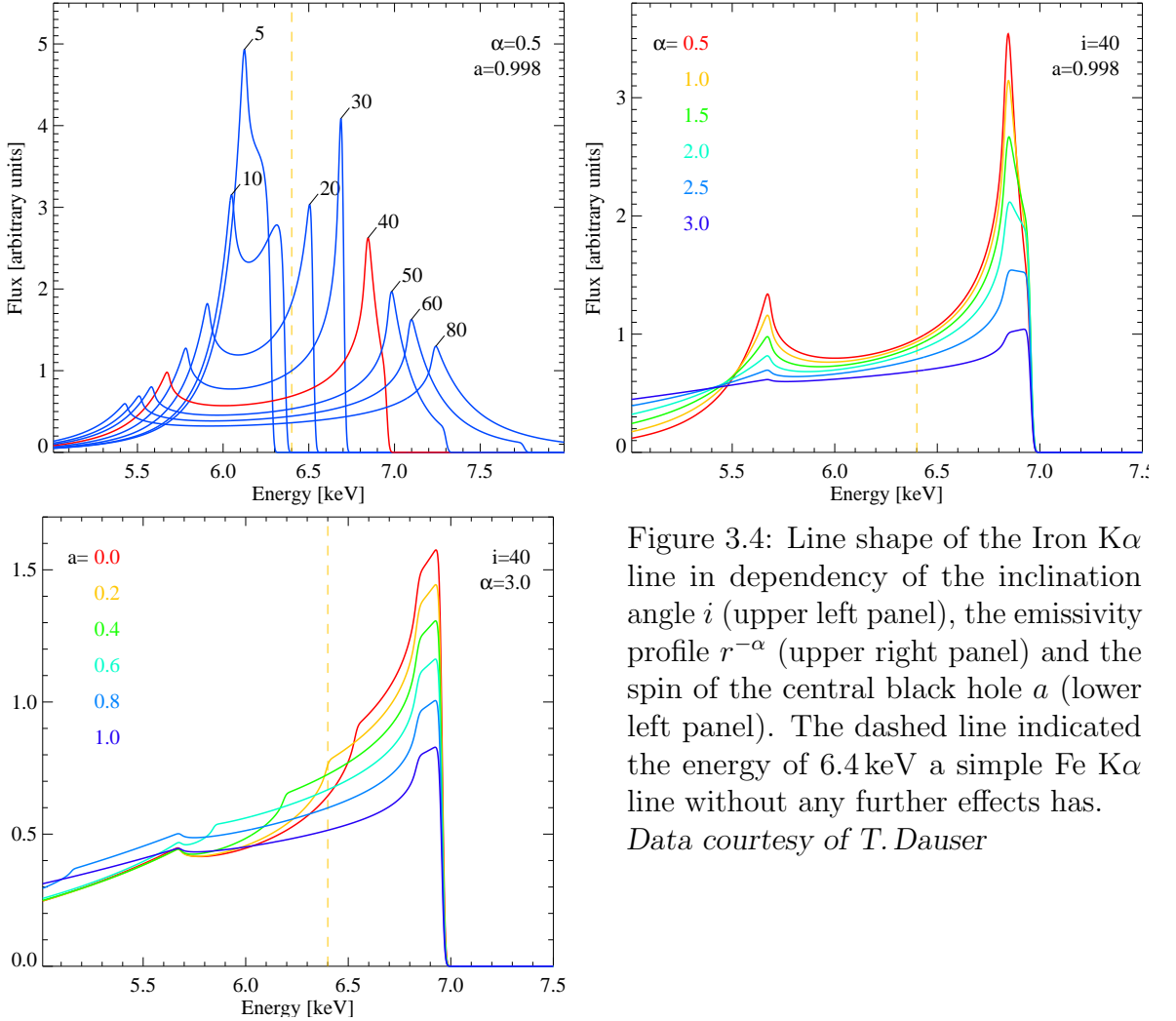


Figure 3.4: Line shape of the Iron K $\alpha$  line in dependency of the inclination angle  $i$  (upper left panel), the emissivity profile  $r^{-\alpha}$  (upper right panel) and the spin of the central black hole  $a$  (lower left panel). The dashed line indicated the energy of 6.4 keV a simple Fe K $\alpha$  line without any further effects has.

Data courtesy of T. Dauser

object by X-rays. The most striking of the so generated features is the K $\alpha$  fluorescence line of Iron (Fe) at about 6.4 keV. The shape of the iron line is hereby one of the few existing probes for the physics in the direct vicinity of a black hole. A detailed overview is given by Reynolds & Nowak (2003), while Fabian et al. (2000) offer a shorter, but very instructive review which mainly concentrates on AGN. Dauser et al. (2010) improve the modelling of the line - most of the figures presented here are results of the calculations performed for their work.

The line profile of a non-relativistic rotating annulus would be double peaked, as part of the emitting region is moving away from and part towards the observer. Effects of special relativity (transverse Doppler shift, beaming) skew the line: the blue peak increases in intensity and moves to lower energies (but is still above 6.4 keV), the red peak is smeared into lower energies. This is enforced by the gravitational redshift. The final line profile as summed over all annuli is broad and skewed (Fabian et al., 2000). Additionally, the line shape is determined by the inclination of the system, i.e., the viewing angle of the disc, by the emissivity profile of the disc and the spin of the central black hole. Relativistically broadened Fe K $\alpha$  lines have therefore been used to constrain the spin of AGNs (Brenneman & Reynolds, 2006).

Fig. 3.4 presents how the line shape is influenced by changes in the inclination  $i$ , the emissivity profile  $r^{-\alpha}$  and the black hole spin  $a$ , with  $a = 1$  being the maximally spinning black hole (Kerr black hole) with the black hole spin parallel and  $a = -1$  the

maximally rotating black hole with the spin anti-parallel to the spin of the accretion disc. Note that  $|a| = 1$  is valid only approximately: Thorne (1974) have shown that a spin-up beyond  $a = 0.998$  is prevented by the fact, that the radiation emitted by the disc and swallowed by the black hole produces a counteracting torque. The case is more complicated for a counterspinning black hole and as far as known not derived in the literature in detail: relativistic boosting and the increased value of the ISCO ( $\sim 9R_g$ ) work against each other when determining the maximal possible value.

# 4 Instrumentation and Data Reduction

To conduct exact analysis, a thorough understanding of the instruments and data reduction pipelines used is required. This will become especially evident in the case of *INTEGRAL* in Chapter 7, where instrumental reasons are a major hindrance for scientific analysis.

In this chapter the basic functional principles of proportional counters and coded mask instruments are explained (Sec. 4.1), which are necessary to understand the following more detailed introduction into the *RXTE* (Sec. 4.2) and *INTEGRAL* (Sec. 4.3) satellites and their respective instruments and data reduction procedures. Lastly, the radio telescope *Ryle/AMI* is shortly introduced in Sec. 4.4.

## 4.1 X-ray Detectors

Although optical astronomy achieves better results with space based experiments, it is doable in high quality on the ground. X-ray astronomy, however, is fully dependent on space experiments<sup>1</sup>, as the atmosphere filters out the X-ray radiation. This introduces additional technical problems when building X-ray detectors: they have to be robust enough to withstand the launch and function in space without repairs but at the same time light enough to be brought into space with reasonable costs. In principle, detectors can be divided in two main categories: non-imaging detectors, such as the proportional counter units (PCUs) on board *RXTE*, or imaging detectors, such as charge coupled devices (CCDs) or position sensitive proportional counters. Images are formed either by means of Wolter telescopes, such as those on board *XMM-Newton* or the planned German experiment *eROSITA*, or via coded masks, as in the ISGRI and JEM-X experiments on board *INTEGRAL*.

Especially important for this work are proportional counters and coded mask instruments.

### 4.1.1 Proportional Counters

A good overview of proportional counters is given, e.g., by Grupen & Schwartz (2008), p. 97ff. Here only the basics as necessary to understand the instruments used can be conveyed.

The simplest kind of X-ray detectors are ionisation chambers, where the basic design is that of a gas-filled parallel plate capacitor. An incoming photon is absorbed in the detector gas and an electron is ejected from the K-shell with an energy proportional to the initial energy of the photon. Further  $N$  charges are produced through collisional ionisation. This leads to the induction of charges on the capacitors. When the charge is drained via a resistance, a measurement of the charge and therefore the initial energy of the photon can be made (Kleinknecht, 1998). This basic principle also underlies the proportional counters.

The signals from a simple ionisation chamber are however very weak since only the primary charge is measured. An amplification is therefore required. This can be

---

<sup>1</sup>Balloon flights, which were used a lot during the beginning phase of X-ray astronomy, are still of some importance, but they do not allow for long-term campaigns as those these work is based on.

achieved by changing the shape of the construction: the anode is implemented as a thin wire in the middle of a cylindrical cathode. Photons then reach the inside of the detectors, e.g., via windows built into the cathode. The electric field next to the anode is very strong, such that the ionised particles are strongly accelerated. Again, collisional ionisation takes place. The ionised particles are now accelerated: a cascade forms. The measured voltage is approximately *proportional* to  $N$ , the number of particles ionised by the ejected K-shell electron. This principle of operation is also used by Geiger counters, which, however, operates at a higher voltage between the anode and the cathode, where the direct proportionality is not valid anymore.

Typical operational voltages for proportional counters are in the order of 100–1000 V, depending on the detector gas used. To be able to operate under a smaller voltage and to minimise excitation losses, inert gases are used.

The choice of Xenon for astronomical detectors is motivated by the probability of absorption which is proportional to the number of the protons  $Z$ :  $\sigma_{\text{abs}} \propto Z^{4\dots 5}$ . As at the same time  $\sigma_{\text{abs}} \propto E^{-3}$ , proportional counters are only usable below a threshold of about 100 keV. An important modification are so-called position sensitive proportional counters where multiple crosswise arranged anodes and modified read-out electronics allow a detection of the position of the initial photon (Kleinknecht, 1998).

An important characteristic is the detector dead time: during an ongoing shower an incoming photon will not be registered as a single event. Therefore cascades have to be short to allow for observations of bright sources. This is achieved by adding ‘quenching gas’ to the primary gas: on very short timescales of under one  $\mu\text{s}$  this gas will absorb the UV photons emitted by the excited ions and prevent the formation of new cascades due to the photoeffect.

An example for an X-ray instrument making use of proportional counters is the Proportional Counter Array (PCA) on board *RXTE*, (Sec. ??

#### 4.1.2 Coded Mask Instruments

No imaging with mirrors<sup>2</sup> is possible above  $\sim 30$  keV. For a 20 keV photon, for example, the critical angle, at which total refraction would occur, drops to about  $0.45 \times 10^{-3}$  (see Fürst, 2008, for the calculation). Other approaches are therefore necessary to allow for imaging at higher energies.

A widely employed possibility are coded mask detectors – basically a combination of a plate with multiple holes with a detector providing positional information (in’t Zand, 1992). Every source will cast a shadow of the mask on the detector plane. The combination of these shadows, the shadowgram, is a convolution of the source distribution with the mask.

The mask pattern is chosen in such a way that the shadow cast from any source at any position on the sky is unique, i.e., the autocorrelation of the mask function should consist of a single sharp peak with no pronounced further features<sup>3</sup> (in’t Zand, 1992). The reconstruction of the image can then proceed in an iterative way reminiscent of the image reconstruction in radio interferometry: the brighter source in the field is found, removed from the shadowgram and the search for the next brightest source

---

<sup>2</sup>For an introduction into X-ray mirrors see Aschenbach (1985); since no imaging instruments using X-ray mirrors are used in this work, they are not explained here in detail.

<sup>3</sup>A perfect pattern will however not be possible for technical reasons including the impossibility to build mask elements that are totally transparent or non-transparent in X- and  $\gamma$ -rays and the fact that the mask elements need sufficient supporting structure.

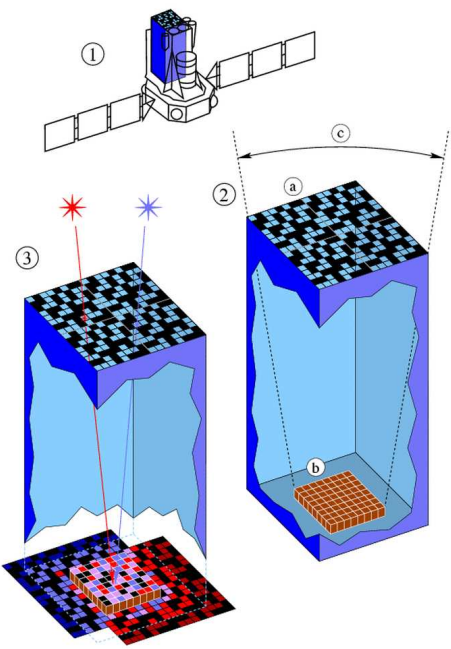


Figure 4.1: Principle of coded mask instruments on the example of the ISGRI instrument on board the *INTEGRAL* satellite. The instrument consists of the partially transparent mask ① and the position sensitive detector plane ②. ③ denotes the field of view. Each source (represented by red and violet stars here) casts a shadow image (shadowgram) – the combined shadowgram is recorded in the detector plane.  
image courtesy of ISDC/Univ.Geneva

continues in the same way. This method is called **Iterative Removal of Sources** or short ‘IROS’-method (Groeneveld, 1999). Computationally this is possible by using the cross correlation function. When the response of a pixel located at  $x, y$  is defined by

$$R(x, y) = C(x, y) - \langle C \rangle \quad (4.1)$$

with  $C(x, y)$  the count rate in the considered pixel and  $\langle C \rangle$  the mean count rate over the whole detector, it can be compared to the response of a source located at  $\alpha, \delta$  on the sky by searching for the maximum of the cross correlation function CCF:

$$\text{CCF}(\alpha, \delta) = \iint_{\forall x, y} R(x, y) R(x, y; \alpha, \delta) dx dy \quad (4.2)$$

The maximum of CCF corresponds to the real source position.

This basic method is however only that simple for an ideal detector. Skinner (1995) offer a short overview over the coding and decoding methods for coded masks and discuss especially the effects imperfection, which will always be present in real detectors, introduce as compared to the well understood ideal case. A discussion of the disadvantages (high intrinsic background, high computational costs of even a single image) and advantages (wide field of view and broad spectral coverage) of the coded mask technique is presented by Skinner (2004)<sup>4</sup>. A comprehensive discussion of coded mask instruments is given by Groeneveld (1999) (in German).

---

<sup>4</sup>The conclusion of Skinner (2004) cannot be left unmentioned in the context of this work:

*Coded mask telescopes are indirect and inefficient. [...] But nevertheless there are important regions of parameter space in which they are the preferred technique and (like certain members of the scientific community) they are likely to continue to be employed despite their idiosyncrasies.*

## 4.2 *RXTE*

### 4.2.1 The Satellite

The first important satellite used for this work is the **Rossi X-ray Timing Explorer** (*RXTE*)<sup>5</sup>, an ongoing hard X-ray mission lead by NASA and launched on 30th December 1995. An overview of the mission is given on the official website of *RXTE* <sup>6</sup>, which is also used as one of the main sources here. The instrumentation of the mission consists of three instruments (see Fig. 4.2): the **Proportional Counter Array** (PCA) (Jahoda et al., 1996, 2006) for the lower energy range of initially 2–60 keV, the **High Energy X-ray Timing Experiment** (HEXTE) (Rothschild et al., 1998) for the higher energy range of 15–200 keV and the **All-Sky Monitor** (ASM) (Levine et al., 1996), which allows to monitor up to 80% of the sky within one *RXTE* orbit in the 1.5–12 keV range. The satellite is in a low Earth orbit with an initial altitude of about 600 km, corresponding to an orbital period of about 90 min<sup>7</sup>. This, together with the existence of the so-called South Atlantic Anomaly (SAA), which is crossed by *RXTE* during some of the orbits, determines the maximal length of an uninterrupted observation of a source.

The X-ray timing capabilities of *RXTE*, which can resolve timescales up to  $1\,\mu\text{s}$ , have been (and due to the lack of a successor in the foreseeable future continue to be so) of crucial importance for understanding and often at all first detecting timing properties of X-ray emitting objects. Hardly any review paper discussing timing properties does so without mentioning *RXTE* as the instrument today's timing analysis in X-rays is dependent on (see Belloni, 2010; McClintock & Remillard, 2006, etc.). Of additional importance is the ability of the ASM to detect X-ray transients and therefore allow to trigger pointed observations with *RXTE* and/or other instruments.

A comprehensive, yet comparatively short overview over the spacecraft and all its instruments is provided by Kreykenbohm (2004).

### 4.2.2 ASM

The ASM (Levine et al., 1996) consists of three Scanning Shadow Cameras mounted on a boom, which can be rotated to allow for better scanning of the sky (Fig. 4.3, left panel). Every camera consists of position sensitive proportional counters behind a slit mask (Fig. 4.3, right panel), the ASM is therefore a simple coded mask instrument.

All three cameras operate in the energy range of 1.5–12 keV, which is subdivided into three channels with the range of roughly 1.5–3 keV, 3–5 keV, and 5–12 keV. If not explicitly stated otherwise all ASM data used for this work are for the full 1.5–12 keV range.

The field of view is  $6^\circ$  by  $90^\circ$  and the spatial resolution  $3'$  by  $15'$ . The nominal sensitivity is 30 mCrab. The sky coverage is highly stochastic and a randomly chosen source is scanned about 5 to 10 times a day, allowing for the monitoring of its long-term behaviour.

Observers do not analyse raw ASM data. Data products are provided at [http://heasarc.gsfc.nasa.gov/docs/xte/asm\\_products.html](http://heasarc.gsfc.nasa.gov/docs/xte/asm_products.html). A 3% uncertainty in flux values is inherent to all the ASM data and already included in the data products provided.

<sup>5</sup>Also referred to as just XTE sometimes.

<sup>6</sup><http://heasarc.gsfc.nasa.gov/docs/xte/XTE.html>

<sup>7</sup>Nowadays, the altitude is about 500 km as the satellite lost  $\sim 100$  km in the past 15 years.

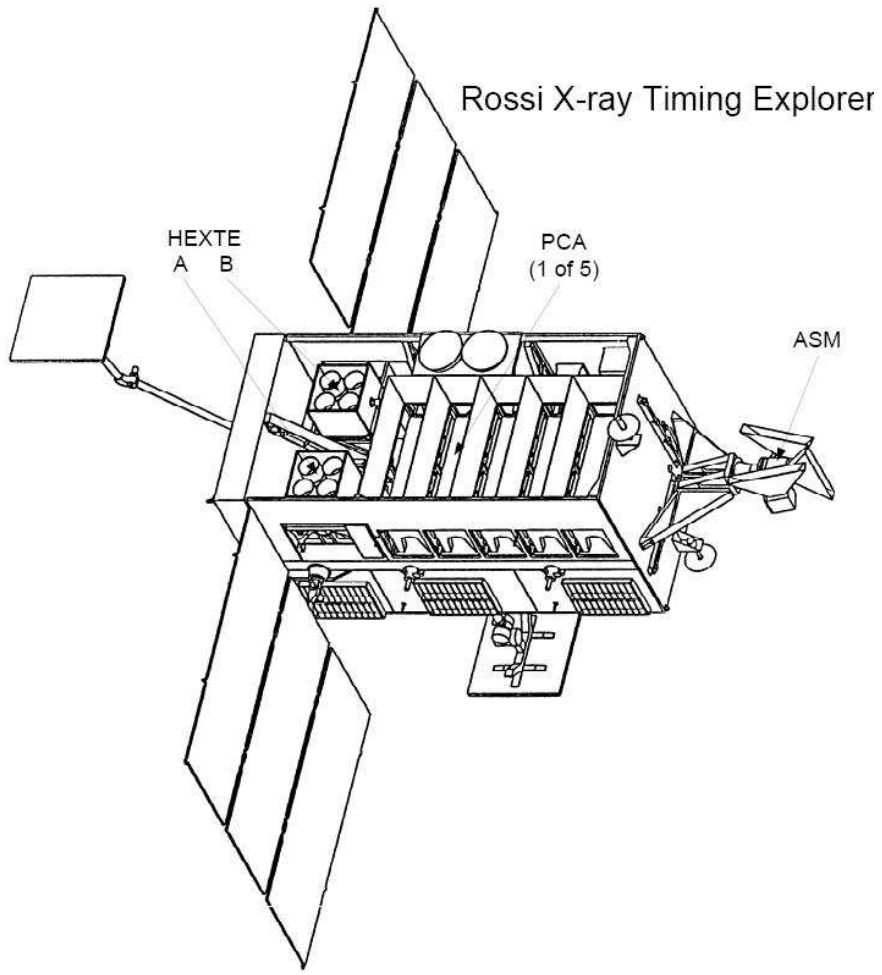


Figure 4.2: Top view on the *RXTE* spacecraft. Visible are the five PCA proportional counter detectors, the two HEXTE clusters, each consisting of four detectors, and the ASM instrument. Solar panels are located on the sides of the spacecraft and the antennas on the outside. Above the PCA instrument the two star trackers of *RXTE* are visible. (Rothschild et al., 1998, Fig. 1)

### 4.2.3 PCA

#### Basic Properties of the Instrument

The PCA<sup>8</sup> (Jahoda et al., 1996, 2006) consists of five identical co-aligned proportional counter units (PCUs), labelled 0 to 4. A cut through one of the PCUs is presented in Fig. 4.4. The detector has five gas layers each of which is a proportional counter itself. The top propane layer acts as a veto layer. It is followed by three Xenon detector layers and a Xenon veto layer. As the size of the detectors is large, a net of anodes is used. The outermost anodes of the three inner layers are used as veto layers (all veto layers are marked in grey in Fig. 4.4). This construction allows to distinguish between real source photons entering from above and unwanted background photons from other directions (Jahoda et al., 2006). Note that layers have different quantum efficiencies, as

---

<sup>8</sup>Official website with a good overview over different PCA related publications and additional unpublished material can be found under <http://astrophysics.gsfc.nasa.gov/xrays/programs/rxte/pca/>

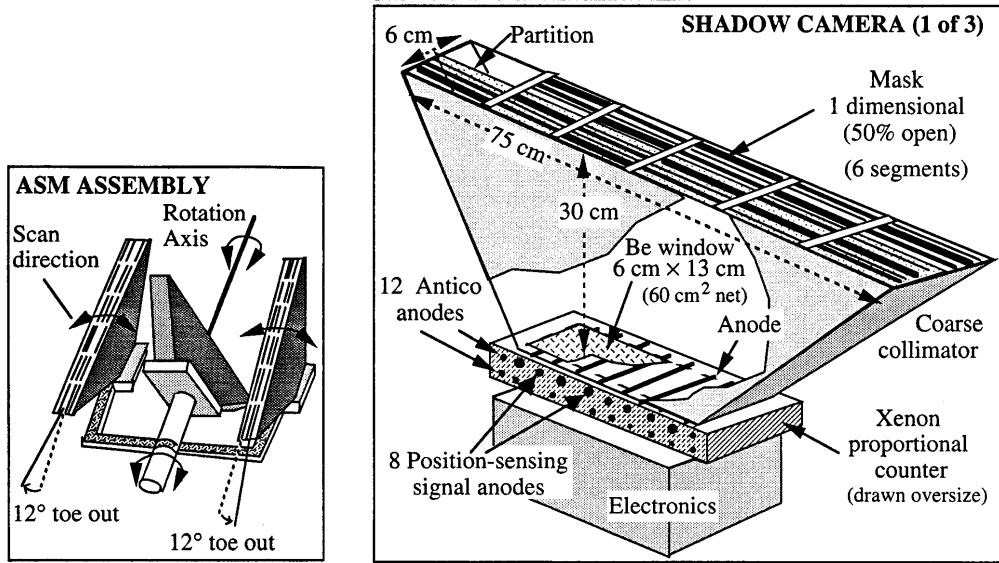


Figure 4.3: *Left panel:* Schematic drawing of the three ASM cameras showing their relative orientation. *Right panel:* Schematic drawing of one of the shadow cameras. (after: Levine et al., 1996, Fig. 1)

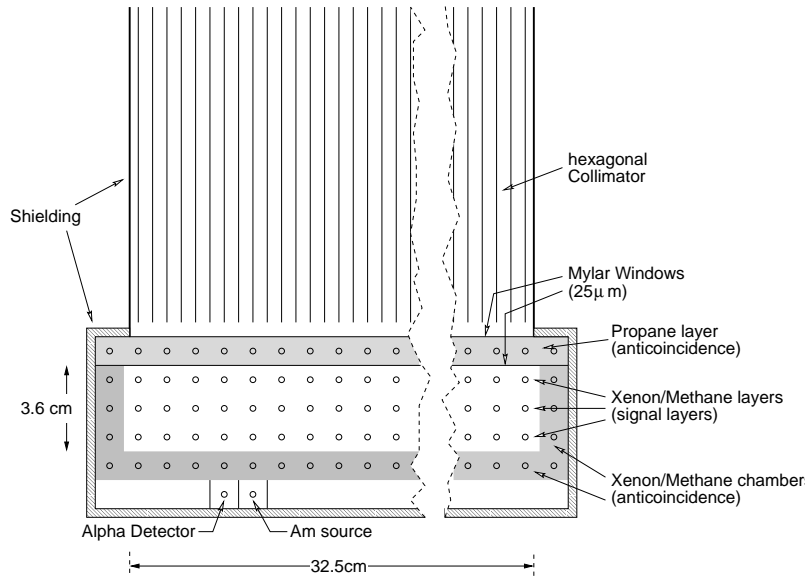


Figure 4.4: Schematic drawing of one of the five proportional counters of the PCA. (Wilms, 1998)

can be seen on Fig. 4.5.

A collimator limits the field of view of the PCA to 1°. This is important as the PCUs are not position sensitive, therefore observations have to happen in such a way that only one source is in the field of view of the PCA during the observation.

All detector layers of all PCUs combine to an effective detector area of  $\sim 6000 \text{ cm}^2$ . The detector is nominally sensitive to photons of 2–60 keV with an original resolution of 18% at 6 keV (Jahoda et al., 2006).  $^{241}\text{Am}$  is used as calibration source as it emits characteristic 59.6 keV photons – for the placement of the calibration source in the detector see Fig. 4.4.

To alleviate the effects of the degradation of the detectors, several measures were taken. Not all PCUs are on during all the observations, with on average only 2 PCUs being on at a time to let the detectors rest. The PCUs are switched off during the

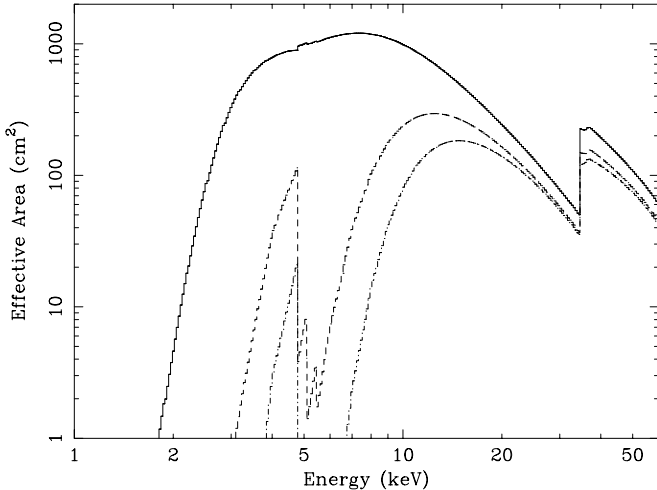


Figure 4.5: Modeled quantum efficiency of PCU 2 on 2002 January 13. The solid line represents the top Xenon layer, the dashed line the second Xenon layer, the dash dotted line the third Xenon layer of the detector. (Jahoda et al., 2006, Fig. 5)

passage through the South Atlantic Anomaly, a region where, due to the shape of the Earth's magnetic field, the background is very high (see Fürst et al., 2009, for a discussion of the evolution of the SAA as measured with *RXTE*). Additionally, the voltage of the PCUs was changed, which led to an increase in the detectable energy range, now 2–100 keV, but also implied a worsening of the detector resolution.

### Background and Useful Energy Range

PCU 0 lost its propane layer in May 2000. On 20th October 2006 also PCU 1 lost its top propane layer due to a micrometeorite impact. The PCUs remain functional but show a stronger background and a different gain. Due to this as well as changes in the high voltage the PCA has several calibration epochs, i.e. periods between discontinuous changes in the response which correspond to such changes in the instrument. An overview over the PCA calibration epochs until 2006 is given by Jahoda et al. (2006). Note that different auxiliary files (response matrices and background models) are necessary for different observational epochs (Kreykenbohm, 2004).

The useful range of the PCA is limited by the background and by Xenon edges: the Xenon L-edge between 4 keV and 5 keV and the Xenon K-edge around 35 keV. Correction of both effects was a big limiting factor in the past when an upper limit of  $\sim 25$  keV was recommended for PCA data. The L-edge was often still visible in the spectra, adding to instrumental uncertainties and making them stronger energy dependent (Wilms et al., 2006). Figure 4.5 shows the quantum modeled efficiency for the PCU 2 on 2002 January 13: the edges can be clearly seen as strong drops in the effective area.

Since August 2009, a new PCA response generator, PCARMF v11.7, has been available which improved the modelling of the edges and allowed for a wider usable energy range from about 3 keV to about 45 keV<sup>9</sup>. Still, the calibration of the bins around 3 keV remains a major uncertainty when working with PCA data. This version of the response has been used for the PCA data in this work.

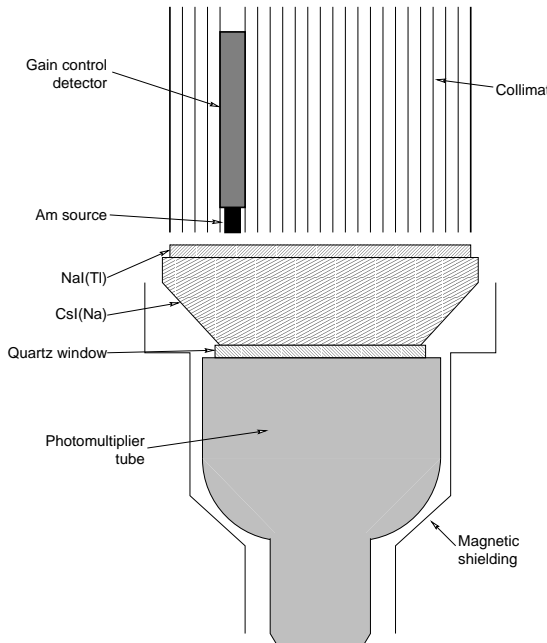


Figure 4.6: Schematic drawing of one of the eight HEXTE detectors. (Wilms, 1998)

#### 4.2.4 HEXTE

##### Basic Properties of the Instrument

The HEXTE (Rothschild et al., 1998) consists of two independent clusters (HEXTE A and HEXTE B), each containing four NaI(Tl)/CsI(Na)<sup>10</sup> phoswich scintillation detectors placed behind a collimator which limits the field of view to  $1^\circ$ , similar to the PCA. Again  $^{241}\text{Am}$  is used as a calibration source, but here dedicated electronics allow to adjust the gain automatically, so that no calibration epochs are necessary. The effective area of all eight detectors is  $\sim 1600 \text{ cm}^2$ . The energy range is 15–250 keV with an energy resolution of 15.4% at 60 keV.

In the first months of the mission, cluster B lost the spectral capability of one of its four detectors, but is still working with the three remaining.

##### Background

The whole HEXTE detector is surrounded by magnetic shielding as scintillation detectors are sensitive to changes in the magnetic field. A further shielding is provided by the anti-coincidence shielding against charged particles.

When analysing HEXTE data, it is nevertheless important to remember that the background is still much higher than in the PCA – in fact, as Kreykenbohm (2004) have pointed out, the background can often be higher than the source count rate itself. It is dominated by internal activation and highly structured.

Background measurements have been done by switching between the clusters during the observation: one of the clusters is pointing at the source, the other at a background field and the cluster positions are swapped every 32 s. This is often referred to as rocking. Two pointing positions for the background measurement labelled ‘plus’ and ‘minus’ are possible.

---

<sup>9</sup>See the instrument team page for the PCA: <http://astrophysics.gsfc.nasa.gov/xrays/programs/rxte/pca/>

<sup>10</sup>Sodium iodide doped with Tellurium and Caesium iodide doped with Sodium.

Following problems and several reboot attempts, HEXTE A was parked in the on-source position on 2006 October 2006 to prevent a freezing of the detector in a position not suitable for scientific work. A model, `hextebackest`, had to be developed to calculate the background of cluster A from the background observations made by cluster B. In December 2009 HEXTE cluster B, again following several problems and reboot attempts, was parked in a background position so that background estimation remains possible<sup>11</sup>.

#### 4.2.5 Data Reduction

From raw data provided from the *RXTE* archives, lightcurves and spectra have to be extracted. For this, the software package HEASOFT is used - in this work the version HEASOFT 6.9 was utilised. Detailed description of the individual steps is provided in the *RXTE* cook-book<sup>12</sup>.

The data mode used for the observation – the way the satellites electronics pre-process the data before sending them to the ground – defines the properties of the final data products such as resolution and energy ranges of the lightcurves. The countrates for bright objects like Cyg X-1 are so high that data has to be pre-processed on board due to telemetry constraints. An overview over the modes, telemetry constraints and other technical details is provided in ‘Appendix F: The XTE Technical Appendix Technical Appendix’ on the official *RXTE* website<sup>13</sup>.

As SAA passages occur in about 6 consecutive orbits per day, a special treatment of those times is required. During the passage with its very high background rates the high voltage is switched off so that no high charges which could damage the detectors are created. However, even after the passage the level of induced radiation might continue to be high for some time. For this reason, as well as to stay consistent with the previous work (Pottschmidt et al., 2003b, and further papers in the series), a very conservative SAA exclusion time of 30 min is used to filter the event data.

The ‘electron ratio’ is a measure for the particle background during the low-luminosity hard states of Cyg X-1. An ‘electron ratio’ upper threshold of 0.1 is therefore used for the extraction of the PCA data. For consistency reasons, HEXTE data are extracted for the same good time intervals (GTI) as the PCA data. This, as well as a maximum pointing offset of 0.01° and minimum source elevation of 10° above the Earth horizon, is also consistent with previous work (Pottschmidt et al., 2003b, and further papers in the series). Also in consistency with previous work, only data from the top Xenon layer of the PCA are used. This approach reduces the overall count rate, but the upper layer is the best calibrated and therefore data extracted in such a way are the most reliable.

### 4.3 INTEGRAL

#### 4.3.1 The Satellite

The second of the main instruments used in this work is the **INTErnational Gamma-Ray Astrophysics Laboratory (INTEGRAL)** – an ongoing soft gamma ray mission operated by ESA (Winkler et al., 2003). The instrumentation of the mission consists of

---

<sup>11</sup>source: <http://heasarc.gsfc.nasa.gov/docs/xte/whatsnew/big.html>

<sup>12</sup> [http://heasarc.gsfc.nasa.gov/docs/xte/recipes/cook\\_book.html](http://heasarc.gsfc.nasa.gov/docs/xte/recipes/cook_book.html)

<sup>13</sup> [http://heasarc.gsfc.nasa.gov/docs/xte/RXTE\\_tech\\_append.pdf](http://heasarc.gsfc.nasa.gov/docs/xte/RXTE_tech_append.pdf)

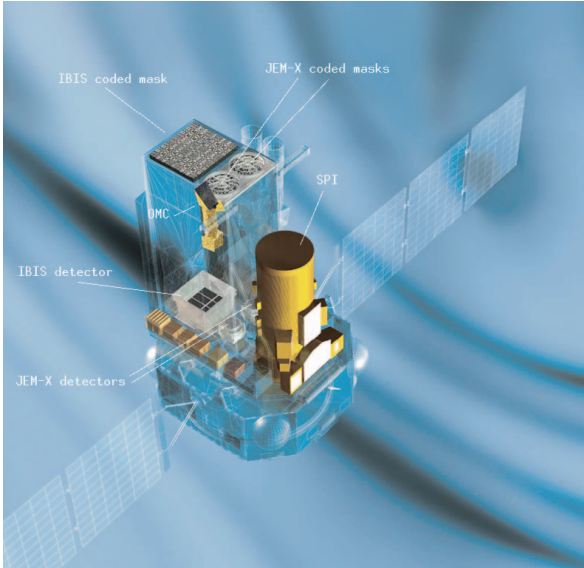


Figure 4.7: The INTEGRAL spacecraft (Winkler et al., 2003, Fig1)

the two main instruments, the Imager IBIS (Ubertini et al., 2003) and the spectrometer SPI (Vedrenne et al., 2003), which both work in the gamma-ray range and are, together with one of the supporting instruments, the X-Ray Imager JEM-X (Lund et al., 2003), coded mask instruments. Additional coverage in the optical range is provided by the Optical Monitoring Camera OMC (Mas-Hesse et al., 2003) (see Fig. 4.7). The so-called Veto system, which completely encloses five sides of the IBIS detector, is used to shield it and with the help of anticoincidence logic to reject events outside from the field of view (FOV).

The energy range of the individual detectors is chosen to allow for the best coverage of the energy regime: JEM-X works in the energy range of 3 keV–35 keV, SPI in the 20 keV–8 MeV energy range, and both detectors constituting IBIS cover the range from 15 keV to 10 MeV. The OMC covers the range between 500 nm and 600 nm.

INTEGRAL is in a highly eccentric orbit with an inclination of 51.6 degrees, a perigee height of 9 000 km and an apogee height of 154 000 km. The long duration of the orbit – 72 hours – allows for long periods of uninterrupted observations. As the observations are carried out outside of the radiation belt, which would cause a high, unstable instrument background, a total of about 90% of the time in orbit can be in principle used for scientific observations (Winkler et al., 2003) with usually about 12 hour out of the 72 hour orbit being too affected by the radiation belts.

### 4.3.2 The IBIS Instrument

IBIS consists of two simultaneously operating detectors, both of which are located behind a tungsten coded aperture mask (Fig. 4.8), one behind the other. Images are reconstructed from the shadowgram that the mask projects onto the detector plane (see 4.1.2). It is important to note that in the gamma ray regime it is not possible to create fully opaque mask elements: here an opaque cell is defined by a minimum of 70% opacity at 3 MeV and an open cell by an off-axis transparency of 60% at low energies and of 95% at high energies (Ubertini et al., 2003). In addition to the actual coded mask, there is the *Support Panel*, which is necessary for the stability of the coded mask during launch and operation. The *Support Panel* has to be taken into account during the data reduction in the background correction step (BKG\_I; see 4.3.5 Chernyakova & Neronov, 2008).

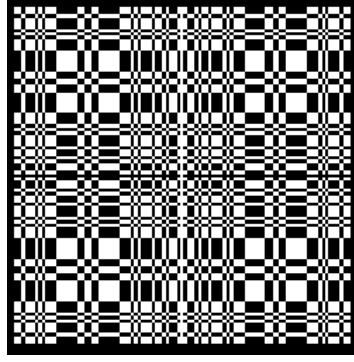


Figure 4.8: IBIS coded mask  
 MURA (Modified Uniformly Redundant Array) of Order 53  
 (Chernyakova & Neronov, 2008, Fig. 5)

The pixels of both detectors are implemented as physically distinct elements, since the spatial resolution of the detector array is crucial for obtaining a good angular resolution (Chernyakova & Neronov, 2008). The frontal detector plane (The **INTEGRAL Soft Gamma Ray Imager** or ISGRI) consists of Cadmium-Telluride Pixels measuring  $4 \times 4 \times 2$  mm (width x depth x height), the second detector plane (*Pixellated CsI Telescope* or PICsIT) is located 90 mm behind ISGRI and consists of  $9 \times 9 \times 30$  mm Caesium-Iodide scintillator pixels. The two layers allow for 3D tracking of photon paths if they interact both in ISGRI and PICsIT, which helps to improve the signal to noise ratio by allowing to reject those events which are unlikely to correspond to source photons in the FOV (Ubertini et al., 2003).

### Coded Mask Imaging System

Coded mask instruments allow to measure simultaneously the combined source and background spectrum and the background spectrum alone in detector areas corresponding to the transparent and the opaque elements of the mask, respectively.

The FOV of such an instrument is determined by the size of both the detector and the mask as well as their relative position to each other. In IBIS, the mask – MURA (Modified Uniformly Redundant Array) of Order 53 (see Groeneveld, 1999, and references therein for further information) – is larger than the detector and the FOV is therefore divided in the fully coded FOV of  $9^\circ \times 9^\circ$ , where all source radiation is modulated by the mask and the partially coded FOV of  $19^\circ \times 19^\circ$  (50% modulation), where only a part of it is modulated. The sensitivity drops to zero at  $29^\circ$  off-axis (Goldwurm et al., 2003). The nominal angular resolution is  $12'$ .

The point spread function<sup>14</sup> of the the MURA array employed for IBIS would be a  $\delta$ -function in the ideal case. However, the actual form of the PSF even for an on-axis source is different, depending on the actual physical implementation of the instrument, such as pixel size, thickness of the mask, as well as the image reconstruction process (Goldwurm et al., 2003). Figure 4.9 shows the point spread function for an on-axis source for ISGRI. Remarkable is especially the flat level of the PSF in the inner part of the FOV, which is, however, accompanied by 8 secondary lobes with ghost peaks, which need to be cleaned out by the software in order to obtain a proper image.

---

<sup>14</sup>Following the definition employed by Goldwurm et al. (2003), the PSF is defined here as the projection of the deconvolved image back onto the sky plane.

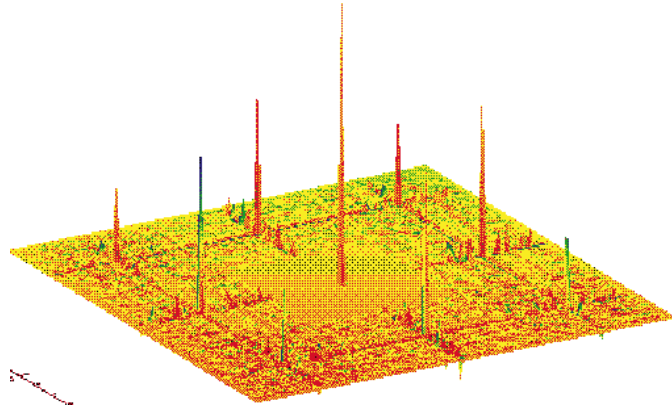


Figure 4.9: PSF over the complete FOV for IBIS/ISGRI  
(Goldwurm et al., 2003, Fig3)

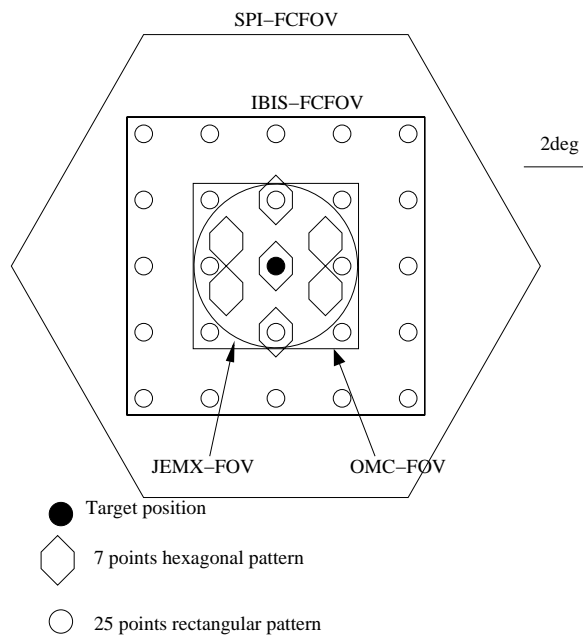


Figure 4.10: The INTEGRAL hexagonal and 25 point dither patterns  
(Courvoisier et al., 2003, Fig1)

### 4.3.3 Observing Strategy

#### Pointing Patterns

The *INTEGRAL* observing strategy is defined by the requirements of the analysis of coded mask detector data. To improve the resolution and to allow for a better quality of the reconstructed data when observing a single known source or a group of known sources in the field of view, a dithering method consisting of a number of pre-defined spacecraft pointings around the source or source region is employed (Chernyakova, 2005). The exact pattern depends on the requirements of the considered observations, the different standard possibilities are shown on Fig. 4.10. The most important pattern for this analysis is the 7 points hexagonal pattern (from here on: hex pattern), employed in the case of a single known source which is to be mainly observed. The individual steps are  $2^\circ$  apart, so that the source will stay in the smaller FOV of the JEM-X instrument. The 25 points rectangular pattern will usually be used for extended emission or when

several sources are to be observed within the FOV. Though the length of a pointing can vary, the typical time spent in a single pointing is about 2000 s (Courvoisier et al., 2003).

Basic quanta of the *INTEGRAL* data are science windows (ScW) with a maximal duration of about 3.5–4.5 ks. Each pointing and each slew will constitute a science window with longer pointing (e.g. so-called staring observations, which are not carried out nowadays) being subdivided in different ScWs.

Any other kind of pointing will also usually include shorter pointing of about the above mentioned length, though with different patterns. Additionally, users can provide a special pattern, individually matched to their observations to improve the scientific output. An example for this approach for the Cygnus X-1 Key Programme observations will be provided in Sec. 7.1.2.

## Key Programmes

Key Programmes (KPs) are scientific investigations which require a significant amount of the available time ( $> 1$  Ms). Because of the large field of view of the satellite, several sources are simultaneously observed within one KP. One year-long data rights for individual sources may be requested by observers. The *INTEGRAL* data for Cyg X-1 presented here are (mainly) from the Cyg X-1 Key Programme.

### 4.3.4 Data Structure

The *INTEGRAL*/IBIS data are available online from the *INTEGRAL* Science Data Centre (ISDC). The consolidated (CONS) data related to a proposal are generally available about 8 to 10 weeks after the actual observations. Shortly after the observation, the so-called **near real-time** (NRT) data are available, which can be used for a preliminary analysis.

Each ScW provided by ISDC contains a plethora of different files including the raw and prepared scientific data as well as housekeeping data. The naming of science windows follows the general convention of the form RRRRPPPPSSSF.VVV, where:

- RRRR : revolution number
- PPPP : assigned pointing number
- SSS : part of the pointing or slew if subdivided
- F : flag (0, 1 or 2) defining the type of science window with 0 standing for pointing, 1 for a slew, 2 for non-science
- VVV : version number of the dataset, different between NRT and CONS data, with usually VVV=001 for CONS data

Here, science windows will usually be referred to as RRRRPPPPSSSF and, unless states otherwise, are CONS data.

The data repository structure contains the following directories:

- aux : auxiliary data products
- cat : observational catalogues for data analysis
- ic : instrument calibration files
- idx : ISDC index files for fast searching of data
- obs : results of the scientific analysis
- scw : results of the science window pipelines on a per-science window basis

The data in the `aux`, `cat`, `ic`, `idx`, and `scw` directories are shared between all data sets<sup>15</sup>.

### 4.3.5 Data Reduction Pipeline

#### Overview

Due to its very nature as a coded mask instrument, the extraction and analysis of *INTEGRAL* is highly complex compared to the more traditional high energy ‘telescopes’. A multitude of possibilities for different modes of extraction is offered by the software and has to be fine tuned to the field and source in question to achieve the best results.

It is also important to keep in mind that though the ultimate goal of the analysis is usually to obtain information about one single source in the field, it is not possible to deal with only one source at once: in every step the whole field has to be taken into account as any source contributes to the background for other sources and the treatment of the whole field will influence the results for the source in question.

The extraction of the *INTEGRAL* data, including the creation of images, lightcurves and spectra is done with the **Off-line Science Analysis** (OSA) software<sup>16</sup>. The algorithms are described by Goldwurm et al. (2003) for IBIS and by Westergaard et al. (2003) for JEM-X. The individual steps follow the Cookbook Chapters of IBIS Analysis and JEM-X Analysis User Manuals (Chernyakova et al., 2009; Chernyakova & Neronov, 2008, respectively).

Figure 4.11 offers a comprehensive overview of the levels of extraction for the standard IBIS science analysis pipeline and the respective products. As only ISGRI is used for this work, the steps involving PICsIT data only are skipped during the data analysis. All data reduction steps can either be started with the help of a graphical user interface or, as done in this work, from the command line.

#### Single ScW-Images and Mosaics

The first step of any IBIS data analysis is the creation of the so-called *observation group* with the `og_create` program. The IBIS Analysis User Manual (Chernyakova & Neronov, 2008) advises the creation of one observation group for all the ScW, which will later be used for the creation of the mosaic image and the summed spectrum. To allow for more flexibility, another approach is taken here: every ScW constitutes its own observation group. The mosaics and summed spectra are then created in extra steps, with the ScWs to be used manually specified as explained by Chernyakova & Neronov (2008), Sec. 9.4. Basic scripts for this approach are `ima_sbs` (image reconstruction), `imalc_sbs` (lightcurve extraction with `ii_light`) and `spe_sbs` (spectral extraction) created by I. Kreykenbohm (priv.comm.).

Once the observation group is set up, image reconstruction and the creation of mosaic images are carried out. A careful examination of mosaics should always be undertaken, as the decision on the exact parameters for further extraction steps depends on the properties of the field (e.g., how crowded is the field? How bright are other sources in the field? How bright are sources next to the source which is of the main interest for the analysis?) and observation (e.g., which pointing pattern was used?).

---

<sup>15</sup>For the NRT data a different set of directories is used, but it is still the same for all of the NRT data.

<sup>16</sup>available from <http://www.isdc.unige.ch/integral/analysis#Software>

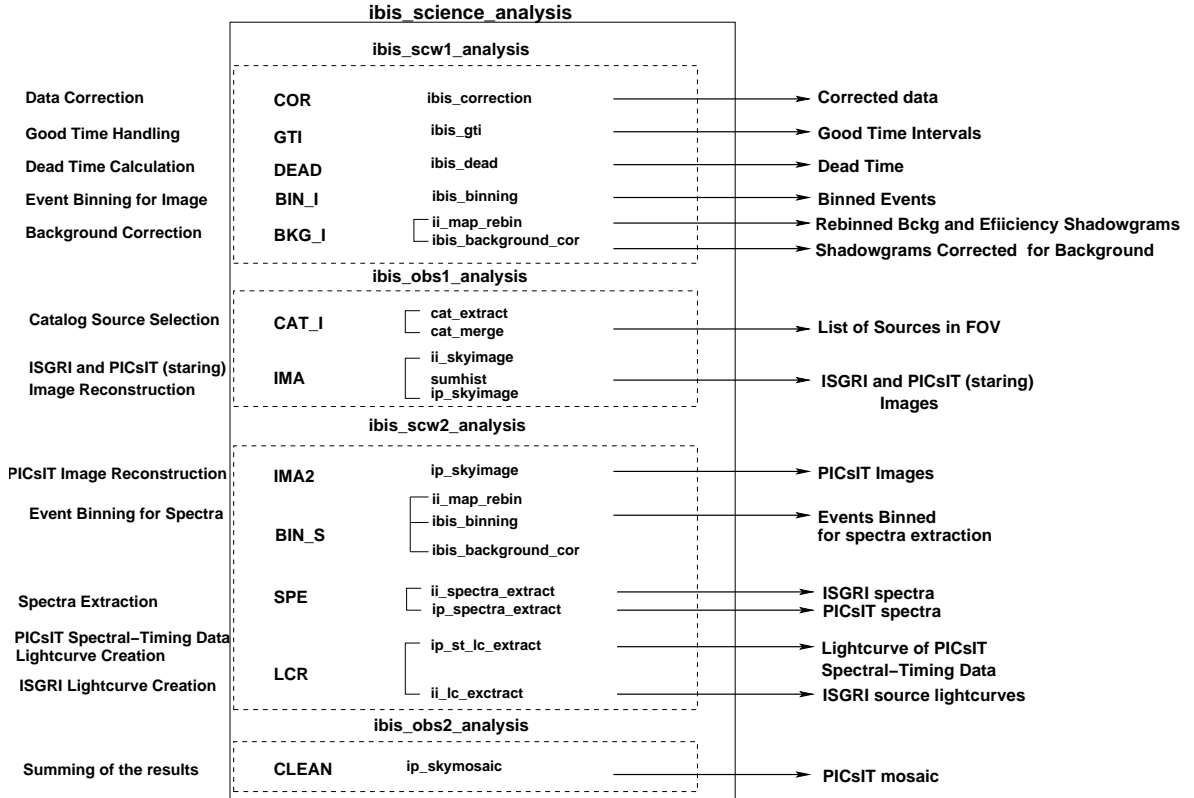


Figure 4.11: Science Analysis Overview  
(Chernyakova & Neronov, 2008, Fig. 10)

Since many sources detected by *INTEGRAL* are transient or highly variable, it is advisable to use the catalogue of detected sources created during the mosaic step as the catalogue for the spectral- and lightcurve extractions. Which sources are kept in the catalogue depends on the main source of interest: for example for a bright source, weak sources in the field do not need to be taken into account, as their influence is marginal, while keeping them in the catalogue would mean a strong increase in the CPU time needed for the extractions.

Also, the software will often not be able to fully clean the ghosts created by the secondary lobes of the PSF (Fig. 4.9) and declare them to be new sources. These artefacts need to be removed from the catalogue.

## Spectral Extraction

It is *not possible* to extract spectra only for one source. Spectral extraction will always be performed for all sources in the specified catalogue.

Like the exact composition of the catalogue, the binning of the spectral response matrix depends on the source analysed. `isgr_rmf_grp_0025.fits`, the latest full response matrix, contains 2048 channels and can be rebinned with the FTOOLS program `rbnrmf` to the number of channels required. The standard rebinning contains 13 energy channels (Chernyakova & Neronov, 2008).

Since Cyg X-1, the source discussed in this work, is very bright and therefore allows for good spectral resolution already in single ScWs, the response used here is rebinned to 64 energy channels. The high number of bin is decisive for this work as it allowed the identification of the Tungsten instrumental background line in Sec. 7.4.1. The

identification would not have been possible for stronger binned spectra.

After the creation of spectra for single ScW, they can be summed up with the `spe_pick` tool to achieve a better signal to noise ratio.

## Lightcurve Extraction

Due to the complexity of the instrumentm, there are different approaches to extract lightcurves from the raw *INTEGRAL* data: lightcurves can be extracted by full deconvolution of short slices of data, by taking into account the pixel illumination fraction or directly from the individual events. Which approach is to be used in a certain analysis is defined by the brightness of the source, the time resolution needed, computational ressources at hand, etc. A explanation of the different algorithms and a comparison between them is presented in Sec. 7.3.

## 4.4 *Ryle/AMI*

The *Ryle* telescope (Pooley, 2006) was a Earth-rotation synthesis telescope (i.e., using Earth rotation for covering the  $u-v$ -plane) and a part of the Mullard Radio Astronomy Observatory, operated by the Cavendish Laboratory. It consisted of five 13 m antenna with baselines of about 100 m<sup>17</sup>.

The majority of the observations conducted with the *Ryle* telescope had a duration of 12 h and were dedicated to microwave-background studies. In the gaps between these observations, observations of individual sources like Cyg X-1 were carried out. Such observations are usually performed at 15 GHz with a bandwidth of 350 MHz (Pooley & Fender, 1997).

The *Ryle* telescope ceased observing in early 2006 when ten 4 m antenna were added to re-build it into the Arcminute Microkelvin Imager (*AMI*), which started observing in middle 2008, also at 15 GHz.

An explanation of radio data of the Cyg X-1 observations is given by Wilms et al. (2007). Raw data are not available for *Ryle/AMI*, but reduced fluxes were provided by G. Pooley (University of Cambridge, Cambridge, UK; priv.comm.).

Important to note, as this will often cause some initial confusion, is that the radio flux is measured in units of Jansky (Jy) with  $1 \text{ Jy} = 10^{-26} \text{ W m}^{-2} \text{ Hz}^{-1}$ .

---

<sup>17</sup>The former configuration had 3 additional antennas at  $> 1 \text{ km}$  baselines, which were not used at the times considered here anymore (Pooley, 2006).

# 5 Analysis Methods

The following chapter concentrates on methods necessary to analyse data obtained with X-ray satellites. First, the basics of spectral analysis are introduced in Sec. 5.1. Special attention is paid to the software package ISIS, which is used both for spectral and timing analysis. Sec. 5.2 is concerned with the mathematical foundations of the timing analysis. The individual fit functions used in this work are introduced in Sec. 5.3.

## 5.1 Spectral Analysis

Good short introductions into X-ray spectral analysis and especially ISIS are given by Nowak (2009) and by Hanke (2007). Only a short overview based mainly on these two sources as well as an overview of the models used for the analysis is given here to allow an understanding of the basic principles used in this work. For a more detailed mathematical background, see Bevington & Robinson (1992).

### 5.1.1 From Source Flux to Detector Counts

An X-ray detector does not directly measure the flux from a source, but instead counts per integrated time bin per channel, that is, the spectral resolution of the source is binned. The count rate in a given bin is not the source flux in the same bin. The formal connection between the spectral energy distribution (SED) from the  $n$  sources  $S_i(E)$  and the measured detector counts  $C(h)$  in the discrete energy channel  $h$  is given by (Davis, 2001)

$$C(h) = \int_0^{\infty} \sum_{i=1}^n R_i(h, E) A_i(E) S_i(E) dE \Delta T + B(h) \quad (5.1)$$

where  $R(h, E)$  is the response function (RMF),  $A(E)$  the effective area or ancillary response function (ARF),  $B(h)$  the background counts,  $E$  the photon energy and  $\Delta T$  the integration time.

The ARF comprises the physics of the telescope used, e.g., mirrors and their collecting area, filters and their throughputs, detectors and their efficiencies, and can therefore be seen as a kind of extended effective area of the detector. The RMF encodes the physical effects of the detector and the actual detection process of a photon that has arrived at the detector after undergoing all the effects included in the ARF and gives the probability that a photon of the energy  $E$  is registered in the detector channel  $h$  – the RMF of an ideal detector would therefore be a  $\delta$ -function. ARF and RMF are both created by the specific software of the satellite used. Their effect can be seen as a mapping of the photon energy on the detector channels.

The background  $B(h)$  is comprised of two main parts: unresolved or diffuse sources which might contribute to the background and could also be added to  $S(E)$  and effects such as detector noise, cosmic rays, particle background, i.e., effects not caused by X-ray sources. The background can be either directly measured, as originally for the HEXTE instrument on board *RXTE* (see Sec. 4.2.4), or modelled, as for the PCA (see Sec. 4.2.3) instrument.

For computational purposes, Eq. 5.1 is typically discretised and can be written as a

matrix equation

$$C_h = \Delta T \sum_{i=1}^n \sum_E R_{hE}^i A_E^i S_E^i dE + B_h \quad (5.2)$$

Theoretically (and assuming only one source, i.e.,  $n = 1$ ), Eq. 5.2 can be inverted to obtain  $S_E dE$  if all the other components are known

$$S_E dE = R_{hE}^{-1} \frac{C_h - B_h}{A_E \cdot \Delta T} \quad (5.3)$$

Practically, this is not possible, as the inverted equation is computationally unstable and the uncertainties of the parameters are too high:  $C_h$  and  $B_h$  is strongly influenced by noise and both ARF and RMF have uncertainties. Besides, the response matrix for a real detector often cannot be inverted. Therefore, an other approach has to be taken.

### 5.1.2 Spectral Fitting and ISIS

To find out the original source spectrum  $S$  a model spectrum  $M$  is set up. The detector counts  $C_M$  that would be measured for this model spectrum are determined through ‘forward folding’, i.e., by calculating

$$C_M(h) = \Delta T \sum_{i=1}^n \sum_E R_{hE}^i A_E^i M_E^i dE + B_h \quad (5.4)$$

Note that models are usually computed on a grid much finer than the detector grid  $h$ . For especially computationally intensive and/or complicated models the proper choice of the computational grid might be decisive in achieving meaningful results in a reasonable time.

The goodness of the model is measured by comparing the detected counts  $C(h)$  to the model counts  $C_M(h)$ . Typically,  $\chi^2$  statistics will be used, i.e.,

$$\chi^2 = \sum_h \left( \frac{C(h) - C_M(h)}{\sigma_h} \right)^2 \quad (5.5)$$

The uncertainties are in many cases estimated for Poisson statistics, i.e.,  $\sigma_h = \sqrt{C(h)}$ .

The model spectrum contains several free parameters which are varied in order to minimise  $\chi^2$ . If the model described the data well,  $\chi^2 \approx \nu$  for  $\nu$  degree of freedom (DOF), with  $\nu$  being here the difference between the number of bin  $h$  and the number of the free parameters of the model spectrum. Therefore, usually the so-called reduced  $\chi^2$  is used

$$\chi_{\text{red}}^2 = \chi^2 / \nu \quad (5.6)$$

A good fit is characterised by  $\chi_{\text{red}}^2 \approx 1$ ,  $\chi_{\text{red}}^2 > 1$  implies that the scatter of the data points is greater than the statistical fluctuations  $\sigma_h$  and the model therefore does not describe the data well.  $\chi_{\text{red}}^2 < 1$  implies that the statistical errors  $\sigma_h$  were overestimated. A thorough discussion of the statistical approach to fitting spectra is given by Bevington & Robinson (1992). A much shorter overview of the  $\chi^2$  statistics and different minimisation algorithms is presented by Hanke (2007).

Different spectral models may result in comparable  $\chi^2$ , the models are therefore not unique. Examples can be found in Nowak et al. (2010) where both thermal and non-thermal Comptonization as well as jet models describe the *Suzaku/Chandra/RXTE*

spectra of Cyg X-1 well or in Wilms et al. (2006) where *RXTE* spectra of Cyg X-1 can be well described by both an purely empirical broken power law and by different Comptonization models.

Important for understanding the results of model fits to the data are moreover confidence intervals for a single parameter and confidence contours for two parameters (as represented, e.g., by the contour plot in Fig. 8.2) which are discussed in details by Hanke (2007). These calculations are, however, CPU expensive, especially in the case of more complex physically motivated models, as a best fit has to be found for any considered combination of the two parameters for which the confidence contours are calculated.

Further important are systematic errors, i.e., uncertainties in the calibration. For a bright source like Cyg X-1 they will dominate over the statistical errors both for the *RXTE*/PCA and *INTEGRAL*/ISGRI. Systematic errors are added in quadrature to the statistical errors

$$\sigma = \sqrt{\sigma_{D_i,\text{stat}}^2 + (D_i \cdot \text{sys\_err}_{D_i})^2} \quad (5.7)$$

where  $D_i$  is the corresponding data value and  $\sigma_{D_i,\text{stat}}$  is the statistical uncertainty. The systematic errors will be given in percent in this work.

In X-ray astronomy, the minimisation is usually carried out by programs such as Interactive Spectral Interpretation System (software packaege ISIS) (Houck & Denicola, 2000; Houck, 2002) or XSPEC (Arnaud et al., 2007).

A short discussion of the benefits of using ISIS is given by Nowak et al. (2005)<sup>1</sup>: scientifically important are the treatment of spectra and the possibility to easily add non-X-ray data – in the case of this work in the radio part of the spectrum. At the same time it is possible to use all the models used in XSPEC (wrappers are used to account for different approaches employed by the two programs) and easily fit non-spectral data such as PSDs. As ISIS is programmable, it provides the possibility to perform tasks which would be delegated to other programs when using XSPEC – e.g., to IDL or shell-scripts – by means of customised `s-lang` functions and scripts. Crucial for this work is that ISIS does not only allow to fit spectra, but that computations of timing properties, such as PSDs, coherence and time lags, which are introduced in the next section, can be directly performed within ISIS.

## 5.2 Timing Analysis

As implied in Sec. 2.4 timing properties are crucial to understand the variability and its underlying physics in X-ray binaries. Fourier statistics are the tool of choice to analyse the characteristic frequencies and the general behaviour of lightcurves. In the following, unless otherwise stated, the explanations of Pottschmidt (2002) are followed.

All computations discussed here have been performed with the software package ISIS<sup>2</sup>.

---

<sup>1</sup>A more detailed discussion in comparison with XSPEC and with examples how to use ISIS can be found on the homepage of M. Nowak at [http://space.mit.edu/home/mnowak/isis\\_vs\\_xspec/](http://space.mit.edu/home/mnowak/isis_vs_xspec/)

<sup>2</sup>A public repository with ISIS functions used by the group at Remeis Observatory which includes most of the custom programs used in this work is accessible under <http://www.sternwarte.uni-erlangen.de/git.public/?p=isisscripts;a=summary>

### 5.2.1 The Discrete Fourier Transform

For the discrete Fourier transform a lightcurve of  $m$  evenly spaces time bins with the length  $\Delta t$  is needed, each with the corresponding count rate  $x_j$  where  $j$  is the number of the time bin. The total length of the lightcurve  $T$  is then  $m\Delta t$ . The discrete Fourier transform  $X_k$  for the frequency  $f_k$  is then given by

$$X_k = \sum_{j=0}^{m-1} x_j e^{2\pi i k j / m} \quad (5.8)$$

i.e., *independent values* of the transform are obtained for every frequency

$$f_k = \frac{k}{T} = \frac{k}{m\Delta t} \quad (5.9)$$

Formally,  $k \in [-m/2, m/2]$ , however for a physical, measured lightcurve the minimal frequency should correspond to the length of the observation  $f_{\min} = 1/T$ , i.e. to  $k_{\min} = 1$ . The maximal frequency (Nyquist frequency) corresponds to the length of the time bin

$$k_{\max} = m/2 \quad \text{and} \quad f_{\max} = 1/2\Delta t \quad (5.10)$$

Thus both a high time resolution and long *continuous* lightcurves are necessary for the best possible timing analysis. Also note that the Fourier transform itself is a complex quantity.

A measured lightcurve however consist not only of the source signal, but also contains noise. The measured count rate  $x_j$  can be written as the sum of a signal component  $s_j$  and a noise component  $n_j$ . The Fourier transform of a sum is the sum of Fourier transforms, as the Fourier transformation is a linear transformation, and thus

$$X_k = S_k + N_k \quad (5.11)$$

where  $S_k$  and  $N_k$  are the respective Fourier transforms of  $s_j$  and  $n_j$  at the frequency  $f_k$ .

### 5.2.2 Power Spectral Density (PSD)

To directly quantify the variance of a lightcurve a derived quantity is used – the power spectral density (PSD)

$$P_k = X_k^* X_k = |X_k|^2 \quad (5.12)$$

with  $P_k$  giving the part of the overall variance of a lightcurve that is due to the variability at the frequency  $f_k$ . Equation 5.12 means that the PSD is defined for the same frequencies as the Fourier transform, but is a real quantity.

Given a single PSD value before any further calculations, its uncertainty will be of the same order of magnitude as the PSD itself, so averaging is crucial as the signal to noise ratio (SNR) increases and the uncertainties are reduced by the square root of the number  $M$  of independent measurements

$$\sigma(\langle P \rangle) = \frac{\langle P \rangle}{\sqrt{M}} \quad (5.13)$$

with  $\langle P \rangle$  denoting an average over  $M$  values (van der Klis, 1989).

Two types of averaging are possible:

- The lightcurve can be divided into several segments and the PSD then calculated for every segment independently. The final PSD is then the average over the individual PSDs.
- The PSD is rebinned to a new frequency grid and the final PSDs is then the average over the individual PSDs at the frequencies corresponding to the frequencies included into the new frequency bin. An often used rebinning is logarithmic rebinning with  $df/f = \text{const}$ .

Different PSD normalisation have turned out to be useful in X-ray astronomy. Generally PSD normalisations can be expressed by

$$\langle P_{\text{norm}} \rangle = A \langle P \rangle \quad (5.14)$$

with the normalisation factor  $A$ . With the time averaged count rate  $R = \langle x_j \rangle$  and the averaged count rate of the signal  $R_s = \langle s_j \rangle$  or, as  $s_j$  and  $n_j$  are independent,  $R_s = R - R_n$ , the normalisations are

$$A_{\text{Leahy}} = \frac{2}{TR} \quad : \quad \text{Leahy - normalisation} \quad (5.15)$$

(Leahy et al., 1983). The units for this normalisation are  $(\text{rms}^2/R_s)/\text{Hz}$  where rms is the mean square variability<sup>3</sup>.

$$A_{\text{Miyamoto}} = \frac{2}{TRR_s} \quad : \quad \text{Miyamoto - normalisation} \quad (5.16)$$

(Miyamoto et al., 1991). Here the value of the PSD is the fractional rms, that means that  $P_{j,\text{Miyamoto}}$  is the contribution of the frequency  $f_j$  to the overall variance of the lightcurve in units of  $R_s$ , the averaged signal count rate, i.e. the units for this normalisation are  $(\text{rms}/R_s)^2/\text{Hz}$ .

When normalising, the statistical uncertainties are given by:

$$\sigma(\langle P_{\text{norm}} \rangle) = A \sigma(\langle P \rangle) \quad (5.17)$$

Under the assumption that signal and noise are not correlated, it follows from Eq. 5.11 that:

$$\langle |S|^2 \rangle = \langle P \rangle - \langle |N|^2 \rangle \quad (5.18)$$

as the term containing both noise and signal components will average out to zero (van der Klis, 1989). The dominant kind of noise for X-ray lightcurves of BHs is Poisson noise. It is independent of the Fourier frequency with

$$\langle |N_{\text{Poisson}}|^2 \rangle = |N_{\text{Poisson}}|^2 = TR \quad (5.19)$$

for the unnormalised power spectrum. For the mentioned normalisations follows:

$$|N_{\text{Poisson,Leahy}}|^2 = 2 \quad (5.20)$$

for the normalisation of Leahy et al. (1983) (Eq. 5.15) and

$$|N_{\text{Poisson,Miyamoto}}|^2 = \frac{2}{R_s} \quad (5.21)$$

---

<sup>3</sup>The rms amplitude or rms variability for a set of  $n$  values  $x_i$  with the mean  $\langle x \rangle$  is defined by:  $\text{rms} = \sqrt{\frac{1}{n} \sum_{i=0}^{n-1} (x_k - \langle x \rangle)^2}$ . The fractional rms variability is a dimensionless quantity obtained by normalising the rms to  $\langle x \rangle$  (van der Klis, 1989; Gleißner, 2004).

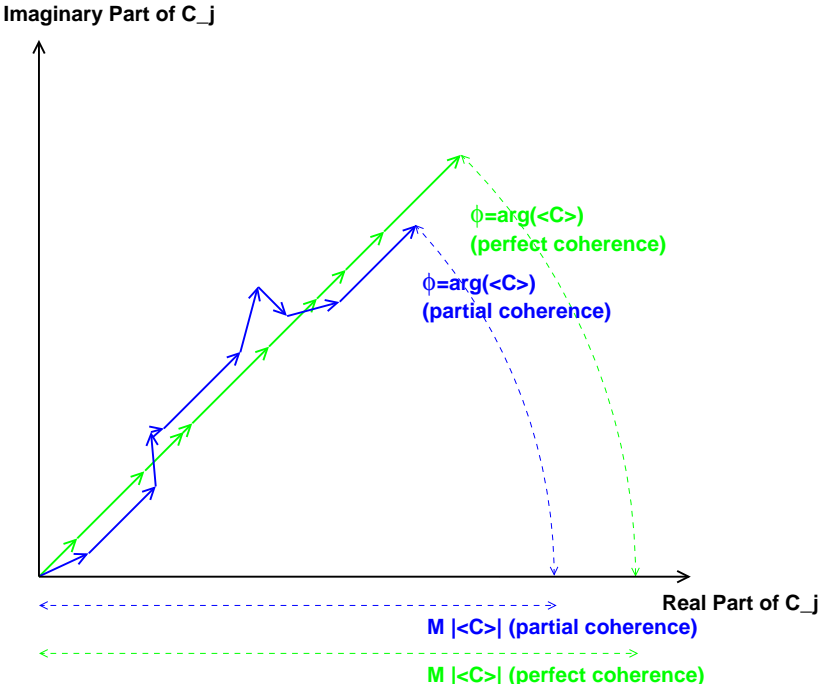


Figure 5.1: Dependency of the CPD sum and lag on the coherence. The Sum of CPDs is represented by vectors. For the case of perfect coherence ( $\gamma_k^2 = 1$ ),  $M\langle C \rangle$  is maximal. For reduced coherence, ( $\gamma_k^2 < 1$ ),  $M\langle C \rangle$  decreases and the phase lag acquires an uncertainty.

(Pottschmidt, 2002;  
Nowak et al., 1999)

for the normalisation of Miyamoto et al. (1991) (Eq. 5.16).

The uncertainty of  $\langle S \rangle$  is in principle the same as for the not noise corrected PSD value  $\langle P \rangle$ . However, since there are uncertainties in the observed noise component, the measured values of  $\langle S \rangle$  have still an effective noise level of

$$E = \frac{1}{\sqrt{M}} \langle |N|^2 \rangle \quad (5.22)$$

As this value is small compared to other uncertainties, it is not taken into account when computing the errors of the noise-subtracted PSDs in this work.

### 5.2.3 Cross Power Density (CPD)

While the PSDs is calculated from one lightcurve, the cross power density (CPD) is calculated from two different lightcurves  $x_{j,1}$  and  $x_{j,2}$  and defined by:

$$C_k = X_{k,1}^* X_{k,2} \quad (5.23)$$

Averaging over lightcurve segments and frequencies can be performed as in case of the PSD.

CPD is a *complex* quantity – information about the original lightcurves is therefore contained both in the magnitude and the phase of the CPD. The first is used to calculate the coherence function and the latter the time lag between  $x_{j,1}$  and  $x_{j,2}$ .

Fig. 5.1 gives a vector illustration for the meaning of the CPD components and the averaging of the CPD.

### 5.2.4 Coherence Function

The coherence function – often referred to simply as coherence – is derived from the squared magnitude of the CPD by:

$$\gamma_k = \frac{|\langle C \rangle|^2}{\langle |S_1|^2 \rangle \langle |S_2|^2 \rangle} \quad (5.24)$$

i.e., the (squared) magnitude of the CPD is compared to the maximal value it could have if the lightcurves were perfectly intrinsically coherent. It measures the degree of linear correlation between two lightcurves at a given Fourier frequency  $f_k$ . Vaughan & Nowak (1997) present a thorough discussion of the computation of the coherence function and apply it to the two microquasars Cyg X-1 and GX 339–4.

For noiseless lightcurves  $0 \leq \gamma_k \leq 1$ . For real lightcurves, with counting noise, two effects influence the coherence function: the noise component leads to an increase of  $|\langle C \rangle|^2$ , while the random phase of the noise reduces the coherence (see Fig. 5.1). Therefore  $\gamma_k > 1$  is possible.

For the details of noise and statistical uncertainties of the coherence function the interested reader is referred to Pottschmidt (2002) and references therein, particularly Vaughan & Nowak (1997), who discuss the calculations in detail: cross terms between noise and signal components of both lightcurves have to be taken into account, which makes the calculations rather lengthy.

### 5.2.5 Phase- and Time Lag-Spectrum

The argument  $\phi_k$  of the CPD is the phase difference between  $X_{k,1}$  and  $X_{k,2}$ , i.e., between variability in the two considered energy bands at the frequency  $f_k$ . Using this frequency this phase lag can be converted into a time lag

$$\delta t_k = \frac{\phi_k}{2\pi f_k} \quad (5.25)$$

The use of phase- and time lag is equivalent. For this work, Fourier frequency dependent time lags will be used throughout the analysis. The abbreviation ‘lag’ does therefore refer to these time lags here. Note that also other ways of defining the time lag, e.g., with the help of the cross correlation function are possible. This approach is not used in this work.

When defining  $X_{k,1}$  as the lightcurve in the soft energy band and  $X_{k,2}$  as the lightcurve in the hard energy band, a positive time lag means that the signal in the hard energy band is delayed with respect to the soft energy band.

The contribution of the measurement noise to the lags is completely random (Nowak et al., 1999) and therefore does not change the expectation value, but only its uncertainty. Therefore an estimate for the usable frequency range, where the time lag spectrum is not dominated by noise, is necessary. Nowak et al. (1999) perform such an estimation and obtain a frequency range of 0.1–30 Hz.

The measurement noise not only adds to the insecurity of the phase of the CPD, but also to the magnitude (the noise estimations of the coherence function have to take this into account!), which in turn influences the uncertainty of the lags. Also, the lags are inherently uncertain when the coherence is not perfect (see Fig. 5.1). Therefore noise terms have to be taken into account by using the full PSD values  $P$ , not only the signal components  $S$ :

$$\sigma(\delta t_k) = \frac{1}{2\pi f_k \sqrt{M}} \sqrt{\frac{1 - g_k^2}{g_k^2}} \quad \text{with} \quad g_k^2 = \frac{|\langle C \rangle|^2}{\langle P_1 \rangle \langle P_2 \rangle} \quad (5.26)$$

## 5.3 Fit Functions

In the following, individual fit functions that will be used for the modeling of spectral and timing data in the later analysis chapters (chapters 6, 7 and 8) are introduced. Except for the Lorentzians and the exponentially cutoff power law for low frequencies, which were written directly for ISIS, all fit functions presented here can be used both in XSPEC and ISIS.

### cutoffpl

`cutoffpl` describes a power law which is exponentially cutoff at a certain energy

$$P_{\text{cutoff}} = N \cdot \left( \frac{E}{1 \text{ keV}} \right)^{-\Gamma} \cdot \exp \left( -\frac{E}{E_c} \right) \quad (5.27)$$

with  $\Gamma$  the photon index,  $E_c$  e-folding energy and  $N$  the normalisation factor [photons  $\text{keV}^{-1} \text{ cm}^{-2} \text{ s}^{-1}$ ], i.e.,  $P_{\text{cutoff}}(1 \text{ keV}) = N \cdot \exp(-1 \text{ keV}/E_c)$ . This is a phenomenological model which describes the general shape of a spectrum without a direct physical interpretation.

### bknpower

`bknpower` describes a broken power law

$$P_{\text{bkn}}(E) = \begin{cases} N \cdot (E/1 \text{ keV})^{-\Gamma_1} & \text{for } E \leq E_{\text{br}} \\ N \cdot (E_{\text{br}}/1 \text{ keV})^{(\Gamma_2-\Gamma_1)} \cdot (E/1 \text{ keV})^{-\Gamma_2} & \text{for } E > E_{\text{br}} \end{cases} \quad (5.28)$$

here  $N$  is defined in the same manner as in the `cutoffpl`-function,  $E_{\text{br}}$  is the break energy, i.e., the energy at which the power law index changes, and  $\Gamma_1$  and  $\Gamma_2$  the photon indices below and above the break respectively. This is an empirical model without a distinct underlying physical process.

### highcut

The `highcut` function describes a high energy cutoff. This is a multiplicative function defined by

$$M(E) = \begin{cases} \exp[(E_{\text{cutoff}} - E)/E_{\text{fold}}] & \text{for } E \geq E_{\text{cutoff}} \\ 1.0 & \text{for } E \leq E_{\text{cutoff}} \end{cases} \quad (5.29)$$

where the free parameters are the cutoff energy  $E_{\text{cutoff}}$  and the e-folding energy  $E_{\text{fold}}$ , both given in keV.

### egauss

`egauss` describes a Gaussian line profile function on the energy grid

$$G(E_l, E_h) = \frac{A}{\sigma \sqrt{2\pi}} \int_{E_l}^{E_h} dE \exp \left[ -\frac{(E - E_0)^2}{2\sigma^2} \right] \quad (5.30)$$

with  $A$  the area under the Gaussian with the centre energy  $E_0$  and the width  $\sigma$  [keV], which is related to the Full Width at Half Maximum (FWHM) by

$$\text{FWHM} = 2\sqrt{2 \ln 2}(\sigma) \quad (5.31)$$

Given the resolution of the data used, this is often a good proxy for the shape of emission ( $A > 0$ ) and absorption ( $A < 0$ ) lines which are not fully resolved.

In this work this function will be typically used to model the Fe K $\alpha$  emission line at about 6.4 keV. Although the shape of this line shows relativistic effects, the resolution of the PCA instruments of about 0.4 keV is too low to allow the exact shape of the line to be seen in the spectra. Another use is to model the Tungsten instrumental background line in the *INTEGRAL* spectra, the exact shape and behaviour of which are unknown.

### **comptt**

**comptt** is the analytical Comptonization model by Titarchuk (1994). It is an analytical model for the Comptonization of soft photons in a hot plasma. The soft photon spectrum is modelled as a Wien law ( $x^2 e^{-x}$  photons) to allow for a particularly simple analytical form. The model has five parameters, one of which, **approx** is a geometry switch. In this work, **approx** = 1 is used, i.e. a disc geometry and an analytic approximation for the calculation of the optical depth. Further free parameters are the redshift, the temperature of the input photons in keV, the plasma temperature in keV, the optical depth of the hot plasma and a normalisation parameter<sup>4</sup>.

Further information about the model can be found in Titarchuk (1994), Titarchuk & Lyubarskij (1995) and Hua & Titarchuk (1995).

### **tbvarabs**

**tbabs** is the Tuebingen-Boulder ISM absorption model which calculates the X-ray absorption in the ISM between the observer and the source

$$I_{\text{obs}}(E) = e^{-\sigma_{\text{ISM}}(E)N_{\text{H}}} I_{\text{source}}(E) \quad (5.32)$$

where  $N_H$  is the hydrogen number density and both the gas and the grain-phase of the ISM as well as the molecules are taken into account via

$$\sigma_{\text{ISM}} = \sigma_{\text{gas}} + \sigma_{\text{molecules}} + \sigma_{\text{grains}} \quad (5.33)$$

To account for the contribution of different atoms and ions,  $\sigma_{\text{gas}}$  is calculated as the sum of the different photoionisation cross section weighted by their abundances normalised to  $N_H$ .

This model was introduced by Wilms et al. (2000), who also updated the the ISM abundances and the different cross sections. To use the updated value, the abundances have to be set to **wilm** in ISIS (the same applies for XSPEC).

**tbvarabs** is a variant of this model which allows the user to vary the elemental abundances and the redshift.

The code of the version of **tbvarabs**, called **tbnew**, used for this work, is an improved version of the model presented by Wilms et al. (2000) with better resolution of the cross

---

<sup>4</sup>An instructive animated overview over the effect of the changes in single parameters of the **comptt**-model on the whole model spectrum can be found on the homepage of D. Maitra under <http://www.astro.lsa.umich.edu/~dmaitra/models/>

sections and – more importantly in the light of the rather poor spectral resolution of the instruments used as compared to instruments like *Chandra* – improved computational behaviour<sup>5</sup>.

### diskbb

**diskbb** is a simple model describing a multicolour accretion disc with  $T \propto R^{-3/4}$  as introduced in Sec. 2.2 (Mitsuda et al., 1984; Makishima et al., 1986). This model has two free parameters, the temperature at the inner disc radius measured in keV and an norm parameter K which takes into account the inner disc radius  $r_{\text{in}}$ , the distance to the source  $d$  and the inclination  $\theta$  of the disc with  $\theta = 0$  for a face-on disc

$$K = \left( \frac{r_{\text{in}}/\text{km}}{d/10\text{kpc}} \right)^2 \cdot \cos \theta \quad (5.34)$$

### reflect

**reflect** is a model for reflection from neutral material as introduced by Magdziarz & Zdziarski (1995). As it is a reflection model, it requires another model the photons of which are reflected. To use this model an extension of the grid on which the model is calculated into higher energies is essential, as photons are Compton down scattered into the considered energy range. This model has five free parameters: the reflection scaling factor, the redshift, the abundance of elements heavier than He, the iron abundance and  $\cos i$ , the inclination angle.

### agnjet

**agnjet** is a physical model describing the broadband emission (radio to X-ray/gamma-rays). It was introduced in a simplified form including only synchrotron emission by Markoff et al. (2001) and further expanded to include Compton processed by Markoff et al. (2003), Markoff & Nowak (2004), and Markoff et al. (2005), as well as an irradiated disc by (Maitra et al., 2009). **agnjet** is the most complex model of all presented here. It has over 20 free parameters which will be explained in detail when used in Sec. 8.3.1.

## Lorentzians

Lorentzians are Fourier transforms of damped harmonic oscillations and have the form

$$L_i(f) = \pi^{-1} \frac{2R_i^2 Q_i f_i}{f_i^2 + 4Q_i^2(f - f_i)^2} \quad (5.35)$$

where  $R_i$  is the normalisation constant,  $Q_i = f_i/\Delta f_{i,\text{FWHM}}$  the quality factor with  $\Delta f_{i,\text{FWHM}}$  the full frequency width of the Lorentzian at half of its maximum value, and  $f_i$  the resonance frequency.

$f_i$  is related to the peak frequency  $\nu_i$ , where  $f \times L_i(f)$  reaches its maximum via

$$\nu_i = f_i \left( 1 + \frac{1}{4Q_i^2} \right)^{1/2} \quad (5.36)$$

---

<sup>5</sup>The **tbnew** absorption model can be found at <http://pulsar.sternwarte.uni-erlangen.de/wilms/research/tbabs/>

These Lorentzian profiles have been implemented into ISIS by Böck (2008). For each frequency bin  $[f_{\text{lo}}, f_{\text{hi}}]$  the model is evaluated by Böck (2008)

$$\int_{f_{\text{lo}}}^{f_{\text{hi}}} L_i(f) df = \frac{R_i^2}{\pi} \left[ \arctan \left( \frac{2Q_i(f_i - f_{\text{lo}})}{f_i} \right) - \arctan \left( \frac{2Q_i(f_i - f_{\text{hi}})}{f_i} \right) \right] \quad (5.37)$$

### Exponentially Cutoff Power Law for Low Frequencies

An exponentially cutoff power law of the form

$$P_{\text{cutoff}} = k f^\alpha \exp(-f/f_{\text{cutoff}}) \quad (5.38)$$

where  $k$  is the norm,  $\alpha$  the power law index and  $f_{\text{cutoff}}$  the cutoff frequency, has in principle already been introduced with the `cutoffpl` function. Böck (2008) discuss the problems they encountered using `cutoffpl` for their fits of PSDs at low frequencies. These are due to approximations employed in the computation of the required integral over  $P_{\text{cutoff}}$ . Böck (2008) therefore introduce a different approximation better suited for small frequencies. Their function is used in this work.

# 6 X-ray Spectral and Timing Analysis: *RXTE*

Being a bright, persistent source Cyg X-1 is among the best candidates both for spectral and timing analysis. An ongoing, bi-weekly observational campaign with *RXTE* allows to assess the spectral and timing variability of the source on timescales from minutes to years (cf. Pottschmidt et al., 2003b; Gleissner et al., 2004b,a; Wilms et al., 2006). The aim of this chapter is on one hand to extend the spectral analysis performed by Wilms et al. (2006), i.e., to include observations after 2004 and to model single orbit spectra instead of observation averaged spectra (Sec. 6.1). On the other hand, state transitions and failed state transition, which are accompanied by radio flaring activity, are of a special interest, as both the accretion and the ejection components change (cf. Sec. 2.4). Therefore a detailed X-ray timing analysis is performed on three *RXTE* observations made during a radio flare to assess the evolution of the timing properties in relation to the radio activity (Sec. 6.2).

## 6.1 Spectral Analysis

### 6.1.1 Overview over the Available Data

#### The Bi-weekly Observational Campaign

Panel 3 of Fig. 6.1 shows an overview over the *RXTE* observations obtained mostly during the extensive ongoing bi-weekly observation program (cf. Pottschmidt et al., 2003b; Gleissner et al., 2004b,a; Wilms et al., 2006) as well as daily averages of the *RXTE*/ASM count rates since the very start of the *RXTE* satellite at the end of 1995. Additionally, lightcurves from different instruments emphasise the connection between the variability in different energy bands. It can, e.g., easily be seen by naked eye that high flux in the soft X-ray band (as measured by the ASM) corresponds to low flux in the radio band, in agreement with the characterisation of the soft state in Sec. 2.4.

Figure 6.2 shows the ASM hardness intensity diagram (HID) for Cyg X-1 with data since the begin of the *RXTE* mission in 1996. Two different regions can be seen in the diagram corresponding to the hard state, with low ASM count rate and a hardness of roughly above 1, and the soft state, with high ASM count rates and a hardness of roughly below 0.5. The scarcely filled regions between these two accumulations of data points corresponds to the jet line. It can be easily seen on this figure, that Cyg X-1 is a good candidate for the analysis of the behaviour of microquasars both in the hard state and when crossing the jet line.

#### Data Used for This Analysis

Since the spectral shape of Cyg X-1 is highly variable already on a timescale of orbits, the approach employed by Böck, VG, et al. (in prep.) was adopted and the spectra were extracted for individual orbits of the *RXTE* satellite. Note that Wilms et al. (2006), who present an earlier spectral analysis of part of the campaign (from beginning of the observations campaign in 1996 up to the end of 2004), do not split their spectra in individual orbits and have therefore only 202 spectra as opposed to the about 1200

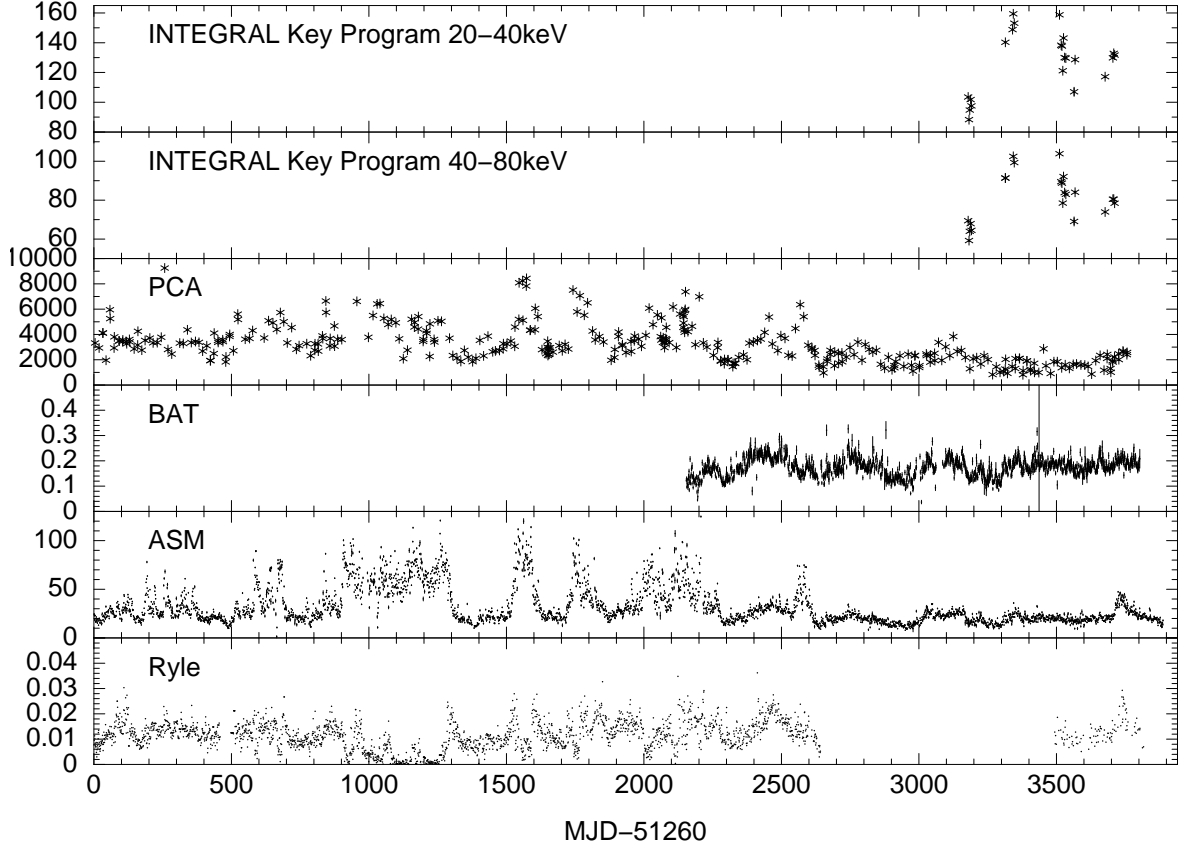


Figure 6.1: Cyg X-1 lightcurves as obtained with *INTEGRAL*/ISGRI during the time of the Cyg X-1 Key Programme (first two panels), with *RXTE*/PCA in the bi-weekly observational monitoring campaign (third panel), with *RXTE*/ASM (fourth panel), with *Swift*/BAT (fifth panel) and the *Ryle*/AMI radio telescope (last panel)

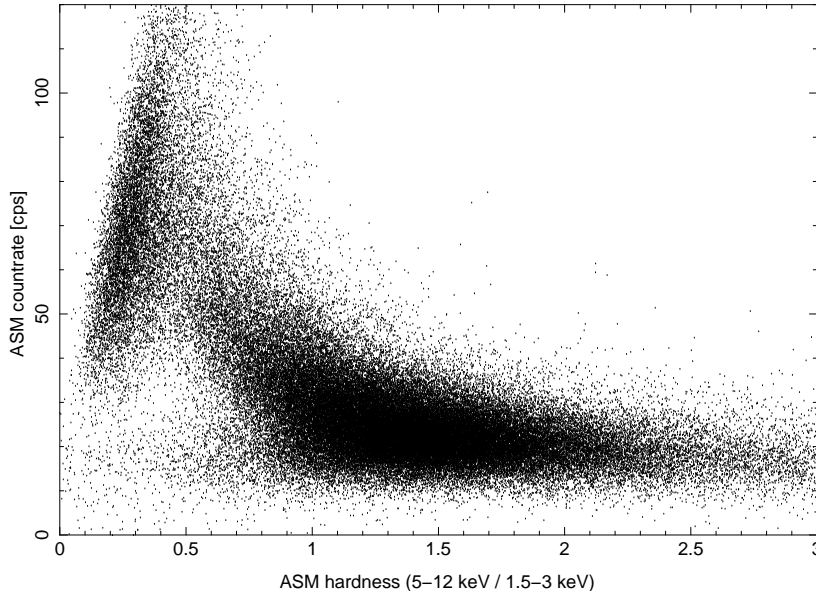


Figure 6.2: Hardness intensity diagram for Cyg X-1 using all ASM data since the start of *RXTE* in 1996.

used in this work which include all the data from the campaign from 1996 to the end of September 2008.

Due to improvements in calibration, it is possible to use PCA data in the range from 3 keV to 40 keV (see Sec. 4.2.3). Systematic errors of 0.5% are added to the PCA data. HEXTE data are used in the range of 20–200 keV with no systematic errors. All

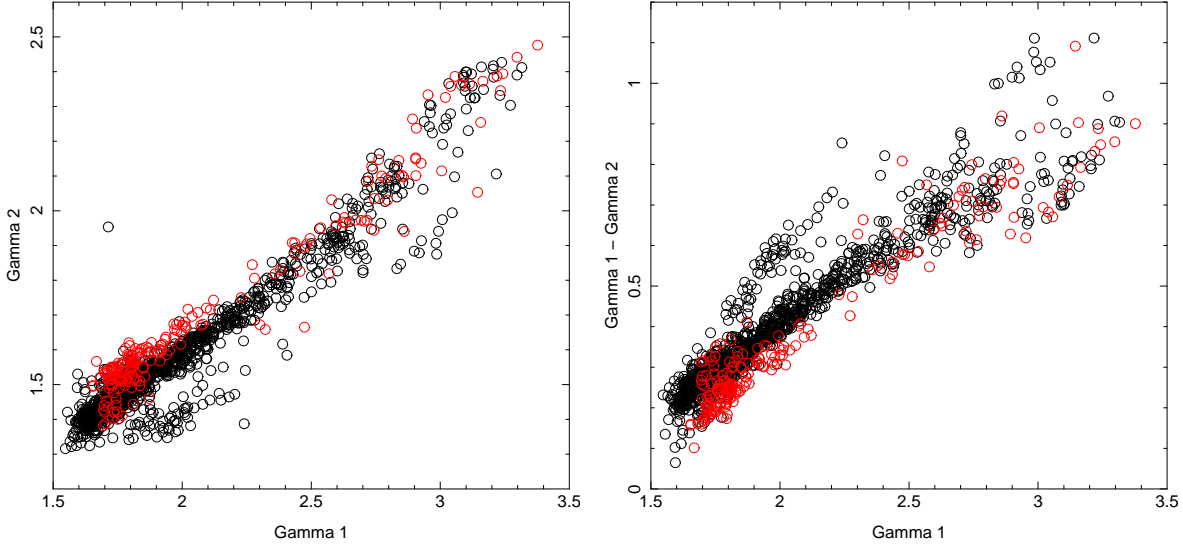


Figure 6.3: Correlation between the soft ( $\Gamma_1$ ) and hard ( $\Gamma_2$ ) photon indices and (left panel) and soft photon index  $\Gamma_1$  and the power law break  $\Delta\Gamma = \Gamma_1 - \Gamma_2$  (right panel) as obtained by Wilms et al. (2006) (red circles) and as obtained in the present analysis (black circles).

data are individually grouped to a minimum signal to noise ratio of 4.5.

All broken power law and Comptonization fits presented in Sec. 6.1.2 and Sec. 6.1.3 were carried out in close collaboration with M. Böck (Remeis Observatory/ECAP, Bamberg, Germany).

### 6.1.2 Empirical Model: Broken Power Law

Wilms et al. (2006) have shown that the spectrum of Cyg X-1 can be well and in case of the hard state even best modelled by a phenomenological model consisting of a exponentially cutoff broken power law, the Fe K $\alpha$  line and a disc component, which becomes prominent only in the soft states. Here, the analysis of Wilms et al. (2006) is extended to include all Cyg X-1 observations until September 2008.

The fit function for the broken power law fits has the form

```
tbnew(1)*constant(Isis_Active_Dataset)*(bknpower(1)*highcut(1)+  
+egauss(1)+diskbb(1))
```

The continuum is modelled by a broken power law with an exponential cutoff and modified by a Gaussian function to account for the Fe K $\alpha$  line and a multicolour black body for the accretion disc component. Additionally, the continuum is modified by interstellar absorption (abundances are fixed to the values of Wilms et al., 2000). The individual model components are introduced in Sec. 5.3.

Less than 10 spectra out of  $\sim 1200$  fitted spectra are modelled with a  $\chi^2_{\text{red}} > 2$ . As some fits of such a big number will always get stuck in an unphysical local minima with a comparatively high  $\chi^2$  value, these fits are omitted in the following analysis.

Figure 6.3 shows the correlation between the soft ( $\Gamma_1$ ) and hard ( $\Gamma_2$ ) photon indices as well as the correlation between the soft photon index  $\Gamma_1$  and the power law break  $\Delta\Gamma = \Gamma_1 - \Gamma_2$ . The correlation observed by Wilms et al. (2006) is confirmed by the present analysis. When comparing the  $\Gamma_1$ - $\Gamma_2$  correlation as obtained here and by Wilms et al. (2006) two features in the present analysis are noteworthy:

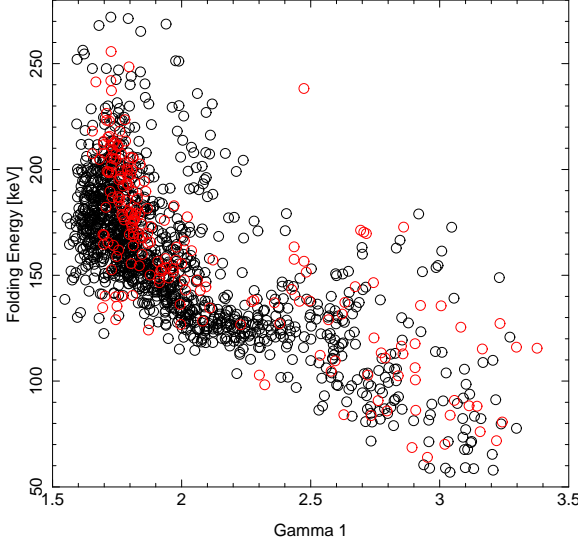


Figure 6.4: Correlation between soft photon index  $\Gamma_1$  and the folding energy  $E_{\text{fold}}$  as obtained by Wilms et al. (2006) (red circles) and as obtained in the present analysis (black circles).

First, the correlation extend to lower values of both  $\Gamma_1$  and  $\Gamma_2$  as compared to Wilms et al. (2006). Interestingly, all data with  $\Gamma_1 \leq 1.65$  stem from observations after MJD 53500, i.e., those observations were not analysed by Wilms et al. (2006) and fall into the prolonged hard state that can be seen on Fig. 6.1 in all presented lightcurves.

Secondly, a noticeable feature are observations with  $1.7 \lesssim \Gamma_1 \lesssim 2.1$  which do not follow the overall correlation having a smaller  $\Gamma_2$  (and therefore a greater difference  $\Delta\Gamma = \Gamma_1 - \Gamma_2$ ) than the main bulk of the data. An examination of the fit values, however, reveals that these observations show an especially high equivalent hydrogen column of  $N_{\text{H}} \geq 2 - 3$  and in some cases even  $N_{\text{H}} \geq 10$ , i.e., clearly not the true values. As will be discussed in Sec. 8.2 on an example of a representative observation,  $\Gamma_1$  and  $N_{\text{H}}$  are correlated: higher  $N_{\text{H}}$  means higher  $\Gamma_1$  (cf. Fig. 8.2 for an example of confidence contour for there two parameters). The departures from the correlations are therefore thought to be caused by this behaviour of the fit parameters and are not physical (Suchy et al., 2008).

Figure 6.4 shows a further correlation found by Wilms et al. (2006) that can be confirmed here: there is a correlation between  $\Gamma_1$  and  $E_{\text{fold}}$  implying that a softer spectrum below 10 keV means higher curvature at high energies. This correlation is not as pronounced as that between  $\Gamma_1$  and  $\Gamma_2$ .

While both  $\Gamma_1\text{-}\Gamma_2$  and  $\Gamma_1\text{-}E_{\text{fold}}$  agree in shape with previous results, the absolute values are different. This is attributed to the differences in the calibration, which has been improved meanwhile.

### 6.1.3 Comptonization Model: CompTT

In more physically motivated model for the Cyg X-1 spectrum the baseline continuum is formed by a Comptonization model, as Comptonization is able to account for the power law shape of the spectrum (cf. Sec. 3.2). The hardening above 10 keV is attributed to reflection of the X-ray photons of the Comptonization corona from the accretion disc.

As before, the presented model is based on that used by Wilms et al. (2006)

$$\begin{aligned} \text{tbnew}(1)*\text{constant}(\text{Isis\_Active\_Dataset})*(\text{reflect}(1,\text{comptt}(1))+ \\ +\text{comptt}(1)+\text{egauss}(1)+\text{diskbb}(1)) \end{aligned}$$

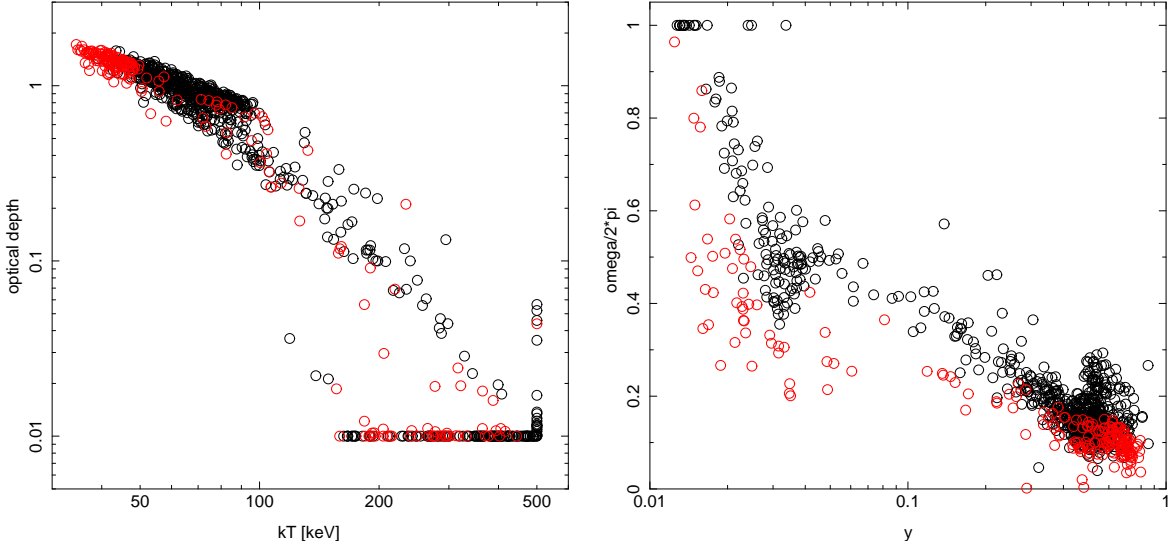


Figure 6.5: Correlations between the plasma temperature  $kT$  and optical depth  $\tau$  (left panel) as well as the Compton- $y$  parameter and the reflection fraction  $\Omega/2\pi$  (right panel) as obtained by Wilms et al. (2006) (red circles) and as obtained in the present analysis (black circles).

In addition to Comptonization, represented by the `comptt` model, and reflection a proper description of the spectrum requires again a Gaussian component to account for the Fe K $\alpha$  line, a multicolour black body to model the accretion disc and absorption. The individual model components are introduced in Sec. 5.3. The temperature of the seed photons for the Comptonization component is tied to the temperature of the multicolour disc to indicate that the Comptonized photons originate in the accretion disc. However, since the input photon distribution of the `comptt` model is a Wien spectrum, not a proper disc spectrum, this approach is therefore only an approximation. The lower limit for the optical depth  $\tau$  was set to 0.01 and the upper limit for the plasma temperature to 500 keV. As the Comptonization model is more CPU expensive than the empirical broken power law model the approach of Wilms et al. (2006) to fix the Fe K $\alpha$  energy at 6.4 keV was followed, as they found that fits with free line energy lead to largely same results.

The left panel of Fig. 6.5 shows the correlation between the temperature and the optical depth of the Comptonizing plasma as seen in this analysis and by Wilms et al. (2006). The right panel of the same figure shows the correlation between the Compton- $y$  parameter, which gives relative energy change of a photon undergoing Compton scatterings (see Eq. 3.8), and the reflection fraction  $\Omega/2\pi$ . As in the case of broken power law fits the trends seen by Wilms et al. (2006) can be confirmed. Note however, that hard observations (high  $\tau$  and low plasma temperature or high Compton- $y$  and relatively low reflection fraction, respectively) occupy a wider range in the parameter space as in the fits presented by Wilms et al. (2006). As before, overall shifts in the distribution can be seen which can be again attributed to changes in the calibration.

#### 6.1.4 Summary

This analysis represents the most up to date results of the whole Cyg X-1 *RXTE* legacy campaign, extending the analysis of the 1996-2004 data by Wilms et al. (2006) to include observations up to the end of 2008 and towards a higher time resolution. The use

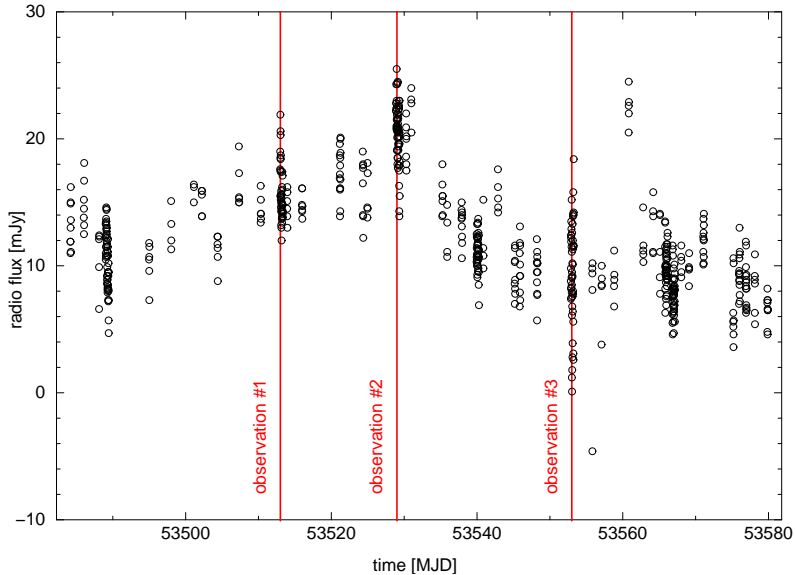


Figure 6.6: Evolution of the *Ryle* radio lightcurve in May–July 2005 (MJD 53500–54550). The corresponding *RXTE* observations are marked by red lines.

of the most up to date calibration allows for a broader energy range for the individual detectors. Spectral correlations observed by Wilms et al. (2006) are confirmed. These results offer a first rough overview over the behaviour of the spectral properties of Cyg X-1 during a period of 12 years on a timescale of down to single *RXTE* orbits ( $\sim 90$  min) and define the context in which the more focused projects that are described in the following have to be interpreted. See For further analysis plans for the *RXTE* monitoring campaign of Cyg X-1 see the outlook in Sec. 9.2.

## 6.2 Timing Analysis During a Radio Flare

The long term timing analysis of Cyg X-1 has been first presented by Pottschmidt et al. (2003b) and extended by Pirner (2009) to encompass all observations until the end of 2008. While the analysis of the whole campaign, whether spectral as presented above or timing, allow to deduce general trends and correlations as well as determine the context in which the single observations have to be interpreted, certain individual periods are of special interests when they allow for additional science. Böck, VG, et al. (in prep.), e.g., present an in depth spectro-timing analysis of a very well sampled state transition.

An other example of an especially interesting period is the long-term radio flare in May–July 2005 which was observed in radio (*Ryle*), infrared (*Spitzer*) and X-ray (*RXTE*) bands and therefore offers a unique opportunity to verify and refine the picture of the behaviour of Cyg X-1 at different energies, e.g., to constrain the behaviour of the jet component through additional data in the IR band, where the break between the optically thin and optically thick emission components is thought to occur.

In this work, timing analysis of the three *RXTE* observations (dubbed observation 1, 2 and 3, cf. Fig. 6.6), which are simultaneous with the *Spitzer* observations, was performed. The results of this timing analysis will provide a basis for further broadband analysis and help to exactly classify the states Cyg X-1 was in during the observations. Table 6.2 contains an overview over the observations and their basic properties. The photon indices derived from broken power law fits can be found in Table 6.3. They reveal that observation 2 is the softest one – this is also the observation at the peak of the radio activity of the source –, while observation 1 and 3 are harder, with 3 being

name	PCA channel	energy range
low	11-13	4.5–5.8 keV
high	23-35	9.5–15 keV

Table 6.1: Channels and corresponding energy ranges used for the timing analysis.

observation	ObsID	PCUs off	total time [s]
1	91096-01-06-00	134off	9600
	91096-01-06-01	134off	
2	91096-01-07-00	134off	2816
	91096-01-07-01	134off	
	91096-01-07-02	134off	
	91096-01-07-03	134off	
3	91096-01-09-00	14off and 34off	7808
	91096-01-09-01	134off	
	91096-01-09-02	14off	

Table 6.2: Overview over the RXTE observations used for the timing analysis present here. Simultaneous Spitzer observations have been performed which will be discussed elsewhere (Rahoui, ..., VG, et al., in prep.).

the hardest one of the given set.

Only lightcurves with the same number of PCUs on can be used to compute the timing properties as the dead time and the background corrections are different for a different number of detectors. Therefore ObsID 91096-01-09-01 is not used in the following analysis, as it is the only part of observation three with only two PCUs on. To allow the calculation of the coherence function and the time lag spectrum, lightcurves have been extracted in two energy bands (dubbed ‘low’ and ‘high’) as listed in Table 6.1. The resolution is with a resolution of  $2^{-9}$  s.

Note that all timing quantities presented here are noise corrected unless explicitly stated otherwise.

Nowak et al. (1999) have estimated that, when taking the dead times of the instruments into account, PSDs for *RXTE* become noise dominated only at high frequencies above 100 Hz. This defines the data mode used for the extraction of the data: a time resolution of  $2^{-9}$  s results in a Nyquist frequency of 256 Hz (Eq. 5.10) .

For Fourier analysis, the lightcurves have to be gap less and evenly binned. Because *RXTE* observations contain gaps due to the orbit of the satellite and the SAA passages, the lightcurves, which are extracted with a resolution of  $2^{-9}$  s, were cut into gapless evenly binned parts consisting of  $2^{16} = 65536$  bins (128 s). This corresponds to a minimum frequency of  $7.8 \cdot 10^{-3}$  Hz when lightcurve segments of full 65536 bins are used. The timing properties are calculated for every segments (or parts of it, if further subdivided) and then averaged. Note that due to the use of Fast Fourier Transform algorithms (e.g., Bracewell et al., 2000) the use of segments with  $2^n$  ( $n \in \mathbb{N}$ ) bins is advisable.

### 6.2.1 PSD Evolution

PSDs are calculated on lightcurve segments with a length of 128 s in the Miyamoto normalisation (Eq. 5.16) and are logarithmically rebinned to  $df/f = 0.15$ , which has

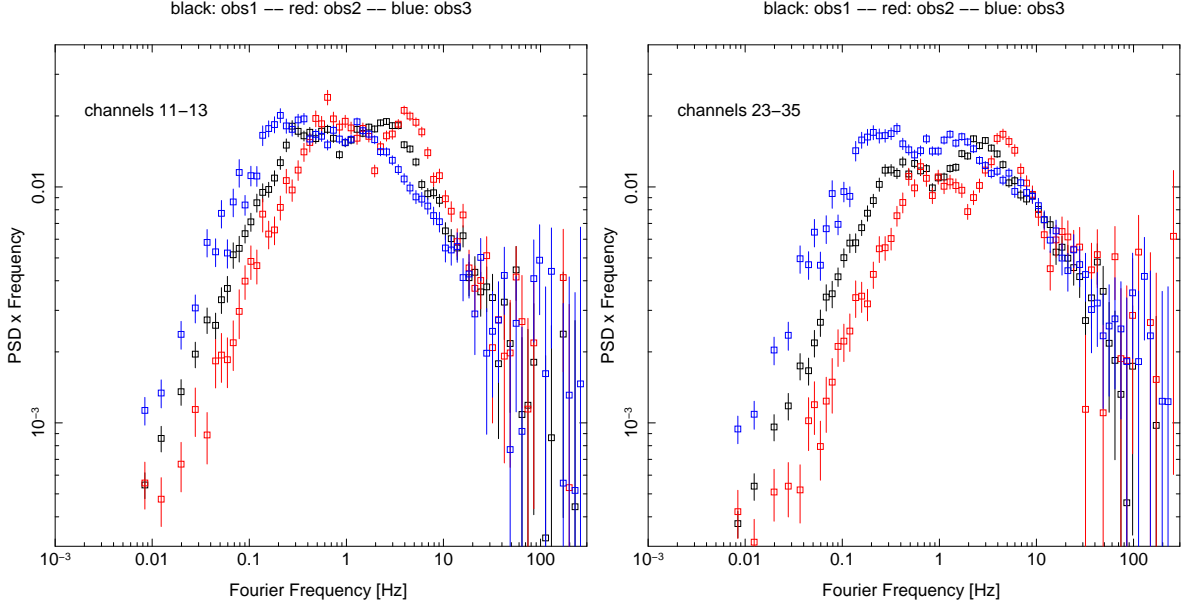


Figure 6.7: PSDs of observations 1, 2 and 3 in soft (left panel) and hard (right panel) energy band. Observation 1 is shown in black, observation 2 in red and observation 3 in blue.

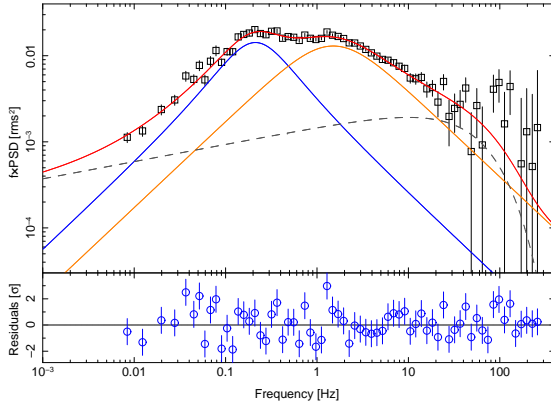


Figure 6.8: PSD of observation 3. Fit with two Lorentzian components and a exponentially cutoff power law. The behaviour of the power law component shows that a third Lorentzian at higher Fourier frequency is required. Colours as in Fig. 6.9, the dashed line represents the power law component.

proven to be useful for broadband PSDs as those presented here (Nowak et al., 1999; Pottschmidt et al., 2003b). Figure 6.7 shows PSDs of all three observations in the soft and hard energy band. A clear evolution of the PSDs can be seen: the whole ‘double hump’ structure wanders to higher energies as the spectrum softens from observation 1 to observation 2 and back, as it is again harder in observation 3. Additionally, as the observation becomes softer, the ‘hump’ at lower energies becomes less pronounced – therefore the strength of the variability components seem to depend on the spectral slope as seen also by Böck, VG, et al. (in prep.). However, a better characterisation of these changes is required, which is achieved by decomposing the PSDs into individual components.

Nowak (2000) have shown that PSDs in the hard state of Cyg X-1 and GX339-4 can be well described as a sum of Lorentzian components, i.e. Fourier transforms of damped harmonic oscillations. Pottschmidt et al. (2003b), Axelsson et al. (2005) and Böck, VG, et al. (in prep.) have shown for Cyg X-1 that the softer a state becomes, the more clearly is an additional power law component required. As the source enters deeper into the transition, the power law component becomes dominant. The soft states

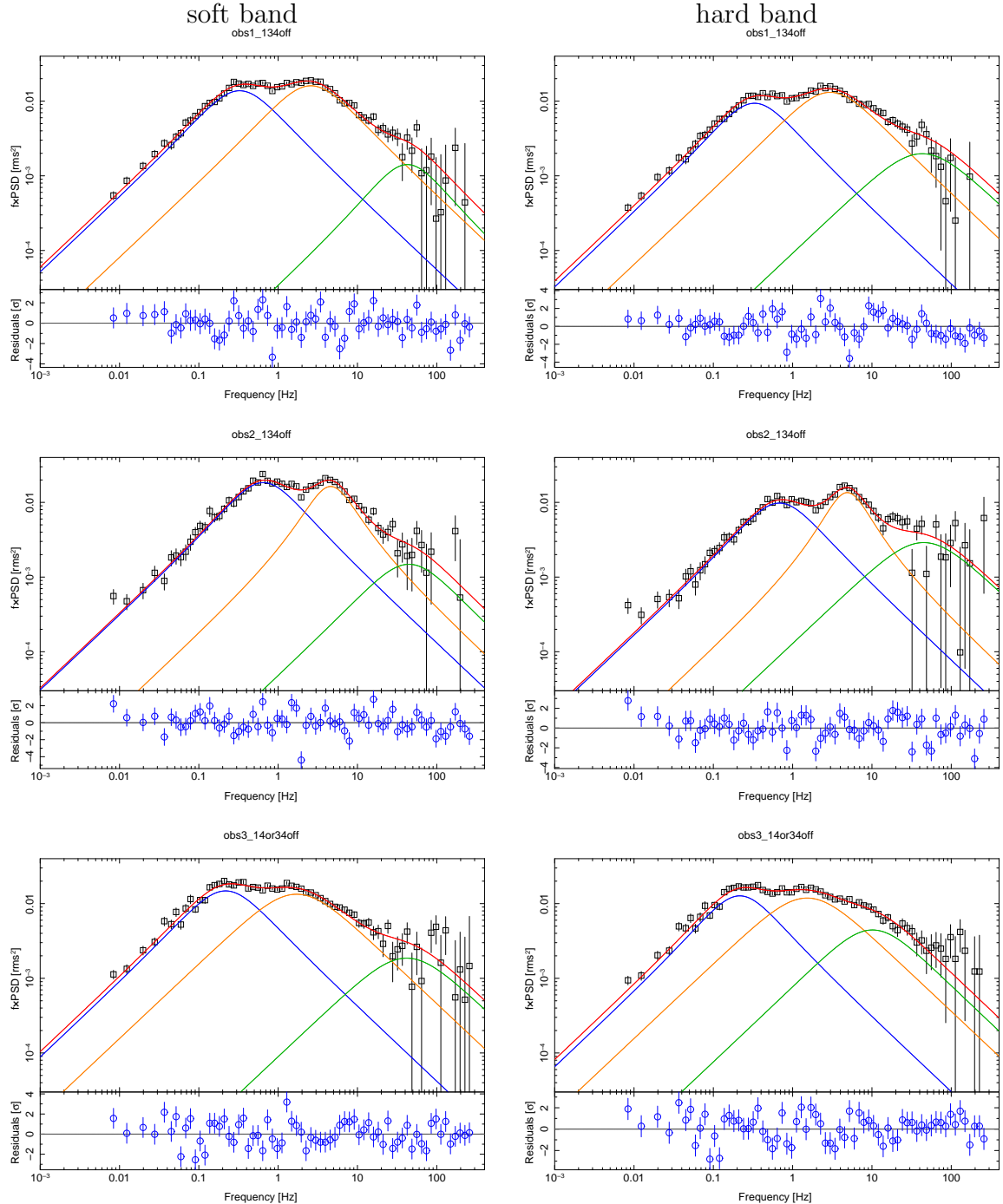


Figure 6.9: PSDs of observations 1 (upper row), 2 (middle row) and 3 (lower row) in the soft (left) and hard (right) energy bands. Fits with three Lorentzian components: Lorentzian 1 is shown in blue, Lorentzian 2 in brown, Lorentzian 3 in green. The overall PSD is shown in red. The fit parameters are given in Table 6.3

themselves can often be described by an exponentially cutoff power law only.

In their spectro-timing analysis of a state transition of Cyg X-1 Böck, VG, et al. (in prep.) use two Lorentzian components and a power law. This allows for fits with  $\chi^2_{\text{red}} \approx 1$  for most of their data (about 80 orbits of *RXTE* treated as individual observations) with the exception of a few hard state spectra which seem to require an additional component at higher energies. Applying the same approach to the data

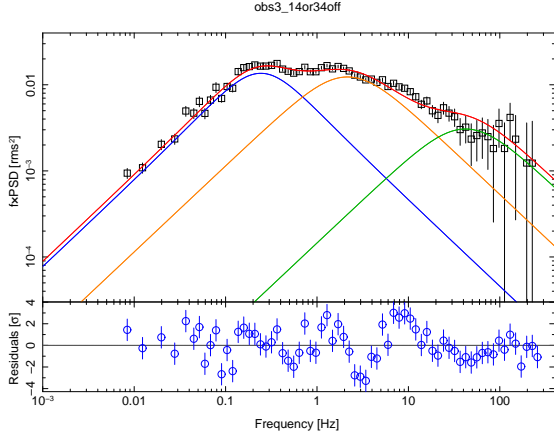


Figure 6.10: Best fit for the hard band of observation 3 with the peak frequency of the third Lorentzian forced into the range of around 40 keV. Colours as in Fig. 6.9

presented here and using two Lorentzian components and an exponentially cutoff power law for low frequencies described in Sec. 5.3 (the same as used by Böck, VG, et al., in prep.) lead to fits such as presented in Fig. 6.8 for observation 3. Although the fit statistics is good, it is clear that the power law component attempts to compensate for the lacking rms amplitude in the model compared to the PSD data at high frequencies. A third Lorentzian component is clearly required for the presented observations. This is reasonable as observations 1 and 3 are harder than those presented by Böck, VG, et al. (in prep.), in whose data  $\nu_1$  varies between 0.5 and 6 Hz. The first two Lorentzians peak at lower frequencies in the observations analysed here, allowing the third Lorentzian to move into the frequency band observed (see Pottschmidt et al., 2003b, for fits using more than 2 Lorentzians).

Fits with three Lorentzian components and without a power law are able to account for all broadband features of the given PSDs as shown in Fig. 6.9. A power law component is not required. An overview over the fit parameters of the PSDs and the overall rms amplitude of the single observations is given in Table 6.3. It has been shown that the peak frequencies of the Lorentzians  $\nu$  (see Eq. 5.36) and not the resonance frequencies are important in terms of correlations (e.g., Nowak, 2000; Nowak et al., 2002), therefore the values of  $\nu_1$ ,  $\nu_2$ , and  $\nu_3$  are given.

While the overall rms remains fairly constant in the soft energy band, the first two Lorentzian components show a clear evolution corresponding to the spectral properties of the observations: the hardest observation (observation 3) shows Lorentzians with the lowest peak frequencies, the softest (observation 2) Lorentzians with the highest peak frequencies. This strengthens the assumption that no power law but instead a third Lorentzian is required for the data presented here.

The same evolution of the first two Lorentzian components can be seen in the hard energy band. Here, however, also the overall rms amplitude changes accordingly to the hardness of the observation. The rms values of the individual Lorentzians show that the rms of the first component decreases more strongly than that of the second one: the decrease for the observation 1 and 2 is about 20% for the first component and just about 10% for the second (cf. Table 6.3). This is consistent with the behaviour seen by Böck, VG, et al. (in prep.) and is therefore considered to be significant even though the three observations analysed here constitute only one example.

Note that the third Lorentzian component, while required, cannot be well constrained as it is both low in amplitude and mainly at frequencies where noise effects become important. The hard band of observation 3 offers a striking example: the best fit

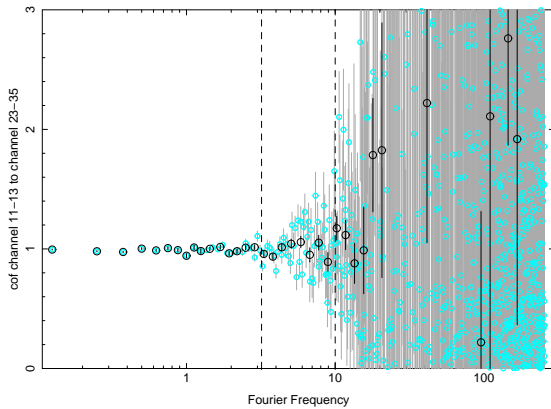


Figure 6.11: Unrebinned and rebinned coherence function for observation 1. Black circles with black error bars represent the logarithmically rebinned values. Cyan circles with grey error bars represent the unrebinned coherence. Dashed lines indicate the Fourier frequency range used for the calculation of the mean coherence.

presented in Fig. 6.9 shows the peak frequency of the third component at 10 Hz, while it is constantly at about 40 Hz in other PSDs presented here. Fig. 6.10 shows the best fit for the hard band of the observation 3 with the third Lorentzian in the 40 Hz range.  $\chi^2_{\text{red}} \approx 2.5$  for 60 degrees of freedom already indicates, that this is not a good description for the data. The residuals also show a clear structure and the second Lorentzian shifts to higher frequencies to account for the missing rms amplitude at around 10 Hz.  $\nu_3 \approx 10$  Hz is in good agreement with the finding of Pottschmidt et al. (2003b) for the hard state, i.e., it is more likely that the value of  $\approx 40$  Hz derived for the soft band is the wrong one, especially as the fit shows peculiar residuals around 10 Hz (see Fig. 6.9, 3rd row, first panel). This could, however, only be confirmed by the analysis of a bigger sample of observations. Therefore, the values for the third Lorentzians are not used to draw any conclusion from them.

### 6.2.2 Coherence

To further characterise the evolution of the timing properties, the coherence is computed. Pottschmidt et al. (2000) have shown that the useful range for calculating average time lags is between 3.2 and 10. Hz. The coherence is then averaged over the same range. Therefore, the lower Fourier frequencies are of less interest here and a different length of lightcurve segments is chosen for the calculation of coherence and time lags than for the calculation of the PSDs. Segments of 8 s (4096 bins of  $2^{-9}$  s) were chosen, as they allow for the coverage of the desired Fourier frequency range and at the same time mean better statistics and smaller error bars since the number of the segments used for averaging the Fourier quantities increases. As the PSDs, the coherence is logarithmically rebinned with  $df/f = 0.15$ .

Figure 6.11 shows an example of non-rebinned and rebinned coherence function for observation 1. Note the strong spread and the large error bars above 20 Hz. The coherence does not show any notable changes between the different observations. The values for the individual observations can be found in Table 6.3. Given the error bars of the individual values, they can be interpreted as consistent with each other and consistent with ideal coherence.

Pottschmidt et al. (2003b, see Fig. 3) discuss several flaring episodes (failed state transitions): while the stronger flares show a clear decrease in the coherence, the coherence does not change during the weaker flare. The coherence values therefore are an indication that the flare analysed here is a weak one, as is also evident from the spectral characteristics of the presented observations.

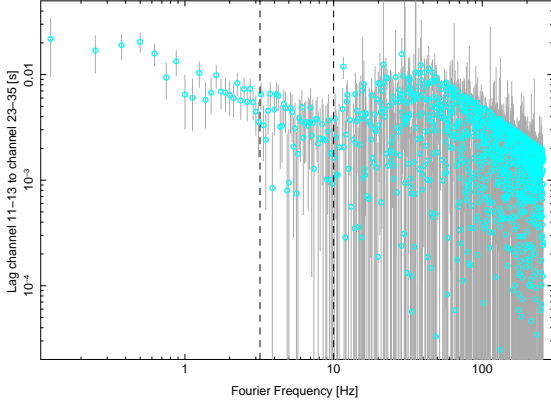


Figure 6.12: Unrebinned time lag spectrum of observation 1. Dashed lines indicate the Fourier frequency range used for the calculation of the mean lag.

The high value of coherence does also allow for a reliable calculation of time lags which will not suffer from uncertainties resulting from a low coherence.

### 6.2.3 Time Lag Evolution

Time lags have been proven to be robust tools to characterise state transitions: already Pottschmidt et al. (2000) have pointed out that enhanced lags are generally associated with transitions or failed state transitions. In a permanent state, whether hard or soft, the shape of the time lag spectrum and the mean value of the lags in the 3.2–10 Hz band will be alike. While Pottschmidt et al. (2000) analyse data from Cyg X-1, a similar behaviour was found by Kalemci et al. (2003) for XTEJ1650–500. Muñoz-Darias et al. (2010) compare their time lag spectrum for XTEJ1752–223 in the hard to those of Pottschmidt et al. (2000) and Nowak et al. (1999) for Cyg X-1 and find a very good agreement in shape and value.

Figure 6.12 shows an unrebinned time lag spectrum calculated between the soft and the hard energy band. The lags become noise-dominated above 20–30 Hz, as expected from calculations by Nowak et al. (1999). The sharp ridge seen at higher frequencies is due to the fact that the time lag is computed from the phase lag (Eq. 5.25). A phase lag  $\phi_k$  cannot be distinguished from the phase lag  $\phi_k + 2n\pi$  (with  $n$  an integer). There is therefore a maximal measurable time lag at a certain frequency. The range in which the mean lag is calculated is not affected by these effects.

The logarithmically rebinned ( $df/f = 0.15$ ) time lag spectra for all three observations are shown in Fig. 6.13. In all the observations the soft band clearly leads the hard energy band. The lag spectra show structure, but not as prominent as in observations presented by Pottschmidt et al. (2000).

The time lag spectrum has typically a power law shape  $f^{-\alpha}$  with  $\alpha \gtrsim 0.7$  (Nowak et al., 1999) in the hard state. This implies that the lag spanning more than an order of magnitude over the range where the lag is not dominated by the noise. To calculate a meaningful value for the mean lag one therefore needs to average over a relatively narrow frequency range. Here following Pottschmidt et al. (2000) the average is taken between 3.2 and 10 Hz.

The mean lags are listed in Table 6.3. They confirm the finding from the PSDs: the 3.1 ms lag in observation 1 is slightly increased compared to the value of 2 ms which was found to be the basic lag for observations in a stable hard state by Pottschmidt et al. (2000, 2003b). It increases further to 5.5 ms in observation 2, but never reaches values as high as 10 to 20 ms observed during the full state transitions by Pottschmidt et al.

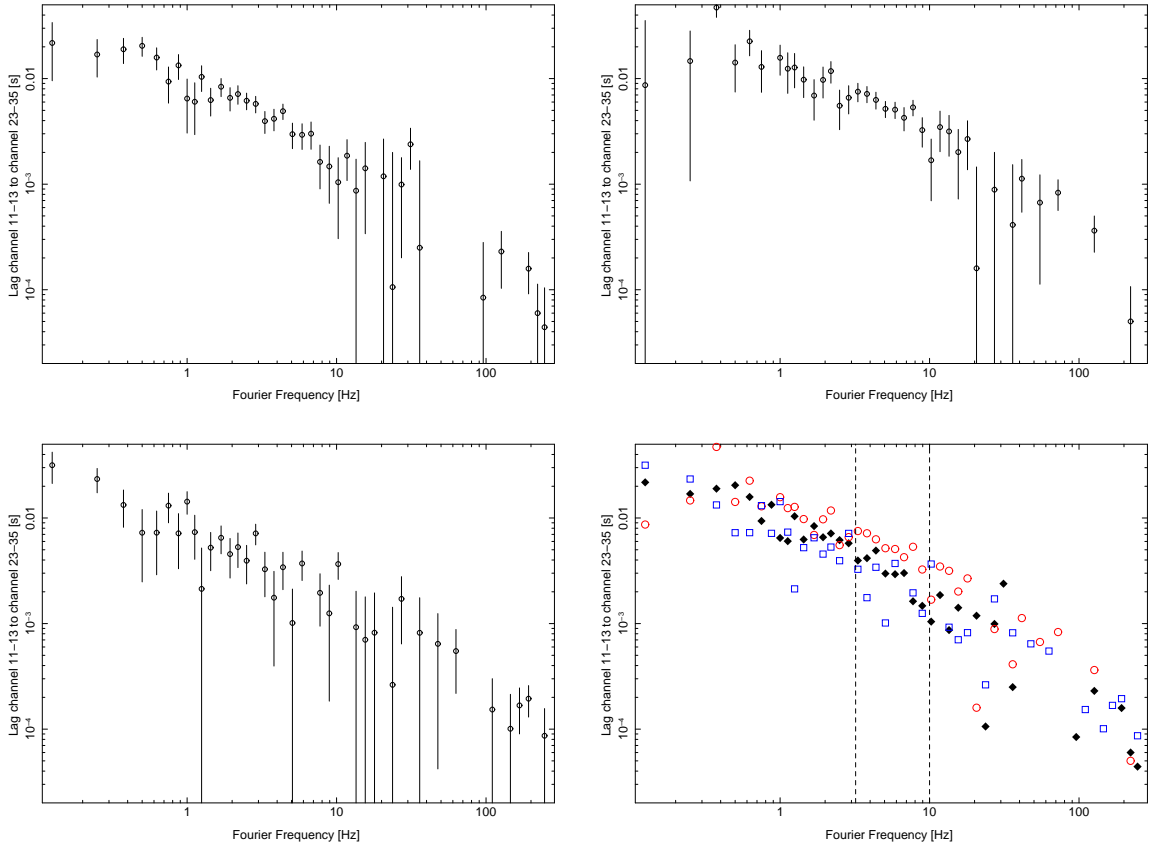


Figure 6.13: Time Lags of observations 1 (left upper panel), 2 (right upper panel) and 3 (left lower panel) between the soft and the hard energy bands. The right lower panel shows time lags of all three observations (observation 1 – black diamonds, observation 2 – red circles, observation 3 – blue squares) without error bars for clarity of the plot. Dashed lines indicate the Fourier frequency range used for the calculation of the mean lag. Negative values in the noise dominated part of the time lag spectrum ( $> 30$  Hz) are omitted for the plot.

(2000). In observation 3 the lag is at 2.0 ms. The general trend seen in the spectral shape and the behaviour of the PSDs and their components (observation 2 being the hardest, observation 1 slightly softer and observation 3 the softest) is confirmed by the behaviour of the time lags.

#### 6.2.4 Interpretation

The results of this timing analysis of *RXTE* data of Cyg X-1 as observed during a radio flare are consistent with those presented by Böck, VG, et al. (in prep.), Pottschmidt et al. (2003b) and Axelsson et al. (2005). A subtle, but clearly significant evolution is seen in the timing parameters which fits the bigger picture of the states and therefore their correlation with spectral hardness and radio flux. The timing properties confirm the indication of the spectral analysis that the three observations cover a failed state transitions, i.e., a phase, where the properties of the source change towards those of the soft state, but never fully reach it and instead return to the hard state values. The full importance of the analysis will only reveal itself once the analysis of the *Spitzer* infrared data is done, i.e., once the timing properties can be seen also in context of

obs	$\Gamma_1$	band	$\chi^2_{\text{red}}$ ( $\nu = 60$ )	rms [%]	$\nu_1$ [Hz]	$\nu_2$ [Hz]	$\nu_3$ [Hz]	coh.	lag [ms]
1	1.83 *	soft	1.5	30.0	0.33	2.6	42.6	0.99	3.1
		hard	1.7	25.3	0.33	3.0	43		
2	2.05 *	soft	1.6	29.9	0.65	4.6	44.6	0.98	5.5
		hard	1.5	23.4	0.68	4.9	45		
3	1.75 *	soft	1.5	30.4	0.20	1.7	42	0.99	2.0
		hard	1.7	29.0	0.22	1.5	10.		

obs	band	rms <sub>1</sub> [%]	rms <sub>2</sub> [%]	rms <sub>3</sub> [%]
1	soft	19	21	6
	hard	15	19	7
2	soft	21	17	6
	hard	16	15	10
3	soft	20	20	8
	hard	18	19	11

Table 6.3: PDS fit parameters, time lags, coherence  
\* spectral data and fits by J. Wilms

the infrared flux and possibly jet fits performed to the joined *RXTE* and *Spitzer* data (Rahoui, ..., VG, et al., in prep.). Because of the low number of observations analysed no general correlations can be derived from the analysed data. This is not the purpose of this analysis, which tries to characterise the timing properties of three individual observation in order to be able to classify the observation in a broader context. For a study of spectro-timing correlations during a state transition see Böck, VG, et al. (in prep.).

The origin of the different frequencies seen in the PSDs of Cyg X-1 and other BHs is still under discussion. Most of the proposed models connect the observed frequencies with the general relativistic frequencies of perturbed orbits in the vicinity of the black hole. Nowak & Lehr (1998) offer a review on such a diskoseismology and discuss different characteristic frequencies. They are able to explain the high frequency (60–300 Hz) quasi-periodic oscillations seen in other BHB sources than Cyg X-1. However, Nowak & Lehr (1998) also point out that stable oscillations in the inner regions of the accretion disc, which they discuss are rather insensitive to luminosity variations and show a low rms variability. They are therefore not to be applied to systems showing  $\gtrsim 10\%$  rms as Cyg X-1 does.

Another approach is made by Kyłafis et al. (2008) whose jet model predicts the observed variability and the dependence of the peak frequency on the spectral index. They demonstrate this explicitly for the first Lorentzian in their Fig. 4 comparing their simulated data to those obtained by Pottschmidt et al. (2003b) for Cyg X-1. This behaviour was also seen for the three observations analysed here. However, some details of their model, e.g. the exact jet ejection mechanism that defines the normalisation of the correlation, are not yet clear.

For time lags, Körding & Falcke (2004) offer a general explantation of their origin and the observed dependency on the energy by a simple pivoting power law. The power law can be produced either in a jet or in a corona. However, they do not address the

return to the small lags in the soft state as observed, e.g., by Pottschmidt et al. (2000).

A more detailed discussion of the lag origin in a jet is given by Kylafis et al. (2008), who are able to reproduce correlation between the spectral index and the time lag for the state transition in their jet model. This would be sufficient to describe the data as presented here, where only the increase in the time lags is seen as the source enters deeper into the flare and becomes softer and again a decrease when the source returns to the hard state. There are, however, no indications how the above mentioned decrease of the time lags in the soft state itself could be explained in the context of the model of Kylafis et al. (2008).

Recent results by Uttley et al. (2010, in prep.) who analyse PSDs and phase lags of Cyg X-1 won with *XMM Newton* at lower energies ( $< 3 \text{ keV}$ ) than those accessible with *RXTE* again suggest the accretion disc and its instabilities as the driving force behind the X-ray variability in the hard state. In the soft states the disc stabilises again. This implies that the variability seen within the *RXTE* energy range as analysed here is a reaction to what happens at lower energies.

# 7 X-ray Spectral and Timing Analysis: *INTEGRAL*

*The Coded Mask Technique  
is the worst possible way of making a telescope.  
Except when you can't do anything better!  
– G. K. Skinner –*

Results presented in Sec. 6.1.1 and references therein make it clear, that while a lot has and still can be gained from the understanding the spectra of Cyg X-1 in the 3–200 keV range and the timing variability properties in the 2–20 keV range, only a more broadband approach will allow to fully understand the physics. *INTEGRAL/ISGRI* with its useful energy range of 20–500 keV does, for example, provide the possibility to better constrain of the e-folding energy for power law descriptions of the spectrum (cf. Sec. 6.1.2). In addition, there is evidence for the existence of a population of non-thermal electron resulting in a hard tail above 200–300 keV (Fritz, 2008), which could originate in the jet. Also, the timing analysis at high energies will allow to better constrain the origin of the different variability components (Pottschmidt et al., 2006).

To investigate the behaviour of Cyg X-1 at high energies is the aim of the Cyg X-1 *INTEGRAL* Key Programme analysed in this chapter. Unless explicitly states otherwise the following analysis is performed with OSA 7.

## 7.1 The Cyg X-1 Key Programme

### 7.1.1 Overview of the Observations

Panels 1 & 2 of Fig. 6.1 show an overview over the *INTEGRAL/ISGRI* Cyg X-1 Key Programme (KP) observations in the context of the observations of the source with other instruments. Table 7.1 lists all the observations and the corresponding times. Near real time (NRT, see Sec. 4.3.4) of two additional observations made in revolutions 875 and 877 were used for tests of different pointing modes (Sec. 7.1.2). Note that the Cyg X-1 KP observations are performed in blocks, i.e., as deep pointings allowing long integration times.

The Cyg X-1 KP falls into a period of low activity of the source. Following the definition for the distinction between states of Wilms et al. (2006), who define hard state as the state with the ASM count rate below 45 cps, almost all observations can be classified as hard states. Only the four observations in May 2009 are in a slightly softer state, but still far away from the soft state lower threshold of 80 cps.

Figure 7.1 show the ASM hardness intensity diagram of Cyg X-1 as presented in Sec. 7.1, with data taken after the start of the *INTEGRAL* Cyg X-1 Key Programme now highlighted in red. The source has clearly not been in a soft state since December 2007.

### 7.1.2 Observing Strategy: From Hex to Random Pointing Mode

The observing strategy of the Cyg X-1 Key Programme was chosen in a way that would allow for a broad band study of the source variability, that is using the hex

revolution	628	629	630	631
date	4.–6.12.07	7.–9.12.07	10.–12.12.07	13.–15.12.07
mean MJD	54440	54443	54446	54449
	632	673	682	683
	16.–18.12.07 54452	18.–19.4.08 54574	13.–16.5.08 54602	16.–19.5.08 54606
	684	739	741	742
	19.–22.5.08 54609	31.10.–2.11.08 54772	6.–8.11.08 54778	9.–11.11.08 54781
	743	744	745	746
	12.–14.11.08 54784	15.–17.11.08 54787	19.–20.11.08 54790	23.11.08 54794
	756	758	794	803
	23.12.2008 54824	27.12.2008 54828	15.–16.4.2009 54938	10.–13.5.09 54964
	804	805	806	
	14.–16.5.09 54967	16.–19.5.09 54970	19.–21.5.09 54972	

Table 7.1: Overview over numbers and dates of the *INTEGRAL* observations of Cyg X-1 since the start of the Cyg X-1 Key Programme. Grey are observations with less than 30 ScW, which are therefore not used for the revolution averaged analysis. Note that due to the dithering pattern of the satellite and inclusion of the data from other observation programs not every science window of a given revolution within the given time interval will have Cyg X-1 in the FOV of the IBIS instrument.

dithering mode (see Sec. 4.3.3) to allow for good coverage with JEM-X. However, the regularity of the hex pattern enhances the so-called ‘ghosts’ – artefacts from the image reconstruction consisting of 8 main intensity maxima aligned with the detector edges, which are inherent to coded mask instruments’ PSF (see Sec. 4.3.2). The data extraction and processing software cannot fully eliminate these ghosts and some of them might be strong enough to be recognised as new sources by the software.

To reduce the spurious structure and therefore improve the quality of the data for the real sources in the FOV of IBIS, a change of the observing strategy consisting of random pointing (see Fig. 7.2) within the JEM-X FOV was proposed. The analysis of the NRT (cf. Sec. 4.3.4) data and a comparison of the imaging results of the random pointing strategy with the traditional hex pointing (CONS data) as well as circular pointing proposed as an intermediate solution by the satellite control centre is part of this thesis, as the ultimate goal of the change of the observing strategy is an improvement of the quality of the available data and therefore the scientific results.

The considered observations were conducted in the revolutions 875 on 12.12.2009 (circular pattern pointing) and 877 on 18.12.2009 (random pattern pointing) in ScWs 087500020010 to 087500520010 and 087700020010 to 087700360010, respectively. Revo-

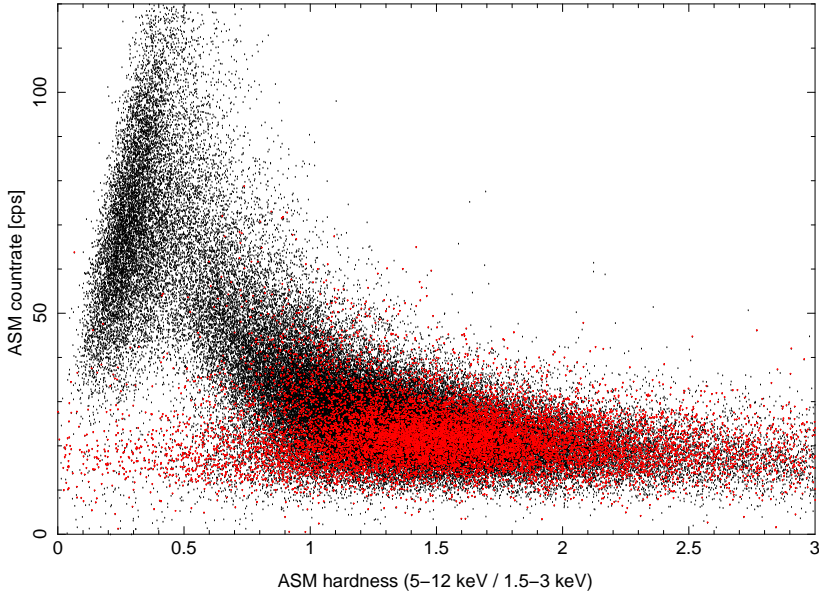


Figure 7.1: Hardness intensity diagramm for Cyg X-1 using all ASM data since the start of *RXTE* in 1996. Data from December 6 2007 on (MJD 54439, start of the *INTEGRAL* Cyg X-1 Key Programme) are shown in red.

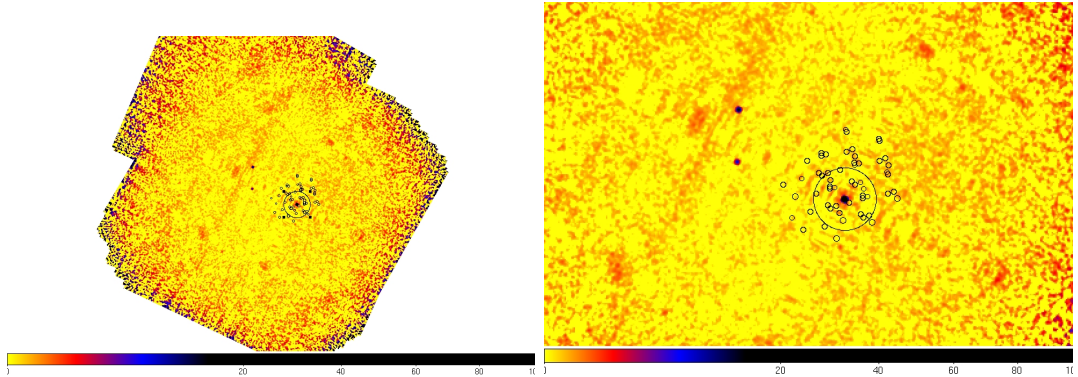


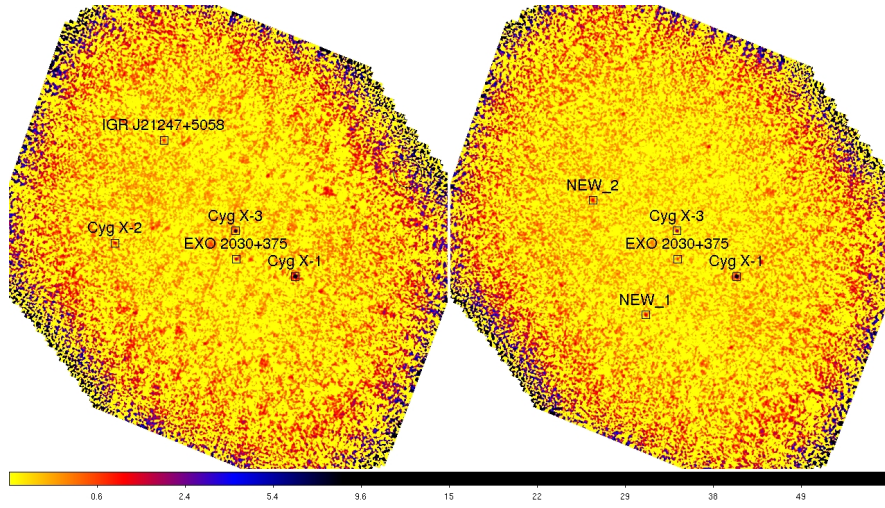
Figure 7.2: *Left*: direction of random pointings in the *INTEGRAL* Cyg X-1 Key Programme revolution. *Right*: a close-up of the left panel.

lution 803, which was one of the latest key programme revolutions available as of the time of analysing the NRT data, e.g., a week after the observations, was used as a typical example for a hex pattern observation.

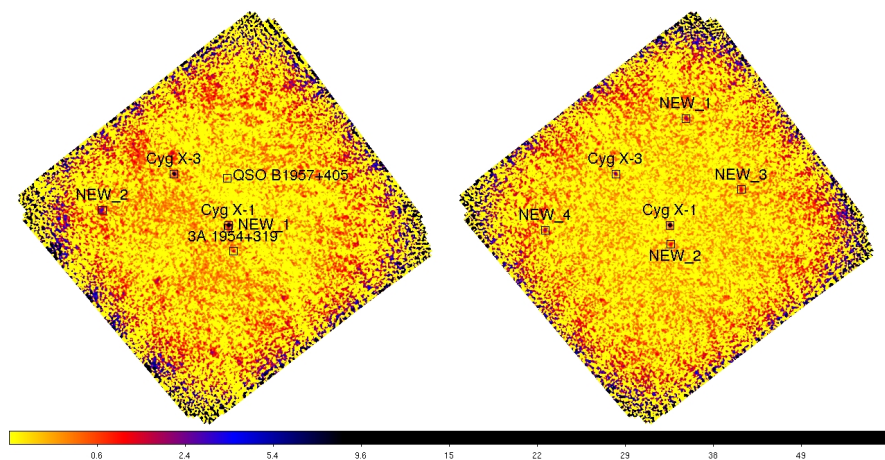
Modifications to (almost) all scripts used in this analysis, which have been already introduced in Sec. 4.3.5, were necessary to accommodate the slightly different structure of the NRT data. Also, even more careful checkups of single ScW data then usually were necessary to exclude any broken or otherwise non-usable data as this was not already taken care of by the satellite team.

Figure 7.3 shows the significance mosaics for these three revolutions. Ghosts are present in all three observations and are often strong enough to be wrongly recognised as sources by the OSA software: all the detections labelled ‘NEW’ are located at the positions of the secondary lobes of the PSF (see Fig. 4.9). However, a simple inspection by eyesight reveals that the general graininess of the image in revolution 877 is lower than in revolution 875 and 803: as expected, the random pattern pointing results in a cleaner image. With the exception of Cyg X-1 and Cyg X-3 all sources in the field are transient and their detection or non-detection on a reasonable ( $\sigma_{\text{detection}} > 6$ ) detection level is not an indication for the quality of an observation.

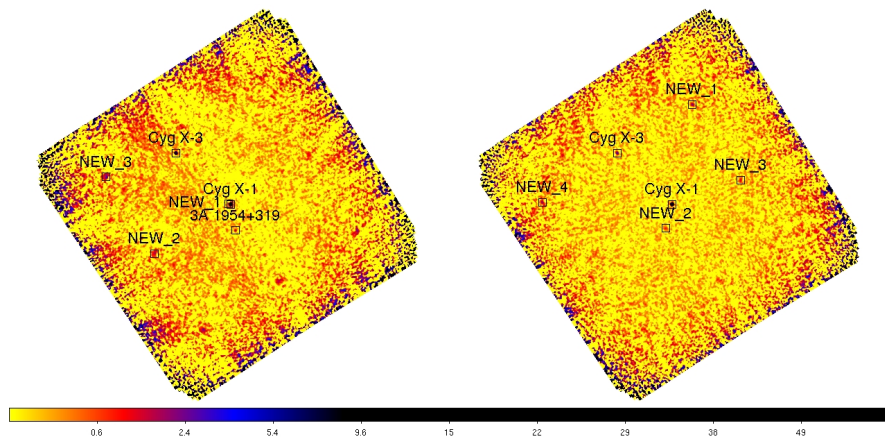
Figure 7.4 shows the JEM-X mosaic for the Cyg X-1 Key Programme observations in revolution 877. The coverage of the field is good and the extraction algorithms



a)  
revolution 803  
hex pattern



b)  
revolution 875  
circular pattern  
NRT data



c)  
revolution 877  
random pattern  
NRT data

Figure 7.3: Intensity mosaics of *INTEGRAL* observations of the Cyg X-1-field within the Cyg X-1 key programme in the 20-40 keV band (left) and 40-80 keV band (right). Shown are all sources detected in the combined mosaics at a detection level above  $6\sigma$ . The ‘NEW’-labelled sources are clearly ghosts.

encounter no problems with the data due to the dithering pattern.

Because of the improvement of the image quality it has been decided to continue the Key Programme observations with random pointings. An interesting aspect of this decision is that better timing studies might be possible in the future, as the source is always in the fully coded FOV during such pointing, so that changing quality of the data has less influence on the results.

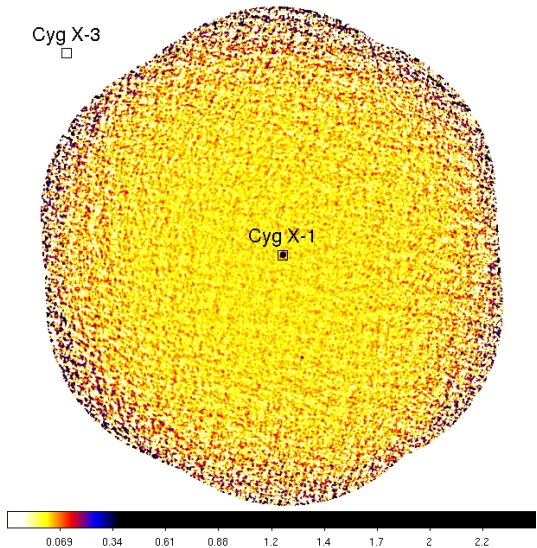


Figure 7.4: JEM-X intensity mosaic image of the Cyg X-1 Key Programme observations in revolution 877 (random pointings). Note the different scale as compared to the ISGRI mosaics which is due to the lower sensitivity of JEM-X. The position of Cyg X-3 is shown for reasons of orientation, as it was not within the FOV of JEM-X.

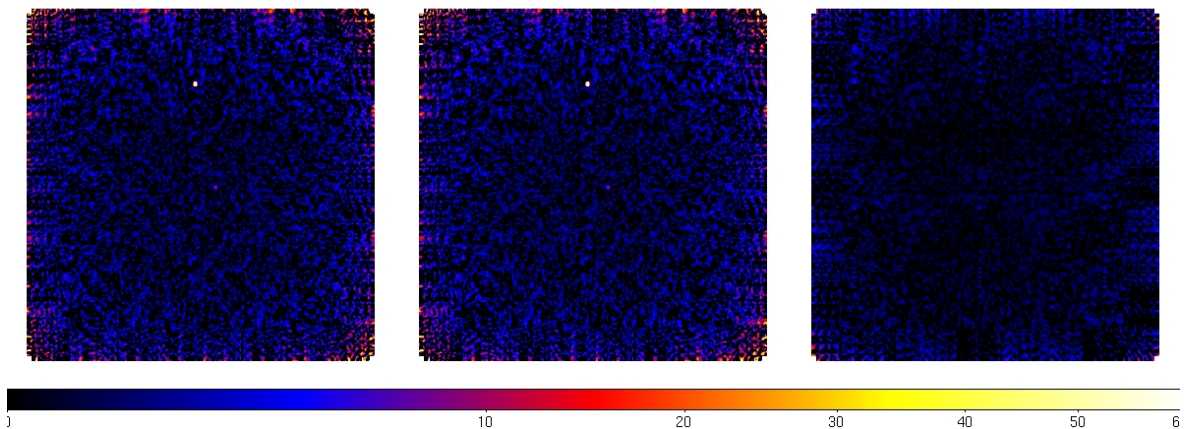


Figure 7.5: Comparison of extractions with different parameters for the Cyg X-1 field.  
*Left panel:* intensity mosaic of the extraction with `OBS1_SouFit` = 0 (fitting source position) and `OBS1_SearchMode` = 2 (looking at K brightest sources in the field, with K set to 15 per default value of the `OBS1_ToSearch` parameter).

*Middle panel:* intensity mosaic of the extraction with `OBS1_SouFit` = 1 (fixed source positions from catalogue) and `OBS1_SearchMode` = 1 (will look at all sources from the input catalogue).

*Right panel:* intensity difference between both extractions.

## 7.2 Image Reconstruction

### 7.2.1 Comparison of Different Extraction Methods

Image reconstruction is the basic step in any analysis of ISGRI data. Due to the very nature of coded mask instruments, the best way of reconstruction is highly dependent on the features of the field in question. It can be influenced and changed by changing extraction parameters in the basic steps of science analysis, especially the IMA step (see Fig. 4.11). In the following, two different approaches are exemplified and their influence on the further analysis are explained.

Figure 7.5 shows a comparison between two different extractions of the same science window, 063200010010, which is part of the Cyg X-1 key program. The parameters changed between the two extractions are `OBS1_SouFit`, `OBS1_SearchMode` and

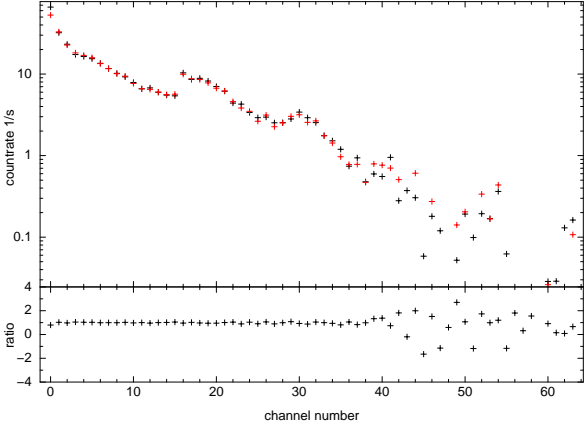


Figure 7.6: Comparison of raw spectra of Cyg X-1 with different values of extraction parameters.  
 Black: `OBS1_SouFit = 0`  
`OBS1_SearchMode = 2`  
`OBS1_ToSearch = 15.`  
 Red: `OBS1_SouFit = 1`  
`OBS1_SearchMode = 1.`  
 Negative values are not shown.

`OBS1_ToSearch` – all three are parameters passed to the `ii_skyimage` routine, which is part of the standard IBIS pipeline and deconvolves the shadowgrams.

- `OBS1_SouFit` defines the approach to defining source positions: setting it to 0 allows to fit the source positions in the vicinity of the catalogued position, setting it to 1 forces the use of fixed source positions from the catalogue, the software will also use *all* the sources listed in the catalogue. Fixed source positions are especially useful in crowded fields, where free fitting would lead to confusion of nearby sources, or for weak sources, which might otherwise not be recognised by the software (Chernyakova & Neronov, 2008).
- `OBS1_SearchMode` defines the source search mode. The search can be performed as a search for significant excess ( $= 0$ ), for all catalogue sources ( $= 1$ ), for a defined number of K sources defined by the `OBS1_ToSearch` parameter ( $= 2$ ) and for all catalogue sources plus K significant excesses ( $= 3$ ).

The intensity image on the left panel of Fig. 7.5 is obtained by setting:

```

OBS1_SouFit = 0
OBS1_SearchMode = 2
OBS1_ToSearch = 15

```

on the middle panel by setting:

```

OBS1_SouFit = 1
OBS1_SearchMode = 1

```

No differences can be seen by bare eye in the intensity mosaics – subtraction however reveals differences which show a clear structure and are therefore systematic. Since the individual images are used further to calculate the mosaics and the catalogues obtained from the mosaics are used for spectral and timing extractions, these differences propagate and strongly influence the final results of the analysis. Fig. 7.6 shows the comparison between single ScW raw spectra<sup>1</sup> obtained for the same ScWs using the same parameters as the images in Fig. 7.5. The spectra are clearly different already on the ScW level and the choice of the exact extraction parameters is therefore crucial.

---

<sup>1</sup>Note that RMF- and ARF-files are the same for both extractions and therefore could not compensate the differences.

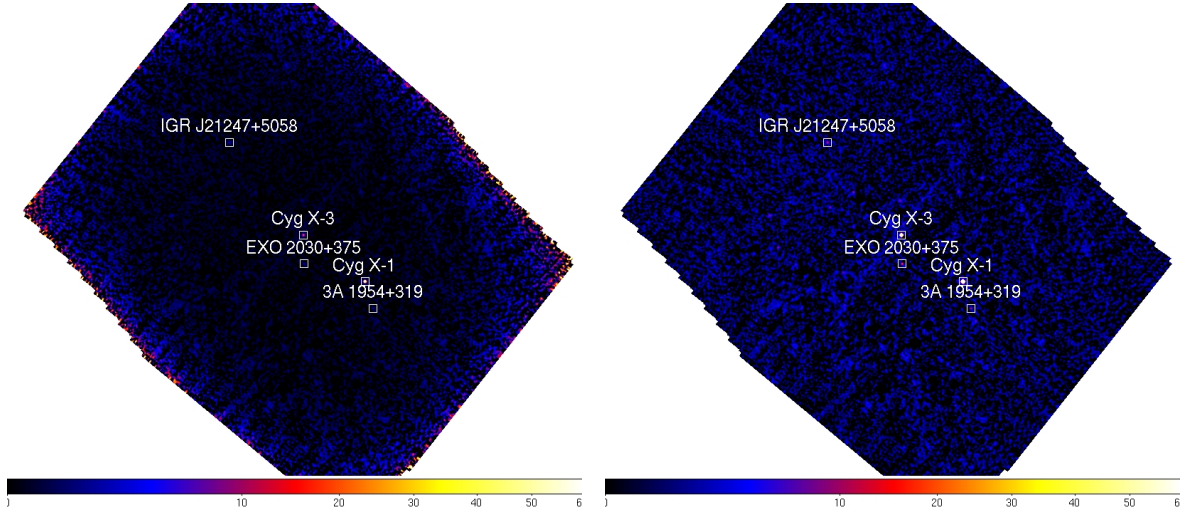


Figure 7.7: IBIS intensity (left) and significance (right) mosaics for revolution 628 of the Cyg X-1 key programme (87 ScWs). Marked are sources detected with  $\sigma_{\text{detection}} \geq 6$ .

As the field of Cyg X-1 is not especially crowded due to its high galactic longitude and therefore the distance to the highly populated galactic centre<sup>2</sup> and Cyg X-1 itself is a very bright source ( $\sigma_{\text{detection}} \sim 9 \times 10^2$ ) `OBS1_SouFit` = 0, `OBS1_SearchMode` = 2 and `OBS1_ToSearch` = 15 are chosen. Since the Cyg X-1 field has at most 6 to 7 sources detected with  $\sigma_{\text{detection}} \geq 6$ , the threshold used in this work between the sources taken into account for the spectral and lightcurve extractions, `OBS1_ToSearch` = 15, does not put any constraints on the results.

Generally, two energy bands are considered for this work: 20–40 keV and 40–80 keV. Although in principle lower energies than 20 keV are detectable, the detector response in this energy range is not well enough understood to use it for scientific purposes.

### 7.2.2 Mosaics

The second basic step after the imaging of single ScWs is the production of mosaics – combined images of different ScWs. Only in mosaics weaker sources can be recognised, the mosaics are therefore basic for source detection as they provide the source catalogues used for spectral and timing extractions.

In this work mosaics are calculated over whole revolutions. Figure 7.7 shows the intensity and significance mosaic images for revolution 628 in the 20–40 keV band for pointing offset angles up to 20°. 87 ScWs have been summed up for this image, resulting in a total exposure of about 210 ks or 2.5 days. Especially striking are the differences on the edges of the respective mosaic: while the reconstructed intensity is high, up to about 20 cps, the significance is low, as these are artificial effects. Besides the intensity and significance maps the image files produced during the mosaic step also contain the variance and the exposure maps.

From here on only sources with  $\sigma_{\text{detection}} \geq 6$  are considered. This is appropriate as Cyg X-1 is detected with a  $\sigma_{\text{detection}} \sim 9 \times 10^2$ .<sup>3</sup> The catalogues are there-

<sup>2</sup>An example for a very crowded field where `OBS1_SouFit` = 1 is required is the galactic centre itself, where source confusion is otherwise a problem even for the brightest sources.

<sup>3</sup>For a weaker source a different threshold might be appropriate – for the detailed analysis of, e.g., 3A 1954+319 which is detected on a level below 10, sources with  $\sigma_{\text{detection}} \geq 3$  were taken into account (D.M.Marcu, K. Pottschmidt, priv.comm.).

fore filtered to contain these sources, which will always include Cyg X-3, the second brightest persistent source in the field, as well as, when especially active, further variable sources, namely: EXO 2030+375, QSO B1957+405, SAX J2103.5+4545, Cyg X-2, SNR 074.0-08.5, IGR J2147+5058 and 3A 1954+319, an especially interesting neutron star LMXB which will be briefly discussed in the following section. An example mosaic in the 20–40 keV band with marked locations of the weaker sources with  $1 \leq \sigma_{\text{detection}} < 6$  is shown on Fig. 7.8.

Due to the imperfection in the extraction mechanism ghosts are often present – as the software cannot distinguish between real new sources and ghosts of the known bright sources (see Fig. 7.3 for some prominent examples), a careful examination of every mosaic is needed. All detections marked as new in the mosaics of the Cyg X-1 Key Programme observations analysed in this work can be attributed to ghosts and are removed from the catalogues used for lightcurve and spectral extractions.

### 7.2.3 3A 1954-319 – an Interesting Source in the Field

An illustration of the importance of the mosaics is the detection of 3A 1954+319 in the mosaics of the Cyg X-1 key programme observations. While this is not a new source the level of activity was not expected: it was detected with  $\sigma_{\text{detection}} \geq 6$  in the revolutions 628–632, 739, 741–746 and 758 in the 20–40 keV band and in the revolutions 739 and 741–745 in the 40–80 keV energy band and is therefore one of the 4 to 6 brightest sources in the Cyg X-1 field at these times.

3A 1954+319 was detected by *Uhuru* (Forman et al., 1978) and *Ariel V* (Warwick et al., 1981). Masetti et al. (2006) identified the companion, a M-type supergiant and therefore placed 3A 1954+319 in the category of the rare symbiotic X-ray binaries, where a neutron star orbits within the inhomogeneous medium close to its giant companion. The data for this interesting source are sparse and have been analysed by Corbet et al. (2008), who used *Swift/BAT* and *RXTE/ASM* data, and Masetti et al. (2007), who used *BeppoSAX*, *EXOSAT*, *ROSAT*, *RXTE* and *Swift* data. *INTEGRAL* observation of the source in the years 2003–2006 were previously presented by Mattana et al. (2006), who point out that the extremely long period of  $\sim 5.2\text{--}5.3$  hours observed in the lightcurves of the source cannot be the orbital period, as this would imply the an neutron star orbit within the radius of the M-type companion, and therefore has to be the spin period on the compact object. 3A 1954+319 is therefore one of the slowest rotating neutron stars know.

The *INTEGRAL* observations of the Cyg X-1 Key Programme offer an opportunity to learn more about this rare class of X-ray sources and especially their properties in the hard X-rays on long time scales of hours to days, as the source was in the FOV of IBIS for a big part of the Cyg X-1 KP. Specifically the long timescales are important for the determination of pulse period evolution.

First results of the analysis have been presented in Marcu, ... ,VG et al. (2010): a very strong spin-up was found during the flaring period in 2008. A full analysis will be presented in the forthcoming paper by D. M. Marcu, ..., VG, et al. (in prep.).

## 7.3 Timing Analysis

### 7.3.1 Comparison of `ii_light` and `ii_lc_extract`

To be able to conduct timing analysis with *INTEGRAL* a thorough understanding of the data extraction mechanisms and their influence on the results is required. Pottschmidt et al. (2006) have already pointed out that the *RXTE*/PCA and ISGRI PSDs (calculated from lightcurves they obtained with `evts_extract` in Miyamoto normalisation) agree well in shape where they are not noise dominated, but the ISGRI PSD normalisations are an order of magnitude too low. Fürst et al. (2010) analyse 6 s lightcurves from Vela X-1 obtained with the `ii_light`-tool and find that the Poisson noise in Leahy normalisation is not as expected at  $2(\text{rms}^2/\text{mean}) \text{ Hz}^{-1}$ , but instead at ca.  $100(\text{rms}^2/\text{mean}) \text{ Hz}^{-1}$ .

#### `ii_light` and `ii_lc_extract`

The two main tools employed for timing analysis with *INTEGRAL* are `ii_light` and `ii_lc_extract`<sup>4</sup>.

`ii_lc_extract` is the standard tool in the *INTEGRAL* data extraction pipeline. In OSA 8 it is also the only one for higher time resolution<sup>5</sup>. `ii_lc_extract` performs a full image deconvolution for every time and energy bin in which the lightcurve is extracted, that is, the imaging step is repeated on very thin slices of data. Because the full deconvolution is performed, this approach is more exact, but also highly time and CPU expensive, with the lightcurve extraction for a single revolution in two energy bands taking about one or two days on a single CPU (J. Rodriguez, priv.comm.). The IBIS Analysis User Manual 7.0 cautions not to use `ii_lc_extract` for lightcurves with less than 1 min resolution Chernyakova & Neronov (2008), but the OSA 8 version is capable of producing meaningful results for a resolution up to 10 s for bright sources (J. Rodriguez, priv.comm.).

`ii_light` uses a different approach. Here the lightcurves are calculated from the pixel illuminated fraction (PIF), a number between 0 and 1 for each pixel which expresses the degree of illumination of the pixel for a given source. The treatment of other sources in the field as well as the weighting of partially illuminated pixels contribute to the final result. Therefore an alternative PIF-based algorithm developed by C. Ferringo (see Sec. 7.3.3) has also been tested in this work.

`ii_light` can be used for higher time resolution of up to 0.1 s for bright ( $\sim 100$  cps) sources. It uses less resources than `ii_lc_extract`: the lightcurve extraction for a single revolution in two energy bands takes a few hours. However, as Kreykenbohm et al. (2008) have shown, the normalisation of fluxes derived from `ii_light` slightly differs from that derived from the more exact deconvolutions algorithms. Therefore an in detail comparison between the two algorithms is necessary.

---

<sup>4</sup>A further approach is to start from the single events without the deconvolution and with no background subtraction (`evts_extract`). It is only suitable only for fast variability studies with up to a millisecond timing resolution. `evts_extract` is not used in this work.

<sup>5</sup>Note, that due to results from this work, which demonstrated that `ii_light` is useful for higher time resolutions than can be reached with `ii_lc_extract`, a newer version of `ii_light` is now part of the most recent version of the Software, OSA 9, released in May 2010.

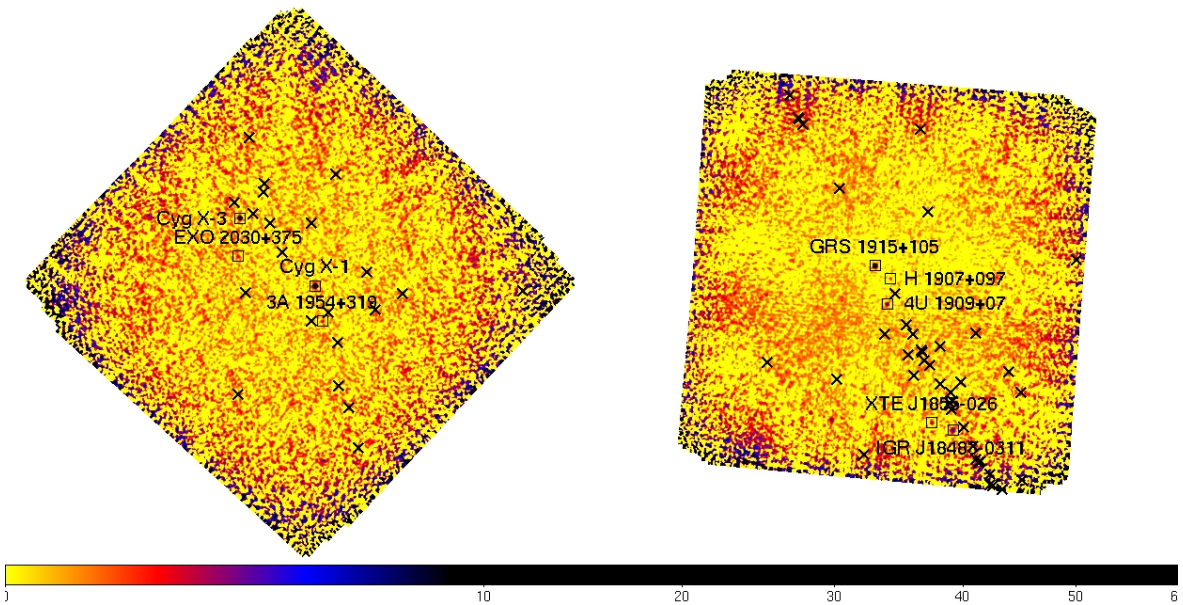


Figure 7.8: Cyg X-1 and GRS 1915+105 fields. Sources with  $\sigma_{\text{detection}} \geq 6$  are denoted by named boxes, weak sources with  $1 \leq \sigma_{\text{detection}} < 6$  are denoted by  $\times$ .

source	energy range	<code>ii_lc_extract</code> data courtesy of
Cyg X-1	20–50 keV	J. Rodriguez (DSM/DAPNIA/SAp, CEA Saclay, France)
GRS 1915+105	18–50 keV	M. Cadolle Bel (ESAC, Madrid, Spain)

Table 7.2: Overview over data used for the comparison between `ii_light` and `ii_lc_extract`.

### The Fields of Cyg X-1 and GRS 1915+105

To be able to quantify differences in the extraction results, a comparison of the performance of `ii_light` with the performance of `ii_lc_extract` is performed. To guarantee that the results are not only source or field specific, the Key Programme observations for two different regions – the Cyg X-1 and GRS 1915+105 regions – are compared.

GRS 1915+105 is an BXB containing a strong black hole candidate which shows a variety of interesting features. The Key Programme observations of GRS 1915+105 have been analysed by Rodriguez et al. (2008a,b).

Figure 7.8 shows mosaics images in the 20–40 keV range of the fields of both sources, Cyg X-1 and GRS 1915+105, including only ScWs within the fully coded FOV. The Cyg X-1 field mosaic consists of 16 ScWs from revolution 628, while the GRS 1915+105 field mosaic consists of 26 ScWs from revolution 852. As both Cyg X-1 and GRS 1915+105 are bright sources, with a count rate of  $\sim 100$  cps and  $\sim 40$  cps respectively in this revolution, only sources with  $\sigma_{\text{detection}} \geq 6$  are taken into account for further steps of the analysis. However, it is important to remember that the weak sources can still have minor influences on the results. In particular it is important that the field of GRS 1915+105 is crowded with  $\sim 35$  weak sources ( $1 \leq \sigma_{\text{detection}} < 6$ ), while the field of Cyg X-1 shows only  $\sim 20$  of those.

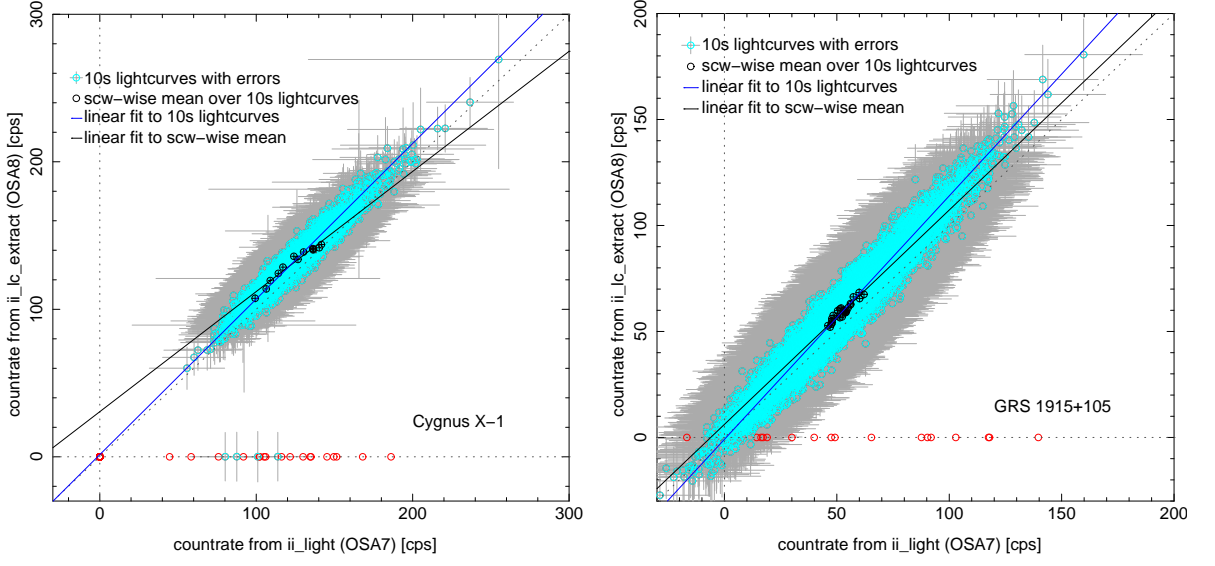


Figure 7.9: Comparison of the `ii_light` and `ii_lc_extract` extraction results for Cyg X-1 and GRS 1915+105 fields. A linear correlation is strongly supported by the data in both cases.

### Linear Correlation between `ii_light` and `ii_lc_extract`: 10 s resolution

For the direct comparison with the newer version of `ii_lc_extract` extractions made with the newest version of *INTEGRAL* OSA, OSA 8, are required. An overview over the energy bands used for the OSA 8 extractions is given in Table 7.2). The `ii_light` extractions have been adjusted accordingly.

A comparison between the results of two extraction mechanisms is presented in Fig. 7.9, where the horizontal axis shows the count rate values from `ii_light` and the vertical axis the corresponding values for the same time bins from `ii_lc_extract`. The cyan circles represent 10s lightcurves with their uncertainties shown in lighter grey. The dashed dark grey lines indicate the zero values and the identity. Already with a 10s time resolution `ii_lc_extract` clearly fails to detect the respective sources in several time bins, resulting in data points with zero count rate and error (red circles), which are excluded in the following analysis. Note that such data points are dangerous: they suggest a detection with zero values and zero uncertainties. A filtering for such time bins should be done for any analysis conducted with `ii_lc_extract` lightcurves. In case of Cyg X-1 several successive time bins ( $\sim 60$ ) appeared with zero count rate in both kinds of extraction. As Cyg X-1 is a persistent source and as there was no indication for any anomalous source behaviour at this time, these data were clearly damaged, a not too uncommon issue when the amount of data analysed is taken into account, even though the exact reason is not evident.

The prolonged, ellipse-like shape formed by the cyan data points obviously indicates a correlation between the two extraction mechanisms for both sources. However, it is also clear, that the cyan ‘ellipse’ is not centred on the dashed grey line, as would be expected for a one-to-one correlation, instead the slope seems higher than 1. This difference is consistent with the finding of Kreykenbohm et al. (2008), who have analysed all publicly available Crab data up to revolution 464 (Crab is a commonly used calibration source in X-ray astronomy in general and for *INTEGRAL* in particular, see e.g. Kirsch et al., 2005) and found an offset of about 5 % between extractions with `ii_light` and with full deconvolution methods. The exact shape of the correlation was however not

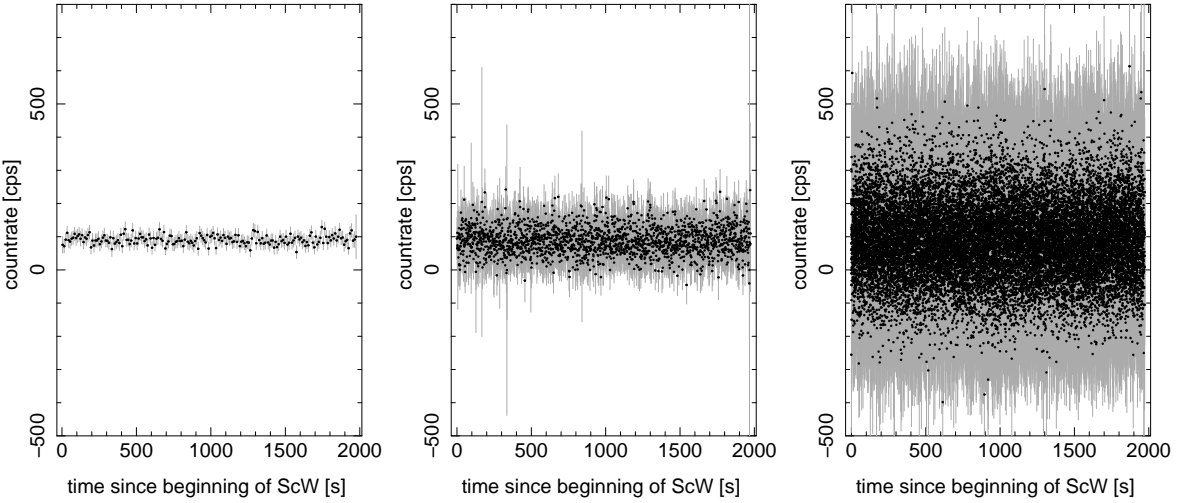


Figure 7.10: *INTEGRAL* lightcurves of Cyg X-1 for ScW 062800020010 in the 20–40 keV band with 10 s (left panel), 1 s (middle panel) and 0.1 s (right panel) time resolution, error bars in grey. Note, that same  $y$ -range is chosen for all three plots.

evident in their analysis.

### Linear Correlation between `ii_light` and `ii_lc_extract`: ScW-resolution

The black circles in Fig. Fig. 7.9 indicate the ScW averaged count rates of 10 s resolution lightcurves from `ii_light` and `ii_lc_extract`, the black solid lines linear fits to them. The correlation obtained from the ScW averages is clearly different from that obtained from the 10 s resolution lightcurves. However, compared to the 10 s resolution lightcurves only a few data points covering a much smaller range on both axes are used for fitting here (16 in case of Cyg X-1, 26 in case of GRS 1915+105) and therefore the exactness of the fit is reduced. Besides, the scatter plots clearly show that the black points still agree well with the fitted 10 s correlation (blue line), as they lie on the intersection of the black and blue correlations.

Therefore, the correlation derived from the 10 s lightcurves is considered correct. However, more testing with other sources in different fields as well as sources covering a greater range in count rates, especially on ScW-averaged basis, is to be recommended.

### 7.3.2 High Time Resolution with `ii_light`

In contrast to `ii_lc_extract`, `ii_light` is suited for the extraction of lightcurves with a higher time resolution than 10 s. For bright sources, such as Cyg X-1, a time resolution of up to 0.1 s can be reached, corresponding roughly to a count rate of  $\sim 10$  photos per time bin in the 20–40 keV band.

In this section the reliability of the `ii_light` extraction with high time resolution of 10 s, 1 s and 0.1 s for all possible pointing offset angles for the revolution 628 from the Cyg X-1 KP, i.e., ScWs 062800020010 to 062800900010, is analysed.

### Scatter

Figure 7.10 shows an example of lightcurves for the same ScW with different time resolutions. It can be clearly seen that both the scatter and the errors increase with

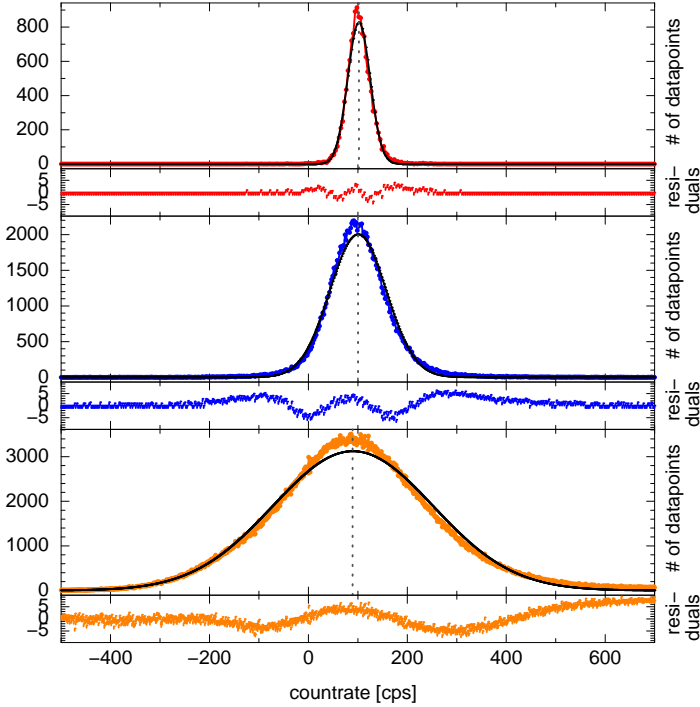


Figure 7.11: Histograms for *INTEGRAL* lightcurves of Cyg X-1 for revolution 628 in the 20–40 keV band with **10s**, **1s** and **0.1s** time resolution with Gaussian fits and fit residuals. Gaussian fits are shown in black, dashed dark grey lines indicate the centres of the Gaussians. Fit results are presented in Table 7.3.

time resolution	$\chi^2_{\text{red}}$	centre	$\sigma$
10 s	0.22	102 cps	22 cps
1 s	2.1	100 cps	57 cps
0.1 s	15	89 cps	162 cps

Table 7.3: Results of the Gaussian fits to the histograms of the count rates of `ii_light` extractions of Cyg X-1 lightcurves with 10 s, 1 s and 0.1 s time resolutions as presented in Fig. 7.11.

decreasing SNR, as expected.

The negative count rate values might seem unphysical and worrisome at first, but are indeed only the results of higher scatter around the mean and the mathematics behind the deconvolution algorithm, as can be seen on the histograms in Fig. 7.11. Negative flux values due to background subtraction are also possible for other instruments, e.g., *RXTE/PCA*.

The histograms of the lightcurves are qualitatively consistent with Gaussian shapes – the deviations apparent in the residuals are due to the high intrinsic variability of the source (see Fig. 7.12 and Table 7.3). Note that when fitting the histograms  $\sigma(N) = \sqrt{N}$  where  $N$  is the number of data points was assumed. An important indication for the consistency of the different extractions is the stability of the centre positions of the Gaussian fits and their consistency with each other. The FWHM of the Gaussian increases by a factor of  $\sqrt{10}$  for one order of magnitude increase in time resolution, consistent with the decreasing SNR as the width of the time bins becomes smaller. The Gaussian shape of the histograms and especially their extension into the negative makes the negative values and the high scatter from the Fig. 7.10 comprehensible.

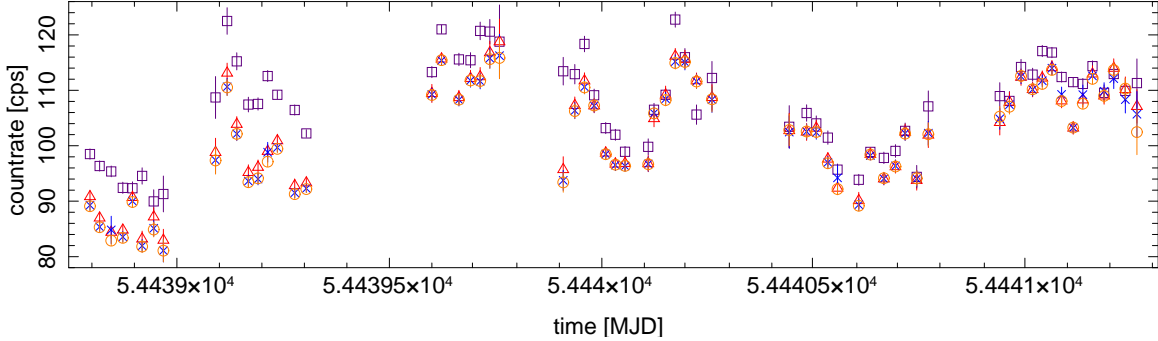


Figure 7.12: Fluxes from image extraction ( $\square$ , deconvolution algorithm consistent with `ii_lc_extract`) of Cyg X-1 in revolution 628 as well as averaged count rates for individual ScW of the `ii_light` lightcurves with  $10\text{s}$  ( $\triangle$ ),  $1\text{s}$  ( $\times$ ) and  $0.1\text{s}$  ( $\circ$ ) time resolution in the 20-40 keV energy band with their errors.

### Intrinsic Source Variability

For the discussion of the stability of the lightcurve extraction algorithms it has to be taken into account that in contrast to, e.g., the Crab pulsar and nebula, Cyg X-1 is a highly variable source. Figure 7.12 shows ScW-averaged lightcurves from different algorithms and different time resolutions. The flux from the image extraction<sup>6</sup>, which is integrated over whole ScWs, shows only the intrinsic source variability. Over the course of the 3 days of the presented observation the flux (which is consistent with `ii_lc_extract` extractions) changes by as much as  $\sim 25\%$ . As expected from the scatterplots, `ii_light` underestimates the source flux – the different time resolutions are, however, consistent among each other and reproduce the shape of the lightcurve well.

### Dependency on Offset Angle

In their analysis of the Crab lightcurves Kreykenbohm et al. (2008) have raised the concern that the flux values obtained with `ii_light` depend on the pointing offset angle for a given observation, see their Fig. A.1. The ratio between the `ii_light` results for different time resolutions and the fluxes from image extraction presented here shows no obvious dependency on the offset angle as seen in Fig. 7.13. The different time resolutions agree again well with each other both in the individual values and in the mean ratio of about 0.95. Note, however, that uncertainties in the flux values will naturally become larger for higher offset angles as the source moves out of the fully coded field of view and illuminates less and less detector pixels.

### 7.3.3 Alternative PIF-based Extraction Algorithm

As `ii_light` was not included in OSA 8 and it was unclear, whether it would become part of the OSA software again, alternatives were needed. With `ii_light` being part of the recent OSA 9 (released in May 2010) again, an alternative extraction method might still help to shed light on some problems `ii_light` has, such as the different absolute flux values or the anomalous noise (see Sec. 7.3.4).

---

<sup>6</sup>as obtained from the `isgrisky_res.fits` files generated during the IMA step.

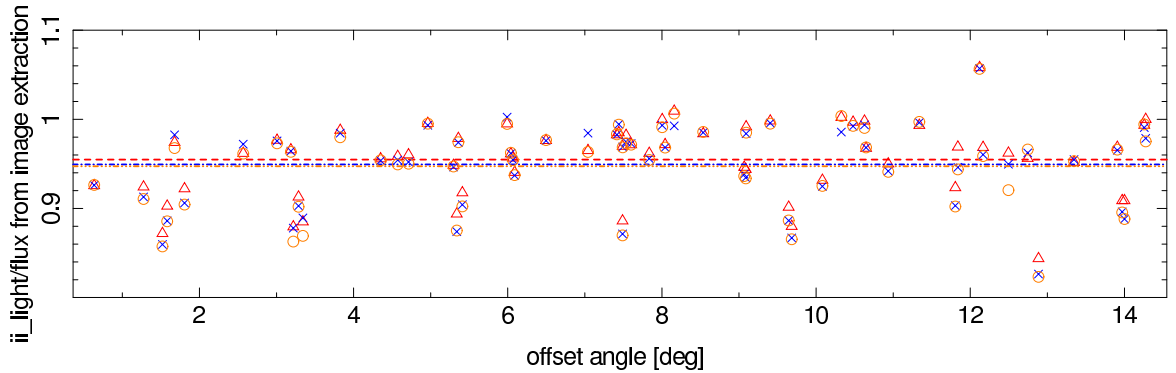


Figure 7.13: Ratio between ScW averaged count rates for individual ScW of the `ii_light` lightcurves with 10s ( $\Delta$ ), 1s ( $\times$ ) and 0.1s ( $\circ$ ) time resolution and fluxes from image extraction (deconvolution algorithm consistent with `ii_lc_extract`) in dependency on the offset angle of the pointing of Cyg X-1 in revolution 628. Mean values of the ratios are represented by the dashed lines. Error bars not shown for clarity of the plot.

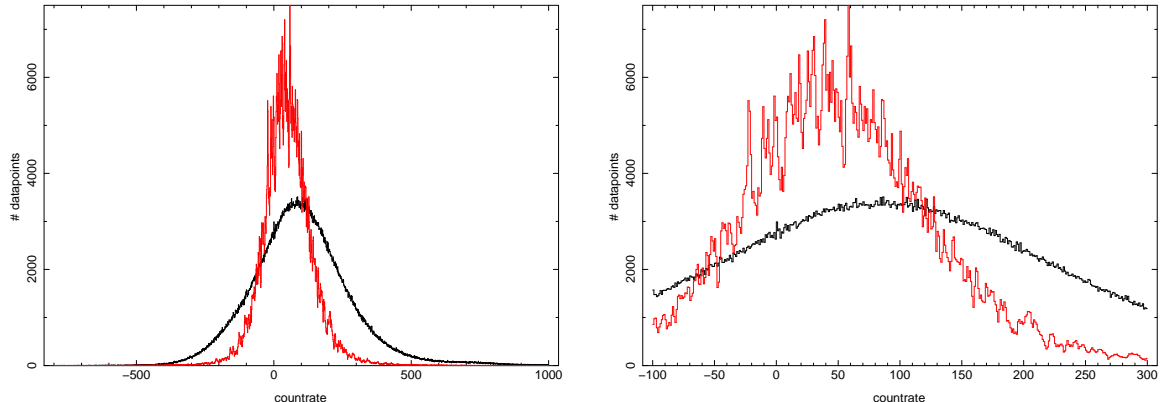


Figure 7.14: Comparison of histograms of `ii_light` 0.1 s lightcurve (black) with the 0.1 s lightcurve extracted with the algorithm by C. Ferringo (red) of Cyg X-1 in revolution 628. The right panel shows a closeup of the peaks of the two distributions shown on the left panel.

*data shown in red courtesy of C. Ferringo*

The left panel of Fig. 7.14 shows a comparison of the 0.1 s `ii_light` extraction with the data extracted with another PIF-based algorithm developed by C. Ferringo (IAAT, Tübingen, Germany & ISDC, Versoix, Switzerland), dubbed cf-algorithm here. These are the very first preliminary comparisons as this algorithm is still in the development phase. The peak of the cf-algorithm histograms is clearly at a lower value – the mean count rate of the lightcurve is  $\sim 55$  cps as opposed to  $\sim 100$  cps with `ii_light`, which does, as shown in Sec. 7.3.2, already underestimate the real flux of the source. This difference in the normalisations was however expected due to the use of different corrections for instrumental effects, especially different treatments of background and dead time correction (C. Ferringo, N. Produit<sup>7</sup>, priv. comm). It can and will be corrected by using observations of the Crab pulsar and nebula to redefine the normalisation. However the time bins have to be large enough to be able to ignore the 33 ms periodicity of Crab pulsar (Staelin & Reifenstein, 1968). This analysis is ongoing.

<sup>7</sup>N. Produit (ISDC, Versoix, Switzerland) is the author of `ii_light`.

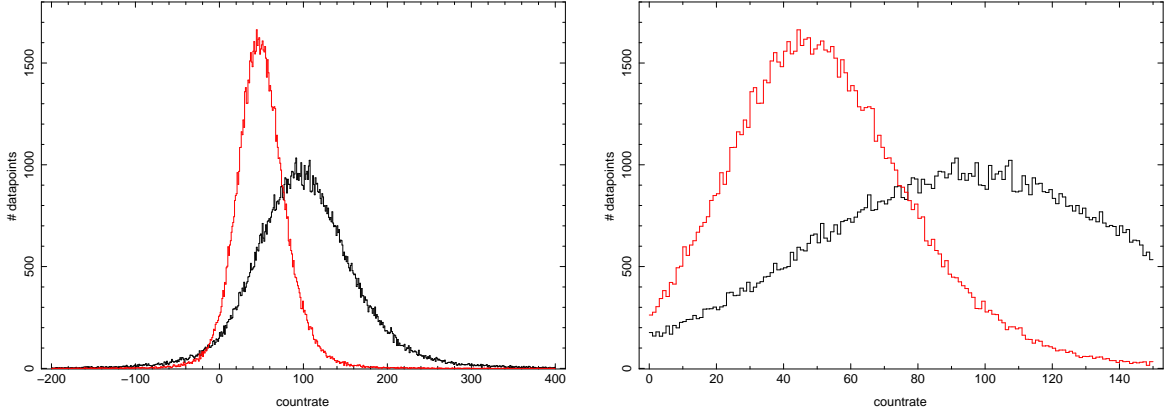


Figure 7.15: Comparison of histograms of `ii_light` 1s lightcurve (black) with the 1s lightcurve extracted with the algorithm by C. Ferringo (red) of Cyg X-1 in revolution 628. The right panel shows a closeup of the peaks of the two distributions shown on the left panel.

*data shown in red courtesy of C. Ferringo*

Note also that the distribution of the cf-algorithm extraction is much narrower than that of `ii_light`. This indicates that the additional noise introduced by the extraction mechanism is smaller, which would improve the lightcurve-based analysis, as e.g., PSDs.

However, the right panel of Fig. 7.14, a closeup of the left panel, illustrates a problem of the cf-algorithm extraction which was found during this analysis: the distribution shows very pronounced peaks at certain count rates. This behaviour lacks any consistent interpretation so far and is still under investigation by C. Ferringo. Figure 7.15 illustrates that it is not seen for the 1s time resolution. The histogram of the `ii_light` 1s lightcurve is less smooth as the amount of individual data point decreases by a factor of 10, but the fluctuations are in a reasonable range to be considered as random. The cf-algorithm histograms do not show the spikes observed in the 0.1s resolution and are, in this regard, consistent with the `ii_light` extraction for the 1s time resolution.

If the problem with the non-smooth distribution of the count rates is resolved, this algorithm is a promising alternative to `ii_light` for timing analysis with high time resolution up to 0.1s, though further testing against `ii_light` and `ii_lc_extract` will be necessary.

### 7.3.4 PSDs

As it has been shown that `ii_light` produces meaningful lightcurves with the time resolution of 10s, 1s and 0.1s, PSDs in the 20–40 keV range are calculated for the lightcurve obtained in the observations discussed in the previous sections.

The timing analysis of ISGRI lightcurves is complicated due to the dithering observing strategy. The single segments, for which individual PSDs are calculated, have to be continuous. However, for *INTEGRAL* data there are always gaps between the individual pointings (here equivalent with individual scientifically usable ScWs), when the satellite slews from one pointing position to the other. The segments have therefore to be chosen in a way that they do not contain any slews of the satellite. As the gaps are of the order of a few tens of seconds, it is possible to interpolate over them for low time resolution lightcurves, as done by Fürst et al. (2010) for their 6s lightcurves,

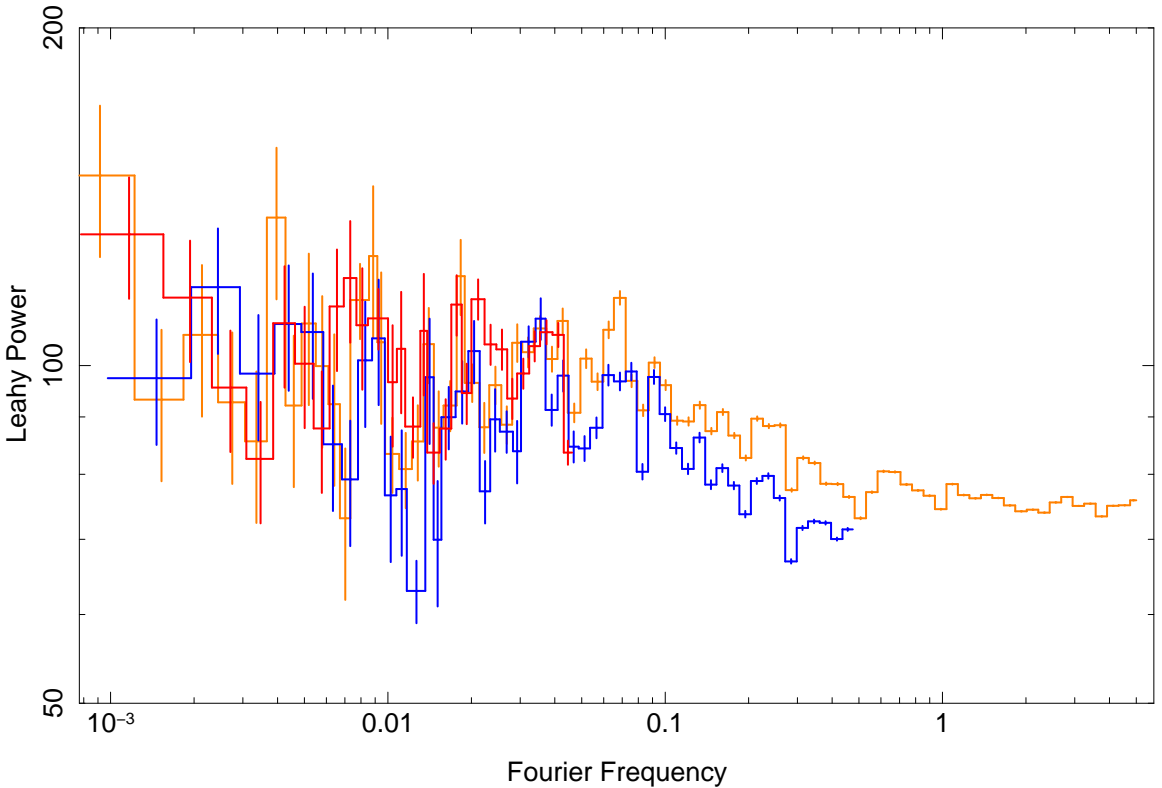


Figure 7.16: PSDs of Cyg X-1 for the `ii_light` lightcurves with **10 s**, **1 s** and **0.1 s** time resolution in the 20–40 keV energy using the Leahy normalisation. Note than the slightly different length of the frequency bins are due to the logarithmic rebinning starting at different points of the frequency spectrum.

without introducing too many artificial features. However, this is not feasible for the high resolution lightcurves of 1 s and 0.1 s resolution and therefore not attempted here as the main goal here is a comparison between the different resolutions. Additionally, the discrete Fourier transformation which is the base of the PSD calculation is implemented in form of Fast Fourier Transform algorithms (e.g., Bracewell et al., 2000), which work fastest and best on series of  $2^n$  ( $n \in \mathbb{N}$ ) values. The highest accessible frequency is determined by the time resolution (see Eq. 5.10), the lowest is determined by the length of the transformed time series, therefore the segments have to be as long as possible.

These three constraints lead to the segment length of  $2^7$  bins (1280 s) for the 10 s lightcurve,  $2^{11}$  bins (2048 s) for the 1 s lightcurve and  $2^{14}$  bins (1638.4 s) for the 0.1 s lightcurve of the analysed revolution 628. These were the longest segment-lengths possible, which resulted in one segment per ScW for most of the ScWs. A calculation of the PSD values for each segments has been performed in Leahy normalisation, see Eq. 5.15, using ISIS. All segments for revolution 628 have been first averaged and then rebinned to a logarithmic frequency binning with  $df/f = 0.1$ .

Figure 7.16 shows the results of these PSD calculations for all three lightcurves. The results for the different time resolutions agree well with each other. However, it can be clearly seen that neither of them flattens out at  $2(\text{rms}^2/\text{mean}) \text{ Hz}^{-1}$ , as expected for the Leahy normalisations (see Sec. 5.2.2), but instead at  $\sim 80(\text{rms}^2/\text{mean}) \text{ Hz}^{-1}$ , i.e., the noise is for instrumental reasons not fully Poissonian. This behaviour has also been seen by Fürst et al. (2010) for the X-ray pulsar Vela X-1, where the noise contributes as much as  $100(\text{rms}^2/\text{mean}) \text{ Hz}^{-1}$  at a given frequency while the prominent frequencies

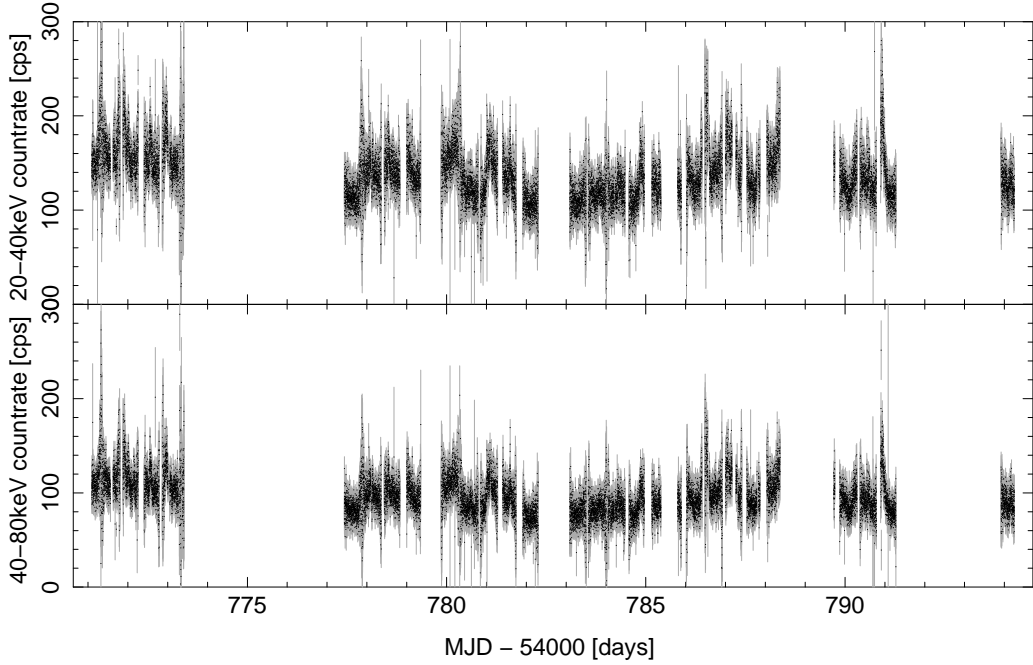


Figure 7.17: 40 s resolution `ii_light` lightcurve of the revolutions 739 and 741–746 in the 20–40 keV and 40–80 keV band.

are exactly reproduced.

Note that for exact timing studies with less noise than in the results shown here – as, e.g., by Fürst et al. (2010) – longer periods than a single revolution have to be considered. In addition, while there are no contemporary *RXTE* observations for this particular *INTEGRAL* revolution, Pottschmidt et al. (2006) have compared ISGRI (extracted with `evts_extract`) and *RXTE*-PCA PSDs and found an overall good agreement in shape, though, because of the peculiarities of the extraction mechanism, the overall normalisations were different.

The conclusion from the presented PSDs is therefore that the `ii_light` lightcurves with as high time resolution as 0.1 s are suited for timing analysis via PSDs. However, the high noise background has to be taken into account. A comparison with PSDs from other instruments, e.g., *RXTE*-PCA for simultaneous observations with *INTEGRAL* and *RXTE*, seems a promising starting point for such an analysis, as it would offer a possibility to assess the noise level.

### 7.3.5 Flux Distribution

Figure 7.17 shows the `ii_light` 40 s lightcurve of the longest quasi-continuous observation of Cyg X-1 during the Cyg X-1 Key Programme, which includes the revolutions 739 and 741–746. As can be seen in Fig. 6.1, the source has been in a constant hard state during this time.

It has been shown in the previous sections that `ii_light` lightcurves are in general suitable for timing analysis. Therefore these 40 s resolution lightcurves are used for the analysis of the flux distribution, as mostly intrinsic source variability will contribute to the lightcurve variability at this timescale. The left panel of Fig. 7.18 shows histograms of the lightcurves presented in Fig. 7.17. Already with the naked eye the non-Gaussian shape of the histograms is clear: they are skewed and show an excess at the higher

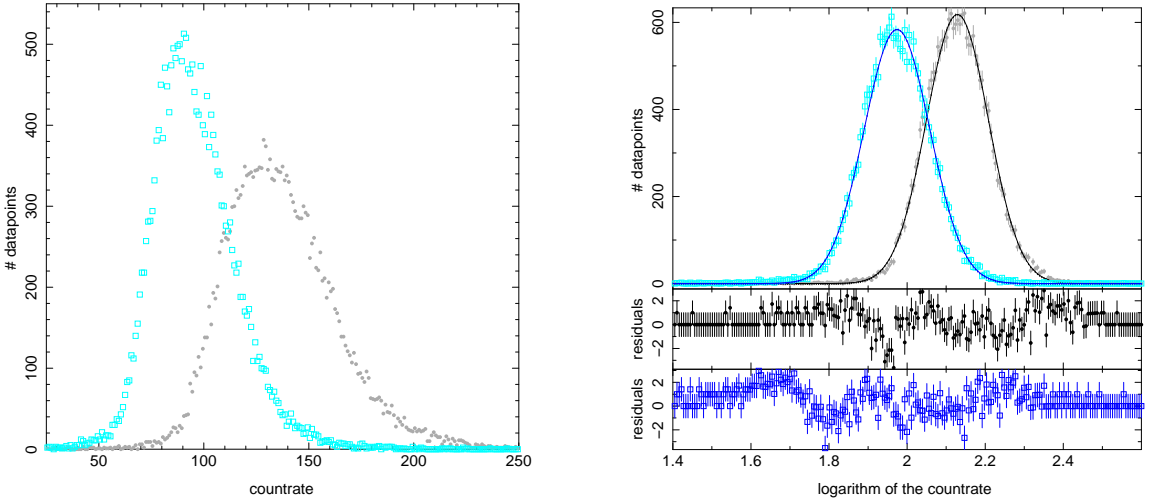


Figure 7.18: Histograms of 40 s `ii_light` lightcurves of revolutions 739 and 741–746 in the 20–40 keV (grey/black) and 40–80 keV (cyan/blue) energy bands; *Left panel*: linearly binned histograms on a linear scale; *Right panel*: logarithmically binned histograms on a logarithmic scale.

count rates as compared to a purely Gaussian shape.

Uttley et al. (2005) have shown that X-ray lightcurves of BHs, as well as other X-ray binaries and AGN, have formally a non-linear, exponential form and data taken in periods with a stable mean will therefore have a log-normal flux distribution. They demonstrated the validity of their assumption on 0.125 s resolution *RXTE/PCA* lightcurves in the 2–13 keV energy band for Cyg X-1. Though their data were far more copious, they lead to an assumption of the same behaviour for the *INTEGRAL* lightcurves. Therefore logarithmically binned histograms of the lightcurves were calculated and fitted with a Gaussian in a log-lin space. Errors of  $\sigma(N) = \sqrt{N}$  were assumed for the fit. Results are presented on the right panel of Fig. 7.18. Although the residuals show some deviations, which are to be expected both because of instrumental effect and because Cyg X-1 is usually not stationary even on timescales as short as a few hours (Böck, VG, et al., in prep.), the fits are good for both the 20–40 keV and the 40–80 keV lightcurves. Additionally at high energies considered here, scattering dips, coincident with the dips at low energies which are caused by photoelectric absorption, also influence the count rates (Hanke et al., 2010). Therefore the natural log-normal shape of the flux distribution is indeed observed with *INTEGRAL/IBIS* at energies above 20 keV.

## 7.4 Spectral Analysis

The hard X-ray/soft gamma-ray part of the spectrum of BHs has been subject to more detailed investigations in the recent years. The evolution of the spectrum of the canonical transient GX 339–4 in state transitions is analysed by Del Santo et al. (2008, 2009). Motta et al. (2009) concentrate on the evolution of the high energy cutoff of the same source, which can be well constrained with the help of the *INTEGRAL* data and can well describe their broadband data in the IBIS range with a cutoff power law or Comptonization models.

For Cyg X-1, Wilms et al. (2006) have shown that the 3–120 keV *RXTE/PCA* and *HEXTE* spectra in the hard state are best described by a broken power law with a

spectral break at  $\sim 10$  keV. Malzac et al. (2008) fit ISGRI spectra averaged over a whole revolution with an e-folded power law and obtain good quality fits. Also, Cadolle Bel et al. (2006b) have shown that the spectrum of Cyg X-1 in the whole IBIS (ISGRI and PICsIT) energy range can be reasonably well fitted with an exponential cutoff power law for those of their observation which were taken in a hard state of the source. Note, however, that both Cadolle Bel et al. (2006b) and Malzac et al. (2008) use 3% systematic errors for their spectra and work with observations from the years 2002–2003 and September 2006 respectively, i.e., with data taken at least 15 months before the data of the Cyg X-1 Key Programme.

Fritz (2008) analysed observations of Cyg X-1 made with *XMM-Newton*, *RXTE* and *INTEGRAL* in 2004 during a hard intermediate state (HID) and found evidence for a non-thermal tail (often also dubbed hard tail): their spectra show excess at high energies when fitted with a thermal Comptonization model. This was also seen by Cadolle Bel et al. (2006b) for the transition to a softer state in June 2003. The hard tail was also observed, e.g., in the canonical transient GX 339–4 (Droulans et al., 2010). The hard tail is an evidence for the existence of a non-thermal electron distribution which can originate, e.g., in a jet.

In this section, spectral data of all revolutions listed in Table 7.1 are considered for Sec. 7.4.1, i.e., for the analysis of the Tungsten instrumental background feature. For spectral analysis in Sec. 7.4.3 revolutions with less than 30 ScWs (746, 756, 758, 794) are not taken into account both on the ScW and revolution averaged level. ISGRI spectra are extracted in 64 energy channels (cf. Sec. 4.3.5) for the full energy range of ISGRI with OSA 7. For the modelling, the energy range from 17 to 500 keV is considered. Further specific treatments required by the data and systematic errors are discussed in the following.

Note that parts of this analysis were presented by on posters by Pottschmidt, ..., VG et al. (2010b) and Pottschmidt, ..., VG et al. (2010a).

#### 7.4.1 Tungsten Instrumental Background Line

The spectral analysis of *INTEGRAL*/IBIS data in this work was highly impeded by the discovery – in cooperation with M. Cadolle Bel (ESAC, Madrid, Spain), D. M. Marcu (CRESST/NASA-GSFC, Greenbelt, MD, USA; UMBC, Baltimore, MD, USA; GMU, Fairfax, VA, USA) and K. Pottschmidt (CRESST/NASA-GSFC, Greenbelt, MD, USA; UMBC, Baltimore, MD, USA) – of a Tungsten instrumental background line. Throughout this section a systematic error of 2% is used, which is the systematic error quoted in the IBIS Analysis User Manual 7.0 (Chernyakova & Neronov, 2008). A more detailed discussion of the systematic errors is included in Sect. 7.4.3.

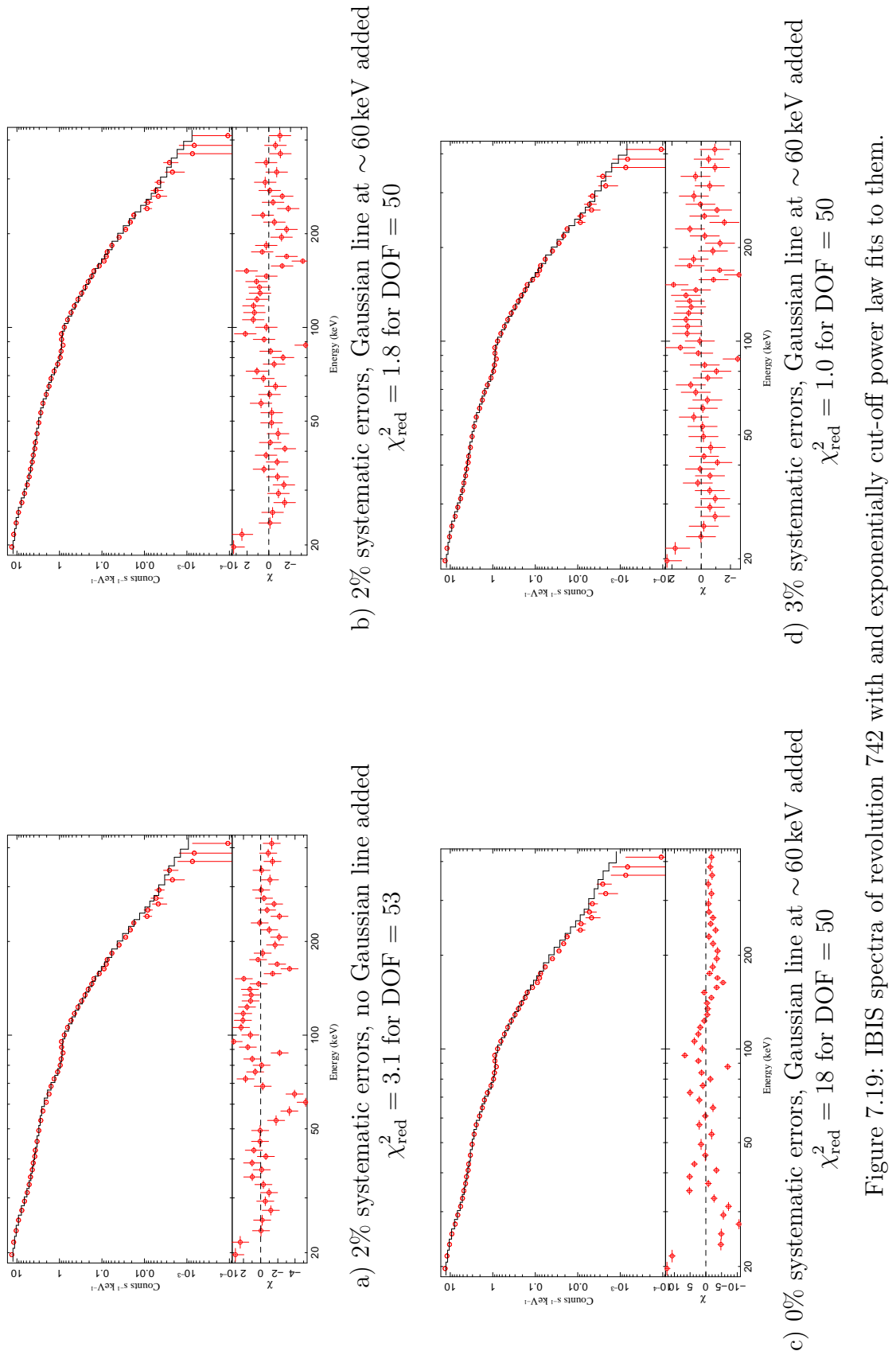
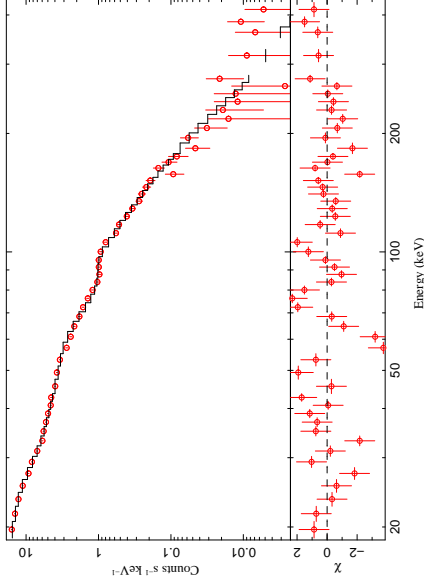
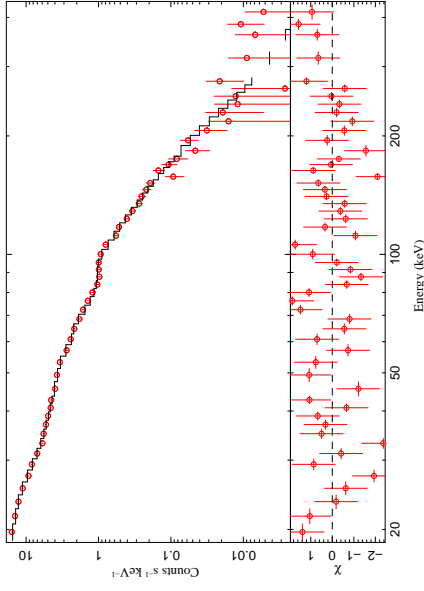


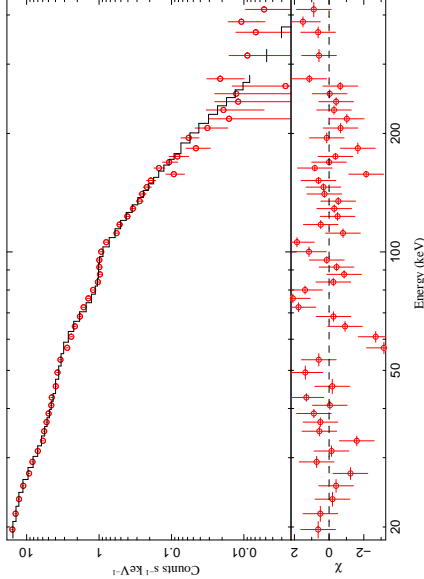
Figure 7.19: IBIS spectra of revolution 742 with and exponentially cut-off power law fits to them.



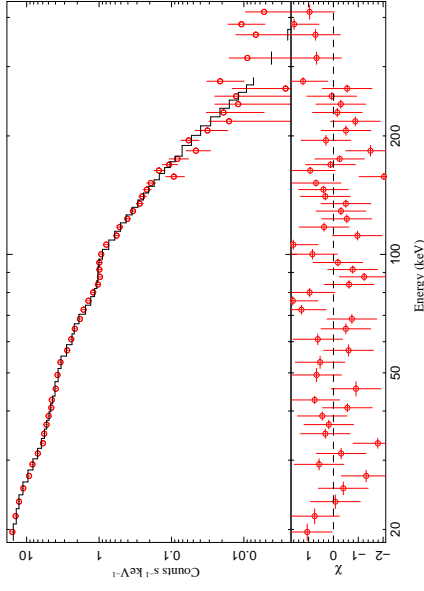
a) no systematic errors, no Gaussian line added  
 $\chi^2_{\text{red}} = 1.6$  for DOF = 51



b) no systematic errors, Gaussian line at  $\sim 60$  keV added  
 $\chi^2_{\text{red}} = 1.1$  for DOF = 48



c) 2% systematic errors, no Gaussian line added  
 $\chi^2_{\text{red}} = 1.2$  for DOF = 51



b) 2% systematic errors, Gaussian line at  $\sim 60$  keV added  
 $\chi^2_{\text{red}} = 0.83$  for DOF = 48

Figure 7.20: IBIS spectra of ScW 074200500010 and exponentially cut-off power law fits to them.

## Existence of the Tungsten Line

It has been shown (Cadolle Bel et al., 2006b; Malzac et al., 2008) that Cyg X-1 data in the IBIS energy range can be well described by a power law with an e-folding energy above 150–200 keV. In ISIS, such a power law is expressed with the fit function:

`cutoffpl(1)`

Fits of all the revolution-averaged spectra have been performed. Figure 7.19 a) shows an example of such a fit in the energy range 17–500 keV. Clearly discernible in the residuals is a line at about 55 keV, which does not correspond to any known feature of the source or the field and contributes strongly to the overall difference between the data and the model. This feature is present in all revolution averaged spectra of the Cyg X-1 Key Programme.

As Fig. 7.20 illustrates for the example of ScW 074200500010, the feature is also present in the spectra of individual ScWs. While there are random features in the residuals, which might reach the same amplitude, none of them is persistent over all ScWs analysed. Due to the low quality of single ScW spectra however, reasonable fits are also possible without the inclusion of further model components, as 7.20 c) illustrates, where the quality of the fit is almost ideal ( $\chi^2_{\text{red}} = 1.2$  for  $\text{DOF} = 51$ ) in spite of the structure in the residuals around  $\sim 60$  keV.

To empirically account for this feature a Gaussian line has been added to the fit function, extending the model to:

`cutoffpl(1)+egauss(1)`

and the fitting repeated. As the line is seen as an absorption feature (the pure cutoff power law model lies above the data) the ‘Area’ parameter of the `egauss` function is constrained to negative values. Figure 7.19 b) shows the same data set as used for Fig. 7.19 a), but with the Gaussian line added. The structure in the residuals is removed.

## Line Evolution and Identification

While consecutive revolutions show similar values for all parameters of the Gaussian line, there is a clear trend over the whole Cyg X-1 key programme as shown in Fig. 7.21. This trend is significant in all the parameters as the values do not lie within each others 90% confidence error bars. The centroid energy of the line  $E_0$  increases as do the line area and the line  $\sigma$ , i.e., the line becomes stronger. Only in few of the few first revolutions (629–632, but notably not 628) the line area is consistent with 0 and therefore with no line – in all the later observations the line is clearly required to achieve a  $\chi^2_{\text{red}} \lesssim 2$ .

Note also the width of the line. The  $\sigma$  parameter is in the range of 5–10 keV, which corresponds to a FWHM of about 10–20 keV (see. Eq. 5.31). This means that a significant part of the spectrum is affected by the line and that in an area with the highest count rates which strongly influences the overall shape of the spectrum.

Note that the line is present and shows the same behaviour both in the extractions with OSA 7, as presented here, and in extractions with OSA 8 (D. M. Marcu, priv. comm.). It should also be pointed out that simply increasing the systematic errors in the energy range of the line does not improve the fits as much as the additional Gaussian component does.

As the line cannot originate in the source (see, e.g., Fig. 8.4 for simultaneous observations with *RXTE*/HEXTE, which covers the line energy range) it must be a

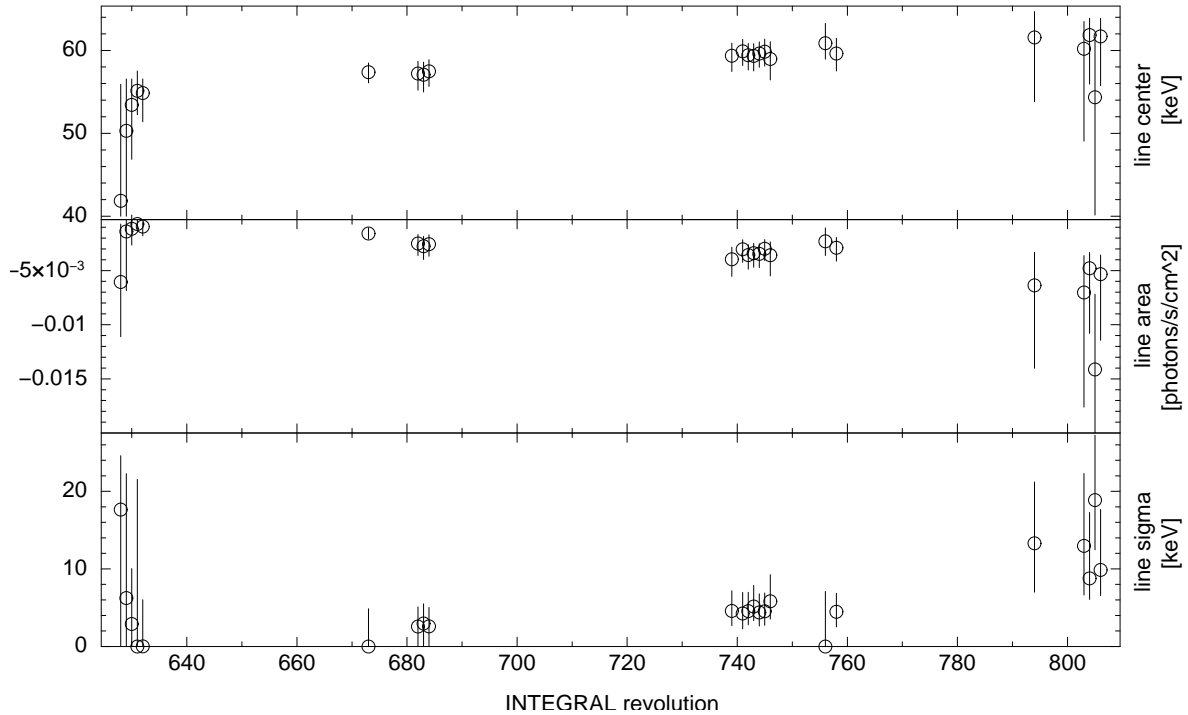


Figure 7.21: Evolution of the parameters of the Tungsten instrumental background line during the Cyg X-1 Key Programme. 90% confidence limit error bars are shown.

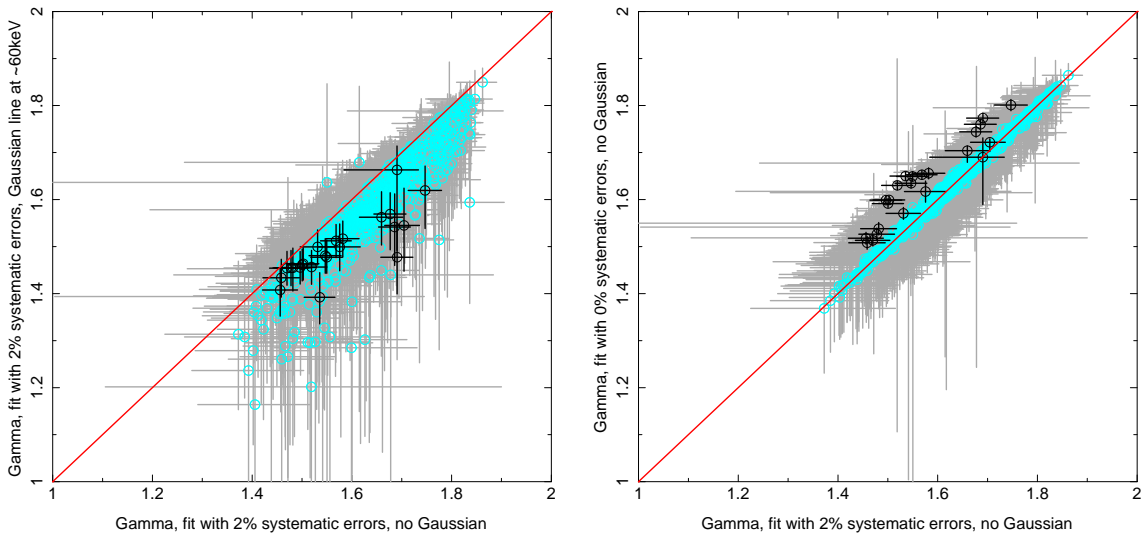


Figure 7.22: Influence of the modelling of the Tungsten instrumental background line and of the systematic errors on the slope of the Cyg X-1 spectrum

feature of the instrument, i.e., an instrumental background line or rather a line that should have been ‘calibrated away’ in the response (ARF or RMF) files. A thorough understanding for the exact reason for the line evolution is lacking as of now. However, the background spectrum of IBIS shows a strong Tungsten fluorescence line at 59.3 keV, as the coded mask of the instrument is made of Tungsten (Klochkov, 2007). A possible explanation for the instrumental line is then a wrong correction of the time dependent gain of the instrument, which may lead to the observed absorption line-like feature.

## Treatment of the Line – Outlook

The existence of the line has a direct effect on this work. Because the line is highly variable and strongly influences the spectra, any spectral models based on *INTEGRAL* data presented here are **not final versions**. The left panel of Fig. 7.22 demonstrates the influence of the Gaussian feature on the slope  $\Gamma$  of the power law fit: for both revolution averaged (black) and single ScW (cyan) spectra, the slope is higher when no Gaussian component is fit and decreases when the Gaussian line is included. This is especially striking for the revolution averaged spectra, where for most revolution the values are not within each others error bars (for that the error bars would have to intersect the identity line on the plot). For the ScW averaged spectra the spreading of the data points indicate that the slope will be on average 0.05 higher in the observations without the inclusion of the absorption feature.

This implies that **any results which rely on comparatively small changes in the slope of the spectrum for the data between about middle 2007 till 2010 reduced with OSA 7 or OSA 8 need to be re-evaluated**. The spectral changes might be not due to intrinsic source behaviour but due to the unresolved Tungsten line.

The existence of the line has been communicated to the instrumentation team (IBIS/ISGRI team at CEA/Saclay – APC). The IBIS/ISGRI instrument team, motivated by the findings presented here, has investigated this issue and new response matrices have been delivered with OSA 9 by the ISDC. A reason for the anomalous behaviour of the line is that there have been changes in the method of the energy reconstruction between OSA 7 and OSA 8. The problem of the Tungsten line was probably related to the fact that the ARF delivered with OSA 8 (valid from revolution 605 on for all versions of OSA) had been calibrated with OSA 7. A new set of ARFs have been delivered that correct this problem (I. Caballero, priv.comm).

Especially important is that the line can only be seen in spectra of bright sources – spectra of weak sources, which are additionally often only sparsely covered during a revolution, have a poor spectral resolution and too low count rates to resolve the line. Nevertheless, the line is present even in weak sources and will influence the results of spectral analysis as has been shown for the single ScW spectra of the Cyg X-1 Key Programme.

The Cyg X-1 KP data are too sparse to be able to constrain the exact evolution of the line parameters – this requires the extraction of all the spectra of all the bright sources observed from the year 2006 on. This work has been done mainly by I. Caballero (DSM/DAPNIA/SAp, CEA Saclay, France). Some of the final testing is still ongoing.

For this work, it has been decided to fit the line for the more simple models – cutoff power law and the simple Comptonization model `comptt` – and to freeze it to the parameter values obtained in the power law fits for the far more complex and CPU intensive `agnjet` model.

### 7.4.2 Systematic Errors

#### Revolution Averaged Spectra

A systematic error of 2% is recommended in the in the IBIS Analysis User Manual 7.0 (Chernyakova & Neronov, 2008) to take into account the calibration uncertainties of the instrument. In the literature, however, a systematic error of 3% was often used (Malzac et al., 2008; Cadolle Bel et al., 2006a,b). Because systematic errors are notoriously hard

to constrain and have a big influence on the quality of a fit, a more in detail look into them was taken in this work, by fitting all the spectra considered with the model:

`cutoffpl(1)+egauss(1)`

i.e., a cutoff power law with a Gaussian to account for the Tungsten instrumental background line introduced in Sec. 7.4.1 with no systematic errors, systematic errors of 2% and systematic errors of 3%. Panels c) and d) of Fig. 7.19 show examples of cutoff power law fits to the data of revolution 742 with no and 3% systematic errors, respectively.

The spectral fit presented on Fig. 7.19 c) shows significant structure in the residuals, which cannot be attributed to any known features of the source and appear random, except for an excess around 20 keV, which is also present in the other spectra. This illustrates that the errors are indeed dominated by systematic errors which need to be taken into account to be able to achieve a proper description of the spectrum with a model. Figure 7.19 d), the fit with 3% systematics has a very good  $\chi^2_{\text{red}}$  of 1.0 – an examination of all the revolutions does however reveal that these high systematics are not required for about the first half of the revolutions observed (revolutions 600–700). Here 2% are enough to account for all the uncertainties in the calibration except for the Tungsten instrumental background line which is, however, also still clearly present when 3% systematic errors are applied. Statistically good fits cannot be achieved for the second part of the observations campaign presented here (revolutions 700–800) with 2% systematic errors (cf. Fig. 7.23). The residuals here are, however, dominated by the problems with modelling the instrumental background line with a Gaussian component and 3% systematic errors do not allow for fits with  $\chi^2_{\text{red}} \approx 1$ .

Systematic errors clearly influence the fit parameters as Fig. 7.22 demonstrates: the slope  $\Gamma$  of the power law fit changes when 2% systematics are applied. To attenuate the influence of the Tungsten instrumental background line, the fits for the scatter plot were performed without modelling it by a Gaussian. However, since the line is very pronounced, it cannot be ruled out that part of the changes in the slope are due to its existence. Note also that the very small errors for  $\Gamma$  for the fits without systematics are not to be trusted: because of the high initial  $\chi^2_{\text{red}}$  value, error calculation cannot be performed properly.

To be able to compare the model parameters it was therefore decided to apply 2% systematic errors to all data and to accept the higher  $\chi^2_{\text{red}}$  values for the revolutions 700–800.

## Single ScW Spectra

Because of the low quality of the single ScW spectra, only revolution-wise averaged spectra are considered for spectral modelling in this work. However, as it is known that Cyg X-1 is highly variable on timescales of below an hour (Böck, VG, et al., in prep.), at least a general characterisation of single ScW spectra should be undertaken before summing them into revolution averaged spectra. Besides, such an investigation will be useful for further studies of spectral variability with higher time resolution than whole revolutions.

Fig. 7.20 shows fits to single ScW spectra of a representative science window for no systematic errors and for 2% systematic errors both with and without inclusion of a Gaussian component to fit the Tungsten absorption line. Such fits have been performed for all science windows of the Cyg X-1 Key Programme. As the example ScW indicates,

both fits with no Gaussian line but 2% systematic errors and a Gaussian line but no systematic errors, lead to comparable results as far the quality of the fits is concerned.

The influence of the systematic errors on the slope  $\Gamma$  of the power law is presented on the right panel of Fig. 7.22. Cyan circles represent value for the single ScW spectra. To exclude the influence of fitting of the Tungsten instrumental background line in the range of 50–79 keV, which has been shown to affect the slope of the spectra in Sec. 7.4.1, fits without the instrumental background line were considered. In the single ScW spectra, where the statistics is rather poor and both the overall features and the line are less pronounced (cf. Fig. 7.20 a) ), the additional systematic errors do not influence  $\Gamma$ . The spread around the unity is minor and well within the error bars of single fits. No outliers can be seen on the right panel of Fig. 7.22.

Therefore, it is decided to use 2% systematic errors for the ScW averaged spectra to stay consistent with the revolution averaged fits.

### 7.4.3 Spectral Modelling

Even though the uncertainties of the calibration have been shown to be a major hindrance for the analysis of the *INTEGRAL* data of Cyg X-1, a first analysis of the Key Programme data is possible. This section relies on the previous results – all fits are performed with an additional Gaussian component to account for the Tungsten instrumental background line and with 2% systematic errors added to the ISGRI data.

For the analysis a purely phenomenological model – a power law – and a physically motivated model – the thermal Comptonization model `comptt` (see Sec. 5.3) – were chosen. Cadolle Bel et al. (2006b), Pottschmidt et al. (2003a) and others have shown that `comptt` describes the high energy spectra of Cyg X-1 as measured with *INTEGRAL* well. Cadolle Bel et al. (2006b) additionally use the spectral data from the JEM-X instrument and therefore require a reflection component to account for residuals around 10 keV. Pottschmidt et al. (2003a) fit joined *RXTE* and *INTEGRAL* data and therefore also require additional components such as the reflection component and a Gaussian line to account for the Fe K $\alpha$  line at about 6.4 keV. Because of the use of ISGRI only these additional components are not required here. The fit functions used in ISIS were therefore:

`cutoffpl(1)+egauss(1)`

and

`comptt(1)+egauss(1)`

Results of both modelling approaches are presented in Fig. 7.23. The rising trend in the  $\chi^2_{\text{red}}$  inherent to both approaches is due to the increase in strength of the Tungsten line whose shape is not a pure Gaussian. This is clearly revealed by a look at the residuals which still show pronounced structure in this region, especially in the revolutions later than 700. Generally, both models are able to reproduce the data equally well.

Both in power law and in Comptonization fits a clear excess around 20 keV can be seen (see Fig. 7.19 b) and Fig. 7.24, respectively). However, the analysis here was performed with OSA 7 to allow the use of `ii_light` for timing analysis. Power law fits to data obtained with OSA 8 do not show this excess (D. Marcu, K. Pottschmidt, priv.comm.). Therefore it is attributed to problems with the OSA 7 calibration.

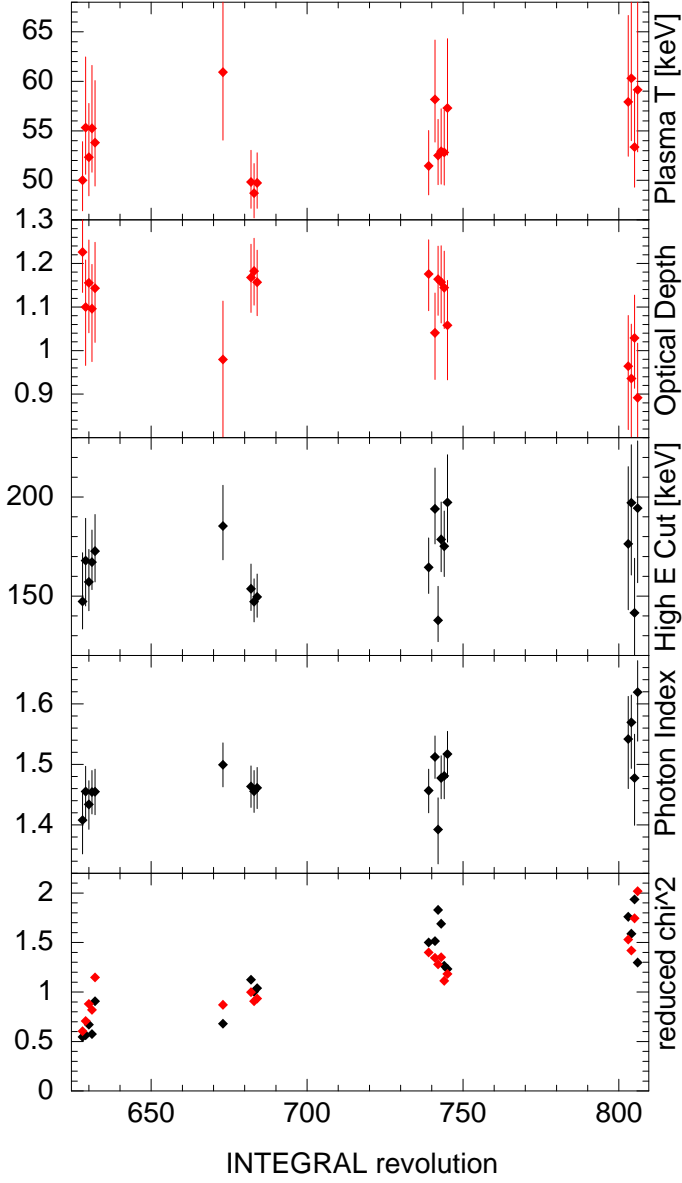


Figure 7.23: Fit parameters for revolution averaged ISGRI spectral fits with a cutoff power law (black) or the Comptonization model `comptt` (red) in both cases with an additional Gaussian function to model the Tungsten instrumental background line and with 2% systematic errors.

### Power Law Model

As the overview plot (Fig. 6.1) already implied, most of the observations were taken during a persistently hard state. A slight increase in the photon index of the power law fit can be seen for the revolutions 803 to 806 indicating a spectral change coincident with the higher radio activity as seen by the *AMI* telescope. The values of the cutoff energy might imply a slight increase, but are in general still consistent with no significant change.

The photon indices  $\Gamma$  are consistent with those found for energies above 10 keV in the combined *RXTE*/PCA-HEXTE fits of Cyg X-1 data during hard states by Wilms et al. (2006), who fitted their 3–120 keV data with a broken power law model with a spectral break at around 10 keV, as well as with the fits in Sec. 6.1.2.

### Comptonization Model

Figure 7.24 shows an example fit to the ISGRI spectra with the `comptt` model. For these fits the temperature of the input photons is not shown in Fig. 7.23. It has been

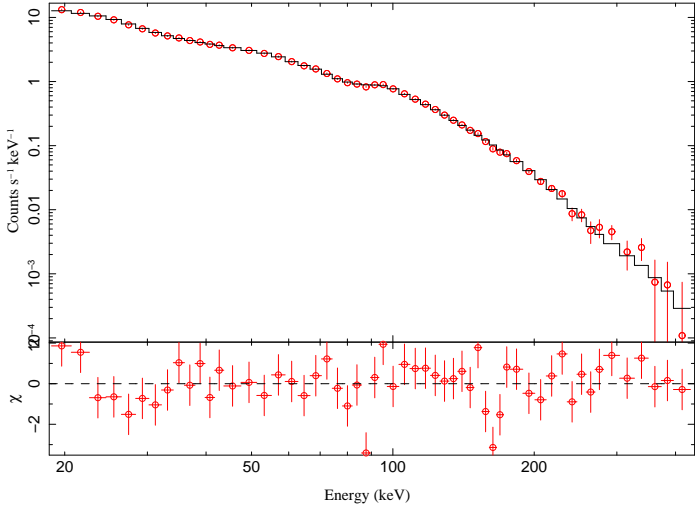


Figure 7.24: `comptt` fit for revolution 742 of the Cyg X-1 Key Programme with  $\chi^2_{\text{red}} = 1.3$  (for  $\text{DOF} = 49$ ). A Gaussian component at  $\sim 60$  keV is included to account for the Tungsten absorption feature.

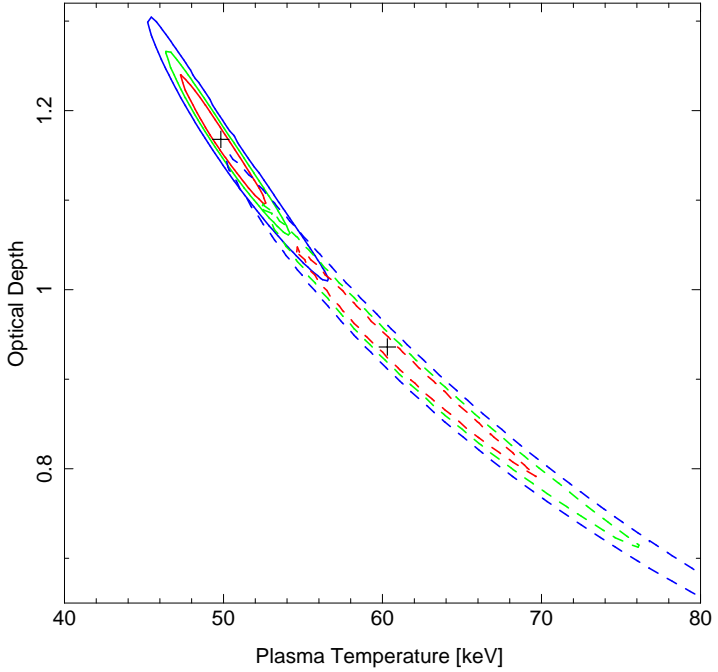


Figure 7.25: Confidence contour plots for the plasma temperature and optical depth parameters of the `comptt` model of two representative revolution of the Cyg X-1 KP: revolution 682 (solid lines) and revolution 804 (dashed lines). 1 $\sigma$  contours (68.3%) confidence contours are shown in red, 90% confidence contours in green and 3 $\sigma$  contours (99%) in blue.

shown in the literature that it lies at about 1 keV (Wilms et al., 2006; Nowak et al., 2010) and can therefore not be constrained when using ISGRI data only. For the presented fits it was left free: the values obtained ranged from 0.5 keV to 3 keV with an error of 2–3 keV and therefore consistent with the known parameter range. Overall, the results of the Comptonization model are consistent with those reported by Pottschmidt et al. (2003a) for hard states of Cyg X-1 observed in the year 2002.

The change in the spectrum for the revolutions 803 to 806 can be more clearly seen in the Comptonization model: the optical depth decreases from about 1.1–1.2 to 0.9–1.1, while the plasma temperature increases from 50–55 keV to about 60 keV. Figure 7.25 shows confidence contours for the plasma temperature and the optical depth parameters of the `comptt` model for two representative revolutions: revolution 682, i.e., one of the revolutions in the stable hard state and revolution 804, i.e., one of the revolutions observed during the slightly softer period. Though the parameters are, as expected, correlated, they occupy distinct regions in the parameter space.

The values presented here for the *INTEGRAL* data agree as in case of the power law fits well with those obtained by Wilms et al. (2006), who see a strong decrease in

the optical depth and at the same time an increase in temperature for the soft states. Although the source never enters the soft state in the Cyg X-1 KP observations, the interpretation is that we indeed see an excursion into a softer state.

## Interpretation and Outlook

Because the existence of the Tungsten line does not allow to constrain the model parameters well, a comparison between the ScW and revolution averaged spectra as well as just an analysis on the ScW basis are not attempted here, although the fits were performed. The differences between single ScWs are strongly influenced by the uncertainties of the Tungsten line fitting, as can already be seen on the left panel of Fig. 7.22.

It should also be again cautioned that the spectral results presented here are not final. However, a clear softening of the spectrum of the source can be seen for the revolutions 803 to 806 corresponding to a decline of a radio flaring period as observed with *AMI*. In the power law description of the spectrum, the slope becomes slightly steeper and the e-folding energy increases, which corresponds to an increase in the plasma temperature and a decrease of the optical depth in the Comptonization interpretation. This implies a heating and thinning of the Comptonization component, whether a corona or the base of the jet. Because of the discussed calibration problems, no attempts of fits with more sophisticated Comptonization models as, e.g., `eqpair` (Coppi, 1992, 1999), were made and therefore no conclusions can be drawn about the the existence of the hard tail in these softer observations.

# 8 Jet Fits: Joint *RXTE*, *INTEGRAL* and *Ryle/AMI* Spectral Analysis

So far, models describing the spectral shape of Cyg X-1 in the 3–200 keV (Sec. 6.1) and the 20–500 keV (Sec. 7.4) range were presented. Their were either purely phenomenological (power law fits) or more physically motivated (`comptt` Comptonization model), but did not offer a consistent description for the non X-ray parts of the spectrum. This chapter therefore concerns with a physically motivated, broadband model for the emission of BHs – the jet model, which is able to explain the full emission range, from radio to gammy-rays. Both *RXTE* and *INTEGRAL* data are taken into account and are complemented by radio measurements with *Ryle/AMI*.

First, an overview over the data used is given in Sec. 8.1. Broken power law fits (Sec. 8.2) allow to classify the observation in the context of the previous analysis of the whole campaign. They are also used to check cross-calibration between ISGRI and HEXTE instrument, which cover the same energy range between 20 and 200 keV, and to constrain the multiplicative constant which corrects the calibration differences between these instruments. The final jet fits are presented and discussed in Sec. 8.3

## 8.1 Overview over the Data

Those observations where simultaneous *RXTE* and *INTEGRAL* data are available are especially interesting for analysis, as they allow to test spectral models over a wide range of energies.

The *RXTE* ObsIDs 93121-01-36-00/01/02/03, which are part of the bi-weekly Cyg X-1 observation campaign, are (quasi) simultaneous with the *INTEGRAL* revolution 742 of the Cyg X-1 Key Programme and there is an *AMI* observation during the *INTEGRAL* observation. These data are therefore best candidates for the first application of the jet model onto joined *RXTE* and *INTEGRAL* data.

ObsIDs 93121-01-36-00 and 93121-01-36-03 are best suited for the analysis because they both have a long exposure time of about 50 min. Even though the constant behaviour of the source as well as the long integration time of the *INTEGRAL* spectrum, which averages over any minor changes in the spectral shape (see Fig. 8.1), should allow to use both observations for joint analysis, it has been decided to use only the simultaneous *RXTE* observation, i.e., ObsID 93121-01-36-03. Only data from the HEXTE cluster B are available for all listed ObsIDs.

The radio coverage throughout the *INTEGRAL* observation is sparse: There is an *AMI* radio observation during ObsID 93121-01-36-00 (MJD 54779.5) resulting in a flux of 10.6 mJy and a further observation on MJD 54782.5 resulting in a flux of 10.0 mJy. Considering the usual errors for less sparsely covered timeperiods, a value of  $10.3 \pm 1$  mJy is used for this analysis. Note that from known correlations between the *RXTE*/ASM and *Ryle* flux (Gleissner et al., 2004a; Nowak et al., 2005) it is even possible to fully estimate the radio flux when no measurements exist, albeit with larger errors, as done by Nowak et al. (2010) for their observations.

Throughout this chapter it should also be kept in mind that the *INTEGRAL* data suffer from the problem with the Tungsten calibration line as introduced in Sec. 7.4.1,

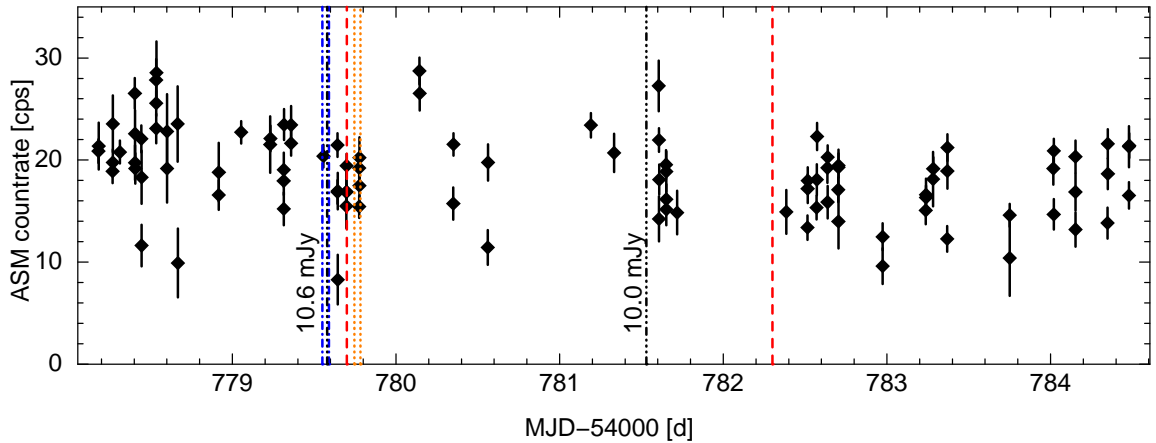


Figure 8.1: ASM count rates during the *RXTE* and *INTEGRAL* observations considered for the joint analysis. Red dashed lines indicate the start and stop times of the *INTEGRAL* revolution 742, the blue dash-dotted lines those of *RXTE* ObsID 93121-01-36-00 and the orange dotted lines those of *RXTE* ObsID 93121-01-36-03. The black vertical lines indicate the times of the *AMI* radio observations, the values of the respective radio fluxes are listed next to them. Note that ObsID 93121-01-36-00 and one of the radio observations are simultaneous.

which might affect the shape of the *INTEGRAL* spectra. This line is taken into account by adding a customized function `calibline` – a Gaussian component for the ISGRI data only – to the fit function. `calibline` was defined in ISIS by

```
define calibline(){
  switch(Isis_Active_Dataset)
  {case iid:  return constant(cid)*egauss(gid); }
  return 0;
}
```

where `iid` is the number of the ISGRI data set defined when loading the data, `cid` is the number of the constant and `gid` is the number of the Gaussian component in the overall fit function. This additional function is fitted for the broken power law fits. For jet fits with the `agnjet` model, the values are frozen to those obtained in the broken power law fits to reduce the CPU time used for fitting the complex jet model.

Due to improvements of the response functions it is possible to use both HEXTE and PCA data for higher energies than previously used in literature (e.g., Wilms et al., 2006): PCA data in the range of 3–40 keV and HEXTE data in the range of 20–200 keV are considered for this analysis. The broad overlap between the two instruments allows to better constrain the multiplicative constant used to compensate the difference in the normalisation of both instruments. Hereby PCA is always assumed as the reference data set. Radio data are assumed to have the same normalisation as the PCA.

Systematic errors of 2% are used for all ISGRI data, 0.5% for the full used energy range of the PCA data and none for HEXTE. All data set are grouped individually to a signal to noise ratio (SNR) of 4.5.

Because of the wide overlap between HEXTE and ISGRI the excess at around 20 keV observed in Sec. 7.4 for HEXTE data is clearly a calibration issue with ISGRI, as explained in Sec. 7.4. Therefore data below 22 keV are not taken into account for ISGRI. The considered ISGRI energy range is therefore 22–500 keV.

## 8.2 Broken Power Law Fits

Wilms et al. (2006) have shown that broken power law fits offer a very good description for the Cyg X-1 spectra as observed with *RXTE* and allow to characterise a given spectrum without making any assumptions about the emission mechanism. This has been confirmed on a larger data set in Sec. 6.1.1. Additionally, the *INTEGRAL*/ISGRI data can be well described with an exponentially cut off power law model, see Sec. 7.4.3 and references therein.

Broken power law fits therefore offer a good first description of the X-ray spectral shape, which allows to characterize the data used in the context of the whole *RXTE* campaign as presented in Sec. 6.1 as well as assess the quality of the observations and their potential calibration problems. The fit function used here in the first step is therefore:

```
tbnew(1)*constant(Isis_Active_Dataset)*(bknpower(1)*highcut(1)+  
+egauss(1)+diskbb(1))
```

The main component modelling the continuum is a broken power law with a high energy cutoff. A multicolour disc and a Gaussian line are added, the Gaussian profile is centered at about 6.4 keV to model the Fe K $\alpha$  fluorescence line. Absorption is taken into account with the `tbnew` model. The individual model components are introduced in Sec. 5.3.

The low soft photon index ( $\Gamma_1 \approx 1.7$ , cf. Table 8.1) as well as the wide confidence intervals on the `diskbb` parameters indicated that the disc component is not necessary, as expected for the hard state. Therefore it was omitted from the fits. Additionally, the *INTEGRAL* data show the Tungsten instrumental background line as introduced in Sec. 7.4.1. The new fit functions therefore are:

```
tbnew(1)*constant(Isis_Active_Dataset)*(bknpower(1)*highcut(1)+  
+egauss(1))
```

for the *RXTE* data only and

```
tbnew(1)*constant(Isis_Active_Dataset)*(bknpower(1)*highcut(1)+  
+egauss(1))+calibline()
```

for the joint *RXTE* and *INTEGRAL* data. Hereby the constant factor inherent to the `calibline` function is set to the same value as the normalisation constant for the whole *INTEGRAL* data set. Fit results are presented in Table 8.1.

### **RXTE Only Spectrum**

A known problem already mentioned in Sec. 4.2.3 for the *RXTE* data is the calibration at low energies where the Xenon K $\alpha$  edge of the filling gas of the PCA detector needs to be taken into account (see also the discussion given in the appendix of Wilms et al., 2006). The lowest data bins are however decisive in constraining the absorption (equivalent Hydrogen number density as given by the  $N_{\text{H}}$  parameter) and with it the slope of the soft power law  $\Gamma_1$  as well as, if present, the disc black body component. Since the  $N_{\text{H}}$  value is not well constrained in the fits, confidence contours for this parameter and  $\Gamma_1$  were calculated (see Fig. 8.2, left panel). An increase in absorption can be compensated by a steeper photon index and vice versa. This correlation is non-physical (Suchy et al.,

instruments	$\chi^2_{\text{red}}$ (DOF)	$N_{\text{H}}$ [ $10^{22}\text{cm}^{-2}$ ]	$\Gamma_1$	$\Gamma_2$	$E_{\text{br}}$ [keV]
P + H	0.85 (182)	$1.5 \pm 0.6$	$1.69 \pm 0.03$	$1.48 \pm 0.02$	$9.8 \pm 0.5$
P + H + I	1.24 (232)	$1.4 \pm 0.5$	$1.68 \pm 0.03$	$1.47 \pm 0.02$	$10.0 \pm 0.6$
instruments	$E_{\text{cutoff}}$ [keV]	$E_{\text{fold}}$ [keV]	$C_{\text{HEXTE}}$	$C_{\text{ISGRI}}$	
P + H	$28 \pm 5$	$249 \pm 22$	$0.845 \pm 0.009$	–	
P + H + I	$31 \pm 4$	$183 \pm 7$	$0.850 \pm 0.009$	$1.028 \pm 0.013$	
instruments		$A_{\text{Tung}}$	$E_{0,\text{Tung}}$ [keV]	$\sigma_{\text{Tung}}$ [keV]	
P + H	–	–	–	–	
P + H + I	–	$-0.0030 \pm 0.0009$	$60 \pm 9$	$4 \pm 2$	

Table 8.1: Best fit parameters for the broken power law fits of PCA and HEXTE (both ObsID 93121-01-36-03) only and of combined spectra of PCA, HEXTE (both ObsID 93121-01-36-03) and ISGRI (revolution 742)

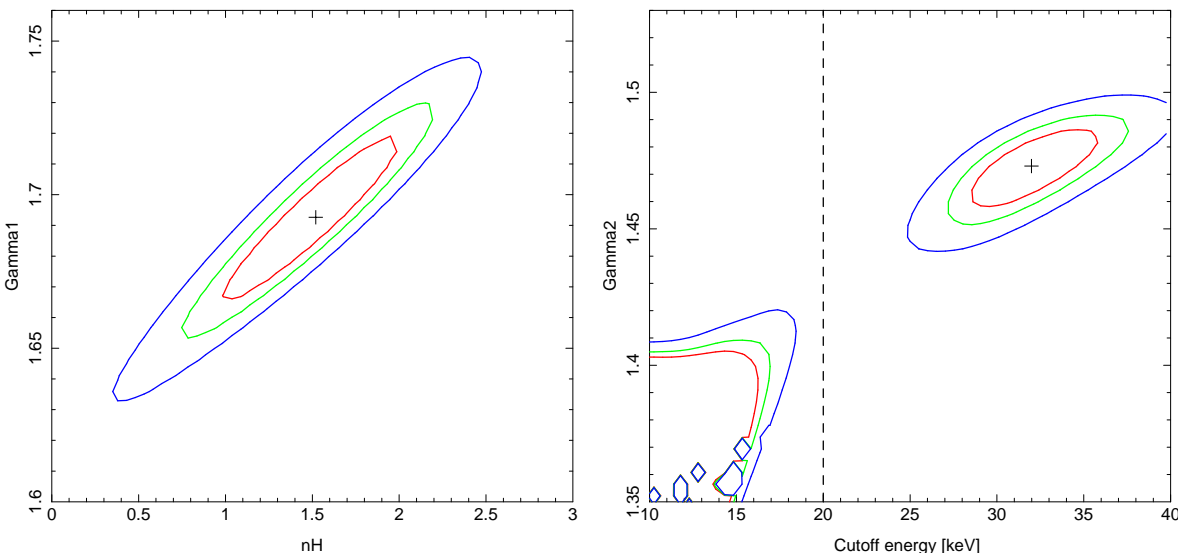


Figure 8.2: *Left panel:* Contour plot for the PCA + HEXTE broken power law fit for the Hydrogen number density  $N_{\text{H}}$  versus the soft photon index  $\Gamma_1$ .

*Right panel:* Contour plot for the PCA + HEXTE + ISGRI broken power law fit for the cutoff energy  $E_{\text{cutoff}}$  versus the hard Photon Index  $\Gamma_2$ . The dashed line indicates where a cut was introduced into parameter space to be able to achieve meaningful fits.  $1\sigma$  contours (68.3%) confidence contours are shown in red, 90% confidence contours in green and  $3\sigma$  contours (99%) in blue.

2008). The  $N_{\text{H}}$  value obtained is different than the often quoted value of  $0.6 \times 10^{22}\text{cm}^{-2}$ . Given the high variability of the absorption which causes the X-ray dips discussed by Hanke (2007), however, the fitted value of  $1.5 \times 10^{22}\text{cm}^{-2}$  is nevertheless still reasonable.

Figure 8.3 shows the placement of the here analysed observation in the context of the observations analysed by Wilms et al. (2006). The soft photon index here is  $\Gamma_1 = 1.69 \pm 0.03$ . For comparison, the values obtained for the 4 observations analysed by Nowak et al. (2010) are 1.63–1.71 and Wilms et al. (2006) obtain values of 1.65–3.4

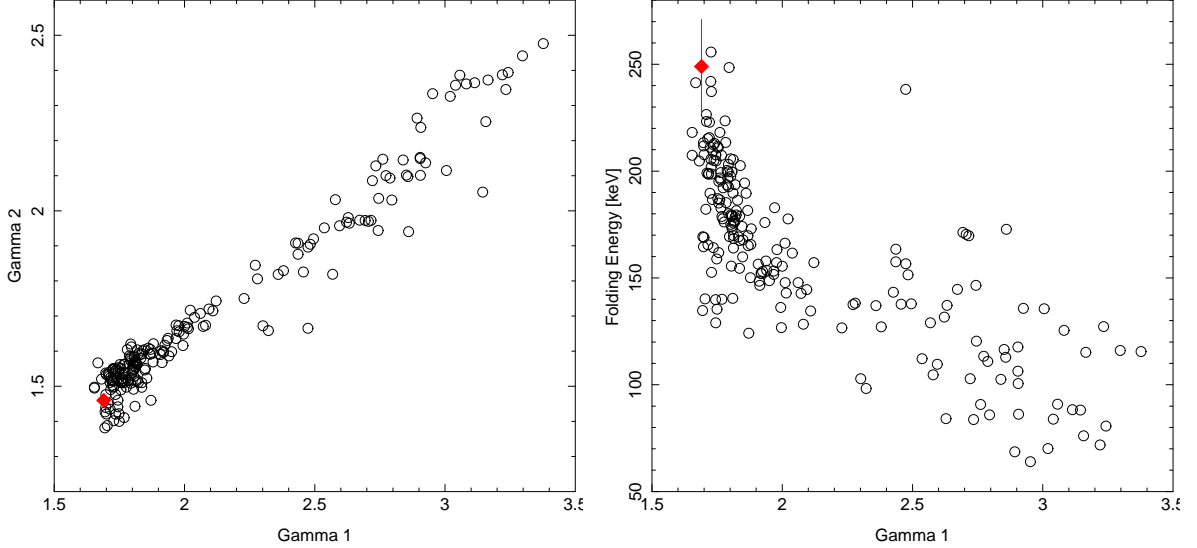


Figure 8.3: Correlation of the soft ( $\Gamma_1$ ) and hard ( $\Gamma_2$ ) photon indices and (left panel) and soft photon index  $\Gamma_1$  and the folding energy  $E_{\text{fold}}$  (right panel) as obtained by Wilms et al. (2006) for broken power law fits (black circles) and the fit parameters obtained for the equivalent fits of *RXTE* ObsID 93121-01-36-03 (red diamond).

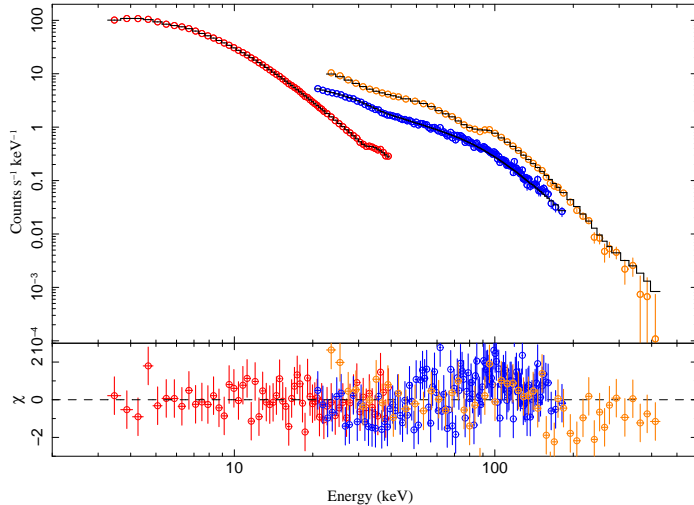


Figure 8.4: Broken power law fit to combined PCA, HEXTE (both ObsID 93121-01-36-03) and ISGRI (revolution 742) spectra. PCA is shown in red, HEXTE in blue and ISGRI in brown.

in their analysis of about 200 observations made during the monitoring campaign from 1996 to 2004. This means that ObsID 93121-01-36-03 belongs to the hardest observations of Cyg X-1 during the *RXTE* monitoring. This notion is strengthened by the high folding energy  $E_{\text{fold}}$ , which also follows the correlation obtained by Wilms et al. (2006) and in Sec. 6.1.2. This is especially remarkable, because Wilms et al. (2006) use HEXTE data up to 120 keV only. Nowak et al. (2010), however, point out that while such very hard states are indeed not yet well studied for Cyg X-1, the overall variability of the parameters in Cyg X-1, e.g., that of the 2–100 keV flux, which is spanning only a factor of about 2, or of the cutoff energies, are not big when compared to other microquasars.

### Joint *RXTE* and *INTEGRAL* Spectrum

Figure 8.4 shows the best fit for the combined *RXTE* and *INTEGRAL* spectra. Interesting is here the behaviour of the residuals: between 100 and 200 keV the model is

slightly underestimating the flux from both HEXTE and ISGRI. Above 200 keV the flux from ISGRI is slightly overestimated. The reason might lie in the uncertainties of the calibration and/or in the fact, that the ISGRI data are averaged over a whole revolution to achieve a reasonable signal to noise ratio. Additionally, due to the rapidly declining sensitivity of ISGRI above 100–150 keV, there are uncertainties in the determination of the slope even for the Crab and ISGRI might slightly underestimate the high energy fluxes (Lubiński, 2009). It might however also be an indication that an cutoff power law is not an adequate description for these high energies, where – assuming a Comptonization origin of the radiation – QED effects and the Klein-Nishina cross section become important. The fit is however still very good, cf. Table 8.1.

Note the peculiar behaviour of the cutoff energy  $E_{\text{cutoff}}$  as apparent from the right panel of Fig. 8.2: there are minima in the  $\chi^2$  space with the cutoff energy of  $E_{\text{cutoff}} \approx 10 - 15$  keV.  $\Gamma_2$  is very low ( $\approx 1.35$ ) in these models, i.e. the cutoff energy is coincident with the break energy of the power law and the higher  $\Gamma_2$  compensates for the following roll off. Note also how the confidence contours are well behaved for  $E_{\text{cutoff}} \approx 30$  keV and how they enclose a very broad region in case of too low cutoff energies. The models with  $E_{\text{cutoff}} \approx 10 - 15$  keV are excluded from the fits by introducing a minimum for the cutoff energy at 20 keV.

As expected, the changes in the parameters, which are determined mainly by the low energy part of the spectrum ( $\Gamma_1$ ,  $N_{\text{H}}$ ,  $E_{\text{break}}$ ), are small and within their mutual errors between the *RXTE* only and the joint *RXTE* and *INTEGRAL* fits. There is however a very significant change in the folding energy, implying that the spectrum in the 200–500 keV range cannot be well described by the best fit in the 3–200 keV range, as already mentioned in the discussion above. This means that already the purely empirical model indicates that the additional high energy data allow to better understand and constrain the models for the spectra of the source and might introduce changes into parameters derived for a smaller energy range.

Although the iron K $\alpha$  line is required both in the *RXTE* and the joint *RXTE* and *INTEGRAL* fits, the width of the line cannot be well constrained due to the poor spectral resolution. Therefore no further conclusions can be drawn from a single *RXTE* spectrum regarding the line except for the mere fact of its existence (for a discussion for what can be learned from a statistical approach for a multitude of spectra see Wilms et al., 2006).

### 8.3 Jet Fits

The broken power law fits have shown that the presented joint observation belongs to the hardest observations of Cyg X-1 made to date. Such hard observations are of high interest for physically motivated models, specifically jet models, as jets are assumed to be especially active in the hard state (see Sec. 2.4). Note that although they are also physically motivated, Comptonization models, as introduced with the `comptt`-models for *RXTE* data in Sec. 6.1.3 and for *INTEGRAL* data in Sec. 7.4.3, are not able to describe the joint X-ray and radio data without introducing further model components.

A jet model has been used to describe the spectra of Cyg X-1 by Markoff et al. (2005) (*RXTE* and *Ryle* observations) and Nowak et al. (2010) (*RXTE*, *Chandra* and *Suzaku* observations and estimated fluxes from *Ryle*). The author is not aware of any publications of jet fits to Cyg X-1 data over 300 keV (Nowak et al. (2010) use *Suzaku/GSO* data up to 300 keV), where the effect of the high energy cutoff becomes

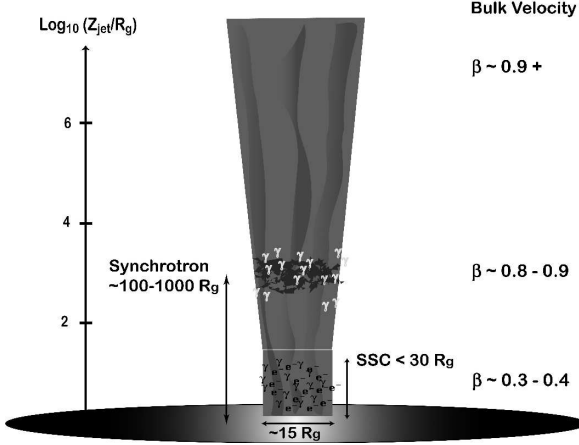


Figure 8.5: Sketched geometry of the jet model by Markoff et al. (2005). Synchrotron emission is produced throughout the jet. The accretion disc gives rise to thermal emission and provides seed photons for the Comptonization at the base of the jet, where also synchrotron self-Compton process takes place. The jet expands freely above the nozzle.

dominant and defines the shape of the spectrum. ISGRI data should allow to constrain the behaviour of the model at high energies and therefore the exact shape of the Synchrotron Selfcompton/External Compton ‘hump’ (dubbed shortly Comptonization hump from here on). As the jet model shows a high degree of degeneracy where different parameter sets allow to fit data in a certain energy range (e.g. the one covered by the two *RXTE* instruments) equally well, the extension to higher energies should allow to break the degeneracy for some parameters and therefore to better determine the jet parameters.

### 8.3.1 ‘agnjet’-Model

The *agnjet* introduced by Markoff et al. (2005) for BHs is the only existing physical model describing the broadband spectrum, i.e., the spectrum from the radio to the X-rays, which is exact enough to allow for statistical fits. In this model, the radio and the soft X-ray ranges are dominated by the synchrotron emission throughout the jet while the hard X-rays originate mainly at the jet base, where they are produced by inverse Compton scattering. Markoff et al. (2005) discuss their model in detail as do Maitra et al. (2009) for their extension of the basic model which contains an irradiated accretion disc. The model used of this work is the model of Maitra et al. (2009). Although possibility to have an irradiated disc, which is offered by this model, is not used, the model contains computational improvements – an important issue since the model is highly CPU intensive. As the *agnjet*-model contains a multitude of free parameters, only the main components used can be presented and the most important points for understanding the model discussed here.

The model is based on five main physical assumptions:

- the total power of the jet scales with  $\dot{M}c^2$ , i.e. the total accretion power.
- the expansion of the jet is free and the acceleration is weak.
- the jet consists of cold protons which account for the bulk of the kinetic energy and hot, radiating leptons.
- particles are accelerated into a power law distribution.
- the power law distribution is maintained along the jet.

A sketch of the geometry of this model is presented in Fig. 8.5. The base of the jet is formed by a small nozzle region of constant radius  $r_0$  and height  $h_0$ . Immediately beyond this region, the jet expands to the sides and is weakly accelerated along the resulting pressure gradient, so that the velocity is roughly logarithmically dependent on

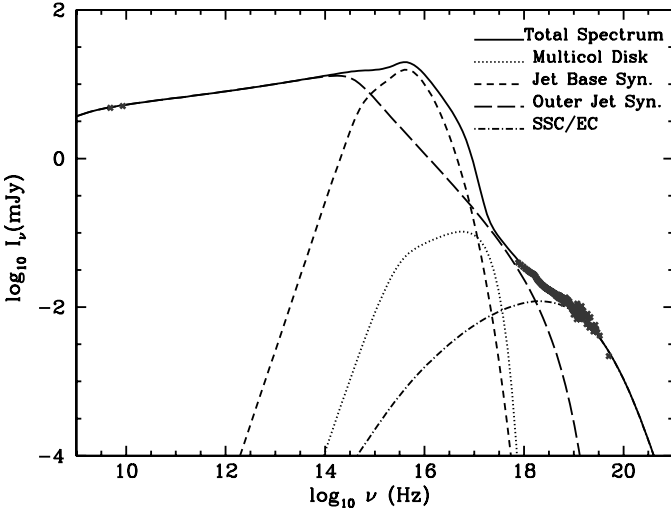


Figure 8.6: Example jet and multicolour black body only fit to data of GX 339-4  
(Markoff et al., 2005, Fig. 1)

the distance  $Z_{\text{Jet}}$ . After this region of more rapid acceleration, the velocity saturates at Lorentz factors  $\Gamma_{\text{J}} \gtrsim 2 - 3$ . Note that the radius of the jet base,  $r_0$ , determines the radius of the jet as a function of the distance to the jet base.

Besides  $r_0$  and  $h_0$ , i.e., the dimensions of the jet base, further main parameters determine the properties of the jet. The input jet power,  $N_{\text{J}}$ , acts as a normalisation parameter. It defines the power input into the particles and the magnetic field at the jet base and is expressed as a fraction of the Eddington luminosity (here defined as  $L_{\text{edd}} = 1.25 \times 10^{38} M_{\text{BH}}/M_{\odot}$  erg s $^{-1}$ , Markoff et al., 2005). Note that a full understanding of the physics of how jets are energised is still lacking.  $T_e$  is the electron temperature of the relativistic thermal plasma entering the jet base. The equipartition factor  $k$  describes the ratio of magnetic to particle energy density.  $z_{\text{acc}}$  gives the location of the point within the jet beyond which the leptons are accelerated into the power law distribution.  $p_{\text{spec}}$  defines the slope of this power law component of the electron energy distribution in this non-thermal tail, with the number of electron with the energy  $E$  being  $N(E) = E^{-p_{\text{spec}}}$ .  $r_{\text{in}}$  and  $T_{\text{in}}$  describe the inner radius and the temperature at the inner radius of the accretion disc. These parameters are not tied, i.e., when increasing the inner disc radius  $r_{\text{in}}$  ‘by hand’ one needs to adjust the temperature  $T_{\text{in}}$  accordingly to achieve the desired effect of diminishing the influence of the disc on the X-ray spectrum. The parameter  $f_{\text{sc}}$  is a measure for the acceleration. As Markoff et al. (2005) have, however, pointed out this parameter does not have a direct physical interpretation, as the initially supposed acceleration mechanism, diffusive Fermi acceleration, seems not to be valid and a full understanding of the acceleration mechanism in the jets is lacking yet.

The model parameters  $m_{\text{BH}}$  (mass of the black hole) and  $i$  (the inclination) of the source have to be frozen at values known for a certain source and are not supposed to be fitted when using the `agnjet` model (S. Markoff, priv. comm).<sup>1</sup>

Figure 8.6 illustrates the contribution of the jet components and accretion disc only. The synchrotron emission contributes strongly to the soft X-ray regime while the hard X-rays are dominated by Comptonization. It is also evident that additional

<sup>1</sup>An instructive animated overview over the effect of the changes in single parameters of the `agnjet`-model on the whole model spectrum can be found on the homepage of D. Maitra under <http://www.astro.lsa.umich.edu/~dmaitra/models/>. In order to understand this complex model and its multitude of parameters it is strongly advised to take a look at the animations before attempting own fits with the `agnjet`-model.

measurements in the optical and infrared wavebands would allow to further constrain the model (see Maitra et al., 2009, for such observations of the transient sources GX 339-4 and XTE J1118+480).

In the presence of a jet as described by this model, reflection will play a major role in shaping the spectrum: a part of the radiation from the jet impacts on the cooler material of the accretion disc and leads to the presence of reflection features, namely a reflection hump and fluorescent line emission. These spectral components need to be modelled separately as it has been shown by Markoff & Nowak (2004) that a direct calculation of the reflection for the jet model is too complicated to allow for spectral fits. Markoff & Nowak (2004) have also shown that when the hard X-rays are dominated by Compton processes (which take place close to the very base of the jet) a reflection fraction of up to 20% is possible. This result allows for an additional consistency check on the fit parameters.

### 8.3.2 Fitting Method and Start Parameters

Especially for complex, physical models the actual fitting has to be preceeded by careful considerations of the fit functions and the fitting strategy. They are discussed in the following for the `agnjet` model introduced above.

#### Fit Function

Already the simple broken power law fits in Sec. 8.2 (and in Sec. 6.1.2 for *RXTE* data only) have shown, that a proper description of the spectrum of Cyg X-1 requires interstellar absorption and a Gaussian component taking into account the iron K $\alpha$  line at about  $\sim 6.4$  keV. Fe K $\alpha$  is a signature of reflection, which has therefore also to be incorporated into a physical model. As discussed above, the `agnjet` model does not intrinsically model reflection, which has therefore to be taken into account directly by an appropriate extra model. The fit function for *RXTE* data only is therefore:

```
reflect(1,(agnjet(1)+egauss(1)))*constant(Isis_Active_Dataset)*
*tbnew(1)
```

The main model component is `agnjet`, which defines the continuum. The iron line is modelled by a Gaussian component and both components are then convolved with the reflection model `reflect`. `tbnew` models the interstellar absorption and the constant takes the different normalisations of the detectors into account. The individual model components are introduced in Sec. 5.3 and Sec. 8.3.1.

To be able to use the *INTEGRAL* data in spite of the problems with the Tungsten line, the model is modified to

```
reflect(1,(agnjet(1)+egauss(1)))*constant(Isis_Active_Dataset)*
*tbnew(1)+calibline()
```

The values of the `calibline` function are frozen to those obtained in the broken power law fits as listed in Table 8.1. Because of the complexity of the jet fits, fitting the line would have resulted in a prohibitive increase in the computational time, especially for the fits presented here, which are mainly meant as a rough exploration of the parameter space and will already take hours to days on an usual CPU, although a low tolerance resolution is set and a fast (though more prone to getting stuck in local minima) fitting algorithm is chosen.

## Fitting Strategy

Since fits with a complicated model such as the `agnjet` model can easily get stuck in false local minima, it is necessary to start the fits already with a good reduced  $\chi^2$  value and with a reasonable parameter set. The model has manually to be brought in a good agreement with data ( $\chi^2_{\text{red}} \approx 3 - 5$ ), only then the model will converge in a reasonable time and at reasonable values (Markoff et al., 2005).

The behaviour of the model when fitting *RXTE* only data is well understood and the data also tend to dominate the  $\chi^2$  because of the high number of data bins and low errors compared to the *INTEGRAL* data. Additionally, the parameters of the fits achieved below 200 keV allow a comparison to the results in the literature. Therefore, both *RXTE* only and joint *RXTE* and *INTEGRAL* fits were carried out.

The model is very sensitive to the radio part of the spectrum, as it strongly influences the parameters of the synchrotron component. Because only few or, as in this case, just one data point in the radio waveband are usually present and these with large uncertainties (as opposed to 100–200 data points in the X-ray range), the fitting strategy sometimes includes an artificial reduction of the radio errors for the preliminary fits to increase the significance of the radio measurement for the fit. Here this strategy was not employed as the radio measurement was not simultaneous with the *RXTE* data.

A new version of the `agnjet` model should be available soon (summer 2010, S. Markoff, priv.comm.). It will address some computational issues and the physics of the high electron temperatures. The current version of the code will sometimes get stuck in unphysical areas of the parameter space, where, e.g., all the particles are cooled down and no emission is emerging. The high electron temperatures should result in pair production prevailing pair annihilation, an effect which is not yet incorporated into the code and might have a strong effect on the high energy part especially of the Comptonization hump (Maitra et al., 2009; Nowak et al., 2010). Maitra et al. (2009) quantify the time costs of the model, which are high even when using a big cluster. Such a cluster was not at disposal for this work. Besides, even with a lot of CPU time available, a careful physically motivated choice of start parameters is important, which can only be achieved if the parameter space is well understood.

Given the new model almost in reach and the fact, that the *INTEGRAL* data are awaiting a better calibration, it was decided to use the present model for a rough exploration of the parameter space and perform the error calculations on the parameters when the newer and better versions of both model and data become available. Note, however, that such error calculations for a model as complicated as `agnjet` do often or almost always lead to the detection of better  $\chi^2$  minima, i.e., when comparing the results of this analysis to those in literature generally a higher  $\chi^2_{\text{red}}$  and more structure in the residuals are expected for the results of this analysis.

## Fixed Parameters

Not all of the multitude of the parameters of the `agnjet` model are supposed or make sense to be fitted, especially taking into account that certain properties of the source (e.g. the approximate mass of the black hole) are either known or can be more reliably determined by other measurements. Additionally, Markoff et al. (2005) and Nowak et al. (2010) have shown that the model is not sensitive to changes in certain parameters for Cyg X-1 while other parameters are strongly correlated.

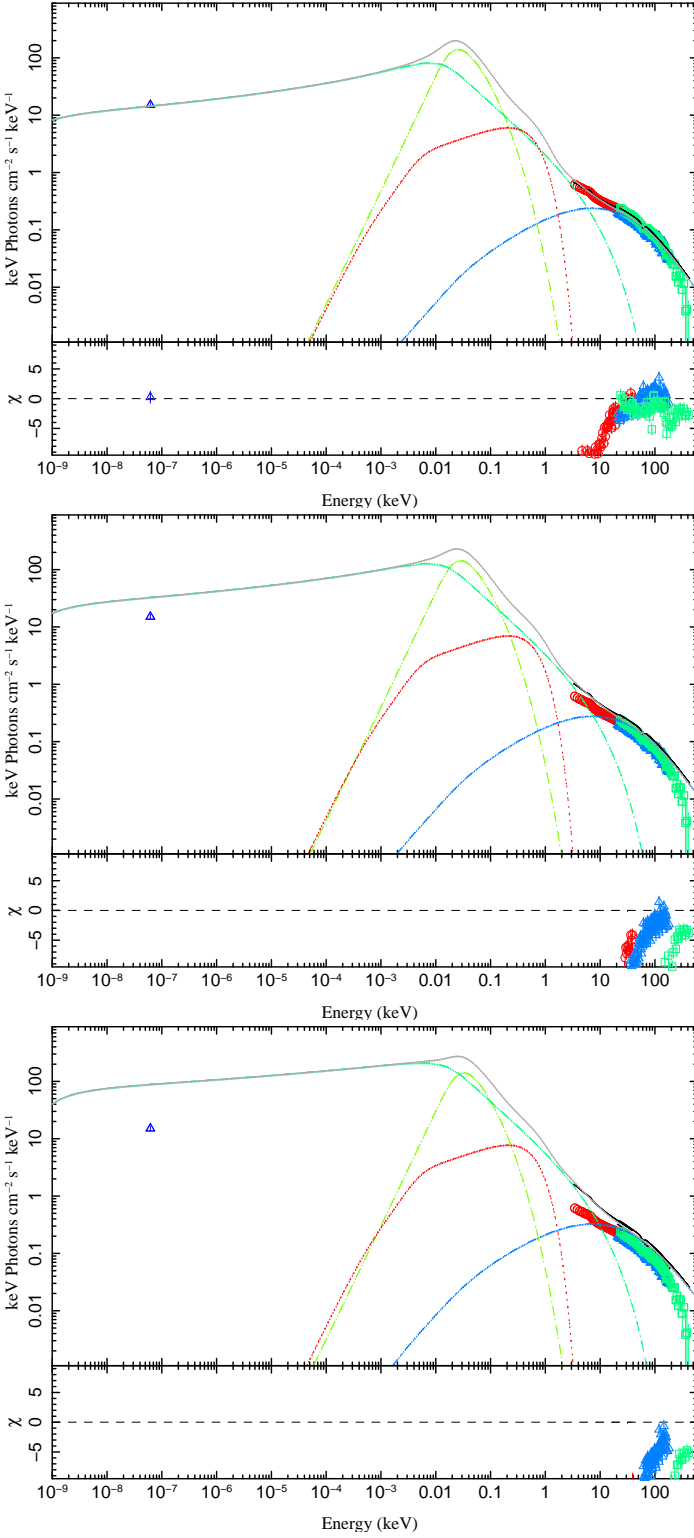


Figure 8.7: Effects of changes of the inclination  $i$  on the model for the high electron temperature best fit model as presented in Sec. 8.3.3. For the uppermost panel the inclination was set to  $45^\circ$ , for the middle panel to  $35^\circ$  and for the lower panel to  $25^\circ$ . For an inclination of  $47^\circ$  see Fig. 8.12.

Parameters which are best determined from other measurements are the black hole mass, the distance and the inclination  $i$ , which are here frozen to the values used by Markoff et al. (2005, see there for respective references):  $10M_\odot$ , 2.5 kpc and  $47^\circ$ , respectively.

Note especially the value for the inclination. Nowak et al. (2010) use an inclination of  $35^\circ$  which is in a better agreement with the current knowledge in the literature (see Sec. 2.5). This, however, does not take into account the known  $\sim 150$  day period

in the lightcurves of Cyg X-1 which might be due to the precession of the disc/jet system (Brocksopp et al., 1999a; Pooley et al., 1999; Lachowicz et al., 2006; Ibragimov et al., 2007; Poutanen et al., 2008) and therefore obsoletes any fixed inclination value independent of the precession phase. The inclination has a major influence on the spectrum as can be seen in Fig. 8.7. Inclination has a strong effect on the jet beaming, as for the higher inclination the fast parts of the jet are beamed more and more out of the line of sight, i.e., the spectrum becomes more inverted and the overall measured flux decreases. However, both effects can be also achieved by changing other parameters and the degeneracy between inclination – which can in theory be well constrained from other observations – and other internal parameters that are inherent to the jet is therefore high. It should therefore *not* be considered a fitting parameter and is kept fixed (S. Markoff, priv.comm.).

The height  $h_0$  of the base of the jet is tied to the radius of the jet base by  $h_0 = 1.5r_0$  as also done by Nowak et al. (2010). Markoff et al. (2005), who tried to fit all the parameters in their initial exploration of the parameter space, have shown that the fits are not sensitive to this parameter. Fits with  $h_0$  as a free parameter were tried without any significant improvements over fits with  $h_0 = 1.5r_0$  or major changes in the parameter itself.

Maitra et al. (2009) have pointed out that, while their fits for XTE J1118+105 and GX 339–4 require a high fraction of non-thermal electrons, they are not very sensitive to the exact value, and have therefore fixed the parameter to a value of 0.75. Here, the same approach is undertaken. Fitting this parameter did not significantly improve the fit nor did indeed the parameter change much itself or did manual changes of the parameter introduce noticeable improvements.

The parameters defining the inner edge of the accretion disc,  $r_{\text{in}}$  and  $T_{\text{in}}$ , have been left free. The fits are however not very sensitive to them, which is to be expected because the disc temperature lies outside of the energy range covered by the instruments used and because the analysed observation is very hard. As had been shown in Sec. 8.2, broken power law fits do not require a disc component at all, i.e., the disc is too weak to be detected.

The abundances for the reflection component were set to those of Wilms et al. (2000) and the inclination to the same value as the inclination of the jet.

### 8.3.3 Fit Results

#### Low Electron Temperature Solution

Prompted by the above presented concern that the high electron temperature at the base of the jet,  $T_e$ , might pose a problem for the model, a fit with  $T_e < 3 \times 10^{10}$  K was first attempted for the *RXTE* data. The start parameters for this fits were provided by M. Böck (priv.comm.). Not only the temperature of the electrons, but also the slope of the power law contribution needs to be constrained:  $2 \leq p_{\text{spec}} \leq 3$ . The values of  $p_{\text{spec}}$  in the literature are well within these limits (Markoff et al., 2005; Nowak et al., 2010), but this is only true for higher values of the electron temperature obtained for these fits. Fig. 8.8 shows the best fit to *RXTE* data using this constrain. An overview of the fit parameters is given in Table 8.2. The reduced  $\chi^2$  of  $\sim 1.4$  indicates a good fit – especially when compared to the best fits of Markoff et al. (2005), who explored the parameter space in more detail but nevertheless get one of their bestfits in the same quality. An inclination of  $i = 40^\circ$  was used for this fit, as attempts to achieve a good

Para- meter	[unit]	Model with $T_e \leq 3 \times 10^{10}$		Model with $T_e \leq 3 \times 10^{10}$ high $k$		Model with free $T_e$	
		P + H	P + H + I	P + H	P + H + I	P + H	P + H + I
$\chi^2$		260	691	253	370	171	399
DOF		180	234	180	234	180	234
$N_H$	$[10^{22} \text{cm}^{-2}]$	3.8	3.1	3.3	3.3	2.6	2.3
$N_j$	$[10^{-2} L_{\text{edd}}]$	4.27	4.19	2.7	2.69	3.94	3.73
$r_0$	$[R_g]$	4.52	4.54	5.79	5.79	6.39	6.13
$T_e$	$[10^{10} \text{K}]$	2.59	2.59	3.0 **	3.0 **	3.90	3.75
$z_{\text{acc}}$	$[R_g]$	4.34	4.34	14	14	10.3	10.3
$p_{\text{spec}}$		2.96	2.96	2.48	2.48	2.59	2.58
$f_{\text{sc}}$	$[10^{-5}]$	6.7	6.4	4.4	4.4	35	40
$k$		3.10	3.35	20.4	20.4	2.11	2.57
$\Omega/2\pi$		0.11	0.16	0.0 ***	0.0 ***	0.045	0.10
$r_{\text{in}}$	$[R_g]$	7	2	5.22	7.0	7.0	50 **
$T_{\text{in}}$	$[10^6 \text{K}]$	3.7	2.8	3.3	3.3	2.6	1.0 ***
$C_{\text{HEXTE}}$		0.876	0.865	0.849	0.849	0.839	0.849
$C_{\text{ISGRI}}$		—	1.053	—	1.042	—	1.031
$i^*$	$[^\circ]$	40 *	40 *	47 *	47 *	47 *	47 *

Table 8.2: Best-fitting parameters for the Jet model

\* The inclination  $i$  was not a fit parameter, but fixed at these values. Attempts to achieve a good  $\chi^2$  with  $i = 47^\circ$  for  $T_e \leq 3 \times 10^{10}$  and low  $k$  were not successful

\*\* Parameter at upper limit.

\*\*\* Parameter at lower limit.

$\chi^2$  with  $i = 47^\circ$  were not successful.

However, a more detailed look at both the parameters and the residuals reveal possible problems of this best fit model: residuals of HEXTE data show overall a slight curvature, a possible indication that the form of the Comptonization hump, which dominates the jet in this energy range does not yet describe the data well. The value of the multiplicative constant describing the normalisation differences between HEXTE and PCA ( $C_{\text{HEXTE,Jet}} = 0.876$ ) is significantly higher than in the case of the broken power law fit ( $C_{\text{HEXTE,bknpl}} = 0.850 \pm 0.009$ ), indicating that the constant compensates for the missing curvature of the model.

Note additionally the very small values of  $r_0$  and  $z_{\text{acc}}$  of  $\sim 4.5 R_g$  for both and the high value of  $N_H$  of  $3.8 \times 10^{22} \text{cm}^{-2}$ . The latter does not agree well with the values obtained in the broken power law fits and lies well outside the confidence values which were presented in Fig. 8.3.

Important to note is that such detailed considerations are only possible for statistical fits. ‘By eye’ comparisons as employed, e.g., by Zhang et al. (2010) for their advection dominated accretion flow plus jet model, do not allow for such a detailed comparison between data and model. This approach for comparing a complex physical model of the jets to the data does not achieve even the goodness of those models used as start parameters here (the automated fits are started once  $\chi^2_{\text{red}} \approx 3 - 5$  is reached by hand).

As a next step, the *INTEGRAL*/ISGRI were included and the fit repeated. The best fit spectra are presented in Fig. 8.9, the parameters are again listed in Table 8.2. This solution clearly does not describe the data well: the reduced  $\chi^2$  is in the order of

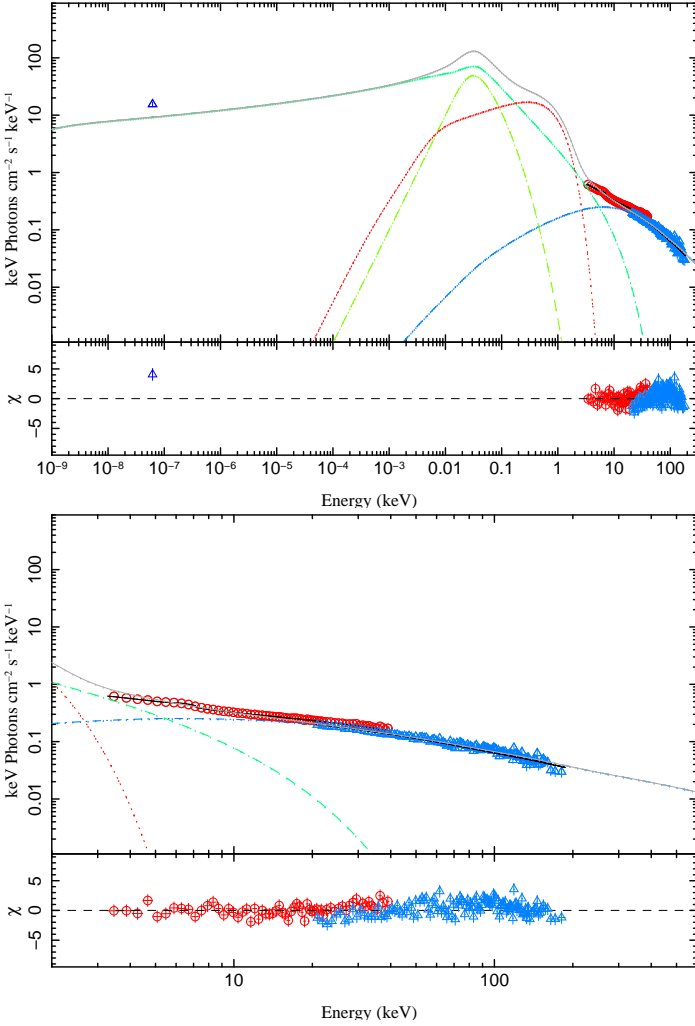


Figure 8.8: Best fit for  $T_e < 3 \times 10^{10}$  K for RXTE data only. PCA data are shown by red circles, HEXTE data by light blue triangles and the Ryle data point by the dark blue triangle. Jet components are indicated as in Fig. 8.6. The lower panel is a close-up of the X-ray portion of the spectrum.

3. Note that the ISGRI residuals show the same curved shape as the HEXTE residuals discussed for the RXTE only fit. The residuals further show high discrepancies between model and data at high energies: the model fails to describe the exponential cutoff in the data.

### Low Electron Temperature, Strongly Magnetically Dominated Solution

Markoff et al. (2005) point out that while they mainly explore solutions where the jet is close to equipartition (this assumption is strengthened by the weak accelerations required by the observations), reasonable minima with the ratio between the magnetic energy and the energy of the radiating leptons  $k \gg 1$ , i.e., solutions for strongly magnetically dominated jets, are possible. Although all models presented in the literature except for a single model of those presented by Nowak et al. (2010), prefer a magnetically dominated jet with  $k \approx 2\text{--}3$ , no solutions with a strong magnetic dominance were looked at yet for Cyg X-1. In the attempt to find a better solution for  $T_e < 3 \times 10^{10}$  K a strongly magnetically dominant model was found. The parameters are listed in Table 8.2. Since the solutions for RXTE only and for combined RXTE and INTEGRAL data do not show any larger differences in the model parameters, only the joint spectrum is shown here, namely in Fig. 8.10. The goodness of the RXTE only fit is slightly better ( $\chi^2 = 253$  instead of 260 for 180 degrees of freedom), but the joint RXTE and INTEGRAL fit is with  $\chi_{\text{red}}^2 \approx 1.6$  significantly better than the solution with  $k \approx 3$ .

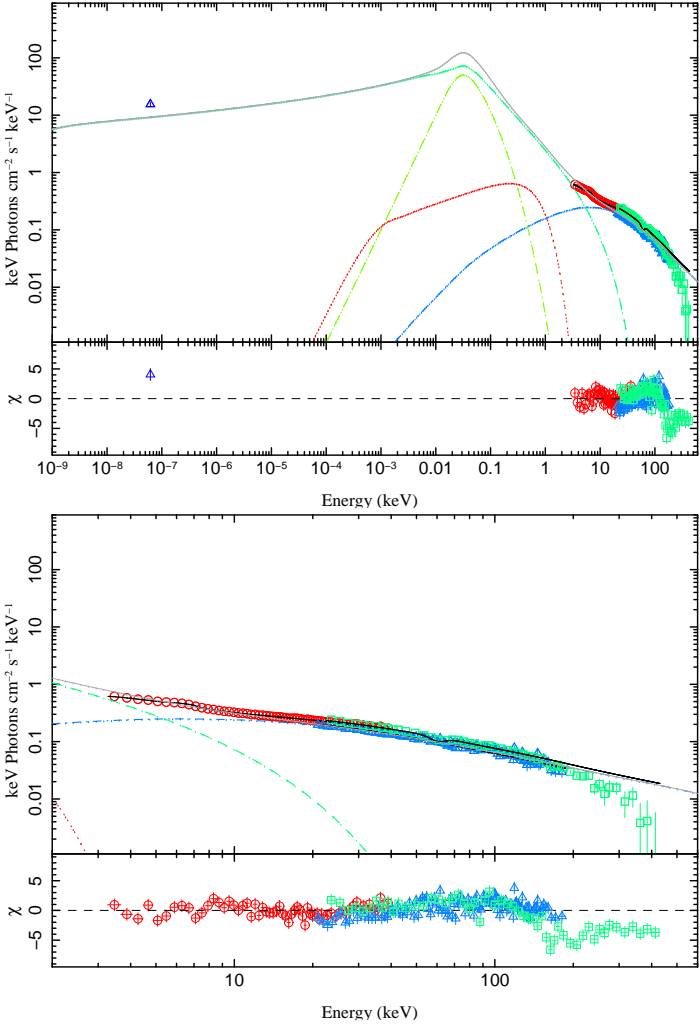


Figure 8.9: Best fit for  $T_e < 3 \times 10^{10}$  K for RXTE and INTEGRAL data. PCA data are shown by red circles, HEXTE data by light blue triangles and the Ryle data point by the dark blue triangle. Jet components are indicated as in Fig. 8.6. The lower panel is a close-up of the X-ray portion of the spectrum. INTEGRAL/ISGRI data and residuals shown by green squares.

Nevertheless, some problems are evident: The reflection component does not contribute to the spectrum, as the reflection fraction is  $\Omega/2\pi = 0.0$ . On the other hand, the iron K $\alpha$  line, itself a reflection feature, is present in the spectra, i.e., reflection should play a role. The electron temperature  $T_e$  runs against the hard limit of  $3.0 \times 10^{10}$  K, implying that a better fit might be found for higher temperatures. It is unclear how this would influence the other parameters and if, e.g., the fit would converge towards the later discussed high electron temperature solution or a different minimum. Note also how the high equipartition  $k$  implies a much lower jet input power  $N_j$  while the synchrotron radiation from the jet (light green dashed line defining the ‘hump’ of the overall spectrum) now contributes to the overall spectrum at higher energies.

Although generally in better agreement with the data than in the previous solution, the residuals at high energies still show a peculiar wave structure, which is especially clearly seen on the upper plot of Fig. 8.10, showing the full broadband spectrum. The flux at the high energies above 200 keV is still overestimated, though less so than in the previous model with  $k \approx 3$ .

## High Electron Temperature Solution

Since the low temperature solutions are not capable to describe the spectral break seen in the INTEGRAL/ISGRI data at energies of about 200 keV, modelling the data with higher allowed electron temperature is attempted. Note that these are temperatures

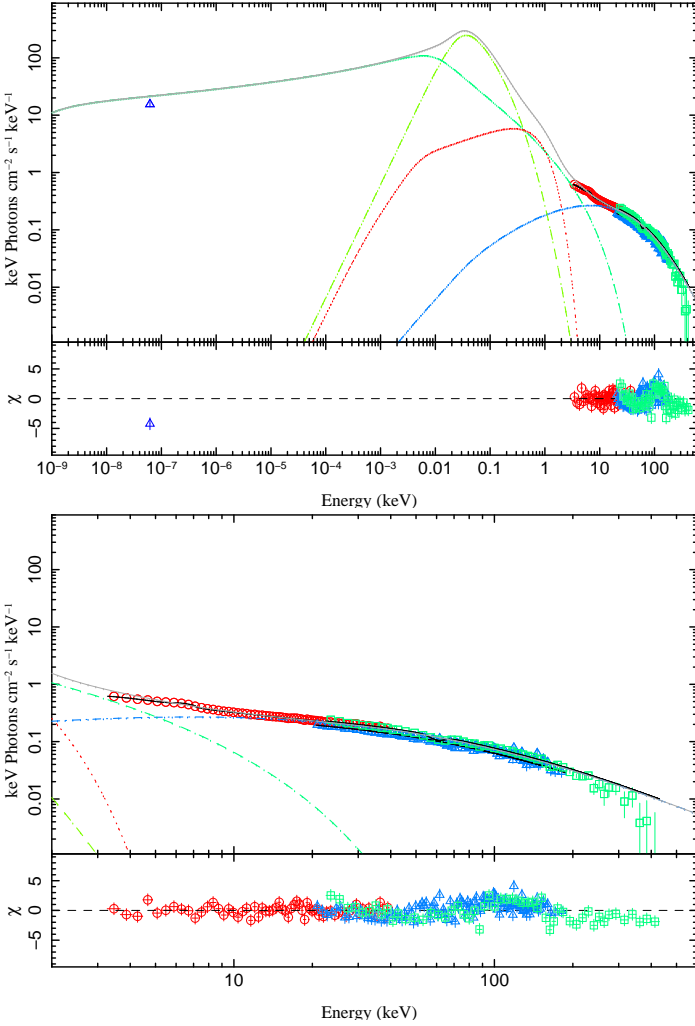


Figure 8.10: Best fit for  $T_e < 3 \times 10^{10}$  K and high  $k$  (strongly magnetically dominated jet) for *RXTE* and *INTEGRAL* data. Representation of data and model components are as explained in Fig. 8.8.

where the pair production becomes important (Nowak et al., 2010), which is not yet included into the model. Although no fundamental changes are expected, the shape of the high energy component is anticipated to change. The good description the old version of the model provided so far for *RXTE* data fitted with  $T_e > 3 \times 10^{10}$  justifies the use of this model on a preliminary basis.

Fits with the current version of the model are presented in Fig. 8.11 for the *RXTE* data only and in Fig. 8.12 for the *RXTE* and *INTEGRAL* data. The parameters of the fits can be found in the right column of Table 8.2. Interestingly, here the best fit parameters for *RXTE* only and for the combined *RXTE* and *INTEGRAL* spectra again differ significantly. For *RXTE* only data a fit with  $\chi_{\text{red}}^2 \approx 0.95$  is achieved, i.e., the best fit presented so far. The residuals do not show any discernible structure.

The Hydrogen number density is with  $N_H = 2.6 \times 10^{22} \text{ cm}^{-2}$  still higher than in the broken power law fits. The normalisation  $C_{\text{HEXTE}}$  is lower than in any other jet fits and in the broken power law fit, but well within the error bars of the broken power law solution. The electron temperature  $T_e$  rises to  $3.9 \times 10^{10}$  K – a value in good agreement with those presented by Markoff et al. (2005) and Nowak et al. (2010). Note that it does not run against the hard set boundary of  $4.0 \times 10^{10}$  K here as opposed to the low electron temperature, strong magnetically dominated solution with its hard boundary of  $3.0 \times 10^{10}$  K. All parameters lie well within the ranges presented so far by Markoff et al. (2005) and Nowak et al. (2010) even though the latter use a different inclination of  $i = 35^\circ$ .

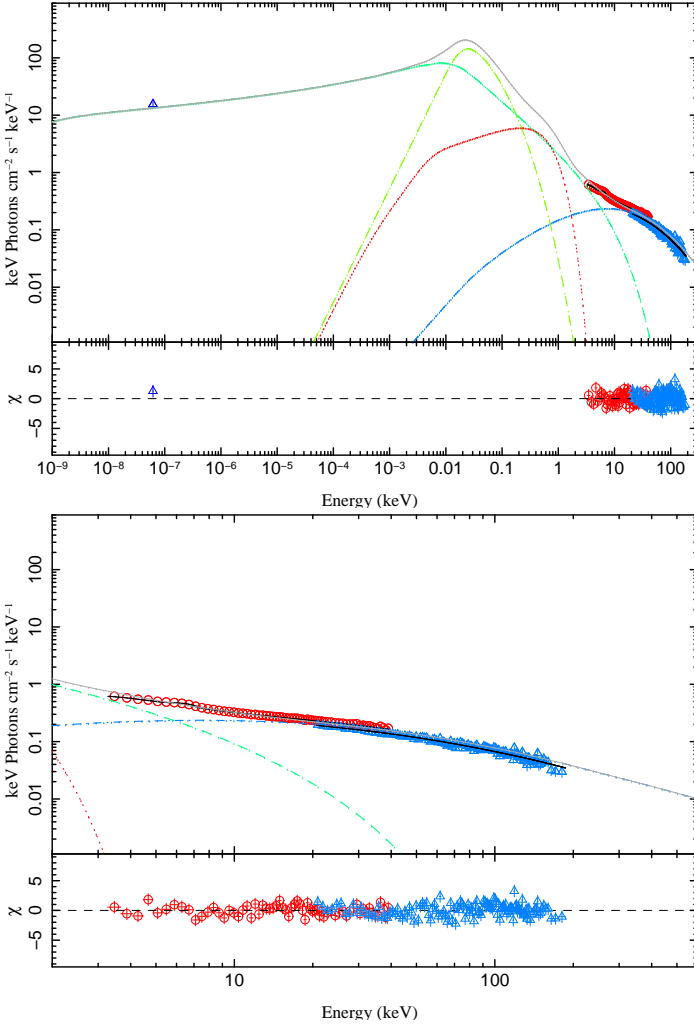


Figure 8.11: Best fit for  $T_e$  free for *RXTE* data only. Representation of data and model components are as explained in Fig. 8.8.

Adding the *INTEGRAL* data to the fits and fitting only the ISGRI normalisation (with additionally modelling the Tungsten instrumental background line, of course), however, clearly shows that this parameter set is not able to describe the high energy data well, as the best achieved  $\chi^2_{\text{red}}$  is 3.0. Therefore, the whole fit is repeated for the joint spectrum.

The best fit for joint data still does not describe the high energy cutoff well (see Fig. 8.12), but as this is the part of the spectrum where changes due to the update of the model are expected and the deviations are less than in the low temperature solution, the overall fit with  $\chi^2_{\text{red}} = 1.7$  is accepted as a good solution. Note that the model describes *RXTE* data seen individually with a  $\chi^2_{\text{red}}$  of 1.2 (this is better than any value obtained for  $T_e < 3 \times 10^{10}$  K), i.e., the deviations between the model and the data are indeed dominated by the ISGRI data in the high energy part of the presented X-ray spectrum.

The seemingly most prominent change is that in the values of  $r_{\text{in}}$  and  $T_{\text{in}}$ . Both parameters run against the boundaries corresponding to the lowest contribution of the disc to the spectrum. However, changing the parameters manually to those obtained in the *RXTE* only fits does not lead to significant changes in the spectrum:  $\chi^2$  increases from 399 to 401 for 234 degrees of freedom, i.e., the parameters  $r_{\text{in}}$  and  $T_{\text{in}}$  do not significantly contribute to the overall spectral shape and the error bars on these parameters would be very large (for *RXTE* only fits they indeed mostly extend over the whole allowed parameter range, M. Böck, priv.comm.).

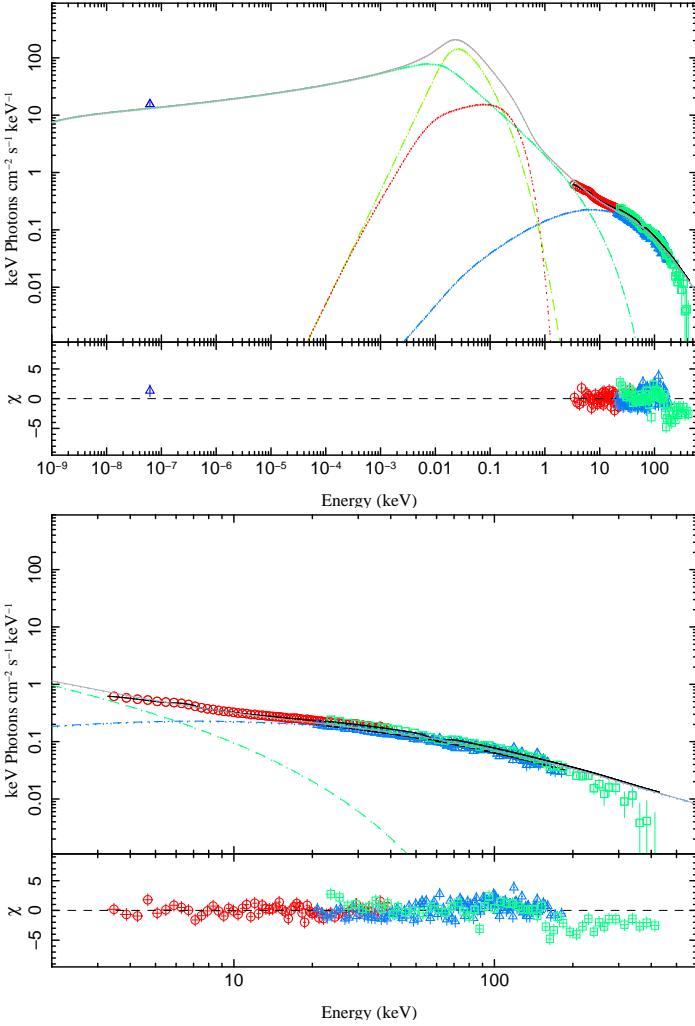


Figure 8.12: Best fit for  $T_e$  free for *RXTE* and *INTEGRAL* data. Representation of data and model components are as explained in Fig. 8.9.

Overall, the reflection fraction increases by a factor of two from the *RXTE* only ( $\Omega/2\pi = 0.045$ ) to the joint *RXTE* and *INTEGRAL* fit ( $\Omega/2\pi = 0.10$ ), while the jet becomes slightly more magnetically dominated (increase in  $k$  from 2.11 to 2.57) and the temperature of the input electrons  $T_e$  and the overall input power  $N_j$  decrease. A slightly smaller  $r_0$  indicates a more compact nozzle region. The normalisation constants  $C_{\text{HEXTE}}$  and  $C_{\text{ISGRI}}$  are in very good agreement with those obtained from the broken power law fits. Note however the change in  $C_{\text{HEXTE}}$  from the *RXTE* only fit (0.839) to the joint fit (0.849). The Hydrogen number density is still high.

### 8.3.4 Conclusions

Best fitting models for different input electron temperature regimes have been presented by Maitra et al. (2009) for GX 339–4. Their data, while including some infrared observations, did not include any observations above 200 keV. Here it has been shown that the high energy data as obtained by *INTEGRAL* can be used to further constrain the model and to help derive the real physical parameters. For the case of Cyg X-1 it implies that solutions with low input electron temperature  $T_e < 3 \times 10^{10}$  K do not allow for a proper description of data above 200 keV though they offer a good description in the energy range of *RXTE* (3–200 keV). Note that changes to be introduced in the next version of the model will have no or very small influence on fits with  $T_e < 3 \times 10^{10}$  K.

The best fit with free  $T_e$  demonstrates that the inclusion of high energy (*INTEGRAL*)

data allows to better constrain the parameters of the model – the best fit solution to *RXTE* data only might not be the one describing the high energy part of the spectrum reasonably well.

However, the results for  $T_e > 3 \times 10^{10}$  K have to be treated with caution. On the one hand, the high electron temperature solution might require a better treatment of pair production in the jet as will be included in the next version of the model. This will introduce changes to the high energy spectrum and should allow for a better modelling of the cutoff. On the other hand the  $\chi^2$  space has not yet been fully explored as such a time and CPU expensive approach is not reasonable knowing the current limitations of model and uncertainties in the data, where the existence of the Tungsten instrumental background line (see Sec. 7.4.1) and uncertainties in the slope (Lubiński, 2009) introduce additional errors.

All the presented fits indicate that the spectral break at about 10 keV (clearly discernibly in the broken power law fits in Sec. 8.2 for the here discussed observation and in all observations of the *RXTE* campaign in Sec. 6.1.2) is not only due to reflection. Though reflection does contribute, the basis continuum is more complex and the intrinsic shape of the Comptonization hump as well as the change from the synchrotron dominated to the Comptonization hump dominated part of the spectrum also contribute to the spectral break. This behaviour was also observed by Nowak et al. (2010, and references therein).

# 9 Summary and Outlook

*Some problems are so complex  
that you have to be highly intelligent and well informed  
just to be undecided about them.  
– Laurence J. Peter –*

In Sec. 9.1 I give a short summary over the individual sub-projects which constitute this thesis and their results. For a more in detail discussion of the individual results, see the referred sections. This is followed by an outlook in Sec. 9.2.

## 9.1 Summary

Data from two different observations campaign of the black hole candidate Cyg X-1 have been analysed in this work: the bi-weekly observation campaign with *RXTE* and the *INTEGRAL* Key Programme. For both data sets spectral and timing analysis was performed.

- A spectral overview analysis of the *RXTE* legacy observation campaign was performed in Sec. 6.1. I could confirm previous results for the spectral behaviour of Cyg X-1 for both broken power law and simple Comptonization models. This long-term analysis of spectra on *RXTE* orbit-to-orbit basis ( $\sim 90$  min) constitutes the context for any further analysis of the source.
- In Sec. 6.2 I performed and discussed X-ray timing analysis of three *RXTE* observations during a radio flare in 2005, which constitute an overview over a failed state transition, which was also observed in the infrared with *Spitzer*. A joint analysis with *Spitzer* data to study jet properties is in preparation (Rahoui, ..., VG, et al. (in prep.))
- A comparison of different dithering pattern of the *INTEGRAL* satellite (observations at end of 2009) and the quality of the data obtained with them was conducted in Sec. 7.1: This directly influences the strategy of the future Cyg X-1 Key Programme (KP) observations, since the customised random dithering pattern and not the so far used standard hex dithering pattern was found to offer best image quality.
- I performed tests of different image reconstruction approaches to decide on the best way to conduct further analysis of the Cyg X-1 KP (Sec. 7.2): fitting the source position offers the best results for the Cyg X-1 field. A larger collaboration including scientists at ESAC in Spain (M. Cadolle Bel) and CRESST/NASA-GSFC and UMBC in the USA (D. M. Marcu and K. Pottschmidt) benefits from this finding, as it allows a consistent treatment of the Cyg X-1 field. In addition, a further interesting source, the symbiotic binary 3A 1954+319 was found to be active within the IBIS and partly JEM-X field of view during the Cyg X-1 KP. This source and the long-term evolution of its period was presented as a poster by Marcu, ..., VG et al. (2010) and is the topic of a forthcoming paper by Marcu, ..., VG, et al. (in prep.)
- I have tested different lightcurve extraction algorithms and evaluated the high time resolution INTEGRAL-ISGRI lightcurves of Cyg X-1 for an exemplary observation in 2007 in Sec. 7.3. This is an important step towards opening the new observational window of studying black hole timing above 20 keV. Results

of this analysis have been presented as a poster<sup>1</sup> at the 7th INTEGRAL/BART Workshop in Karlovy Vary, Czech Republic (14.–18. April 2010). A refereed publication in the proceeding of the workshop is forthcoming (Grinberg et al., 2010, in prep.). The conclusion that only the `ii_light` algorithm does offer the possibility for high time resolution studies and provides reliable results led to the return of the algorithm into the *INTEGRAL* standard software package OSA with OSA 9.

- I modelled the 17–500 keV ISGRI spectra of Cyg X-1 from the 2007–2009 period to probe the parameter space of these mainly exceptionally hard observations (Sec. 7.4). This assessment allowed for a better understanding of calibration features, especially the Tungsten instrumental background line and prompted improvements in the instrumental responses for the instruments in the newest software version OSA 9. Parts of the spectral analysis have been included into posters by Pottschmidt, ..., VG et al. (2010b) and Pottschmidt, ..., VG et al. (2010a).
- The last step of this thesis was the application of jet models to a selected multi-wavelength data set of Cyg X-1 as observed in 2008 (Sec. 8). I have shown that the additional ISGRI data allow to better constrain the model and to exclude certain areas of the parameter space (here: low input electron temperature solution) where a comparatively good fit for *RXTE* data only is possible. Additionally, the fits showed that the spectral break seen in the spectrum of Cyg X-1 at about 10 keV is only partly due to reflection, which agrees with previous results of jet model fits to data not including the 200–500 keV range.

## 9.2 Outlook

Even though Cyg X-1 is one of the best studied black holes candidates there is still plenty to understand both regarding this individual source and the big context of galactic black holes and even AGN. This thesis is only a first step in my work towards an understanding of the broadband variability of Cyg X-1.

I will use the timing analysis techniques learned during the analysis of three example observation in Sec. 6.2 to conduct timing analysis of the whole bi-weekly *RXTE* observation campaign of Cyg X-1 from 1996 to today and analyse the possible spectro-timing correlation to extend the work of Böck, VG, et al. (in prep.), who performed spectro-timing analysis of a single, exceptionally well-sampled state transition. The full Cyg X-1 campaign offers an unique possibility to track the behaviour of a source over now 14 years and to connect the short- and long term evolution of the spectral and timing properties, both during flaring and exceptionally hard phases.

For *INTEGRAL* data, the first step will be a thorough testing of the new version of the *INTEGRAL* software, OSA 9, which should include an improved treatment of the time-dependent gain of the ISGRI instrument and therefore not show the problems with the Tungsten instrumental background line found in Sec. 7.4. This will allow a detailed analysis of the *INTEGRAL* spectra, including the use of the more complex and physically justified Comptonization model `eqpair`.

Though only few exist, the contemporary *INTEGRAL* and *RXTE* data sets will offer the possibility to better understand the anomalous noise in the *INTEGRAL* PSDs and therefore pave the way for timing analysis above 20 keV. These data sets will, once

---

<sup>1</sup><http://eos.asu.cz/ibws10/media/uploads/Grinberg.pdf>

better calibrated, offer the unique opportunity to test the improved jet-model in the high energy regime, where higher order corrections to the classic approach become important, and to compare it to pure Comptonization models.

# References

- Abubekerov M.K., Antokhina E.A., Cherepashchuk A.M., 2004, *Astronomy Reports* 48, 550
- Arnaud K., Dorman B., Gordon C., 2007, XSPEC Users Guide, HEASARC, NASA/GSFC, <http://heasarc.gsfc.nasa.gov/docs/xanadu/xspec/>
- Aschenbach B., 1985, *Rep. Progr. Phys.* 48, 579
- Axelsson M., Borgonovo L., Larsson S., 2005, *A&A* 438, 999
- Belloni T., Homan J., Casella P., et al., 2005, *A&A* 440, 207
- Belloni T., Mendez M., van der Klis M., et al., 1996, *Astrophys. J., Lett.* 472, L107
- Belloni T.M., 2010, In: T. Belloni (ed.) *The Jet Paradigm, Lecture Notes in Physics* 794, Berlin Springer Verlag, p.53
- Bevington P.R., Robinson D.K., 1992, Data reduction and error analysis for the physical sciences, 2nd ed., McGraw-Hill, New York
- Blandford R.D., Znajek R.L., 1977, *MNRAS* 179, 433
- Böck M., 2008, Spectral-Temporal Correlations in the X-ray Emission of Cygnus X-1, Diploma thesis, Dr.-Remeis Sternwarte, Universität Erlangen-Nürnberg
- Boeck M., Hanke M., Wilms J., et al., 2008, In: VII Microquasar Workshop: Microquasars and Beyond., PoS (MQW7)
- Bowyer S., Byram E.T., Chubb T.A., Friedman H., 1965, *Science* 147, 394
- Bracewell R.N., 2000, *The Fourier Transform and Its Applications*, McGraw-Hill, New York
- Brenneman L.W., Reynolds C.S., 2006, *ApJ* 652, 1028
- Brocksopp C., Fender R.P., Larionov V., et al., 1999a, *MNRAS* 309, 1063
- Brocksopp C., Tarasov A.E., Lyuty V.M., Roche P., 1999b, *A&A* 343, 861
- Cadolle Bel M., Goldwurm A., Rodriguez J., et al., 2006a, In: Barret D., Casoli F., Lagache G., Lecavelier A., Pa-  
gani L. (eds.) SF2A-2006: Semaine de l'Astrophysique Francaise., p.119
- Cadolle Bel M., Sizun P., Goldwurm A., et al., 2006b, *A&A* 446, 591
- Carroll B.W., Ostlie D.A., 2006, An introduction to modern astrophysics and cosmology, San Francisco: Pearson
- Carter B., 1971, *Phys. Rev. Lett.* 26, 331
- Cattaneo A., Faber S.M., Binney J., et al., 2009, *Nat* 460, 213
- Chandrasekhar S., 1931, *ApJ* 74, 81
- Charles P., Fabian A., 2001, *Astronomy and Geophysics* 42, Issue 6, p.11
- Chernyakova M., 2005, Introduction to INTEGRAL Data Analysis, [http://isdcu3.unige.ch/Soft/download/osa/osa\\_doc/osa\\_doc-8.0/osa\\_um\\_intro-5.1.pdf](http://isdcu3.unige.ch/Soft/download/osa/osa_doc/osa_doc-8.0/osa_um_intro-5.1.pdf)
- Chernyakova M., Kretschmar P., Neronov A., Beckmann V., 2009, JEM-X Analysis User Manual, [http://isdcu3.unige.ch/Soft/download/osa/osa\\_doc/osa\\_doc-8.0/osa\\_um\\_jemx-8.0.pdf](http://isdcu3.unige.ch/Soft/download/osa/osa_doc/osa_doc-8.0/osa_um_jemx-8.0.pdf)
- Chernyakova M., Neronov A., 2008, IBIS Analysis User Manual 7.0, [http://isdcu3.unige.ch/Soft/download/osa/osa\\_doc/osa\\_doc-8.0/osa\\_um\\_ibis-7.0.pdf](http://isdcu3.unige.ch/Soft/download/osa/osa_doc/osa_doc-8.0/osa_um_ibis-7.0.pdf)
- Coppi P.S., 1992, *MNRAS* 258, 657
- Coppi P.S., 1999, In: J. Poutanen & R. Svensson (ed.) *High Energy Processes in Accreting Black Holes*, Astronomical Society of the Pacific Conf. Proc. 161, p.375
- Corbet R.H.D., Sokoloski J.L., Mukai K., et al., 2008, *ApJ* 675, 1424
- Courvoisier T., Walter R., Beckmann V., et al., 2003, *A&A* 411, L53
- Dauser T., Reynolds C.S., Brenneman L.W., et al., 2010, *MNRAS*, submitted
- Davis J.E., 2001, *ApJ* 548, 1010
- Del Santo M., Belloni T.M., Homan J., et al., 2009, *MNRAS* 392, 992
- Del Santo M., Malzac J., Jourdain E., et al., 2008, *MNRAS* 390, 227
- Dhawan V., Mirabel I.F., Rodríguez L.F.,

- 2000, ApJ 543, 373
- Droulans R., Belmont R., Malzac J., Jourdain E., 2010, ApJ, in press, ArXiv <http://arxiv.org/abs/1005.3195>
- Dunn R.J.H., Fender R.P., Körding E.G., et al., 2010, MNRAS 403, 61
- Ebisawa K., Ueda Y., Inoue H., et al., 1996, ApJ 467, 419
- Fabian A.C., Iwasawa K., Reynolds C.S., Young A.J., 2000, PASP 112, 1145
- Fender R., 2010, In: T. Belloni (ed.) The Jet Paradigm, Lecture Notes in Physics 794, Berlin Springer Verlag, p.115
- Fender R.P., Belloni T.M., Gallo E., 2004, MNRAS 355, 1105
- Fender R.P., Homan J., Belloni T.M., 2009, MNRAS 396, 1370
- Fender R.P., Stirling A.M., Spencer R.E., et al., 2006, MNRAS 369, 603
- Forman W., Jones C., Cominsky L., et al., 1978, ApJS 38, 357
- Frank J., King A., Raine D.J., 2002, Accretion Power in Astrophysics: Third Edition, Cambridge University Press, Cambridge
- Friend D.B., Castor J.I., 1982, ApJ 261, 293
- Fritz S., 2008, X-ray observations of black hole and neutron star binary systems, Ph.D. thesis, Universität Tübingen
- Fürst F., 2008, Investigations of the SAA and the long-time behavior of Vela X-1, Diploma thesis, Dr.-Remeis Sternwarte, Universität Erlangen-Nürnberg
- Fürst F., Kreykenbohm I., Pottschmidt K., et al., 2010, A&A, submitted
- Fürst F., Wilms J., Rothschild R.E., et al., 2009, Earth and Planetary Science Letters 281, 125
- Gallo E., 2010, In: T. Belloni (ed.) The Jet Paradigm, Lecture Notes in Physics 794, Berlin Springer Verlag, p.85
- Gallo E., Corbel S., Fender R.P., et al., 2004, MNRAS 347, L52
- Gallo E., Fender R., Kaiser C., et al., 2005, Nat 436, 819
- Gallo E., Fender R.P., Pooley G.G., 2003, MNRAS 344, 60
- Giacconi R., Gursky H., Paolini F.R., Rossi B.B., 1962, Phys. Rev. Let. 9, 439
- Gierliński M., Done C., 2004, MNRAS 347, 885
- Gies D.R., Bolton C.T., 1986, ApJ 304, 371
- Gleißner T., 2004, Ph.D. thesis, Universität Tübingen
- Gleissner T., Wilms J., Pooley G.G., et al., 2004a, A&A 425, 1061
- Gleissner T., Wilms J., Pottschmidt K., et al., 2004b, A&A 414, 1091
- Goldwurm A., David P., Foschini L., et al., 2003, A&A 411, L223
- Golian S.E., Krause E.H., Perlow G.J., 1946, Physical Review 70, 223
- Groeneveld H.A., 1999, Design, Simulation und Optimierung kodierter Aperturen, Ph.D. thesis, Universität Tübingen
- Grupen C., Schwartz B., 2008, Particle Detectors: Second Edition, Cambridge University Press
- Hanke M., 2007, High-resolution X-ray Spectroscopy of the Black Hole Cygnus X-1 with the Chandra X-ray Observatory, Diploma thesis, Dr.-Remeis Sternwarte, Universität Erlangen-Nürnberg
- Hanke M., Wilms J., Nowak M.A., et al., 2010, Proc. 3rd Suzaku Conf. ‘The Energetic Cosmos: From Suzaku to Astro-H’
- Hanke M., Wilms J., Nowak M.A., et al., 2009, ApJ 690, 330
- Herrero A., Kudritzki R.P., Gabler R., et al., 1995, A&A 297, 556
- Hjellming R.M., Wade C.M., 1971, Astophys. J., Lett. 168, L21+
- Hjellming R.M., Wade C.M., Hughes V.A., Woodsworth A., 1971, Nat 234, 138
- Houck J.C., 2002, In: G. Branduardi-Raymont (ed.) High Resolution X-ray Spectroscopy with XMM-Newton and Chandra., Proc. High resolution X-ray spectroscopy with XMM-Newton and Chandra, MSSL
- Houck J.C., Denicola L.A., 2000, In: N. Manset, C. Veillet, & D. Crabtree (ed.) Astronomical Data Analysis Software and Systems IX, Astronomical Society of the Pacific Conf. Proc. 216, p.591
- Hua X., Titarchuk L., 1995, ApJ 449, 188
- Hutchings J.B., 1978, ApJ 226, 264

- Ibragimov A., Zdziarski A.A., Poutanen J., 2007, MNRAS 381, 723
- in't Zand J.J.M., 1992, A Coded-Mask Imager as Monitor of Galactic X-Ray Sources, Ph.D. thesis, Space Research Organization Netherlands, Sorbonnelaan 2, 3584 CA Utrecht, The Netherlands
- Jahoda K., Markwardt C.B., Radeva Y., et al., 2006, ApJS 163, 401
- Jahoda K., Swank J.H., Giles A.B., et al., 1996, In: O. H. Siegmund & M. A. Gumin (ed.) Proc. SPIE 2808, p. 22
- Kalemci E., Tomsick J.A., Rothschild R.E., et al., 2003, ApJ 586, 419
- Kerr R.P., 1963, Phys. Rev. Lett. 11, 237
- Kirsch M.G., Briel U.G., Burrows D., et al., 2005, Crab: the standard x-ray candle with all (modern) x-ray satellites, In: O. H. W. Siegmund (ed.), Proc. SPIE 5898, p. 22
- Kleinknecht K., 1998, Detectors for particle radiation, Cambridge University Press
- Klochkov D., 2007, Ph.D. thesis, Universität Tübingen
- Körding E., Falcke H., 2004, A&A 414, 795
- Körding E., Rupen M., Knigge C., et al., 2008, Science 320, 1318
- Körding E.G., Jester S., Fender R., 2006, MNRAS 372, 1366
- Kreykenbohm I., 2004, Ph.D. thesis, Universität Tübingen
- Kreykenbohm I., Wilms J., Kretschmar P., et al., 2008, A&A 492, 511
- Kylafis N.D., Papadakis I.E., Reig P., et al., 2008, A&A 489, 481
- Lachowicz P., Zdziarski A.A., Schwarzenberg-Czerny A., et al., 2006, MNRAS 368, 1025
- Leahy D.A., Darbro W., Elsner R.F., et al., 1983, ApJ 266, 160
- Levine A.M., Bradt H., Cui W., et al., 1996, Astrophys. J., Lett. 469, L33
- Liu Q.Z., van Paradijs J., van den Heuvel E.P.J., 2006, A&A 455, 1165
- Lubiński P., 2009, A&A 496, 557
- Lund N., Budtz-Jørgensen C., Westergaard N.J., et al., 2003, A&A 411, L231
- Magdziarz P., Zdziarski A.A., 1995, MN- RAS 273, 837
- Maitra D., Markoff S., Brocksopp C., et al., 2009, MNRAS 398, 1638
- Makishima K., Maejima Y., Mitsuda K., et al., 1986, ApJ 308, 635
- Malzac J., Belmont R., Fabian A.C., 2009, MNRAS 400, 1512
- Malzac J., Lubiński P., Zdziarski A.A., et al., 2008, A&A 492, 527
- Marcu D., Fuerst F., Grinberg V., et al., 2010, Bull. AAS 41, p.726
- Markoff S., 2010, In: T. Belloni (ed.) The Jet Paradigm, Lecture Notes in Physics 794, Berlin Springer Verlag, p.143
- Markoff S., Falcke H., Fender R., 2001, A&A 372, L25
- Markoff S., Nowak M., Corbel S., et al., 2003, A&A 397, 645
- Markoff S., Nowak M.A., 2004, ApJ 609, 972
- Markoff S., Nowak M.A., Wilms J., 2005, ApJ 635, 1203
- Mas-Hesse J.M., Giménez A., Culhane J.L., et al., 2003, A&A 411, L261
- Masetti N., Orlandini M., Palazzi E., et al., 2006, A&A 453, 295
- Masetti N., Rigon E., Maiorano E., et al., 2007, A&A 464, 277
- Mattana F., Götz D., Falanga M., et al., 2006, A&A 460, L1
- McClintock J.E., Remillard R.A., 2006, Black Hole Binaries, Cambridge University Press, Cambridge, p.157
- McConnell M.L., Ryan J.M., Collmar W., et al., 2000, ApJ 543, 928
- McConnell M.L., Zdziarski A.A., Bennett K., et al., 2002, ApJ 572, 984
- McKinney J.C., 2006, MNRAS 368, 1561
- Mitsuda K., Inoue H., Koyama K., et al., 1984, PASJ 36, 741
- Miyamoto S., Kimura K., Kitamoto S., et al., 1991, ApJ 383, 784
- Motta S., Belloni T., Homan J., 2009, MNRAS 400, 1603
- Muñoz-Darias T., Motta S., Pawar D., et al., 2010, MNRAS 404, L94
- Murdin P., Webster B.L., 1971, Nat 233, 110
- Ninkov Z., Walker G.A.H., Yang S., 1987,

- ApJ 321, 425
- Nowak M.A., 2000, MNRAS 318, 361
- Nowak M.A., 2009, X-ray Spectroscopy: In Theory and Practice, talk at '1st Summerschool for Multiwave-length Astronomy', CEA Saclay, Paris [http://pulsar.sternwarte.uni-erlangen.de/black-hole/1stschool/coursematerial/X-ray-Spectroscopy\\_School\\_Final.pdf](http://pulsar.sternwarte.uni-erlangen.de/black-hole/1stschool/coursematerial/X-ray-Spectroscopy_School_Final.pdf)
- Nowak M.A., Hanke M., Trowbridge S.N., 2010, ApJ, submitted
- Nowak M.A., Lehr D.E., 1998, In: M. A. Abramowicz, G. Bjornsson, and J. E. Pringle. (ed) Theory of Black Hole Accretion Disks, Cambridge University Press, Cambridge, p.233
- Nowak M.A., Vaughan B.A., Wilms J., et al., 1999, ApJ 510, 874
- Nowak M.A., Wilms J., Dove J.B., 2002, MNRAS 332, 856
- Nowak M.A., Wilms J., Heinz S., et al., 2005, ApJ 626, 1006
- Oppenheimer J.R., Volkoff G.M., 1939, Physical Review 55, 374
- Padmanabhan T., 2000, Theoretical Astrophysics - Volume 1, Astrophysical Processes, Cambridge University Press, Cambridge
- Pirner S., 2009, Timing Analysis of the Accreting X-Ray Binary Cygnus X-1, Diploma thesis, Dr.-Remeis Sternwarte, Universität Erlangen-Nürnberg
- Pooley G.G., 2006, In: VI Microquasar Workshop: Microquasars and Beyond, PoS (MQW6).
- Pooley G.G., Fender R.P., 1997, MNRAS 292, 925
- Pooley G.G., Fender R.P., Brocksopp C., 1999, MNRAS 302, L1
- Postnov K.A., Yungelson L.R., 2006, Living Reviews in Relativity 9, 6
- Pottschmidt K., 2002, Ph.D. thesis, Universität Tübingen
- Pottschmidt K., Marcu D.M., Grinberg V., et al., 2010a, Bull. AAS 41, p.225
- Pottschmidt K., Marcu D.M., Grinberg V., et al., 2010b, Bull. AAS 41, p.671
- Pottschmidt K., Wilms J., Chernyakova M., et al., 2003a, A&A 411, L383
- Pottschmidt K., Wilms J., Nowak M., et al., 2006, Advances in Space Research 38, p. 1350
- Pottschmidt K., Wilms J., Nowak M.A., et al., 2000, A&A 357, L17
- Pottschmidt K., Wilms J., Nowak M.A., et al., 2003b, A&A 407, 1039
- Poutanen J., Zdziarski A.A., Ibragimov A., 2008, MNRAS 389, 1427
- Pringle J.E., 1981, ARA&A 19, 137
- Rappaport S., Zaumen W., Doxsey R., 1971, ApJ 168, L17
- Remillard R.A., McClintock J.E., 2006, ARA&A 44, 49
- Reynolds C.S., Nowak M.A., 2003, Physics Reports 377, 389
- Rodriguez J., Hannikainen D.C., Shaw S.E., et al., 2008a, ApJ 675, 1436
- Rodriguez J., Shaw S.E., Hannikainen D.C., et al., 2008b, ApJ 675, 1449
- Rothschild R.E., Blanco P.R., Gruber D.E., et al., 1998, ApJ 496, 538
- Rybicki G.B., Lightman A.P., 1979, Radiative Processes in Astrophysics, New York, Wiley-Interscience
- Sabatini S., Tavani M., Striani E., et al., 2010, Astrophys. J., Lett. 712, L10
- Shakura N.I., Sunyaev R.A., 1973, A&A 24, 337
- Shapiro S.L., Teukolsky S.A., 1983, Black holes, white dwarfs, and neutron stars: The physics of compact objects, New York, Wiley-Interscience
- Skinner G.K., 1995, Experimental Astronomy 6, 1
- Skinner G.K., 2004, New Astronomy Review 48, 205
- Staelin D.H., Reifenstein, III E.C., 1968, Science 162, 1481
- Stirling A.M., Spencer R.E., de la Force C.J., et al., 2001, MNRAS 327, 1273
- Suchy S., Pottschmidt K., Wilms J., et al., 2008, ApJ 675, 1487
- Tananbaum H., Gursky H., Kellogg E., et al., 1972, Astrophys. J., Lett. 177, L5
- Tananbaum H., Kellogg E., Gursky H., et al., 1971, Astrophys. J., Lett. 165,

- Thorne K.S., 1974, ApJ 191, 507  
 Titarchuk L., 1994, ApJ 434, 570  
 Titarchuk L., Lyubarskij Y., 1995, ApJ 450, 876  
 Ubertini P., Lebrun F., Di Cocco G., et al., 2003, A&A 411, L131  
 Uttley P., McHardy I.M., Vaughan S., 2005, MNRAS 359, 345  
 van der Klis M., 1989, In: H. Ögelman & E. P. J. van den Heuvel (ed.) Timing Neutron Stars., Proc. of the NATO Advanced Study Institute on Timing Neutron Stars, Kluwer Academic / Plenum Publishers, New York p.27  
 Vaughan B.A., Nowak M.A., 1997, Astrophys. J., Lett. 474, L43  
 Vedrenne G., Roques J.P., Schönfelder V., et al., 2003, A&A 411, L63  
 Warwick R.S., Marshall N., Fraser G.W., et al., 1981, MNRAS 197, 865  
 Webster B.L., Murdin P., 1972, Nat 235, 37  
 Westergaard N.J., Kretschmar P., Oxborrow C.A., et al., 2003, A&A 411, L257  
 Wilms J., 1998, X-rays From Galactic Black Holes: Theory and Observation, Ph.D. thesis, Universität Tübingen  
 Wilms J., Allen A., McCray R., 2000, ApJ 542, 914  
 Wilms J., Nowak M.A., Pottschmidt K., et al., 2006, A&A 447, 245  
 Wilms J., Pottschmidt K., Pooley G.G., et al., 2007, ApJ 663, L97  
 Winkler C., Courvoisier T.J.L., Di Cocco G., et al., 2003, A&A 411, L1  
 Zhang H., Yuan F., Chaty S., 2010, ApJ, in press, ArXiv <http://arxiv.org/abs/1005.4245>  
 Ziolkowski J., 2005, MNRAS 358, 851

# Acknowledgements

This thesis would not have been possible without the support of many people:

Jörn Wilms of Dr Remeis Observatory in Bamberg not only offered me the possibility to perform this thesis in Bamberg, but also, together with Katja Pottschmidt, convinced me to follow my heart and focus on astrophysics back at the summer academy in LaVilla. He is also the person who infected me with the love for Cyg X-1, introduced the works of Neil Gaiman to me, made it possible for me to go to the conferences in Bologna and Ferrara, never failed to calm me down whenever I was on the verge of panic because of deadlines, untamed software or just so, and much more. If I start listing all the things I learned from you, Jörn, this thesis will get a few and more than a few more pages, so I will just say: thank you! I owe far more to you than just this thesis.

Katja Pottschmidt of now NASA-GSFC and UMBC organised the black hole collaboration telecons, gave many the ideas for analysis and always found time to answer my questions and address the problems I had, both during her visit here last summer and on the phone or via e-mails. Thank you a lot for this! And also for San Diego, for LaVilla, for the Jelly Beans and just for being there! To see you and your work gave me courage to stay in the field.

Ingo Kreykenbohm (Remeis) have taught me a lot about *INTEGRAL* and its idiosyncrasies and without his scripts the analysis would have been less ... Well, I cannot say smooth, but it would have been even worse without your help! Not to mention all the times when you helped me with computer troubles.

Manfred Hanke (Remeis) never sent me away when I came with questions, whether about ISIS, or science or just computers. He is also the person who caught perhaps the most slips in my argumentation. Thank you for all the help and all the fruitful and heated discussions, whether live or via e-mail. And I cannot thank you enough for all the work you've done improving ISIS and teaching us how to use it. The ISIS tutorials were great!

The *RXTE* part of this work would not have been possible without the help of Moritz Böck (Remeis) and Felix Fürst was the person who introduced me to *INTEGRAL* analysis and *INTEGRAL* timing. I've also learned a lot about coding from the programs they provided as examples. Thank you, guys!

The black hole telecons, organized by Katja Pottschmidt, never failed to inspire me. The discussion – with Katja, Jörn, Marion Cadolle Bel (ESAC/Madrid), Jerome Rodriguez (CEA/Saclay), Diana M. Marcu (NASA-GSFC and UMBC), Anne Lohfink (Remeis and now UMBC) and Maria Obst (Remeis) – were a major input for this work. Special thanks here to Marion and Jerome, for providing the OSA 8 data for the comparisons and for the in depth discussion of the extraction pipelines and to Diana, whom I worked with closely for the *INTEGRAL* extractions.

Carlo Ferringo (IAAT/Tübingen and ISDC/Versoix) developed the alternative PIF based lightcurve extraction mechanism and provided the data. Isabel Caballero (CEA Saclay) invested a lot of her time on improving the *INTEGRAL* calibration and helped me better understanding the problems. Alex Markowitz (UCSD/San Diego) helped to improve my poster for the Karlsbad conference and had interesting ideas on how the timing analysis can proceed. Thomas Dauser (Remeis) provided some great iron line plots and the corresponding literature. Sera Markoff (API/Amsterdam) provided the jet model and, together with Michael Nowak (MIT/Cambridge), additional information on its usage. Guy Pooley made the *Ryle/AMI* data available, without which a real

broadband analysis would not have been possible available. I think it is pretty clear that this work would not have been possible in this form without their input.

Some others contributed with their ideas and through discussions and kind words. Hermann Brunner (MPE/Garching) and Slawomir Suchy (UCSD/San Diego) have sacrificed more than a few hours of their weekends for e-mail discussions and comments. Thank you also for bearing with me during the worst phases!

Thanks goes also to Pablo Cassatella (University of Southampton) for his ideas and especially for the photo with Roy Kerr!

Even if we did not work together, I want to thank Matthias Kadler (Remeis) for the kind words when I was down and needed them. The same goes for everyone from the Remeis Gang, whether X-ray or optical astronomers. Thank you, guys and girls!

Flo - I would not be me without you. Thank you for everything: for knowing when to push me and when to hold, when to discuss and when just to listen, for letting me go to Bamberg and visiting here ... Just for everything!

My parents always have been there for me. Without their encouragement I would not be here. Spasibo!

Harald Lesch (USM/Munich) made it possible for me to write this thesis at the Remeis Observatory. I am deeply thankful for that.

And last, but not least, I am deeply indebted to the Studienstiftung des deutschen Volkes, both as itself and as the representatives of the Max Weber Programm Bayern, especially Hella Kohrs-Kaumanns, Julia Apitzsch and Margrit Lichtschlag. It is not only, that I received financial help throughout my studies and could enjoy both additional seminars and financial help for my time abroad in Amsterdam, but the Summer Academy in LaVilla was also the turning point in my university career, the very moment when I realised that I should follow my heart and go for astronomy, no matter what others say.



## **Erklärung**

der Diplomandin  
**Victoria Grinberg**  
geboren in Chishinau

Mit der Abgabe der Diplomarbeit versichere ich, dass ich die Arbeit selbstständig vefasst und keine anderen als die angegebenen Quellen und Hilfsmittel benutzt habe.

*Ort, Datum*

*Unterschrift*